Quenching and Partitioning

A New Steel Heat Treatment Concept

Timothy David Bigg

Submitted in accordance with the requirements for the degree of
Doctor of Philosophy

The University of Leeds
School of Process, Environmental, and Materials Engineering

February 2011

The candidate confirms that the work submitted is his own, except where work which has formed part of jointly-authored publications has been included. The contribution of the candidate and the other authors to this work has been explicitly indicated below. The candidate confirms that appropriate credit has been given within the thesis where reference has been made to the work of others.

Publications have been made based on material contained in Chapter 7 and Chapter 9 of this thesis. The citations for these publications are as follows:

T.D. Bigg and D.V. Edmonds, Microstructural evolution during the novel Quenching and Partitioning (Q&P) heat treatment of steel, presented at PRICM7, The 7th Pacific Rim International Conference on Advanced Materials and Processing, 2-6th August 2010, Cairns, Australia, published in: Materials Science Forum Volumes 654-656 (2010) pages 33-36

T.D. Bigg, D.K. Matlock, J.G. Speer and D.V. Edmonds, Dynamics of the Quenching and Partitioning (Q&P) Process, presented at PTM2010, Solid-Solid Phase Transformations in Inorganic Materials, 6-11th June 2010, Avignon, France, to be published in a special issue of Solid State Phenomena

For both of the publications cited above, the candidate was the lead author and the publication was based on research conducted solely by the candidate.

Acknowledgements

I would like to express my gratitude to **Professor David Edmonds** for his proposal and supervision of the research project, and the UK **Engineering and Physical Sciences Research Council** (EPSRC) for financial support via the provision of a Doctoral Training Award (DTA). Within the Institute for Materials Research, thanks are due to **Diane Cochrane** for training on laboratory equipment and techniques, **Donald Forder** for repairs to laboratory equipment, and **Joy Bielby** for assisting with many administrative tasks. For X-ray diffraction measurements I am grateful to **David Wright** and **Dr. Tim Comyn** for performing measurements in the Institute for Materials Research X-ray laboratory, **Lesley Neve** and **Dr. Juan Rodríguez-Blanco** are acknowledged for performing measurements in the School of Earth and Environment (SEE) X-Ray laboratory. Neutron diffraction measurements were made with a beamtime allocation from the UK **Science and Technology Facilities Council** (STFC) for the use of the High Resolution Powder Diffractometer (HRPD) at ISIS, Rutherford Appleton Laboratory. I am grateful to **Dr. Richard Ibberson** for performing trial measurements on HRPD and **Dr. Aziz Daoud-Aladine** for assisting with the use of HRPD during the beam time allocation, **Dr. Edwin Eardley** is also acknowledged for forming an essential part of the team from the Institute of Materials Research that made the measurements on HRPD. **Dr. Richard Walshaw** provided electron microscopy training. Computer simulation source code was made available by the **Materials Algorithms Project** website hosted by the University of Cambridge, I am also grateful to **Dr. Andrew Watson** for performing MTDATA predictions in support of the computer simulations. I am indebted to **Dr. Robert Cochrane** and **Professor Robert Cochrane** for their valuable critique and suggestions at the first year review stage of the project. Lastly, I would like to thank **My Family** for their support during my studies.

Abstract

Steel continues to be one of the primary materials in use today, however, even after 200 years of published research, innovative methods are being discovered and exploited to produce steel with enhanced properties. One such recent discovery has been termed Quenching and Partitioning (Q&P). The Q&P heat treatment process is reported to produce a multiphase microstructure consisting of retained austenite stabilised to room temperature, and a harder martensitic phase. This combination is prospected to form a new generation of high strength, formable sheet steel well suited to the demands of the automotive industry. Previous research has reported on the application of Q&P to commercial grades of steel, however, the temperatures required have hampered study of the process. In this investigation a model alloy has enabled separation of Q&P into its individual stages for closer inspection. Standard metallographic techniques were used to examine the microstructure of the material, followed by X-ray diffraction measurements to determine the stability of the austenite phase fraction before and after partitioning, confirming the effectiveness of the partitioning process in stabilising retained austenite. Estimations of carbon concentration via lattice parameter measurements have provided evidence of austenite carbon enrichment, but also suggest that some carbon remains unaccounted for, possibly as an equilibrium distribution between epsilon carbides and strained interstitial sites. In-situ partititioning in a neutron diffractometer has been utilised to obtain real-time measurements of the partitioning process. These measurements suggest that redistribution of carbon within martensite occurs before partitioning to austenite becomes kinetically significant. The trapping of carbon within energetically favourable locations is postulated to be a major factor in retarding carbon migration from martensite to austenite when compared to mathematical models of the partitioning process. Neutron diffraction measurements of carbon interstitial occupancy in austenite have also provided further evidence of austenite carbon enrichment during the partitioning process.

Contents

Figures

Tables

Chapter 1
Literature Review

This chapter contains a review of published works that have been considered relevant to a study of the Quenching and Partitioning (Q&P) process. The chapter commences with a brief review of existing heat treatments, and a justification of the impetus for new, innovative heat treatments for steel. As the Q&P process is composed of several existing heat-treatment steps, there is much relevant literature on the individual steps of the process. Therefore, appropriate publications have been used to illustrate the controlling factors which must be considered at each step of the Q&P process.

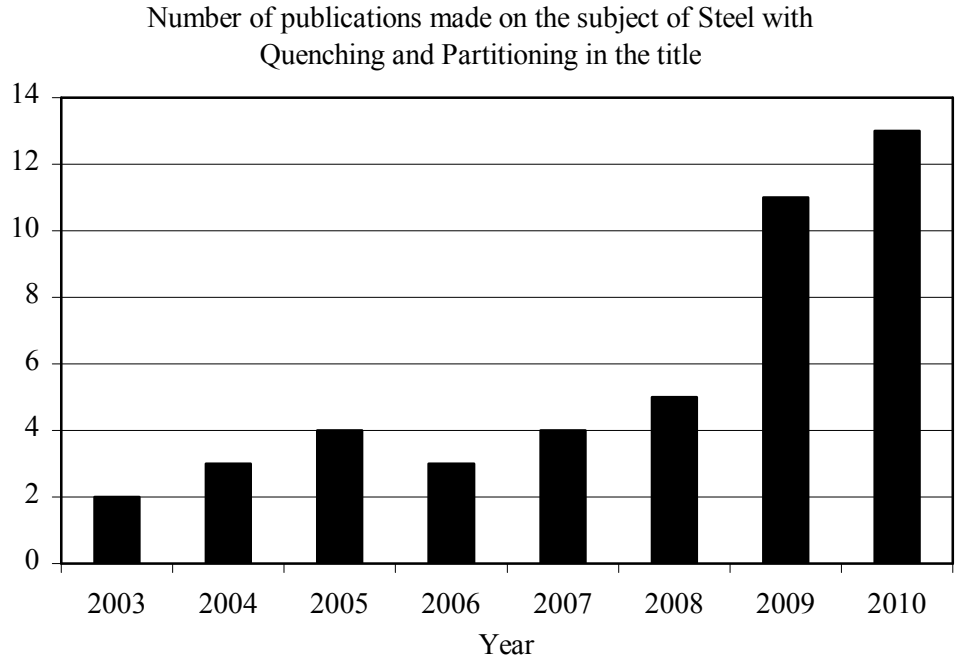

Figure 1.1 – Publishing activity in the area of Quenching and Partitioning, including variations such as Q-P-T (data compiled January 2011)

Also included, is a review of some of the publications which have resulted directly from research on the Q&P process. Although Q&P research initially progressed relatively slowly (Figure 1.1), in recent years research has accelerated to the point where it is becoming difficult to keep track of all developments, particularly as a significant number of papers are now being published in Chinese. Hence, for this project, priority has been given to including those publications which are closest to the research that is reported herein. As this project is concerned chiefly

with elucidating the mechanism by which Q&P occurs, priority has been given to publications in this area, rather than, for example, research which is more focused upon characterising and categorising the effect of the Q&P process on different grades of steel.

1.1 The driving force for development of high strength sheet steels

Manufacture of automobiles represents the most significant single market for sheet steel (Llewellyn 1992). As such, a significant amount of research effort has been expended in the development of sheet steels for this area of usage. Takechi identified three distinct periods of development activity that took place, starting in the 1970s and continuing into the 1990s (Takechi 1987). The first stage was associated with increasing safety for vehicle occupants, the second stage was centred around energy conscious vehicle design and was a direct consequence of the oil crises in the 1970s, the last stage was related to further improvements in strength. Other reviewers (Matlock and Speer 2010) refer to 'generations' of steel development, the first generation including such developments as Dual Phase, TRIP and Martensitic steels, and the second generation consisting of austenitic steels. The third generation is envisaged to surpass first generation steels in terms of mechanical properties, but without the expensive alloying additions required by second generation steels .

In response to automotive industry demands, steel manufacturers developed new products offering opportunities for reductions in vehicle mass via increases in strength and corresponding reductions in section thickness. In more recent years, environmental and safety concerns such as climate change and crashworthiness have become increasingly important issues in automobile development and have added further impetus to the development of high strength sheet steels (Efron 2004) (Fujine, Hayashi et al. 2004). Estimates of the fuel savings that can be achieved through vehicle weight reduction have been published by Magee; these range from 0.26 to 1.07 gallons per pound of vehicle weight reduction (based on a vehicle life of 10 years and 10000 miles per year). The issue of material cost has, of course, always been an important consideration in the design and manufacture of a consumer product such as the automobile, on this front the use of steel offers good opportunities for both weight saving and cost reduction when compared to alternative materials (Magee 1982).

1.2 Developments in High Strength Sheet Steels for automotive applications

The primary mechanical requirements for steels in automotive use are high strength and high elongation (Davies and Magee 1979). However, in many materials the properties of elongation and strength are directly opposed to each other. Therefore, to address the requirements of modern automobile manufacture, sheet steels have become increasingly complex in terms of composition, processing and resulting microstructures. There is no single steel type that currently suits all automotive requirements and for this reason manufacturers use a combination of steels in each vehicle design. The following sections outline some of the steel types that have been successfully used in the automotive industry.

1.2.1 Microalloyed steels

Microalloyed steels rely on alloying additions such as aluminium, vanadium, niobium and titanium for their mechanical properties. The 'micro' term is used to denote that only very small quantities of these alloying elements are required to bring about the desired effect, typically less than 0.1% either as additions of a single element or a combination of elements (Gladman 1997). The primary purpose of the microalloying elements is to cause grain refinement and/or precipitation strengthening (Towers and Woodhead 1994) (Listhuber 1970). The resulting fine-grained ferritic structure with precipitates exhibits higher yield stress and superior brittle fracture characteristics compared to unmodified coarse grained steels. The link between grain size, yield strength and stress required for brittle fracture having already been established by Hall (Sylwestrowicz and Hall 1951) (Hall 1951a) (Hall 1951b) and Petch (Petch 1953).

1.2.2 Rephosphorized steels

The presence of phosphorous in steel is normally carefully controlled as it has a propensity to segregate. Upon rolling, phosphorous inclusions can become elongated into bands of weakness that harm the mechanical properties of the steel (Rollason 1968). Phosphorous may also segregate to grain boundaries and at low temperatures can cause intercrystalline fracture at stresses significantly below the expected yield stress (Allen 1961). Rephosphorized steels are therefore steels in which a controlled quantity of phosphorous has been introduced. The purpose of the phosphorous additions is to make use of the potent solid solution strengthening property of phosphorous in iron (Leslie 1972). In addition, research carried out on steels processed by cold rolling followed by annealing in a suitable temperature

range has shown that phosphorous additions varying from 0.015-0.12% can result in greatly improved formability. The improved formability is a consequence of the annealing texture which was found to consist mainly of textures that aid formability. The mechanism by which phosphorous influences formation of desirable annealing textures is thought to be associated with segregation of phosphorous to grain boundaries (Hu 1976).

1.2.3 Dual Phase (DP) steels

Dual phase steels consist of a matrix of ferrite and martensite, and exhibit continuous yielding behaviour (Davies 1978a) (Honeycombe and Bhadeshia 1995). The ferrite and martensite composite structure has been shown to possess enhanced elongation and equivalent UTS when compared to material of the same composition consisting mainly of ferrite and a dispersion of carbides (Rashid 1977). Experiments on Iron-Manganese-Carbon DP steels found that although ferrite grain size and solid solution strengthening effects contributed to strength, the main factor was volume fraction of martensite, with the ductility observed to be a consequence of the low interstitial content ferrite matrix (Davies 1977). It was also found that strength and ductility conformed to Mileiko's theory of composites consisting of two ductile phases (Mileiko 1969) and Garmong's theory of ductile metal fibres in a ductile metal matrix (Garmong and Thompson 1973) (Davies 1978b). The strength and ductility of DP steels can therefore be controlled by varying the volume fractions of martensite and ferrite. Other researchers have identified a correlation between the mean free path in ferrite expressed as a function of the Hall-Petch equation and the yield and tensile strength of DP steel (Chang and Preban 1985). The correlation was explained by a dislocation pile up theory assuming that deformation of martensite is negligible and the volume fraction of martensite controls the probability of a dislocation encountering either a ferrite/ferrite boundary or a ferrite/martensite boundary.

1.2.4 Bake Hardening steels

Bake hardening steels in automobile structures make use of the paint baking stage to increase the strength of the steel after it has been formed and painted. The combination of the material, a low carbon steel of around 0.001 wt% C (Cahn, Haasen et al. 1992) and the process of baking at around 170ºC affords low yield strength and excellent formability during pressing operations, followed by higher strength after bake hardening (Wuebbels, Matlock et al. 2002) (De, Vandeputte et al. 1999). The mechanism of strengthening during bake hardening is based on the strain ageing effect, in the course of which, interstitial atoms such as carbon and nitrogen

diffuse to low energy sites in and around dislocations (Baker, Daniel et al. 2002). The dislocations are then 'pinned' by the interstitial atoms, causing a rise in strength. The theory of strain ageing is not particularly new, having been reported by Cottrell in 1949 (Cottrell and Bilby 1949). A secondary hardening reaction can also take place after a longer time interval, this is assumed to occur by the formation of precipitates at the carbon enriched dislocation sites (Elsen and Hougardy 1993).

1.2.5 Interstitial Free (IF) steels

Interstitial free steels have been developed for deep drawing applications, the high formability being a consequence of the low levels of carbon and nitrogen (Llewellyn 1992). The concentration of interstitial elements is controlled during production by the use of vacuum degassing equipment, and additions of sequestering elements such as titanium or niobium (Takechi 1994). Further improvements in formability can be achieved in IF steel sheet when the grains are favourably oriented for deformation. A favourable orientation can develop during hot rolling in the austenite phase, if upon transformation to ferrite, the crystallographic texture of the austenite is inherited by the ferrite (Ray, Jonas et al. 1994). It has been shown that when surface grains are favourably orientated relative to the surface of the sheet-steel, gains in elongation can be achieved (Caul and Randle 1997) (Ray, Jonas et al. 1994). An advantage of IF steel is that the extremely high formability can allow the use of a single pressing where two or more pressing operations would have otherwise been required (Tsunoyama 1998); however, this attribute is countered by the fact that the formability must be carefully balanced against a minimum allowable strength (Takechi 1994).

1.2.6 Transformation Induced Plasticity (TRIP) Steels

Transformation induced plasticity steels represent a branch of metallurgy characterised by the use of mechanical means to bring about a displacive phase change (Schmatz and Zackay 1959) (Zackay, Parker et al. 1967) (Llewellyn and Hudd 1998). This phenomenon is also known as strain induced transformation and involves a transformation from austenite to martensite. Transformation from the softer austenitic phase to the harder martensitic phase brings with it an increase in strength, and hence, uniform elongation during forming operations. The work hardening during straining has been found to be proportional to the transformation of austenite to martensite and the carbon content of the martensite formed (Angel 1954). Similarly, 'the degree of austenite decomposition was directly proportional to the amount of strain' (Gerberich, Martin et al. 1965). Production of TRIP steel typically involves an intercritical or full anneal followed by controlled cooling and

an isothermal hold in the bainite formation region (Tsukatani, Hashimoto et al. 1991) (Bhadeshia 2001). During bainite formation, carbide precipitation is suppressed by alloying additions. Therefore, carbon rejected from bainite enriches the surrounding austenite to the extent that austenite is stabilised to room temperature (Bhadeshia and Edmonds 1979). This results in a multiphase structure, typically consisting of ~20% bainitic ferrite, ~10% austenite, with a balance of allotriomorphic ferrite (Sherif, GarciaMateo et al. 2004).

1.3 Prospects for Q&P steels

The dual-phase/multi-phase approach to formable steel sheet has been relatively successful on account of the excellent mechanical properties exhibited by these types of steels (Bleck 1996). Q&P steels fall into the category of dual-phase/multi-phase steels and initial investigations have shown that Q&P steel can surpass or equal the strength and elongation properties of TRIP, conventional dual-phase and martensitic steels (see Figure 1.2). In particular, they can exhibit the best combination of both strength and elongation, thus usefully filling a gap between the more ductile TRIP steels and the higher strength martensitic steels.

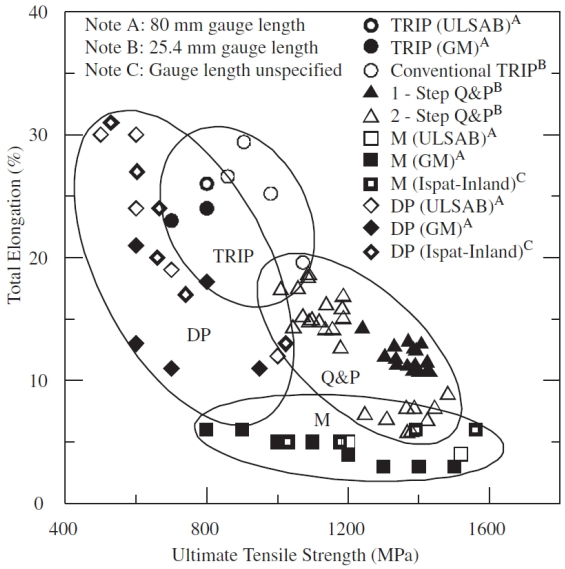

Figure 1.2 - Total elongation vs. ultimate tensile strength for TRIP, Dual Phase (DP), Martensitic (M), and Q&P sheet steel products (Streicher, Speer et al. 2004).

One of the more recent developments in dual/multi-phase steel sheet has been the application of TRIP-assisted steel to automotive components manufactured by the sheet forming route. In terms of concept, TRIP steels are possibly the closest comparable steel to Q&P. TRIP steels and Q&P steels both take advantage of

retained austenite, both require alloying additions to suppress carbide formation and both rely on stabilisation of austenite by carbon enrichment/partitioning, with the opportunity existing for transformation to martensite under applied stress. Q&P steels can therefore be regarded as having the potential to form the basis for a third generation of high strength formable sheet steels (see Figure 1.3).

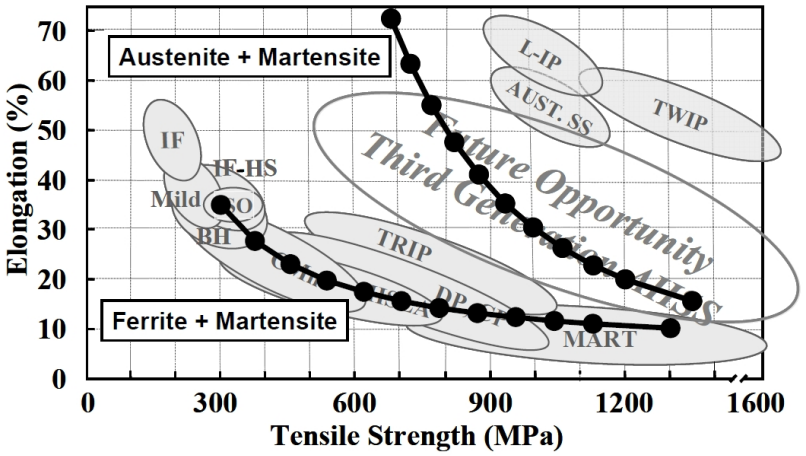

Figure 1.3 - Predicted strength/ductility levels for ferrite/martensite and austenite/martensite mixtures, showing the potential for austenite/martensite mixtures to achieve property targets for "Third Generation AHSS" (Matlock and Speer 2006).

1.4 Galvanisability of Q&P steels

A potential obstacle to the take-up of Q&P steel technology is the ease of galvanisability for corrosion prevention purposes. Coatability of steel strip using zinc may be considered to be of high importance, given the fact that 'About 60% of the total UK automotive coated sheet steel usage is now made up of hot-dip coated products' (John and Challinor 1997). One of the requirements for the production of both TRIP and Q&P steels is the use of an alloying element to control carbide formation. Minimisation of carbide formation is essential to maximise the amount of 'free' carbon that is available to stabilise austenite.

A standard TRIP-assisted steel has a chemical composition (in weight percent) of approximately 0.15% C, 1.5% Mn and 1.5% Si (Mahieu, Maki et al. 2002). The primary purpose of the silicon content is to control carbide formation. However, during annealing of TRIP steel it has been found that elements with a high affinity for oxygen are liable to oxidise. In the case of silicon, a stable layer of Mn_2SiO_4 can form on the surface of the steel (Maki, Mahieu et al. 2003). During hot-rolling, the

oxide layer formed can become rolled into the surface of the steel, causing poor surface properties, and proving difficult to remove by pickling (De Meyer, Vanderschueren et al. 1999).

Surface oxides are problematical to a hot-dip galvanising process line because surface wettability is affected by the oxide layer, leading to bare spots on the finished product (Mahieu, Claessens et al. 2001). As a result of these coatability difficulties, TRIP steels are 'currently generally electrogalvanised rather than hot-dip galvanised' (Maki, Mahieu et al. 2003). This situation is unfortunate because in TRIP steels electrogalvanising introduces an additional process step, whereas for hot-dip galvanising the potential exists to combine galvanising with the isothermal bainitic transformation stage, as both processes take place in a similar temperature range. Q&P steels also contain elements that are easily oxidised, therefore the same problems might be expected to exist with respect to hot-dip galvanisability.

Options that have been investigated to try and improve the hot-dip galvanisability of TRIP steels have included substituting aluminium for silicon, and modifying the dew point of the atmosphere in the furnace used for the annealing stage. Aluminium also has a tendency to form oxides during the annealing stage; however, research has established that it is possible to manipulate the mode of oxide formation by adjusting the annealing furnace atmosphere dew point. In CMnAl TRIP steel it has been found that surface oxide ($FeAl_2O_4$) formation during annealing at a dew point of -30ºC was sufficiently low to allow adequate wetting of the steel during hot-dip galvanising. This outcome in the CMnAl steel was attributed to the low dew point which served to promote internal oxide (Al_2O_3) formation. By contrast, in CMnSi TRIP steel it was determined that a dew point starting at +10 and eventually reducing to -50ºC (the gradual reduction with time was designed to avoid external oxidation during the isothermal hold) was more favourable (Maki, Mahieu et al. 2003). Other researchers have investigated the effects of replacing silicon with aluminium in terms of processing conditions, microstructures, phases formed, and resulting mechanical properties, and found the results to be promising (Mahieu, Maki et al. 2002) (De Meyer, Vanderschueren et al. 1999).

1.5 The Quench and Partition (Q&P) concept

The Quench and Partition concept is composed of four stages; austenitisation, quenching to form a controlled amount of martensite, partitioning at an elevated temperature to stabilise residual austenite, followed by quenching to room

temperature (Edmonds, He et al. 2006) (Matlock, Brautigam et al. 2003) (Speer, Rizzo et al. 2005) (De Moor, Lacroix et al. 2006) (Speer, Streicher et al. 2003) (Gerdemann, Speer et al. 2004). The temperature/time profile of the Q&P process is not too dissimilar from the conventional heat treatment that has been applied to steels for centuries, known as quenching and tempering, but the resulting microstructure and properties are significantly different. Whereas the microstructure of a quench and tempered steel consists of tempered martensite and precipitated carbides, the microstructure of Q&P steel consists optimally of tempered martensite and retained austenite.

1.5.1 The temperature-time profile of the Q&P process

To date, two temperature-time profiles have been reported for the production of Q&P microstructures (Edmonds, He et al. 2006) (Speer, Streicher et al. 2003) (Speer, Rizzo et al. 2005) (Matlock, Brautigam et al. 2003) (Gerdemann, Speer et al. 2004). These can be described as the single-step and two-step processes (Matlock, Brautigam et al. 2003). While the single-step process employs a sustained hold at the quenching temperature to effect carbon partitioning, the two-step process employs a separate step at a higher temperature to bring about carbon partitioning. The two methods are illustrated in Figure 1.4 and Figure 1.5, respectively.

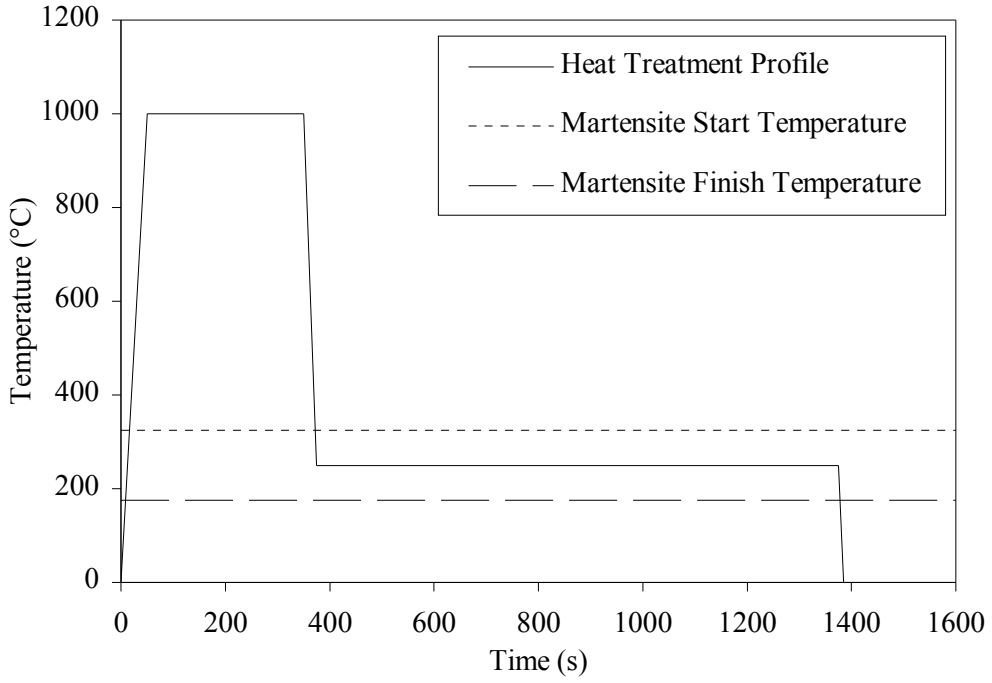

Figure 1.4 – Temperature/Time profile for a single-step Q&P process

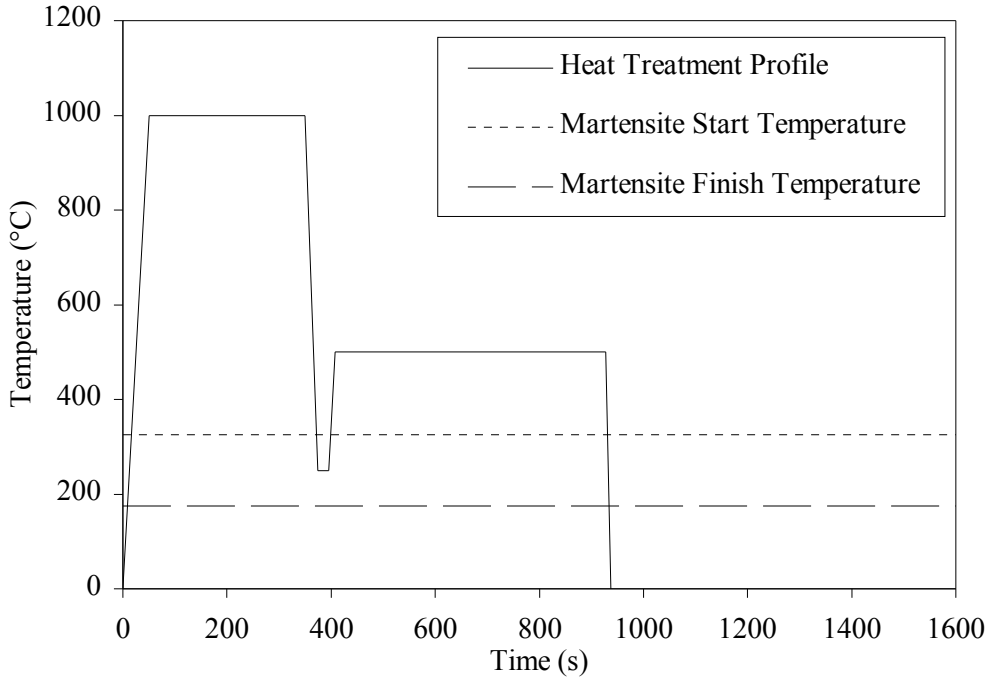

Figure 1.5 - Temperature/Time profile for a two-step Q&P process

1.5.2 Thermodynamics and kinetics of Quenching and Partitioning

The changes that occur during the various stages of the Q&P process are all driven by the potential for reducing the free energy of the system, and enabling a state that possesses the highest stability for a given set of conditions. The conditions that can influence the stability of the system include temperature and pressure; for systems that contain more than one component, composition is also a variable. For each system, at a given temperature and pressure, an equilibrium condition exists at which the system possesses the lowest possible free energy, and is therefore in its most stable state. In some cases a system is able to reach complete equilibrium, while in others a state of metastable equilibrium exists almost indefinitely. For example, at room temperature and pressure, graphite is the most stable carbon structure. Diamond (an allotrope of carbon) only forms under conditions of extreme pressure, however it is able to exist at atmospheric pressure as a metastable structure; but, given enough time, diamond will eventually transform to graphite. The question of how rapidly a system approaches its equilibrium state is determined by its kinetics (see Section 1.5.4) (Porter and Easterling 1992).

1.5.3 The iron-carbon system

As carbon is the most universal alloying element employed in the making of ferrous alloys, it follows that the development and understanding of the iron-carbon equilibrium diagram has been an important milestone in iron and steel technology. The first iron-carbon equilibrium diagram with the same general form of the diagram currently now in use was put forward by Roberts-Austen (Kim 1968). The iron-carbon diagram is a convenient representation of the most stable state for any proportion of iron and carbon at any temperature. However, although an equilibrium diagram can provide useful information concerning the phases expected to be present at a specific composition and temperature, some important limitations apply. An equilibrium phase diagram cannot predict the locations at which nucleation will occur or the morphology of the phases formed (Rollason 1968).

1.5.4 Kinetics of phase transformations

In order for a phase transformation to take place, an activation energy must first be overcome before the free energy reduction of the transformation can be realised. The theory for activation energy; the requirement that a reactant possesses a minimum amount of energy before a reaction (transformation) can occur was first physically justified by Arrhenius. The Arrhenius equation has been found to apply to many different thermally-activated phase transformations, and to the process of diffusion; it may be simply expressed as in Equation 1.1 (Porter and Easterling 1992)

$$rate \propto \exp(-\frac{\Delta H^{a}}{RT})$$

Equation 1.1

where ΔH^a is the activation energy, R is the gas constant and T is the absolute temperature

The theory behind the progress of diffusional, or nucleation and growth phase transformations was explored by Johnson, Mehl and Avrami (Johnson and Mehl 1939) (Avrami 1939) (Avrami 1940) (Avrami 1941), resulting in the well known equation of the same names (Kolmogorov also published on this subject in Russian and this name is sometimes included in the name of the equation). Johnson and Mehl (Johnson and Mehl 1939) presented an arithmetic model for the nucleation and

growth of one phase from another, allowing for the eventual impingement of the growing nuclei on each other. Their model included separate parameters for nucleation rate and growth rate. They also considered the effect of nucleation occurring only on grain boundaries, rather than at random throughout the untransformed matrix. One of the assumptions employed by Johnson and Mehl was that nucleation was a continuous process that occurs throughout the time of a transformation.

Avrami (Avrami 1939) disagreed with the continuous nucleation assumption made by Johnson and Mehl, stating that the grain size distribution curve for this supposition did not match experimental observations. Avrami believed that experimental evidence supported the hypothesis that nucleation could only occur from a finite number of pre-existing 'germ nuclei' within the matrix. As the transformation progresses these 'germ nuclei' are used up by one of two processes; they become active growth nuclei, or they are consumed by growing grains of the new phase. In some cases these 'germ nuclei' will become exhausted part way through a transformation, while in others, some 'germ nuclei' may persist until almost the end of the transformation (Avrami 1940). However, even with significant supercooling or superheating these nuclei may not grow. This is because although the internal energy of the new phase is lower than that of the old phase, the energy associated with interface creation restricts growth. To enable steady growth of the new phase a critical size must be exceeded, with nuclei below this critical size having a greater tendency to dissolve than grow. Avrami described the number of nuclei exceeding the critical size as the 'granulation rate' or 'pop rate' (Avrami 1941). The general shape of the transformation curve given by the equation is that of the figure S when plotted as fraction-complete versus time. The start of the transformation being relatively slow as the 'germ nuclei' develop into viable growth nuclei, a maximum transformation rate is then reached, followed by a tailing-off as the growing new phase impinges on neighbouring new phase growth. A general form of the Johnson Mehl Avrami equation is given in Equation 1.2 (Porter and Easterling 1992)

$$f = 1 - \exp(-kt^n)$$

Equation 1.2

where f is the fraction of the transformation completed as a function of the time, t. The value of n can vary between 1 and 4 and may be relatively independent of

temperature ‘provided there is no change in the nucleation mechanism’. The factor k ‘depends on the nucleation and growth rates and is therefore very sensitive to temperature’ (Porter and Easterling 1992). Since the Johnson-Mehl-Avrami equation was first proposed there have been numerous studies involving the application of the equation to phase transformations in steel.

1.6 Austenitisation

Austenitisation is often the first step when steel is subjected to a heat treatment process. However, although the manner in which the steel is austenitised can have a significant effect on the end result, the actual process of austenitisation is studied less frequently, because the final properties are commonly considered to depend on the steps that follow austenitisation. Austenitisation can affect final properties by controlling the levels of homogenisation and grain growth, both of which impact on hardenability. From a quality control and production economics point of view, the time taken to reach the desired level of austenitisation is also an important consideration (Roosz, Gacsi et al. 1983) (Law and Edmonds 1980) (Oliveira, Andrade et al. 2007). Appropriate austenitisation is important if Quenching and Partitioning is to be carried out with maximum efficiency. The Q&P process is dependent upon stabilisation of austenite via carbon enrichment of residual untransformed austenite. Therefore, it is imperative that carbon is available for diffusion, and not locked up in carbides that have had insufficient time or temperature to dissolve during the austenitisation stage.

1.6.1 Austenitisation in high-purity and low carbon iron

In high-purity zone-refined iron (4 ppm C), the transformation from ferrite to austenite is almost instantaneous, even at heating rates as high as 10^6 degrees Celcius per second, using pulsed laser heating methods (Speich, Szirmae et al. 1969). Rapid heating followed by rapid quenching brings about significant refinement of the ferrite grain structure. The refinement of the ferrite grain structure is caused by the large numbers of austenite nuclei that are formed during the heating cycle, and subsequently transformed to ferrite during quenching. Nucleation sites for austenite lie on ferrite grain boundaries (Speich, Szirmae et al. 1969). In low carbon iron (0.013 wt% C) similar results were obtained.

1.6.2 Austenitisation in the presence of interstitial solutes

When Carbon is present as an interstitial solute, the carbon concentration and the form of the starting microstructure both have a significant effect on the

transformation to austenite. It is logical that the sites at which austenite nucleation occurs are those at which conditions are the most energetically favourable (Dasarathy 1959). Nucleation of austenite has typically been observed to occur at the 'intersection of pearlite colonies' (Speich, Szirmae et al. 1969). The areas between pearlite colonies are regions of high interfacial energy, therefore, the increase in free energy required for austenite nucleation to occur is offset. Although the surface area between cementite and ferrite lamellae in pearlite is very large, these interfaces have not been observed to act as nucleation sites. The interfaces between cementite and ferrite in pearlite are considered unviable for nucleation due to the constant orientation existing between the two phases. Hence, the surface energy is constant across a ferrite/cementite interface, and so energetically favourable sites for austenite nucleation do not exist (Dasarathy 1959).

In the case of microstructures containing spheroidised cementite, the orientation of the cementite with the ferrite matrix is not constant around the periphery of the cementite particle. Therefore, around any cementite particle there exist sites where austenite nucleation is energetically favourable (Dasarathy 1959). Experimental observations have demonstrated that in a spheroidised, high carbon (0.97wt %C) steel, cementite particles are indeed favourable sites for austenite nucleation (Speich, Szirmae et al. 1969). The location of cementite particles has also been shown to be an important factor. Those particles situated at grain boundaries are found to nucleate austenite after a shorter incubation time, and at a higher rate than particles wholly enclosed within a ferrite grain (Judd and Paxton 1968). These findings reaffirm that surface energy has a strong influence on nucleation.

Although initial austenite nucleation can take place relatively quickly, the achievement of full equilibrium requires complete dissolution of cementite particles and homogenisation of carbon throughout the austenite matrix. Experimental data has shown that the hypothesis of carbon diffusion as the rate controlling step during cementite dissolution is correct (Judd and Paxton 1968).

1.6.3 The effects of substitutional alloying elements on austenitisation

Experimentation with substitutionally alloyed material has shown that carbon diffusion as a rate-controlling process for austenitisation cannot be successfully correlated with results. This leads to the conclusion that a different rate-determining process must be in operation (Molinder 1956) (Judd and Paxton 1968). The

mechanism by which austenite forms in substitutionally alloyed steel has been subject to different hypotheses.

Speich et al. proposed that the effect of substitutional alloying elements is to significantly retard the transformation to austenite at lower temperatures, due to the low mobility of manganese (Speich, Szirmae et al. 1969). In a later paper, Speich et al. add weight to this argument by reporting that, at lower temperatures, achieving full equilibrium in the austenite of a manganese alloyed steel can take as long as 2000 to 4000 hours. This result is attributed to the low diffusion rate of manganese in austenite (a slower process than diffusion of manganese in ferrite) (Speich, Demarest et al. 1981).

Navara and Harryson put forward a hypothesis involving the partitioning of manganese during austenitisation in low-carbon manganese steels. The proposed mechanism proceeds by dissolution of high-carbon austenite (initially formed from pearlite), while a more thermodynamically stable, high-manganese, high-carbon austenite nucleates and grows. The higher manganese content reduces the free-energy of the austenite formed. This concept was thought to offer a more comprehensive explanation of their own experimental observations, and those of Speich and others (Navara and Harrysson 1984).

Further research by Navara, Bengtsson et al. resulted in the conclusion that there was little evidence to suggest that carbide particles acted as favourable nucleation sites for austenite in manganese alloyed steel. In some cases carbides were believed to act as ‘sinks’ for manganese, leading to further stabilisation of the carbide. Instead, the initial rapid growth of austenite is proposed to occur by Diffusion Induced Grain-boundary Migration (DIGM) (Navara, Bengtsson et al. 1986). However, this finding goes against some of the research reported for plain carbon steels.

The DIGM concept entails formation of austenite behind the moving boundary, in areas of manganese and carbon enrichment. This mechanism is postulated to occur within relatively constrained temperature ranges, the distinguishing characteristic being that it occurs at a temperature where grain-boundary diffusion is significantly more rapid than volume diffusion. Suitably orientated dislocations are also required. Following the DIGM stage, austenitisation is proposed to progress

more slowly. The transformation front spreads away from the initial nucleation points along grain boundaries, and then widens, becoming reliant on volume diffusion through the ferrite lattice (Navara, Bengtsson et al. 1986).

Observations of pearlite/ferrite structures have led to the proposal by Yang et al. of a four stage process for austenitisation in a carbon, manganese, silicon steel. The process is believed to be initiated in pearlite, and involves spheroidisation of cementite and coarsening of cementite particles at ferrite/ferrite boundaries. Nucleation of austenite then occurs, first around cementite particles at ferrite/ferrite boundaries, and later at cementite particles within ferrite grains. This observation follows the theory that cementite at grain boundaries represents a more energetically favourable site for austenite nucleation than cementite within bulk ferrite (Yang, Brown et al. 1985).

1.6.4 Kinetics of austenite formation

The kinetics of austenite formation have been studied, although not as frequently as the kinetics of austenite decomposition. Dilatometry has been used as a convenient technique to monitor the progress of transformation to austenite (Oliveira, Andrade et al. 2007). With a pearlite/ferrite starting structure, austenite formation is observed to occur in two stages. The initial stage is pearlite dissolution, while the second stage is the ferrite to austenite transformation. Austenite nucleation was observed to occur 'preferentially at the points of intersection of cementite with the edges of the pearlite colony' (Oliveira, Andrade et al. 2007). The progress of the transformation observed by dilatometry was successfully fitted to the Avrami equation, the parameter 'k' was found to vary strongly with the heating rate employed, while the parameter 'n' displayed only a small variation with heating rate.

1.6.5 Predicting the parameters required for austenitisation

Empirical formulae have been developed to predict austenitisation as a function of chemical composition. Andrews used data from different steel compositions to determine formulae for Ae3, Ac1 and Ac3 temperatures. These are the austenite-equilibrium finish temperature, and the austenite-critical start and finish temperatures respectively. The Ac temperatures are dependant on heating rate, while the Ae temperatures are representative of true equilibrium conditions (Andrews 1965). A more modern method of predicting these characteristics involves the use of bespoke computer software. For example, the software package MTDATA (National Physical Laboratory 2006) (Davies, Dinsdale et al. 2002) is

able to make predictions based on a specific steel composition, expressed as mass/kg versus temperature for the phases expected to be present under equilibrium conditions.

1.6.6 Structural changes during austenitisation

During austenitisation the transformation in steel from the ferritic, Body Centred Cubic (BCC) structure to the austenitic, Face Centred Cubic (FCC) structure occurs. Cementite and other carbides decompose, and the carbon released is held within austenite at interstitial sites. Carbon has a significantly higher solubility in austenite than ferrite; this characteristic is explored more fully in a later Section (see Section 1.8).

1.7 Quenching

The changes brought about by quenching steel have been viewed as being among the most complex and challenging in metallurgy. Many years of uncertainty passed before the use of X-ray analysis was able to elucidate some of the structural changes taking place (Kurdjumov 1960).

1.7.1 Characteristics of martensitic transformations

Sinha (Sinha 1989) describes some key characteristics of martensitic transformations, some of which are detailed in the following paragraphs.

The martensitic transformation is diffusionless, and so the chemical compositions of the parent and product phases are identical. In contrast, the equilibrium (ferrite/pearlite/carbide) structures form via a diffusional reconstructive process involving many individual random atom displacements. Therefore, in diffusional transformations, time is required to achieve the equilibrium state, and chemical inhomogeneity can occur. By comparison, formation of martensite occurs by an instantaneous shear mechanism, whereby for each martensite plate formed, the atoms that form the new plate shift less than one atomic spacing in a coordinated movement (Christian 1965) (Porter and Easterling 1992). In some alloys it is possible to form more than one type of martensite, the alternative being a Hexagonal Close Packed (HCP) structure known as ε-martensite (Parr 1952)

The interface between the parent and growing phase is highly glissile (Bhadeshia 2004), and may be coherent or semi-coherent (although usually semi-coherent in ferrous martensites, with the misfit accommodated across the boundary (Sinha 1989)). The semi-coherent nature of the parent-product interface is readily demonstrated by experiments employing surface scratches (Bowles 1951). The shape change that occurs during transformation causes a macroscopic surface relief to occur parallel to the transformation plane, thereby providing compelling evidence of the nature of the transformation (Bain 1924) (Whiteley 1925).

The morphology of martensite is of plates or laths, with nucleation occurring on specific planes (e.g. the Kurdjumov-Sachs, Nishiyama and Greninger-Troiano relationships). The habit plane on which martensite forms is normally a complex form of Miller indices (irrational habit plane), with specific alloys displaying unique habit planes (Qiu and Zhang 2003). Therefore, the orientation relationship between the parent and product phase is predictable when the composition of the alloy is kept constant.

With few exceptions, transformation during cooling advances by the establishment of new plates rather than by the continual growth of existing plates (Pati and Cohen 1971). Since the formation of martensite is dependent upon a level of coherency between parent and product phase, each plate is able to advance within the parent material until defects are encountered which cannot be accommodated by the interface between the two phases. Therefore, the first martensite plate to form in an austenite grain may span the entire grain before it encounters the insurmountable obstacle of the grain boundary. Subsequent martensite plates are obstructed by existing martensite plates; consequently, as the transformation progresses the plate size becomes progressively smaller (Porter and Easterling 1992). Within each martensite plate or lath exists a fine substructure (Sandvik and Wayman 1983).

1.7.2 Prerequisites for martensitic transformation

In the case of rapidly quenched, high-purity, zone-refined iron (4 ppm C), the lack of a significant number of defects in the resulting ferrite structure is considered to indicate that the transformation from austenite to ferrite occurs by a massive transformation, rather than a martensitic transformation (Speich, Szirmae et al. 1969). Massive transformations are characterised by ‘a rapid non-cooperative transfer of atoms across a relatively high-energy interface’ (Massalski 1968). Unlike conventional diffusional transformations, massive transformations occur at a speed

which precludes long range diffusion; the chemical composition of the product phase is therefore identical to that of the parent phase. The reconstructive nature of massive transformations is not hindered by grain boundaries within the parent phase, hence, the product grain size can equal or exceed that of the parent phase (Bhadeshia 1985).

However, in low carbon iron (0.013 wt% C), the same quench produces a ferrite structure containing numerous defects, characteristic of an austenite to ferrite, martensitic mode of transformation (Speich and Warlimont 1968) (Speich, Szirmae et al. 1969). Therefore, it may be concluded that in ultra-pure iron no driving force exists to create a metastable martensitic product; a ferritic structure that is closer to equilibrium being readily achievable. Consequently, alloying elements are an important consideration in attaining a martensitic structure (and in terms of quenching and tempering, alloying additions also play an important role in facilitating carbide dispersion strengthening mechanisms). The other important requirement that must be fulfilled in order to bring about a martensitic transformation is the application of a suitable quenching operation. Quenching provides the thermodynamic driving force that enables the transformation to take place.

1.7.3 Structural changes during martensite formation

The structure of martensite is universally accepted to consist of a Body-Centred arrangement of iron atoms, in which the carbon atoms preferentially occupy interstitial sites on only one axis, thus giving rise to a distortion from the Body-Centred-Cubic (BCC) to the Body-Centred-Tetragonal (BCT) structure (Zener 1946) (Kurdjumov 1960) (Honeycombe and Bhadeshia 1995) (Porter and Easterling 1992) (Cahn, Haasen et al. 1992) (Sinha 1989). Although Bain (Bain 1924) provided an elegant model for the means by which this diffusionless crystallographic change could occur in 1924, the intricacies of the mechanism by which the transformation takes place have been subject to continuous research effort since that time.

1.7.4 Effect of austenitisation parameters on martensite formation

The austenitisation conditions applied prior to quenching affect the formation of martensite in more than one way. The austenite grain size must have some effect on the way in which martensite is formed since austenite grain boundaries prevent the semi-coherency/coherency between growing martensite and its parent phase which is essential to continuation of the transformation. Although austenite grain

size does not affect the proportion of austenite that transforms to martensite, a relationship does exist between martensite plate size and prior austenite grain size. Grossmann and Stephenson found that not only was the hardenability increased at larger grain sizes, but that steels of higher hardenability (due to greater alloying additions) are more sensitive to grain size variations (Grossmann and Stephenson 1941). Another effect of prior austenite grain size concerns the dilatational strain that accompanies the transformation. In large grain size material the stress that builds up between adjacent grains is greater, and less easily accommodated. In extreme cases this can lead to grain-boundary rupture, which is observed as quench cracking. A finer prior-austenite grain size minimises these stresses and gives a tougher and stronger structure (Porter and Easterling 1992). In some cases, the austenitisation process also plays an important role in homogenisation prior to quenching so that martensitic transformation occurs evenly throughout the material. When the starting material contains carbides, a sufficiently high temperature must be employed for a period of time sufficient to ensure complete dissolution of all carbides.

1.7.5 Thermodynamic and kinetic considerations of martensite formation

As is the case for any other phase transformation, the process of martensite formation must be accompanied by a reduction in free energy. A schematic diagram for the free energy (G) of the parent (austenite) phase (γ), and product (martensite) phase (α') is shown in Figure 1.6. When the free energy of the austenite and martensite structures becomes equal at T_0, a further undercooling initiates the transformation. Although the overall effect is a decrease in free energy, the nucleation of a martensite plate brings with it an increase in the strain energy and interfacial energy. In the austenite to martensite transformation, the interfacial energy of a coherent nucleus is relatively small compared to the strain energy (Porter and Easterling 1992).

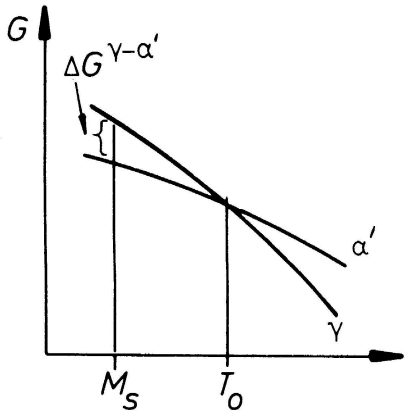

Figure 1.6 - Free energy versus temperature for austenite and martensite of fixed carbon concentration (Porter and Easterling 1992)

The speed with which the martensite transformation nucleates and proceeds (equatable to the speed of sound in the matrix) has made studies of the transformation mechanism difficult. Once a new martensite plate begins to form, growth of the plate is so rapid that some researchers have considered the nucleation stage as the most important issue in the study of martensite. If the nucleation of new plates can be accurately predicted then a model can be developed for the response of a steel alloy during the quenching stage of a heat treatment process. The analytical function presented by Magee predicts that the number of nucleation sites increases linearly with the thermodynamic driving force (Magee 1970).

In terms of nucleation, experiments with small, defect-free crystals have shown that the transformation is nucleated heterogeneously (Huizing and Klostermann 1966) (Easterling and Swann 1971). This has led some researchers to investigate the way in which dislocations might act as nucleation sites for martensite transformation. Martensitic transformation in steel is usually considered to be an athermal transformation (requiring continued cooling to initiate further plate nucleation), although some alloys have been investigated that exhibit isothermal transformation characteristics (Kaufman and Cohen 1958).

1.7.6 Predicting the martensite start temperature (M_s) and the fraction transformed

Empirical methods which use chemical composition to predict the temperature at which martensite formation is initiated have been proposed by various researchers. Two of the most popular formulae currently in use and often cited by other researchers are those developed by Andrews (Equation 1.3) (Andrews 1965) and by

Steven and Haynes (Equation 1.4) (Steven and Haynes 1956). In these formulae chemical composition is expressed as weight percent (wt %):

$$M_s(°C) = 539 - 423C - 30.4Mn - 17.7Ni - 12.1Cr - 7.5Mo$$

Equation 1.3

$$M_s(°C) = 561 - 474C - 33Mn - 17Ni - 17Cr - 21Mo$$

Equation 1.4

The question of how best to predict the fraction of martensite formed for a given undercooling below the martensite start temperature has been answered by the work of Koistinen and Marburger. By quenching four different iron-carbon alloys to three different temperatures, they created sufficient data to identify a relationship between the level of undercooling below the martensite start temperature, and the fraction of material transformed from austenite to martensite. The equation obtained (Equation 1.5) dictates that 'at any temperature below M_s, a constant fraction of the austenite remaining will be transformed by a given additional temperature decrement' (Koistinen and Marburger 1959). In a theoretical assessment of the nucleation process, Magee derived an analytical function which agreed with experimental data and the empirical formula devised by Koistinen and Marburger (Magee 1970).

$$V_\gamma = e^{-1.10\times10^{-2}(M_s - T_q)}$$

Equation 1.5

where V_γ is the fraction of austenite remaining after quenching, M_s is the martensite start temperature (as calculated by one of the empirical formulae) and T_q is the quenching temperature.

Use has been made of the relationship developed by Koistinen and Marburger in research relating to the Q&P process. By applying the Koistinen-Marburger equation to the initial and final quench stages of a Q&P heat treatment (and assuming 100% of the carbon in the martensite from the first quench partitions to untransformed austenite), Gerdemann has had some success in predicting the phase

fractions of martensite and retained austenite that will result (Gerdemann, Speer et al. 2004).

1.8 Partitioning

The structure that exists after initial quenching has taken place is somewhat unstable. The martensitic ferrite contains a non-equilibrium carbon content, and the untransformed austenite is vulnerable to martensitic transformation should a sufficient undercooling be provided. Therefore, the partitioning section of the heat treatment performs two functions; the stability of the martensite is improved by permitting some escape of interstitial carbon, the stability of untransformed austenite against martensitic transformation is increased by its receipt of carbon rejected from the supersaturated martensite (Matlock, Brautigam et al. 2003) (Speer, Edmonds et al. 2004) (Gerdemann, Speer et al. 2004) (De Moor, Lacroix et al. 2006) (Edmonds, He et al. 2006) (Edmonds, He et al. 2007). Although the current application of carbon partitioning from martensite to austenite (now known as Q&P) is believed to be a novel and recent development (Edmonds, He et al. 2006), the partitioning of carbon from martensite to austenite in dual phase structures is not a particularly recent discovery. In previous years, studies of the tempering process have revealed that untransformed austenite can act as a sink for carbon escaping from the supersaturated martensite (Matas and Hehemann 1960).

1.8.1 The driving force for partitioning

The driving force for the migration of carbon atoms from martensite to austenite can be schematically represented by the use of a molar gibbs free energy diagram for the two phases, martensite and austenite (Speer, Edmonds et al. 2004). Figure 1.7a illustrates that there exists only one combination of ferrite and austenite composition that can be at full equilibrium, i.e. the chemical potential of both iron and carbon are equal in both phases (ignoring other alloying elements).

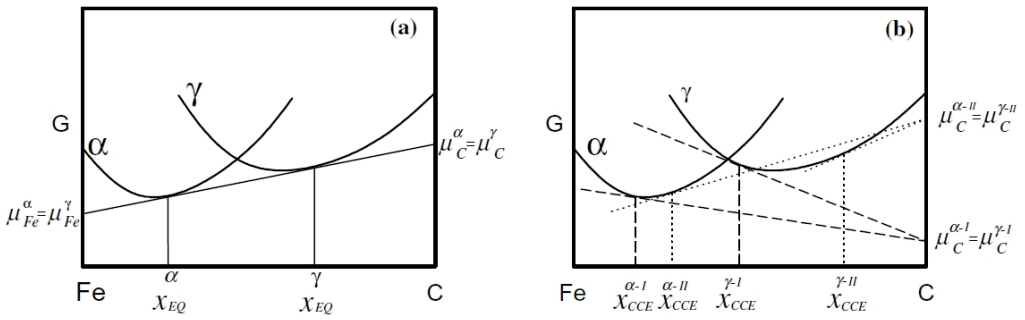

Figure 1.7 - Schematic molar Gibbs free energy vs. composition diagrams illustrating metastable equilibrium at a particular temperature between ferrite and austenite in the Fe–C binary system. (a) Equilibrium (EQ) (b) Two possible constrained carbon equilibrium conditions (I and II) (Speer, Edmonds et al. 2004)

However, if as in Figure 1.7b, the equilibrium condition is required to apply only to the carbon within the system, then an infinite number of phase compositions can exist, each of which represents a state of para-equilibrium. The point at which equilibrium is reached between the two phases must then correspond to the time at which the driving force for carbon partitioning is diminished. This condition was initially termed Constrained-Para-Equilibrium (CPE) (Speer, Streicher et al. 2003), the ‘constrained’ term referring to the nature of the interface between the martensite and the austenite, which is assumed to remain static (provided the partitioning temperatures employed are too low for significant movement of iron or substitutional atoms to occur). The ‘para’ term referred, as customarily, to the fact that only the carbon is in equilibrium, not the substitutional atoms. The driving force for carbon partitioning exists until the free energy of carbon in martensite and austenite is equal. The free energy of the iron (and substitutional alloy) atoms is assumed not able to reach equilibrium due to the limited mobility of these atoms at the partitioning temperatures and times employed. However, after objections to the use of the traditional term ‘para-equilibrium’ in this way (Hillert and Agren 2004a) (Speer, Matlock et al. 2004), it was agreed to refer to the Q&P partitioning mechanism as ‘Constrained-Carbon-Equilibrium’ (CCE) (Hillert and Agren 2004b).

It has been postulated by Speer et al. (Speer, Matlock et al. 2003), that if the chemical potential of the iron in the system is fixed, i.e. the system is in the process of reaching CCE, then the endpoint of the carbon partitioning can be calculated via the equation developed by Bhadeshia (Bhadeshia 1981b). The equation published by Bhadeshia utilised the data of Lobo and Geiger (published in two consecutive papers) (Lobo and Geiger 1976a) (Lobo and Geiger 1976b) to arrive at the constants included within Equation 1.6:

$$RT\ln\frac{\Gamma_c^{\alpha}}{\Gamma_c^{\gamma}} = 76789 - 43.8T - (169105 - 120.4T)x$$

Equation 1.6

where R is the gas constant, T is the absolute temperature, Γ_c^{α} and Γ_c^{γ} are the activity coefficients of carbon in ferrite and austenite respectively, and *x* is the molar fraction of carbon in the steel composition.

Based on the fact that 'the activity of carbon in each phase is given by the product of the activity coefficient and the mole fraction of carbon' (Speer, Matlock et al. 2003), Equation 1.6 was modified to calculate the equilibrium quantity of carbon in each phase. Equation 1.7 represents this modification (Speer, Matlock et al. 2003)

$$X_c^{\gamma} = X_c^{\alpha} \cdot e^{\frac{76789 - 43.8T - (169105 - 120.4T)X_c^{\gamma}}{RT}}$$

Equation 1.7

where X_c^{γ} and X_c^{α} are the mole fractions of carbon in austenite and ferrite respectively, R is the gas constant, and T is the absolute temperature.

When Equation 1.7 is computed for various carbon compositions and a range of temperatures, the equilibrium carbon content that is theorised to exist within the ferrite and austenite of a dual phase steel is obtained. Figure 1.8 illustrates the result of this exercise and demonstrates that, thermodynamically, it is preferential for almost all of the carbon within a dual phase steel to be situated within the austenitic component of the steel (assuming no other reactions compete for carbon).

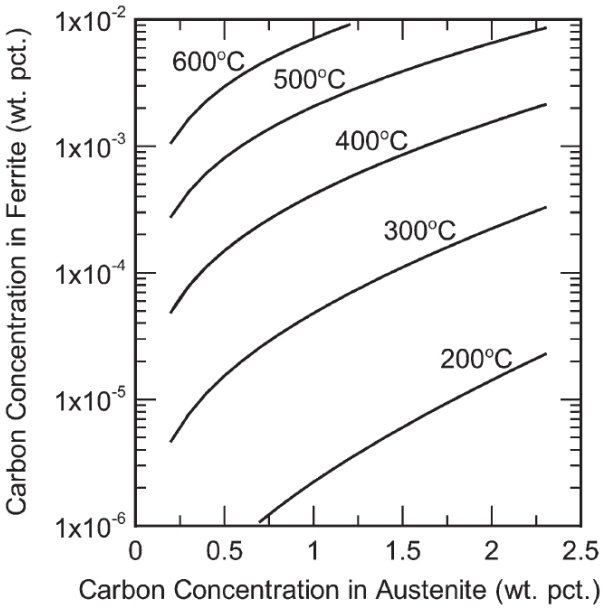

Figure 1.8 – Calculated loci of ferrite and austenite compositions having equal carbon activities at temperatures between 200 and 600 degrees C (Speer, Matlock et al. 2003)

Speer et al. acknowledge that the model is not perfect, as it does not account for effects such as could be caused by changes in density and lattice parameters, leading to elastic strain effects. However, although the model was based on the iron-carbon system, it was considered to be approximately correct for, and applicable to low alloy steels. The issue of carbon trapping within energetically favourable locations such as dislocations was also floated (this topic is fully considered in Section 1.10.5).

1.8.2 The kinetics of partitioning (diffusion)

Unlike the preceding stages of austenitisation and quenching, there is no nucleation and growth process associated with the partitioning stage. The kinetics of the partitioning stage are governed by the diffusion of carbon out of the martensitic ferrite, across the ferrite/austenite boundary, into the austenite adjoining the boundary, and lastly, full homogenisation of the carbon within the austenite. If the CCE concept does not apply then the diffusion of iron and substitutional alloying elements must also be included in the partitioning process.

In iron, self diffusion (and substitutional diffusion) is dependant upon a suitably located vacancy, and the vibrational movement of surrounding atoms. For interstitial diffusion, the requirement is similar in that there must be a suitably

located vacant interstitial site, and the matrix atoms must move sufficiently to allow the interstitial atom to pass through. The size difference between carbon and iron atoms (and other substitutional alloying elements) is such that carbon atoms are accomodated within interstitial sites. When considering diffusion of carbon in the phases of austenite, martensite and ferrite, it is appropriate to consider the nature and number of interstitial sites, as it is these factors which influence the probability that an adjacent interstitial site will be vacant, and therefore available for a carbon atom to move (diffuse) into.

For the austenitic structure, which has a Face Centred Cubic (FCC) arrangement of iron atoms, two types of interstitial sites exist; octahedral and tetrahedral. The octahedral sites are located mid-way along the cube edges and in the centre of the unit cell. Octahedral sites acquire their name from the surrounding six iron atoms, which create an octahedron shaped space; each unit cell of FCC iron contains four octahedral sites. Tetrahedral sites are surrounded by four iron atoms (one corner atom and three face centre atoms), these sites are located along the cube diagonals; each unit cell contains eight tetrahedral interstices. Research has shown that of the two types of interstices available in the FCC unit cell, carbon normally occupies the octahedral sites (Petch 1942) (Mazzone 1987) (Butler and Cohen 1992).

In the ferritic Body Centred Cubic (BCC) structure, the interstices available also comprise both octahedral and tetrahedral. Octahedral interstices are located midway along cube edges, and at the face centres of the unit cell. Tetrahedral interstices are positioned at the interface between two unit cells, midway between any two adjacent octahedral interstices. The octahedral interstices in a BCC unit cell number six, while the number of tetrahedral interstices is twelve. Although the tetrahedral interstices are larger in size, and at first sight more able to accommodate carbon atoms with minimum lattice strain, it is actually found that strain energy is minimised by occupation of the octahedral interstices (occupation of tetrahedral interstices requires displacement of four nearest-neighbour iron atoms, whereas occupation of octahedral interstices affects only two nearest-neighbour iron atoms) (Williamson and Smallman 1953).

For the Martensite Body-Centred-Tetragonal (BCT) crystal lattice structure, carbon atoms are normally considered to occupy the octahedral interstices; although Mossbauer studies on plain carbon steel have indicated that sub-zero quenching may

cause a proportion to occupy tetrahedral sites (Fujita, Moriya et al. 1970). For the regular situation, whereby carbon atoms chiefly reside in the octahedral interstices, a preferential distribution of carbon atoms along the interstices situated midway along the z-axis of the unit cell is observed. The coordinated distribution of carbon along only one axis represents a means of decreasing free energy via a reduction in strain energy. It is this preferential distribution which results in a measureable distortion, from the BCC structure to the BCT structure. Hence, there is only one interstitial site per unit cell in BCT iron (martensite); however, if sufficient carbon can be precipitated via an energetically favourable process, then the crystal structure will revert to BCC and many more interstitial sites become available for diffusion.

It is interesting to draw a parallel between the coordinated distribution of carbon that is produced by martensitic transformation, and the experimental technique developed by Snoek (Snoek 1941) (Snoek 1942) (Zener 1948a) (Zener 1948b) (Koiwa 2004), which involves measuring the damping effect when carbon atoms oscillate between random and coordinated distribution. In both cases the driving factor is reduction of free energy, however, in the former, preferential distribution of carbon gives rise to anisotropic lattice strain; in the latter, an externally applied stress modifies the carbon distribution from random, to coordinated occupation of interstitial sites. The Snoek experimental measurement technique produces results which show a peak in damping effect (maximum energy absorption) at a specific temperature. Snoek peak measurements are an extremely sensitive method of measuring small quantities of carbon (or nitrogen) in solution, and so can be applied to investigations into tempering, or any other area where it is required to determine very small changes to interstitial site occupancy. The Snoek effect is not unique to the iron-carbon system, but can be used for other systems where the size difference causes one component of a system to exist as an interstitial solute.

In dilute solutions it can be assumed that every interstitial site surrounding each interstitial atom is vacant. In this case it is possible for steady state diffusion to exist and Ficks first law of diffusion applies (Porter and Easterling 1992). However, as will be discussed in Section 1.8.3, the situation with respect to partitioning of carbon from martensite to austenite is somewhat more complex than this.

All atoms within a solid vibrate about a minimum energy position. Since the atoms are continually colliding with their neighbours, at any one time there are some

atoms which possess a greater than average energy and displacement. When, by a random series of collisions and greater than average atomic vibration the right situation arises, a gap may open up in the matrix that permits an interstitial atom to move to a neighbouring interstitial site. At any time the probability of an interstitial atom possessing an amount of energy ΔG or more than the average energy is given by Equation 1.8 (Porter and Easterling 1992)

$$e^{-\Delta G/RT}$$

Equation 1.8

where ΔG is the difference between the average energy of an interstitial atom and a hypothetical level of energy, R is the gas constant and T is the absolute temperature.

The likelihood of an interstitial atom having enough energy to migrate to the next interstitial site is given by Equation 1.9 (Porter and Easterling 1992)

$$e^{-\Delta G_m/RT}$$

Equation 1.9

where ΔG_m is the increase in free energy that must momentarily occur during a migration from one interstitial position to the next (the same as the activation energy for migration).

For an interstitial atom vibrating with an average frequency of ν, that is bordered by z vacant interstitial sites, the jump frequency (Γ_B) that can be expected is given by Equation 1.10 (Porter and Easterling 1992)

$$\Gamma_B = z\nu \exp\frac{-\Delta G_m}{RT}$$

Equation 1.10

By further simplification, and banding together the terms that are almost independent of temperature, the diffusion rate D is given by Equation 1.11 (Porter and Easterling 1992), which has a similar form to the Arrhenius equation (Equation 1.1)

$$\log D = \log D_0 - \frac{Q}{2.3R}\frac{1}{T}$$

Equation 1.11

where D_0 is a material specific constant (which includes the terms that are not significantly affected by temperature), and Q is the activation enthalpy.

1.8.3 Carbon distribution in retained austenite

The efficiency with which an ideal partitioning stage is able to prevent transformation to martensite during final quenching is dependent upon effective homogenisation of carbon within the austenite. While the situation of steady-state diffusion is readily solvable by Ficks First Law, the conditions existing during partitioning are significantly more complex for two reasons. Firstly, the diffusion is not steady-state because there is a continuous depletion of carbon from the martensite and corresponding increase in carbon concentration in the austenite. Secondly, the diffusion coefficient of carbon in austenite varies according to its own concentration (Smith 1953).

There have been various studies into the diffusion of carbon from ferrite into austenite, both of an experimental and mathematical modelling type. Experimental results confirm that although carbon partitioning definitely takes place, the variation in carbon concentration within both ferrite and austenite is significant (Barnard, Smith et al. 1981) (Sarikaya, Thomas et al. 1981). Of particular interest is the fact that the peak carbon concentration was to be found at the austenite/martensite interface. These experimental observations are supported by computer simulations carried out using DICTRA software (Borgenstam, Engstrom et al. 2000), which show that although carbon is able to exit martensite relatively quickly, full homogenisation of carbon within austenite occurs much more slowly (Figure 1.9 and Figure 1.10) (Edmonds, He et al. 2006) after (Rizzo, Edmonds et al. 2005).

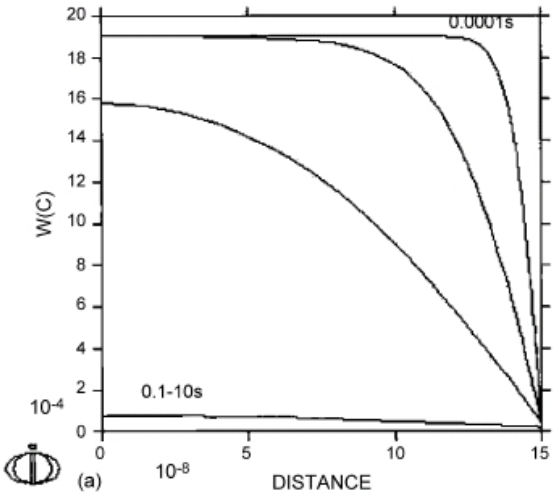

Figure 1.9 - Calculation of the carbon concentration profiles in wt. fraction ($\times 10^{-4}$) normal to the planar interface for a martensite plate for times of 0.0001, 0.001, 0.01, 0.1, 1 and 10 s, in Fe–0.19% C–1.59% Mn–1.63% Si (wt.%) partitioned at 400 ◦C. (Figure 1.9 and Figure 1.10 represent a half-plate width in metres ($\times 10^{-8}$), with centre on the left and interface on the right.) The curves for the three longer times overlap because the martensite plate is depleted of carbon within 1 s (Edmonds, He et al. 2006) after (Rizzo, Edmonds et al. 2005).

These observations are not particularly surprising, as it is considered that the diffusion of carbon is somewhat slower in austenite than it is in ferrite. Figure 1.11 shows the diffusion coefficients and ‘jump times’ for carbon in ferrite and carbon in austenite, in support of the experimental observations of carbon partitioning (although it must be cautioned that high temperature diffusion data has been extrapolated to lower temperatures). Also included is data for self diffusion of iron in austenite and ferrite for normal lattice conditions, and in the vicinity of defects (pipe and boundary diffusion).

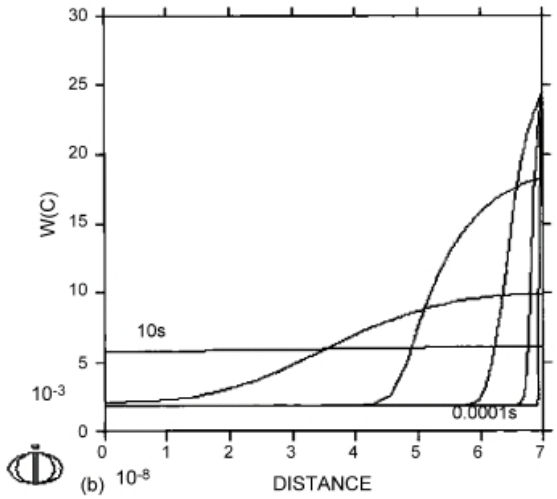

Figure 1.10 - Calculation of the carbon concentration profiles in wt.fraction ($\times 10^{-4}$) normal to the planar interface for a an adjacent austenite plate-shaped region, for times of 0.0001, 0.001, 0.01, 0.1, 1 and 10 s, in Fe–0.19% C–1.59% Mn–1.63% Si (wt.%) partitioned at 400 ◦C. (Figure 1.9 and Figure 1.10 represent a half-plate width in metres ($\times 10^{-8}$), with centre on the left and interface on the right (Edmonds, He et al. 2006) after (Rizzo, Edmonds et al. 2005).

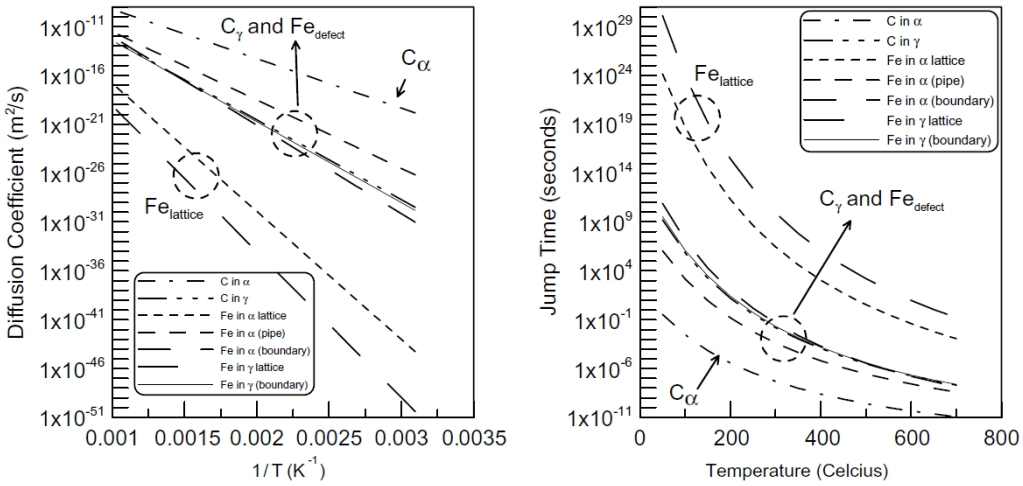

Figure 1.11 - Estimated diffusivities and 'jump times' for carbon and iron in ferrite and austenite, including both lattice and boundary diffusion of iron, and 'pipe' diffusion of iron in ferrite (Speer, Edmonds et al. 2004).

1.9 Final Quenching

The final quenching that follows the partitioning stage is in many ways similar to the first-step quenching, however, some distinctions do apply. The martensite start temperature criteria apply equally to untransformed austenite as to the initial 100% austenite or intercritically annealed ferrite/austenite structure. Therefore, any

austenite that has not benefited from sufficient carbon enrichment during the partitioning stage (which lowers the M_s temperature) may be vulnerable to martensitic transformation. Austenite that transforms to martensite following partitioning has been referred to by some researchers as 'fresh martensite' (Edmonds, He et al. 2006).

1.10 Competing Reactions

Various competing reactions can occur, all of which reduce the efficiency with which the Q&P heat treatment process stabilises austenite to room temperature.

1.10.1 Ferrite and pearlite formation

With appropriate alloying additions, the formation of equilibrium ferrite and pearlite structures can be avoided provided quenching is sufficiently rapid. The effect of alloying additions is to shift the nucleation and growth of these structures to longer times, this is also known as increasing the hardenability. The hardenability of a steel is conveniently represented using either Time-Temperature-Transformation (TTT) diagrams or Continuous-Cooling-Transformation (CCT) diagrams. Each type of diagram is a representation of the austenite decomposition products that can be expected for a specific alloy under conditions of isothermal transformation and continuous cooling respectively (Honeycombe and Bhadeshia 1995). Such diagrams are routinely made use of to devise industrial heat treatment processes (Atkins Year of publication not known).

1.10.2 Bainite formation

Bainite formation is a possibility whenever austenite is cooled sufficiently slowly, or held isothermally within a bainite transformation temperature region. In terms of the Q&P heat treatment process, this could occur either during a quenching operation (although avoidable by increasing the hardenability or increasing the cooling rate) or, of more importance in the present instance, during the post-quenching partitioning stage.

Some of the earliest research on bainitic (troostite) structures was reported in the first part of the twentieth century. At this time it was hypothesised that bainite formed from martensite as part of a transformation sequence, starting with austenite, and ending with pearlite (with martensite and bainite as intermediate structures) (Bendicks 1905). In the 1920s and 1930s, Bain (from whom the name of the bainite

microstructure originated), Davenport, Robertson and other researchers questioned whether the transformation-sequence hypothesis was correct, and if transformation to each observed structure could occur directly. By this stage, the use of X-ray analysis had also enabled more accurate definitions of austenite and martensite (Honda 1926) (Robertson 1929).

The 1940s saw some useful research which distinguished between the transformation mechanisms of pearlite and bainite. Carbides within pearlite were found to always have substitutional alloy compositions greater than that of carbides in bainite. This observation was interpreted by Hultgren as evidence of orthoequilibrium and para-equilibrium conditions in pearlite and bainite formation respectively (Hultgren 1947). Zener was also active, proposing that bainite forms with a supersaturation of carbon, relieved by the partitioning of carbon to untransformed austenite, and the precipitation of carbides (Zener 1946).

However, despite some relatively early discoveries, and proposed mechanisms of transformation, much of the period from the discovery of bainite up to comparatively recent times has seen disagreement over the correct identification of, and the mechanisms of bainite formation in its different manifestations (Hehemann, Kinsman et al. 1972) (Bhadeshia and Edmonds 1979). On the Time Temperature Transformation (TTT) or Continuous Cooling Transformation (CCT) diagram Bainite sits between the diffusional Ferrite/Pearlite formation processes, and the diffusionless process of martensite formation. The formation of bainite and the resulting microstructure contain similarities to both diffusional and diffusionless processes (Hehemann 1968) (Bhadeshia 2001). Hence, many of the differences in opinion on the subject have related to whether the bainite formation mechanism is diffusional, diffusionless, or some combination of the two.

As recently as 1972, a debate on the Bainite reaction showed up significant differences in opinion between those that believed bainite was the result of a shear transformation, and those that supported a reconstructive mechanism (Hehemann, Kinsman et al. 1972). A paper published by Christian and Edmonds in 1983 examined some of the reported characteristics of the bainite transformation while comparing these features to the opposing theories proposed for the bainite reaction. Christian and Edmonds supported the displacive mechanism of bainite formation, mainly on the basis of the plane strain nature of the reaction product (Christian and Edmonds 1983).

Technological advances in the form of atom probe experimental techniques have added further weight to the argument for a displacive mechanism of bainite formation, by demonstrating that unlike reconstructive processes such as ferrite and pearlite formation, there is no diffusional redistribution of substitutional elements during the bainite reaction (Bhadeshia and Waugh 1982). The growth of bainite laths is therefore believed to progress by a diffusionless process. Carbon within the laths may be rejected concurrently during the diffusionless growth of laths, or following lath formation (Bhadeshia 2001). This transformation mechanism was postulated as far back as 1946 by Zener, who found that bainite growth was dependant upon the carbon composition of un-transformed austenite, at higher austenite carbon contents bainite growth was not possible until the temperature was lowered to the critical temperature for that specific composition (Zener 1946). Further research in this area led to the incomplete-reaction concept illustrated by the experimental data published by Bhadeshia and Edmonds, and reproduced in Figure 1.12. The reaction is said to be incomplete because although the bainite has reached the point at which its free energy is equal to that of untransformed austenite, the austenite composition has not yet reached its equilibrium point at Ae_3'.

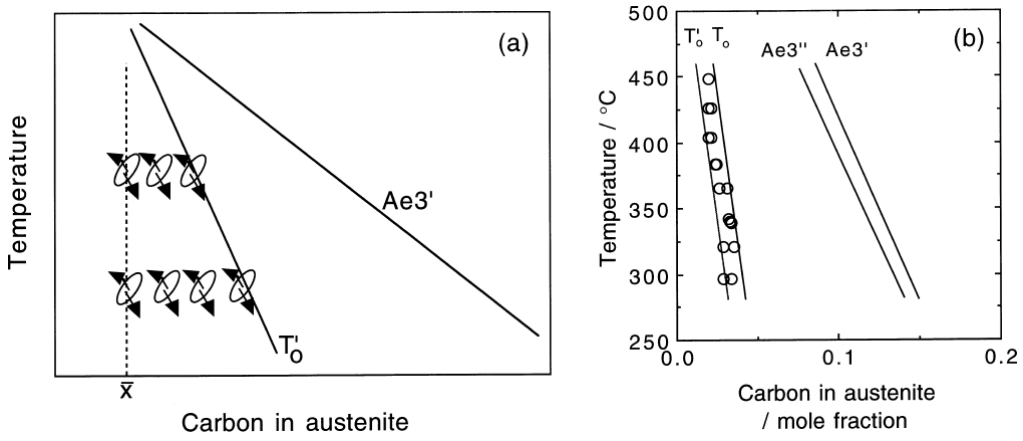

Figure 1.12 - The incomplete-reaction phenomenon. A plate of bainite grows without diffusion, then partitions its excess carbon into the residual austenite. The next plate thus grows from carbon-enriched austenite. This process can only continue until $x_\gamma = xT'_0$. For paraequilibrium growth, the transformation should proceed until the carbon concentration reaches the Ae_3'' curve. (b) Experimental data on the incomplete reaction phenomenon for Fe-0.43C-3Mn-2.12Si wt% alloy. Bhadeshia, after Bhadeshia and Edmonds (Bhadeshia 2001) (Bhadeshia and Edmonds 1979)

In most steels the type of bainite that has formed can be conveniently classified as either upper or lower bainite, the upper and lower nomenclature referring to the temperature range over which each type forms. In upper bainite the carbides precipitate from carbon enriched austenite such that the bainitic ferrite is free from carbides; therefore, the structure of the bainite is that of bainitic ferrite laths with intralath carbides. In lower bainite two types of carbides precipitate, as for upper bainite intralath carbides precipitate, in addition, some interlath carbides form within the ferritic bainite (Bhadeshia 2001) (Bhadeshia and Edmonds 1979). This microstructural classification is now fairly widely accepted (although this has not always been the case).

By using appropriate alloying to suppress formation of equilibrium carbides, as employed by Hehemann et al. and Bhadeshia and Edmonds during their studies of the reaction mechanism, the bainite reaction has become the basis of the production route for TRIP steel. The carbide precipitation component of the bainitic transformation is commonly inhibited by silicon alloying additions, causing carbon in the bainite laths to be rejected into the surrounding austenite. The carbon enriched austenite then becomes stabilised to room temperature. Consequently, the mechanism of austenite stabilisation is similar to that which occurs in the Q&P process, but with one major important difference. Carbon rejected to austenite during the bainite reaction must be coupled with austenite decomposition to bainitic ferrite; whereas during Q&P, the concentration of carbon in the austenite will not be so limited, and thus could potentially be very much higher.

There are two important considerations of how the bainite reaction might interact with the proposed Q&P heat treatment. One is that during a one-step process, or even a two-step process, little martensite might have formed, and that the observed microstructure is simply the result of a bainite reaction. It has previously been proposed that there is little difference, certainly recognisable by casual metallographic observation, between a carbide-free bainite (as produced in a high-Si containing steel) and lath martensite. The second consideration is that bainite could form during the partitioning stage, thereby reducing the quantity of stabilised austenite. Clarke and co-workers have published research to counter the argument that Q&P may just be another isothermal heat treatment process, producing bainite and retained austenite in a mechanism very similar to the TRIP process (Clarke, Speer et al. 2008). The reasoning against a bainite transformation is based on the high levels of retained austenite, which are considered to be inconsistent with this mode of reaction (see Figure 1.28 in Section 1.11.3). Although the levels of retained

austenite fall short of those predicted to result from the Q&P process, explanations exist as to how these shortfalls can occur (see Sections 1.10.5 and 1.11.1).

The most recent research on the Q&P process (Li, Lu et al. 2010b) has produced evidence of bainite formation as a competing reaction during partitioning. Li, Lu et al investigated a medium carbon steel (0.41C, 1.27Si, 1.3Mn, 1.01Ni, 0.56Cr). Following initial quenching to 180°C, bainite was found to be present after partitioning at 300°C for partitioning times ranging from 30 to 900 seconds. Epsilon carbide was observed within the bainite, therefore it must be concluded that some or all of the carbon rejected from the newly formed bainite did not partition to austenite.

1.10.3 Carbide precipitation

The formation of carbides is the normal outcome of a conventional quench and temper heat treatment process, whereby the non-equilibrium carbon supersaturation of the quenched martensite is relieved by carbide precipitation. During traditional tempering this will relieve internal stresses in the martensite and improve toughness, but also, in 'locking' the carbon, favour full decomposition of austenite, thus also improving the stability of the final microstructure. However, as previously mentioned, carbon that forms carbides is not available to stabilise austenite via the proposed Q&P route, and so carbide precipitation is a process that must be suppressed as far as possible to maximise the efficiency of the Q&P process. The commercial importance of quench and tempered products has generated significant research output related to the study of the various stages of tempering, especially carbide precipitation. Of more importance to the Q&P process, however, are the mechanisms by which alloying elements are able to inhibit the nucleation and growth of carbides.

One of the most stable carbide structures found in plain carbon steels is that known as cementite, which appears on the iron-carbon equilibrium diagram and has the chemical formula Fe_3C. However, numerous other metastable carbides are possible, such as Hagg Carbide, χ-carbide, Fe_5C_2, Fe_7C_3, η-carbide (Fe_2C) and ε-carbide ($Fe_{2.4}C$) (Sinha 1989) (Porter and Easterling 1992). The tempering process is generally described as occurring in a succession of stages, albeit with some overlaps between temperature ranges for each stage. In a recent text, Honeycombe and Bhadeshia (Honeycombe and Bhadeshia 1995) consider four stages, while others detail a higher number of stages (Porter and Easterling 1992).

Stage one commences with the segregation of carbon to low-energy areas such as dislocations and lath boundaries, this process occurs between room temperature and 100 ºC and is followed by formation of epsilon-carbide between 100 and 200 ºC (Porter and Easterling 1992) (Sinha 1989) (Honeycombe and Bhadeshia 1995). At this stage of the tempering reaction an important distinction exists between low carbon steels and medium to high carbon steels. Steels containing less than 0.2 wt% carbon are observed to omit the epsilon-carbide formation stage (see Section 1.10.5). Tempering experiments show that following epsilon-carbide precipitation the carbon content of the martensite matrix is approximately 0.2 wt% and the structure is still tetragonal (Honeycombe and Bhadeshia 1995).

During stage two, temperatures between 230 and 300 ºC are reported to decompose retained austenite (Honeycombe and Bhadeshia 1995). The decomposition of austenite is covered in some detail in Section 1.10.4 and illustrated in Figure 1.14 and Figure 1.15 in the same section.

The third stage of tempering is associated with the appearance of cementite within the structure. It is believed that rather than epsilon-carbide transforming to cementite, that cementite nucleates and grows at the expense of dissolving epsilon-carbide particles.

The fourth stage includes coarsening (300 to 400°C) and spheroidisation (up to 700ºC) of the cementite particles. At the highest temperature ranges the martensite lath boundaries are affected, ‘the lath martensite boundaries are replaced by more equi-axed ferrite grain boundaries in a process which is best described as recrystallization’ (Honeycombe and Bhadeshia 1995).

Due to the commercial importance of the Quenching and Tempering process, inhibition of carbide nucleation and growth has received less attention. Nevertheless, there has been some useful research reported in this area. Although several alloying elements exist that are believed to possess carbide inhibiting properties when added to steel (Silicon, Aluminium, Phosphorous and Copper) (Traint, Pichler et al. 2002), the majority of in-depth research and hypotheses for inhibition mechanisms apply to the use of Silicon (Saito, Abiko et al. 1993) (Hobbs, Lorimer et al. 1972) (Burke and Owen 1954) (Gordine and Codd 1969).

Silicon is reported to retard the formation of carbides over a wide range of temperatures. At the lower temperature range, when epsilon-carbide is expected to be viable, studies using electrical resistance to measure the extent of carbide precipitation, and TEM to count the number of precipitates present have shown that silicon is effective in reducing the rate at which epsilon-carbide forms. The mechanism by which this occurs was reported to be by a 'decrease in number density of carbide particles'. Silicon is therefore assumed to act by reducing the number of sites at which epsilon-carbide nucleation is thermodynamically viable (Saito, Abiko et al. 1993).

Other research offers a slightly different perspective. The work of Gordine and Codd suggests that silicon acts to stabilise epsilon-carbide to higher temperatures. This has the combined effect of preventing carbon trapped in epsilon-carbide from being released to form the more stable cementite, and of delaying recrystalization of the matrix structure. The silicon is postulated to reduce the lattice parameter of epsilon-carbide, thereby causing it to persist to a higher temperature, and delaying the onset of cementite formation (Gordine and Codd 1969).

A study of the graphitisation of silicon steels also yields useful information, as the requirements for cementite formation are similar to those for graphitisation; both processes necessitate the diffusion of carbon to the growing particle. Burke and Owen (Burke and Owen 1954) propose that as a graphite nucleus develops, silicon must be rejected, leading to the formation of a silicon rich skin around the nucleus. Silicon increases the activity of carbon in iron (see Figure 1.13), thereby impeding carbon migration into the growing particle. To permit growth of the graphite particle, iron atoms must also diffuse away from their lattice sites. Measurement of reaction rates by Burke and Owen has shown that the rate controlling step for graphitisation is diffusion of silicon or iron rather than diffusion of carbon (Burke and Owen 1954).

The effect of silicon when cementite is already established has also been studied, and it is reported that silicon delays grain growth. The mechanism by which this occurs is to delay the point at which cementite particles become too large to pin grain boundaries. Therefore, silicon holds back the coarsening of cementite to higher temperatures and longer times (Hobbs, Lorimer et al. 1972). However, although silicon is an effective carbide suppressant, alternative alloying elements have been

evaluated from the perspective of their suitability to produce a TRIP steel which does not suffer from the surface oxidation issues (see Section 1.4) that are commonly encountered in materials which have silicon alloying additions (Traint, Pichler et al. 2002).

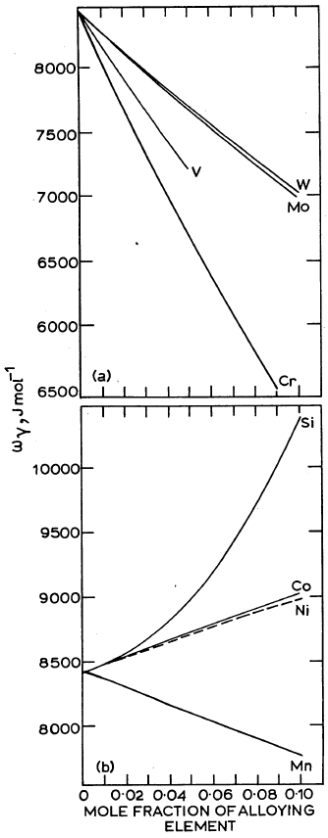

Figure 1.13 - Variation of carbon-carbon interaction energy in austenite as a function of concentrations of various alloying elements (Bhadeshia 1981a)

The precipitation of alloy carbides forms the basis for the most common method of strengthening by heat treatment, namely quenching and tempering. The alloying elements serve two purposes. Firstly, the hardenability of the steel is increased; this enables martensite formation in deep sections. Secondly, during tempering, dispersions of very fine alloy carbides form leading to increased strength. The tempering stage is flexible and can be tailored to produce a range of mechanical properties from the same starting material. The formation of carbides with alloying elements such as Vanadium, Titanium and Molybdenum is not considered here, except to state that these alloying elements are intentionally avoided in Q&P steels at the moment, because of their strong carbide forming properties (Porter and Easterling 1992). However, some researchers consider that owing to the much lower chemical potential of carbon in austenite (compared to martensite), once carbon has

successfully partitioned to austenite the potential to form carbides is much reduced (Speer, Rizzo et al. 2005).

1.10.4 Decomposition of retained austenite to ferrite and carbides

A secondary purpose of the tempering stage in a conventional quench and temper heat treatment may be to decompose any retained austenite (Honeycombe and Bhadeshia 1995). In some cases, such as the use of quenched and tempered steel for bearing applications, the presence of retained austenite is undesirable as it can cause dimensional instability (Mikus, Hughel et al. 1960). In Q&P steels the decomposition of retained austenite is disadvantageous because the presence of this phase is fundamental to the Q&P concept.

The decomposition of austenite to ferrite and carbides is a possibility during the partitioning stage of the Q&P process. Detailed studies concerning this are not yet believed to have been made. However, some useful information exists from the work of Gerdemann (Gerdemann 2004) (Gerdemann, Speer et al. 2004), which indicates that for partitioning temperatures of 300, 400 and 500°C, the retained austenite volume fraction is progressively reduced at longer partitioning times.

In the area of TRIP-steels, research effort has been ongoing for some years and more detailed investigations have been conducted. There exist sufficient similarities between TRIP-steels and the Q&P concept (dual-phase ferritic/austenitic structure, stabilised austenite, similar chemical composition and alloying philosophy) that the research relating to TRIP-steels can be usefully consulted. Dynamic experimentation on TRIP-steel has provided a unique perspective on the stability of retained austenite during re-heating (Jun, Park et al. 2004) (Choi, Kim et al. 2002).

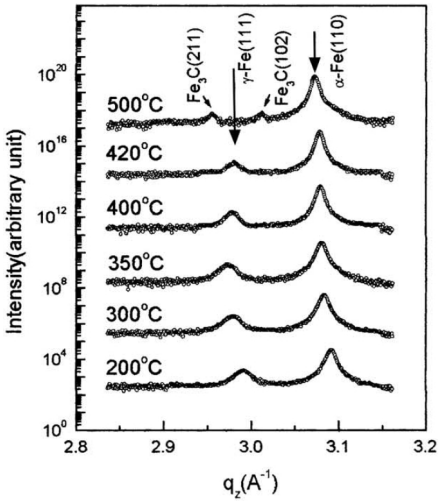

Figure 1.14 - X-ray diffraction profile observed using synchrotron radiation (Pohang Light Source) during in-situ heating of a TRIP steel (Jun, Park et al. 2004)

Figure 1.14 and Figure 1.15 show the effect of a continuous heating rate of 0.2°C/second from room temperature to 500 ºC on the structure of a TRIP-steel containing retained austenite.

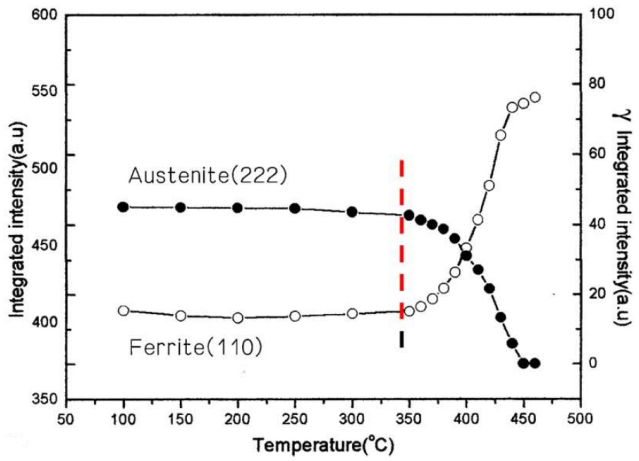

Figure 1.15 - Integrated intensity of ferrite (1 1 0) and austenite (2 2 2) peaks using X-ray diffraction profile observed using synchrotron radiation (Pohang Light Source) during in-situ heating of a TRIP steel (Jun, Park et al. 2004)

1.10.5 'Trapping' of carbon within dislocations and other low-energy areas

Cottrell and Bilby were the first to propose that the yield phenomena of body-centred-cubic metals could be explained by the diffusion of carbon to dislocations (Cottrell and Bilby 1949). Since this initial discovery there have been various publications concerning the segregation of interstitial alloying elements to lattice defects, including several involving the 'artificial' creation of lattice defects

specifically to study this topic (Wagenblast and Damask 1962) (Fujita and Damask 1964) (Arndt and Damask 1964) (Wagenblast, Fujita et al. 1964). Dislocations and other lattice defects represent an energetically favourable location for interstitial atoms by bringing about a reduction in the strain energy of the lattice (Cochardt, Schoek et al. 1955) (Kalish and Cohen 1970). Therefore, it is considered highly likely that segregation of carbon to low energy locations could provide an energetically competitive alternative to the diffusion of carbon into adjacent untransformed austenite.

A well known limitation occurs in the early stages of tempering by which steels containing up to 0.2wt% carbon do not undergo precipitation of metastable ε-carbide (King and Glover 1959). Instead, the carbon is reported to move into low energy positions in and around dislocations and lath boundaries, therefore becoming unavailable for ε-carbide formation (Porter and Easterling 1992). Speich found that 'in martensites containing less than 0.2pct C, almost 90 pct of the carbon segregates to dislocations and to lath boundaries during quenching' (Speich 1969). Some texts (Porter and Easterling 1992) suggest that the 0.2wt% carbon limit is due to the higher martensite start temperatures of low carbon steels (the higher temperatures enable carbon to move to low-energy, lath-boundary positions during the quenching stage).

Other texts state that in medium/high carbon steels martensite is not stable at room temperature because carbon diffusion is able to occur (Honeycombe and Bhadeshia 1995). Kalish and Roberts developed a theoretical model which predicts that 85% of carbon in a low alloy steel will segregate to dislocations, at higher carbon contents the martensite structure becomes twinned and a maximum of 66% of carbon in a 0.8wt% steel was predicted to become segregated in the same way (Kalish and Roberts 1971). Wilson demonstrated the affinity of carbon for dislocations by showing that in medium carbon steels cold work can inhibit carbide precipitation and bring about the dissolution of previously formed carbides (Wilson 1957). Other workers have supported the concept of carbon 'trapping' using techniques such as electrical resistance and internal friction measurements (Speich and Leslie 1972) (Speich 1969).

More recently, researchers have utilised atom probe measurements (Waugh, Paetke et al. 1981) to prove conclusively that during room-temperature-ageing carbon diffuses from its quench positions to more energetically favourable locations

in and around dislocations (see Figure 1.16). In a 0.1wt%C alloy the martensitic matrix carbon concentration was observed to reduce by more than a factor of five compared to the nominal composition of the alloy (Wilde, Cerezo et al. 2000). Atom probe techniques have also provided evidence of carbon segregation to lath boundaries; either to within the boundary itself or to a very thin film of retained austenite located at the boundary (Miller, Beaven et al. 1981).

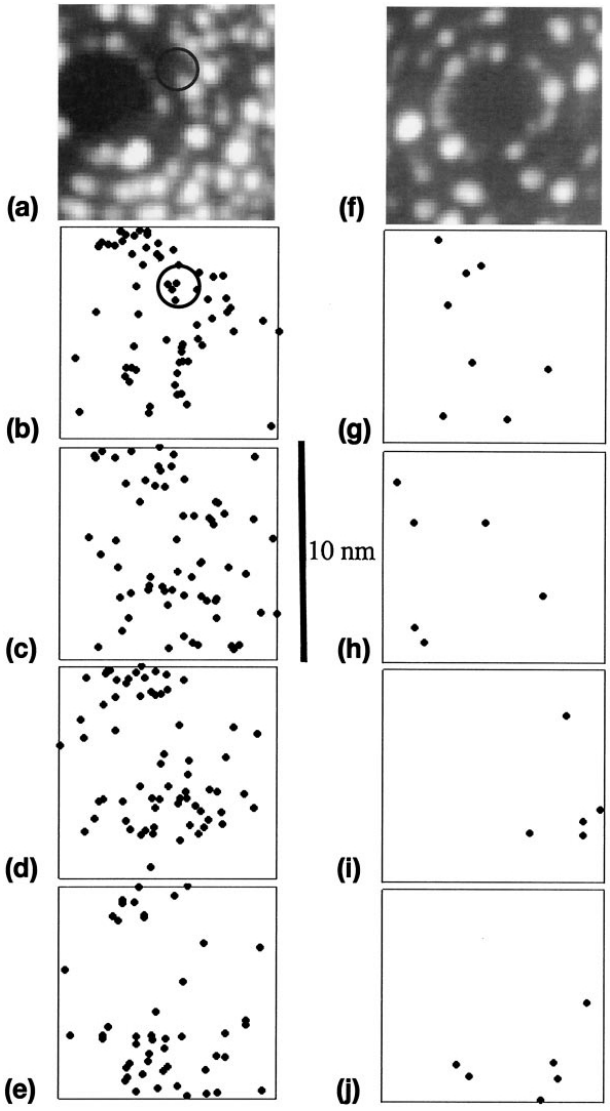

Figure 1.16 - Results of ECOPoSAP analysis of carbon atmosphere made (a-e) directly over a dislocation and (f-j) over a dislocation free region. Field ion micrographs showing areas of analysis, (a) and (f), taken at 12kV in Ne at 50K. The analyses are divided into four successive sections, (b-e) and (g-j) respectively, each containing exactly five atomic planes. In each case the width of the analysed region is 10± 1.5 nm. The initial position of the dislocation is shown by the dark circles in (a) and (b) (Wilde, Cerezo et al. 2000).

1.11 Research on Quench and Partitioned Steels

Although it is considered that some heat treatment processes may have done, or do currently follow the Q&P temperature/time profile, the intentional use of a heat treatment process to bring about the multiphase Q&P microstructures and associated mechanical properties that have been achieved in recent years is thought to be a new development (Edmonds, He et al. 2006) (Edmonds, He et al. 2007). A number of studies have now been published examining Q&P over carbon ranges from low-carbon TRIP steels to medium-carbon bar steels; although it is well to bear in mind that it is the carbon concentration of the quenched austenite which is important, which in the case of austenite carbon enrichment is not the same as that of the bulk steel.

1.11.1 Predicting the outcome of a Q&P heat-treatment process

The first report of Q&P as a ‘fundamentally new process’ was made in 2003 (Speer, Streicher et al. 2003). This initial report focused on the thermodynamic driving forces for carbon partitioning, and the means of suppressing carbide precipitation. A theoretical model was also included (see Figure 1.17) for predicting the phase fractions after quenching and partitioning via use of the Koistinen-Marburger relationship (Koistinen and Marburger 1959).

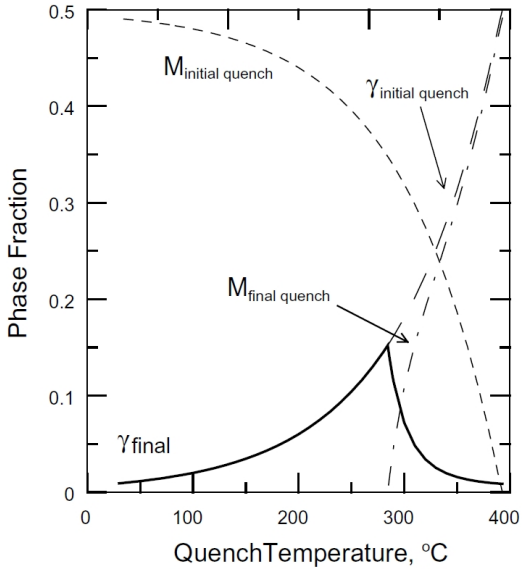

Figure 1.17 – Predicted Q&P microstructure components for experimental steel containing 50% intercritical ferrite, vs. quench temperature, assuming full partitioning prior to final quenching to room temperature. The final austenite fraction at room temperature is given by the solid bold line. Dashed lines represent the austenite and martensite (M) present at the initial quench temperature, and the additional martensite formed during the final quench to room temperature. It should be noted that $\alpha_{IC} + M_{initial\ quench} + M_{final\ quench} + \gamma_{final} = 1$, and $\alpha_{IC} = 0.5$ in this example (Speer, Streicher et al. 2003).

The theoretical prediction features a maximum retained austenite fraction with an exponential fall-off either side of the maximum. At the highest quenching temperatures the quantity of austenite predicted to be retained to room temperature is controlled by the availability of carbon. The quantity of martensite formed during the initial quench is lower, and so less carbon is available to stabilise austenite. Hence, some austenite transforms to martensite during the final quench. At the lowest quenching temperatures, the quantity of austenite predicted to be retained to room temperature is controlled by the initial quench. The fraction of austenite that is retained is simply the fraction that did not transform to martensite during the initial quench, sufficient carbon is available from the martensite (formed during the initial quench) to stabilise all of the austenite that did not transform during the initial quench. It should be noted that this model assumes that 100% of the martensite carbon content is partitioned to untransformed austenite. Attempts to validate this model with experimental data have met with mixed success. Although the distinctive peak predicted by the model has been replicated (see Figure 1.26 in Section 1.11.3), this has only been achieved for a select set of conditions (Gerdemann 2004);

predictions of retained austenite fraction have in general exceeded measured levels (Rizzo, Martins et al. 2007) (Gerdemann 2004) (Clarke, Speer et al. 2008).

Following the work of Speer and co-workers (Speer, Streicher et al. 2003), research has shown the assumption that 100% of the carbon within martensite partitions to austenite is probably somewhat optimistic. X-Ray diffraction studies involving the use of the Koistinen-Marburger method of predicting optimum quench temperature returned a measured austenite content of zero, versus a predicted content of 12% (Kim, Kim et al. 2007). The authors attributed this discrepancy to the low carbon content of the alloys being used (0.15wt%C). At this point, it is worth noting that in steels with carbon contents below 0.2wt% the epsilon carbide precipitation step is omitted during tempering (King and Glover 1959). As previously mentioned in Section 1.10.5, Speich (Speich 1969) postulates that in steel with carbon content of below 0.2wt%, 90% of the carbon in the martensite is accommodated by low energy sites, such as lath boundaries and dislocations. Therefore, there appears to be a justification for the existence of a minimum carbon content, below which Q&P may be ineffective in stabilising austenite; and also, an explanation as to why the Q&P process may sometimes return lower than predicted retained austenite fractions.

More recent research (Clarke, Speer et al. 2009) has involved a re-work of the theoretical Q&P model, such that cognisance is taken of the time required for the partitioning process to attain equilibrium. In the revised model DICTRA (see Section 1.8.3) has been used to estimate the carbon concentration gradient in austenite after different partitioning times. The austenite carbon concentration gradient is then used to perform ‘local’ calculations of retained austenite fraction (as per the original model, but on a ‘local’ basis). The outcome of this is illustrated in Figure 1.18, from this it can be seen that the austenite carbon distribution at the time of the final quench is, as would be expected, of great importance. Additionally, the behaviour predicted in Figure 1.18 is reported to agree with some of the trends encountered in laboratory experiments.

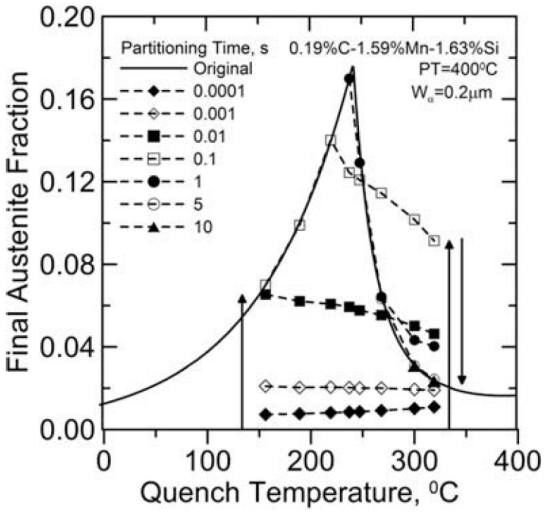

Figure 1.18 – Calculated final austenite fraction as a function of quench temperature for a 0.19C-1.59Mn-1.63Si (wt%) alloy (Clarke, Speer et al. 2009)

1.11.2 Mechanisms occurring during Q&P and supporting evidence

Following the initial report of and naming of the Q&P process, research has been conducted to determine the mechanisms by which the Q&P process is effected and the mechanical properties of the resulting microstructures. Theoretical models have been devised to describe the processes occurring at each stage of the heat treatment. The Q&P process has often been represented as in Figure 1.19 (Speer, Streicher et al. 2003) (Matlock, Brautigam et al. 2003) (Gerdemann, Speer et al. 2004) (Speer, Rizzo et al. 2005) (Edmonds, He et al. 2006) For simplicity, the schematic ignored competing reactions. An important premise was that following the initial quenching stage the austenite/martensite interface is static, this state was initially termed constrained para-equilibrium (CPE) and later termed constrained carbon equilibrium (CCE) (see Section 1.8.1).

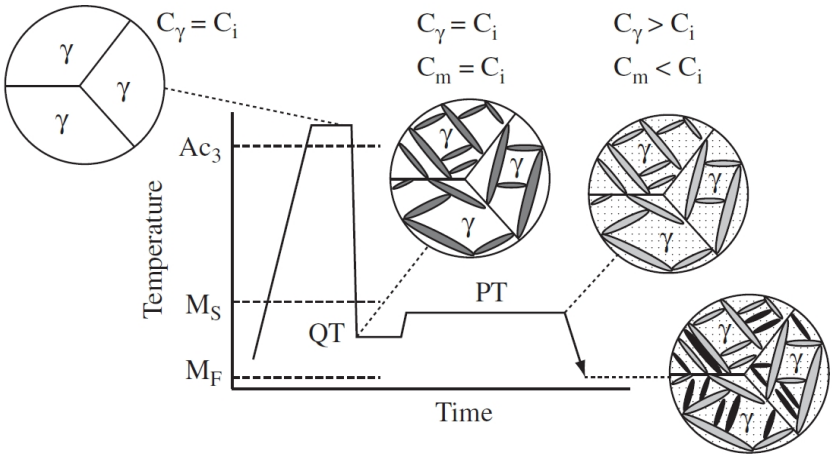

Figure 1.19 – Schematic illustration of the Q&P process for producing of austenite-containing microstructures. C_i, C_γ, C_m represent the carbon contents of the initial alloy, austenite, and martensite, respectively. QT and PT are the quenching and partitioning temperatures (Speer, Streicher et al. 2003).

The schematic shown in Figure 1.19 has been supported by XRD data which demonstrates an increase in austenite lattice parameter following carbon partitioning. An example of the lattice parameter shift that occurs is shown in Figure 1.20.

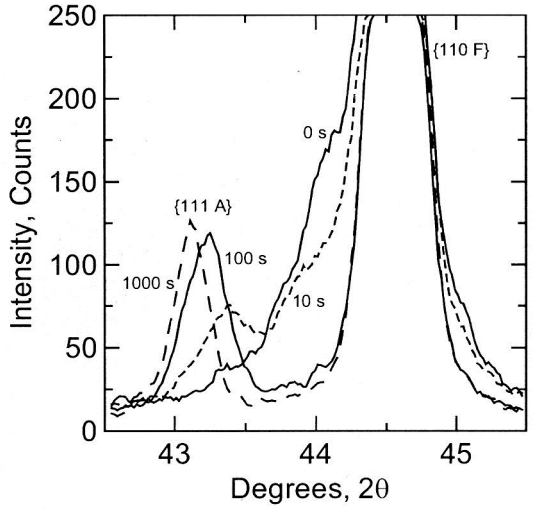

Figure 1.20 – X-ray spectra illustrating changes in the $\{111\}_\gamma$ and $\{110\}_\alpha$ peaks during partitioning at 400°C in experimental steel intercritically annealed at 805°C and quenched to 284°C (Speer, Streicher et al. 2003).

Transmission Electron Microscopy (TEM) has been used to carry out detailed investigations of the structures that exist following Quenching and Partitioning (Edmonds, He et al. 2007). These studies confirmed the existence of a dual phase

microstructure consisting of martensite and retained austenite, as illustrated in Figure 1.21, Figure 1.22, and Figure 1.23.

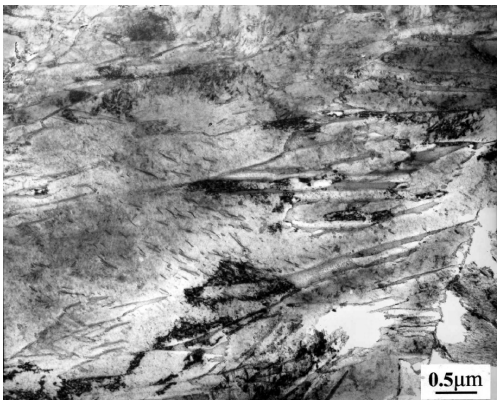

Figure 1.21 – Brightfield TEM micrograph of Q&P microstructure after 30 s partition at 400 deg. C (Edmonds, He et al. 2007).

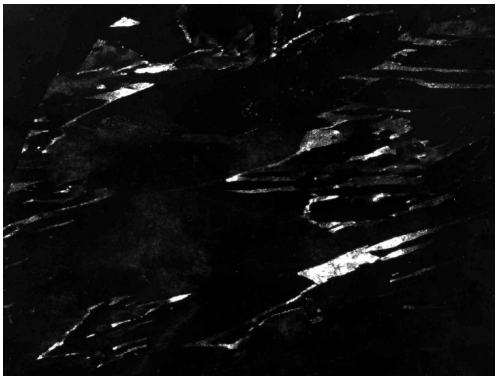

Figure 1.22 – Dark-field TEM micrograph of Q&P microstructure after 30 s partition at 400 deg. C showing (020)γ reflection (Edmonds, He et al. 2007).

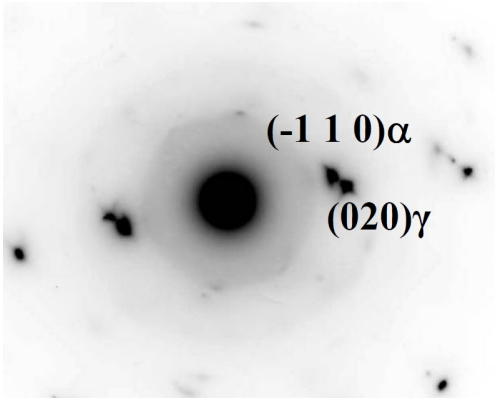

Figure 1.23 – Diffraction pattern corresponding to Figure 1.21 and Figure 1.22 (Edmonds, He et al. 2007).

1.11.3 Effect of Q&P heat-treatment process variables

Research published by Matlock, Brautigam et al. highlighted some interesting differences between single-step and two-step Q&P processing (Matlock, Brautigam et al. 2003). While the single-step process appeared to be more efficient at producing retained austenite (Figure 1.24), the response to partitioning time was far less predictable than that of the two-step process (Figure 1.25). Although the predicted quantities of retained austenite were not achieved, the measured austenite carbon content exceeded that predicted in all cases. This indicated some complexities not included in the theoretical model and it was postulated that a gradient in carbon concentration existed within the retained austenite, i.e. at the time of final-quenching equilibration of carbon within austenite was incomplete.

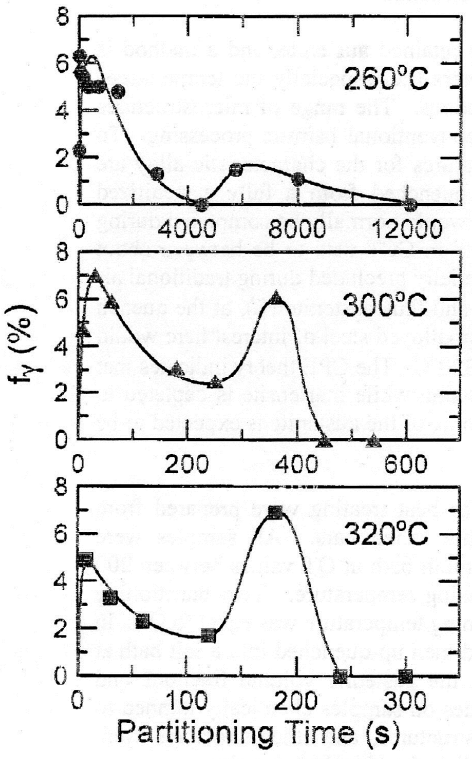

Figure 1.24 – Effect of partitioning temperature on the amount of retained austenite, f_γ, in samples processed by the single step treatment, i.e. QT = PT (Matlock, Brautigam et al. 2003).

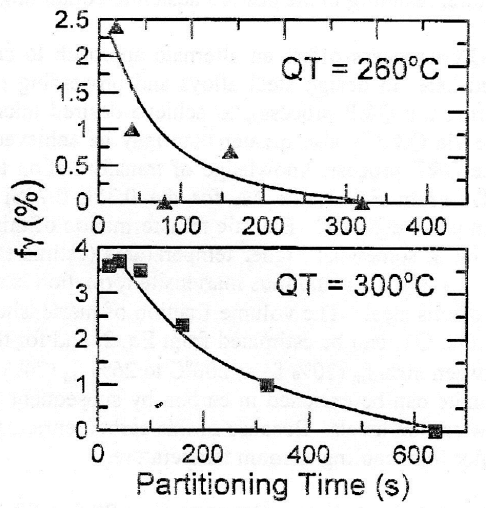

Figure 1.25 – Effect of partitioning temperature on the amount of retained austenite, f_γ, in samples processed by the two-step treatment for samples with PT = 425°C after rapid cooling to the indicated quench temperatures (Matlock, Brautigam et al. 2003).

Investigations into the effect of employing different partitioning temperatures (in a two-step process) have been published by Gerdemann. Partitioning temperatures between 500 and 250ºC were found to give widely differing results in terms of retained austenite fraction, partitioning time at which the maximum fraction of retained austenite was recorded, and hardness of the resulting microstructure. Comparisons were also made between the result of a Q&P heat treatment, and that of a bainitic heat treatment utilising the same starting material. (Gerdemann, Speer et al. 2004) At the highest partitioning temperature of 500ºC it was found that only the shortest partitioning time of 10 seconds produced any stabilised austenite, this was also the only partitioning temperature which gave a correlation with predictions using the Koistinen-Marburger relationship (see Figure 1.26).

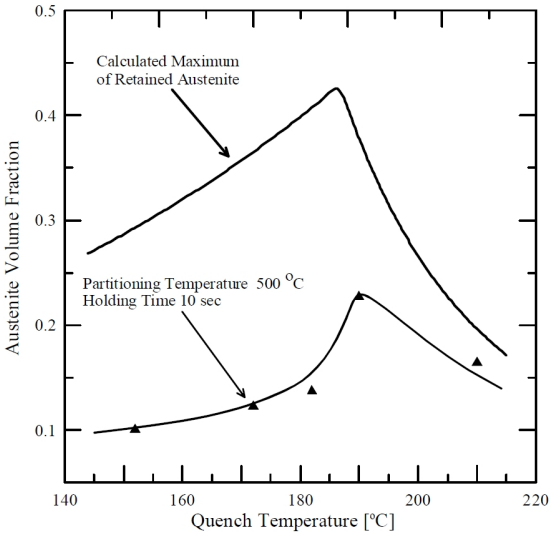

Figure 1.26 - Final volume fraction of retained austenite depending on the quench temperature at a partitioning temperature of 500°C and the calculated austenite volume fraction at this quench temperature range (Gerdemann 2004)

At partitioning temperatures of 300 and 400ºC the fraction of austenite decreased with each increase in partitioning time. However, the response at a partitioning temperature of 250ºC was different, austenite fraction steadily increased with partitioning time up to a maximum. The variety of partitioning responses displayed in Figure 1.27 suggests that the kinetics of carbon partitioning and competing reactions varies significantly with partitioning temperature.

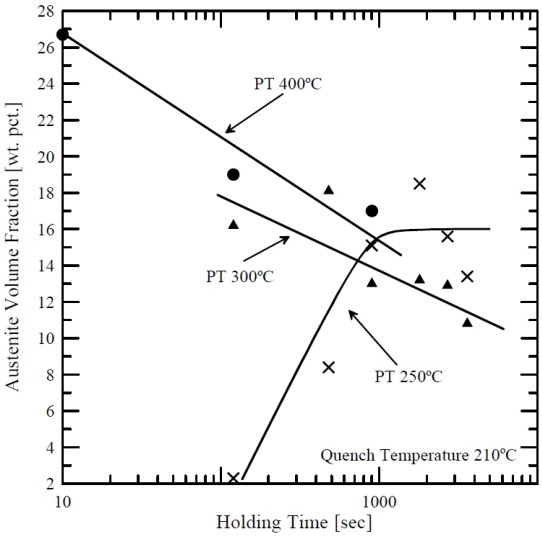

Figure 1.27 - Volume Fraction of retained austenite versus partitioning time at different temperatures, after quenching to 210 deg. C (Gerdemann 2004)

An interesting correlation between partitioning response and initial quench temperature is to be found in the work of Clarke, Speer, et al. Although partitioning times of 1000 seconds always gave the lowest fraction of retained austenite, the times of 10, 30 and 100 seconds showed behaviour that varied depending on initial quench temperature (Clarke, Speer et al. 2008). At lower initial quench temperatures the shortest partitioning times gave the highest retained austenite fraction, while the opposite was true for the highest quench temperatures (Figure 1.28). This observation suggests that equilibration of carbon within austenite is, as might be anticipated, related to the austenite fraction that exists following the initial quench.

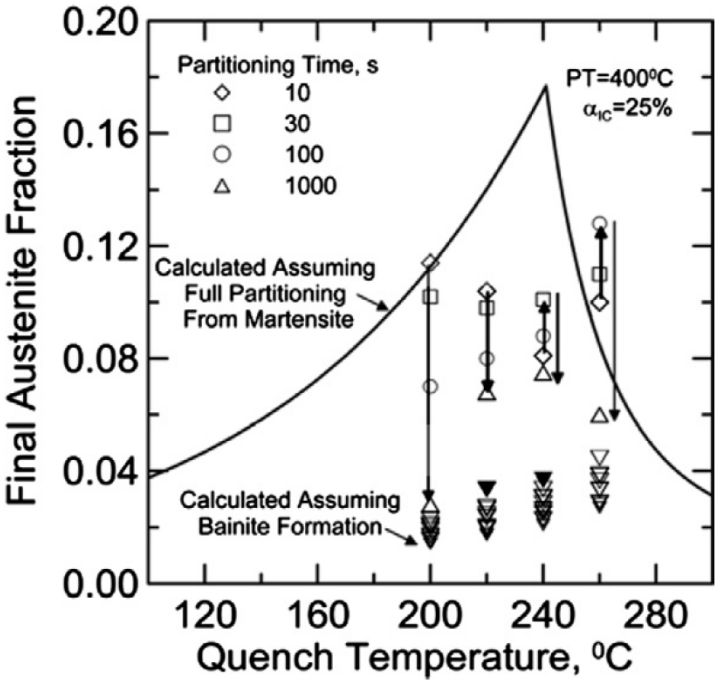

Figure 1.28 – Comparison of experimental austenite fractions (open symbols, not including inverted triangles) with calculated austenite fractions assuming two different possible mechanisms for austenite stabilization. A calculated (see Section 1.11.1) theoretical final austenite fraction curve (solid line) is shown based upon idealized full partitioning of carbon to austenite from martensite during Q&P processing. Calculated austenite fractions (open and solid inverted triangles) that assume carbide-free bainite formation are also shown. The two solid inverted triangles were calculated with carbon concentrations for both austenite and ferrite obtained from APT data. The other calculated austenite fractions (open inverted triangles) were calculated with austenite carbon concentrations obtained from XRD and ferrite carbon concentrations obtained from APT data. PT = 400°C designates the partitioning temperature and α_{IC} = 25% designates the intercritical ferrite amount. (Clarke, Speer et al. 2008)

An important subject in increasing understanding of the Quenching and Partitioning process is that of partitioning dynamics. It is considered that the rate of

diffusion of carbon differs somewhat depending on whether the matrix is of a Body-Centred-Cubic or Face-Centred-Cubic structure (see Figure 1.11 in Section 1.8.3). To this end, there has been an interest in modelling the diffusion of carbon from martensite to austenite using software such as DICTRA (Edmonds, He et al. 2006) (Clarke 2006). Further details on research relating to partitioning dynamics are given in Section 1.8.3 and 1.11.5.

1.11.4 Alloying additions to suppress carbide formation during Q&P

A limited amount of research has so far been carried out in the area of alloying additions to suppress carbide formation in Q&P steels. However, the applicability of alloying elements is thought to be similar to that for TRIP steels, hence, other useful research that is not specific to Q&P steels does exist (Section 1.4); studies of conventional quenching and tempering are also relevant (Section 1.10.3). De Moor, Lacroix et al. considered three different approaches, Silicon alone, Aluminium alone and a combined addition of Aluminium and Silicon. Experimentation with Differential Scanning Calorimetry (DSC) and dilatometry techniques showed that while the Aluminium addition was thought to be less effective in suppressing transition carbides, a higher activation energy for cementite formation existed in the steel alloyed with Aluminium (De Moor, Lacroix et al. 2006).

1.11.5 Applicability of the Constrained Carbon Equilibrium (CCE) Concept

Although initial research has sought to understand the Q&P process on the basis of a state of Constrained Carbon Equilibrium (CCE), more recent research has identified transformation behaviour that is not readily explained by the CCE model and instead supports a mobile austenite/martensite interface concept. The schematic molar Gibbs free energy diagram first published in 2003 (Speer, Streicher et al. 2003) (Matlock, Brautigam et al. 2003) (Speer, Matlock et al. 2003) and reproduced in Figure 1.7 of Section 1.8.1 has been considered by Zhong, Wang et al. They propose that under conditions of sufficiently high carbon concentration it may be thermodynamically favourable for iron atoms to cross the ferrite/austenite boundary, bringing about an increase in the austenite fraction (Zhong, Wang et al. 2006). The feasibility of this is of course dependent upon the kinetics of iron atom diffusion, and therefore requires a sufficiently high partitioning temperature (activation energy) to occur. In this situation the concept of Constrained Carbon Equilibrium cannot apply because the interface between austenite and martensite is not considered to be static.

Speer, Hackenburg et al. have published schematic Gibbs free energy diagrams illustrating that following achievement of CCE it is possible for full equilibrium to be accomplished by an increase or decrease in the fraction of retained austenite. Whether full equilibrium involves an increase or decrease in the fraction of retained austenite is dependent upon the carbon concentration in the martensite and the austenite. The two scenarios are shown in Figure 1.29. Unless nucleation of fresh grains was to occur then any increase in the fraction of either austenite or ferrite would be assumed to occur by the transfer of iron atoms across phase boundaries. It is hypothesised that in the event of long range carbon diffusion occurring concurrently with short range iron diffusion the dynamics of the situation could lead to a reversal of the interface resulting in an increase in austenite phase fraction. (Speer, Hackenberg et al. 2007).

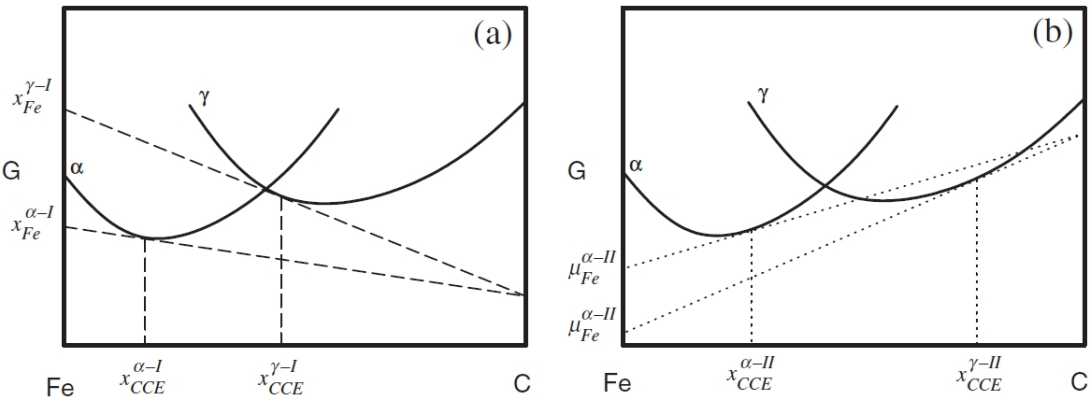

Figure 1.29 - Schematic tangent intercepts showing ferrite and austenite compositions having equal chemical potentials for carbon. In (a), the phase compositions are depleted in carbon relative to equilibrium and the chemical potential of iron is lower in ferrite than in austenite, while in (b), the phases are carbon enriched relative to equilibrium and the chemical potential is lower in austenite than in ferrite. X are phase compositions and μ are the corresponding chemical potentials (Speer, Hackenberg et al. 2007).

Further to the work of Speer, Hackenburg et al, a theoretical model and attendant computer simulation have been developed to investigate the possibility of interface migration with respect to the Q&P process (Santofimia, Zhao et al. 2008). Modelling results suggest that such experimental results as are illustrated in Figure 1.24 can be readily explained by migration of the martensite-austenite interface during the partitioning stage of the Q&P heat treatment (Santofimia, Speer et al. 2009). An example of this is depicted in Figure 1.30, however, it must be cautioned

that the model is somewhat sensitive to the value of activation energy that is chosen for interface migration. The activation energy for interface migration is selected based on the assumed characteristics of the interface; 140 $kJmol^{-1}$ for an incoherent interface (i.e. as for austenite ferrite transformation), or, 180 $kJmol^{-1}$ for a semi-coherent interface (i.e. as formed during austenite to martensite transformation). In addition, the author suggests that during partitioning (annealing) the nature of the interface may be subject to change, resulting in a variation in activation energy.

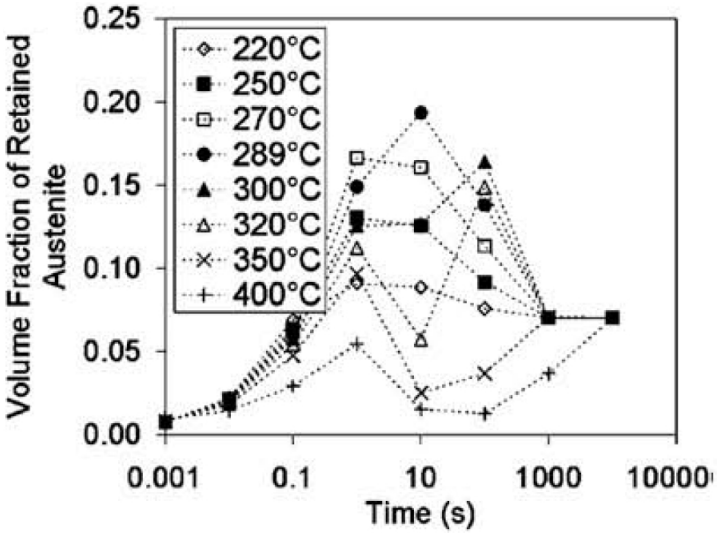

Figure 1.30 – Predicted volume fraction of austenite as a function of annealing time at 400°C, assuming an activation energy for interface migration of 180 $kJmol^{-1}$, results for initial quench temperatures from 220 to 400°C are plotted individually (Santofimia, Speer et al. 2009) Note, the final zero of 100000 seconds is missing in the original publication

1.11.6 Mechanical properties of Q&P steels

The mechanical properties of Q&P steels have not yet been as widely studied as some other areas of the Q&P process, however, some useful research has been published. One of the characteristics of dual/multi phase structures is that they commonly exhibit continuous yielding behaviour (Section 1.2.3). In this respect Q&P steels do not disappoint and Figure 1.31 shows a response recorded by Clarke (Clarke 2006). The difference in properties achieved by relatively small changes in the heat treatment procedure is noteworthy; this characteristic of the Q&P process led De Moor (who also studied the tensile properties of Q&P steel) to state that, ‘a variety of properties can be obtained even with a single chemical composition by adapting the heat treatment parameters’ (De Moor 2009).

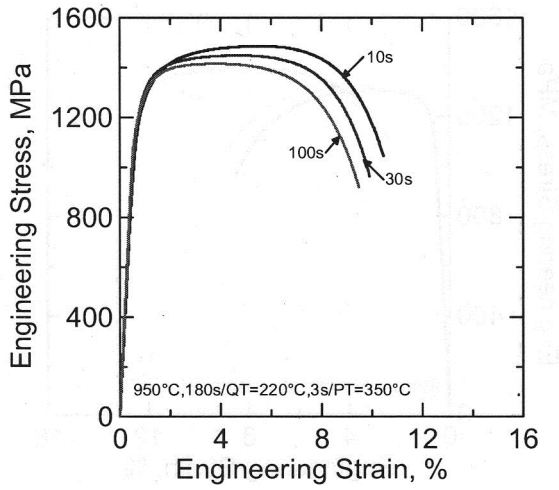

Figure 1.31 – Engineering stress as a function of engineering strain for Q&P samples austenitised at 950 deg. C for 180 s, quenched to 220 deg. C and held for 3 s, partitioned at 350 deg. C for 10, 30, or 100 s, and then water quenched to room temperature (Clarke 2006).

In more highly alloyed steels than those initially investigated, it has been shown (Figure 1.32) that enhancements to strength are feasible over and above those illustrated in Figure 1.2

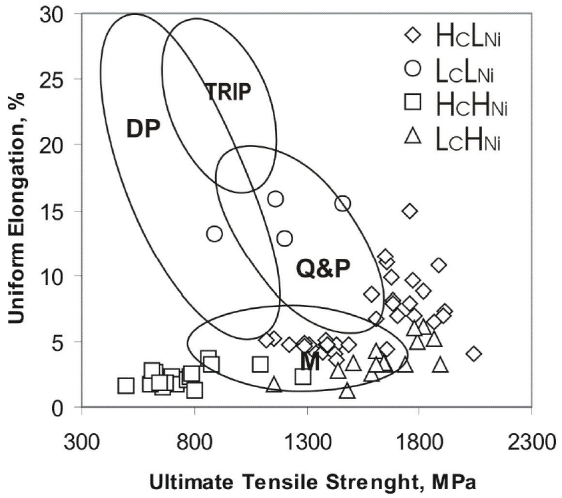

Figure 1.32 – Elongation and tensile strength of samples subjected to Q&P processing, compared to high performance grades (L, H, C and Ni refer to Low, High, Carbon, and Nickel respectively) (Rizzo, Martins et al. 2007)

1.12 The TRIP effect

1.12.1 Elastic and plastic inducement of transformation

The existence of stress, or strain induced solid state transformation in steel is not a recent discovery. Honda and Iwase were studying the stability of retained austenite in steel as far back as 1927, and determined via magnetometry measurements that it was possible to modify phase fractions by hammering samples (Honda and Iwase 1927). Furthermore, the so called 'TRIP effect' is not unique to iron based systems and need not involve plastic deformation, transformations may also be reversible. In 1952 Reynolds and Bever were experimenting with a reversible transformation in a copper-zinc alloy (Reynolds and Bever 1952). They found that application of an elastic strain caused clearly visible martensitic plates to appear on a polished surface. On subsequent removal of the stress some of these plates disappeared, re-application of stress caused plates to reappear at the originally observed locations. It was therefore concluded that in situations of elastic-strain martensitic transformations in this particular material are reversible.

1.12.2 Thermodynamic driving forces for elastic and plastic induced transformation

When an external stress is applied it is possible for this stress to contribute to the Bain Strain; the free energy barrier which must be overcome before the martensitic transformation can take place is therefore lowered and the martensite start temperature is raised (Porter and Easterling 1992). Figure 1.33 illustrates the effect of stress on the driving force available for martensite transformation via a schematic Gibbs Free Energy Diagram (Perlade, Bouaziz et al. 2003).

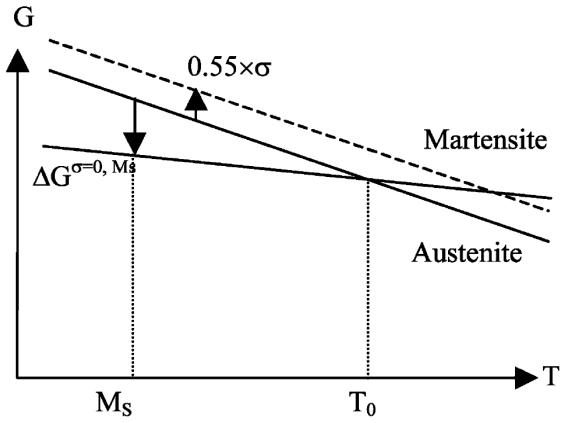

Figure 1.33 - Gibbs free energy curves versus temperature and effect of an applied stress σ (the factor of 0.55 is experimentally determined with units J mol^{-1} MPa^{-1}) (Perlade, Bouaziz et al. 2003)

1.12.3 Nucleation of martensite during loading

When material containing retained austenite is subjected to loading, the nucleation of martensite is believed to differ depending upon the temperature (Figure 1.34). In the highest temperature regime plastic deformation of retained austenite is able to occur without nucleation of martensite. At intermediate temperatures the straining of retained austenite produces potent martensite nucleation sites. At the lowest temperature range the application of stress (without strain) is sufficient to activate existing martensite nucleation sites (Perlade, Bouaziz et al. 2003).

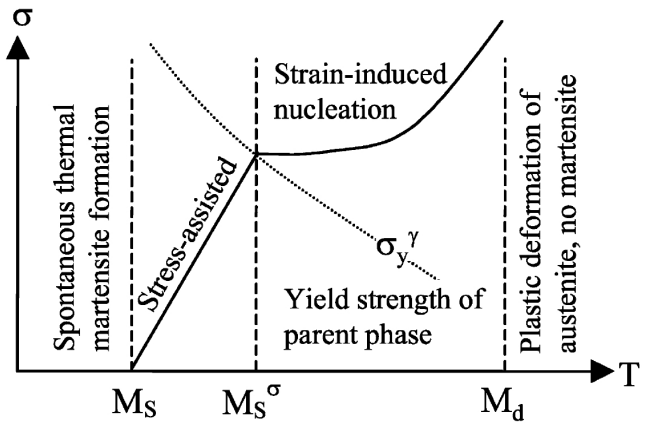

Figure 1.34 - Evolution of the martensitic nucleation stress with temperature (Perlade, Bouaziz et al. 2003)

1.12.4 Stability of retained austenite against transformation to martensite during loading

Research has been conducted to establish the determining factors in the stability of retained austenite subjected to loading. As might be expected, increasing carbon concentration has the effect of reducing the tendency of retained austenite to transform to martensite under loading (Jimenez-Melero, van Dijk et al. 2007). Chemical composition is believed to affect the ease of transformation to martensite by modification of the stacking fault energy (Samek, De Moor et al. 2006). The dimensions and morphology of retained austenite have also been found to be influential in susceptibility to martensitic transformation. Larger volumes of austenite and more granular austenite transforms more readily under loading than smaller volumes and thin film austenite (Park, Oh et al. 2002).

The means by which austenite morphology influences stability against the TRIP effect is believed to occur by several different mechanisms. Jimenez-Melero and co-workers evaluated thermal stability of retained austenite (rather than mechanical stability) and found that while carbon enrichment was the dominant influence in the stability of large austenite grains, for smaller austenite grains below $15\mu m^3$ the grain volume became an important factor (Jimenez-Melero, van Dijk et al. 2007). Other researchers have determined that encapsulation of austenite by martensite during the straining process can act as a stabilising factor (Yi, Yu et al. 1983). Some success has been reported in the prediction of the stability of retained austenite as a function of 'plastic strain, chemical composition, deformation temperature and the starting amount of austenite' (Sherif, GarciaMateo et al. 2004).

1.12.5 The mechanism by which the TRIP effect improves mechanical properties

TRIP steels and Q&P steels are multi-phase steels consisting of a hard phase (martensite or bainite) and a softer phase (austenite), if intercritical annealing is employed then ferrite may also be present. It is reasonable therefore to consider that the behaviour of both types of steel under mechanical test may give similar responses (e.g. continuous yielding) and this has of late been confirmed by Clarke (Clarke 2006). The mechanism by which carbon steels with retained austenite exhibit their combination of strength and ductility was proposed in 1967 by Zackay et al to occur by a strain hardening process which, at the time was more commonly known to researchers of stainless steels (Zackay, Parker et al. 1967). With the advent of TRIP steels the same mechanism has been supposed to apply.

The means by which the TRIP effect brings about favourable mechanical properties has been postulated to occur by two mechanisms which occur simultaneously during loading (Marketz and Fischer 1995). Firstly, the martensitic transformation of austenite that is suitably orientated to the strain axis. Secondly, the plastic deformation of the surrounding phases caused by the volume expansion and shape change when austenite transforms to martensite. The first mechanism increases the proportion of 'hard' phase existing in the material while the second mechanism creates a strain hardening effect. The combined result is a delay to the point at which increases in stress exceed the increase in strength of the material (De Meyer, Vanderschueren et al. 1999). The point at which the applied stress exceeds the ability of the material to harden is more commonly known as the onset of necking (Dieter 1988). The mechanisms that have been theoretically supposed to apply are supported by experimental data indicating transformation of retained austenite to martensite during loading. Research data (e.g. Figure 1.35) shows that a good correlation between ductility and retained austenite volume can exist (Zrnik, Muransky et al. 2006) (Jencus, Lukas et al. 2004).

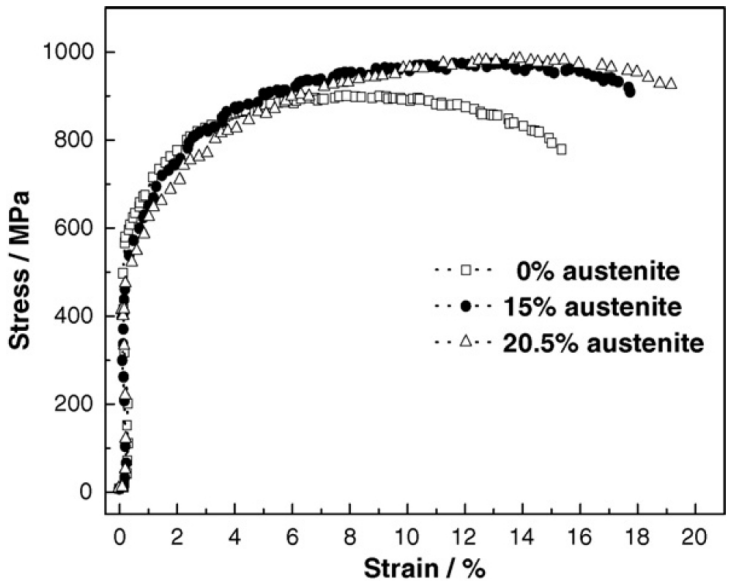

Figure 1.35 - Stress–strain curves of thermomechanically treated steel with different volume fraction of retained austenite (Zrnik, Muransky et al. 2006)

Although the TRIP designation is now well accepted, Bhadeshia has questioned the applicability of the term 'Transformation Induced Plasticity'. Mathematically the contribution of the volume increase on transformation (from austenite to martensite) to the overall ductility is shown to be small, even for the

case where all retained austenite is orientated favourably to the stress axis (Bhadeshia 2002).

1.13 Variations on the Q&P concept

1.13.1 Quenching-Partitioning-Tempering

Some researchers have built upon the Q&P heat treatment process by describing a process which commences with a conventional Q&P heat treatment, followed by an additional tempering heat treatment (Hsu and Xu 2007) (Wang, Zhou et al. 2010), this process has been termed Quenching-Partitioning-Tempering (Q-P-T). During tempering, the properties of the steel are further modified by precipitation of metastable carbides. This is reported to result in an enhancement to mechanical properties such that Figure 1.2 has been reproduced as depicted in Figure 1.36.

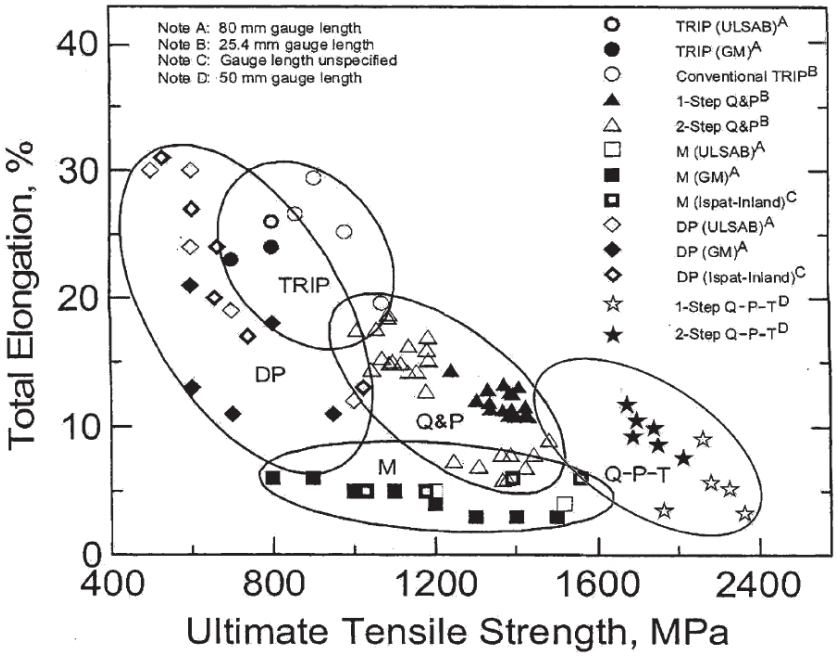

Figure 1.36 – Total elongation vs. ultimate tensile strength for DP, TRIP, Martensitic, Q&P and Q-P-T sheet steels, Wang, Zhong et al, after Streicher, Speer et al (Wang, Zhong et al. 2009) (Streicher, Speer et al. 2004)

In the Q&P concept, strong carbide forming elements (e.g. Titanium and Niobium) are sometimes excluded, as consumption of carbon by carbides is regarded as a competing reaction to austenite carbon enrichment. For Q-P-T, an upward adjustment is made to the carbon alloying addition to allow for carbide formation,

such that austenite stabilisation by carbon enrichment is not compromised e.g. a composition of 0.485C, 1.195Mn, 1.185Si, 0.98Ni, 0.21Nb (Wang, Zhong et al. 2009). However, the Q-P-T concept has also been reported for a much lower carbon alloy of 0.2C, 1.5Mn, 1.5Si, 0.05Nb, 0.13Mo; in this case, the published mechanical properties appear to possess an elongation much closer to that of Q&P, but with a lower UTS than higher carbon Q-P-T alloys (Figure 1.37). A secondary mechanism by which the Q-P-T philosophy is reported to improve mechanical properties is by grain refinement, hence, the Q-P-T concept can be described as a combination of Q&P and Micro-Alloying.

However, some researchers believe that Q-P-T does not represent a new development, as Q&P has previously been performed on steels that contain prominent carbide forming elements, e.g. Molybdenum, and microalloying elements such as Vanadium and Titanium (Matlock, Brautigam et al. 2003). As carbide formation has previously been acknowledged as a potential or actual competing reaction in Q&P, it could be argued that the term 'Q-P-T' is redundant. Furthermore, the most recent research (Li, Lu et al. 2010a) on the one-step Q&P process has indicated that a UTS of over 2400MPa, in combination with an elongation of greater than 10% is possible. Therefore, from a commercial perspective, it could be considered that Q-P-T introduces an extra time-consuming and expensive step to the heat treatment process, without providing any improvement in strength or elongation.

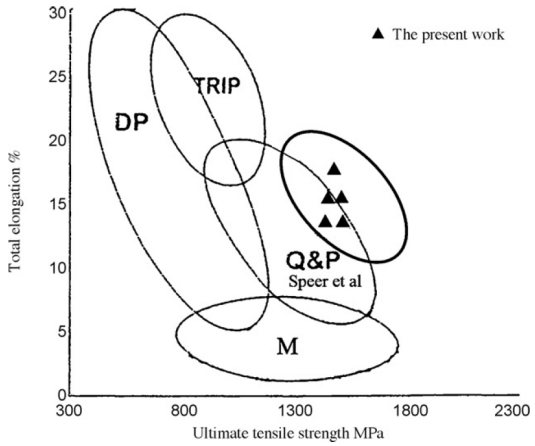

Figure 1.37 – A schematic comparison of UTS and total elongation for Dual Phase (DP), TRIP, Martensitic (M), Q&P and Nb microalloyed Q-P-T steels Zhong, Wang et al, after Streicher, Speer et al (Zhong, Wang et al. 2009) (Streicher, Speer et al. 2004)

1.13.2 Quenching-Partitioning-Austempering

Another variation has been reported, termed Quenching-Partitioning-Austempering (Q-P-A) (Hongyan and Xuejun 2009). In Q-P-A, the objective is to produce a three phase microstructure consisting of (tempered) martensite, retained austenite and nano-structured-bainite. Such a combination is reported to result in mechanical properties ranging from 1999MPa UTS and 12.5% elongation, to 1482MPa UTS and 18.9% elongation; comparing these values to Figure 1.2 indicates that progress has been made. However, these improvements come at a high cost in terms of processing time, to obtain these properties austempering times of 24 or 48 hours were employed.

1.13.3 Q&P heat treatment of plate material

Although Q&P might be considered most suited to sheet steels, where the relatively high cooling rates required to obtain martensite are easily obtained, some research has been undertaken with a view to applying the process to thicker, plate steel. The intended application for such a product is envisaged to be material for line pipe, where retained austenite could improve toughness. Hong, Ahn et al describe a study during which samples intended to be representative of plate material were subjected to a Q&P heat treatment. The resulting microstructure was reported to consist of martensite, retained austenite and possibly also bainite (due to an insufficiently high rate of cooling). Mechanical properties (toughness and yield strength) were considered to be improved compared to existing heat treatment schemes (Hong, Ahn et al. 2007). More recently, application of the Q-P-T process to plate materials has also been reported (Zhou, Wang et al. 2010).

Chapter 2
Experimental Procedures

This chapter contains detailed descriptions of all the experimental methods used to produce the results reported herein. Additionally, the philosophy behind many of the choices made are also explained.

2.1 Production of steel for experimentation

After surveying the available literature on the subject of Q&P, a prospective steel composition was arrived at. The requirements to be satisfied in the derivation of a suitable chemical composition numbered two; a low martensite start temperature to enable observation of the steel between the quenching and partitioning stages of the heat treatment, and, in most but not all samples, the inclusion of an appropriate alloying addition to inhibit as far as possible the competing reaction of equilibrium-carbide (cementite) precipitation.

2.1.1 Manipulating the martensite start temperature and inhibiting equilibrium carbide formation

The well known formula of Andrews (Equation 1.3) (Andrews 1965) was used in conjunction with the Koistinen-Marburger equation (Equation 1.5) (Koistinen and Marburger 1959) to determine a chemical composition which would likely result in a suitable quantity of retained austenite for study. It is recognised that the composition of the alloy chosen to carry out the investigation is somewhat outside the recommended limits for use of the M_s formula. However, a starting point was required and so the M_s formula was used with a mind to adjusting the composition if practical experimentation showed the retained austenite fraction to be unsuitable for study of the Q&P process.

Carbon and manganese were chosen as the alloying elements to lower the martensite start temperature and also to increase the hardenability. Both of these elements increase hardenability by retarding transformation to an equilibrium ferrite/pearlite structure. Since the project is based on a study of the role of carbon in the Q&P process this element must clearly be included. In steel with sufficiently high carbon content it is not uncommon to retain some austenite to room temperature (Jaffe and Hollomon 1946) as carbon is an extremely powerful austenite stabiliser (Andrews 1956).

Although carbon is highly influential in the lowering of the martensite start temperature, excessive use of this element results in martensite of extreme brittleness and the risk of quench cracking (Honeycombe and Bhadeshia 1995). Therefore, a second alloying element was also selected; manganese was chosen as the preferred element for bringing about additional lowering of the martensite start temperature for three reasons. Firstly, excepting carbon and nitrogen, manganese is one of the most potent austenite stabilisers (Andrews 1956). Secondly, manganese has a relatively strong effect on M_s temperature per unit addition (Jaffe and Hollomon 1946). Thirdly, manganese has only a relatively weak tendency to form alloy carbides (Porter and Easterling 1992), although some researchers have reported that the structure Mn_3C is more stable than Fe_3C (Bain, Davenport et al. 1932). Since it is desired to make use of the carbon content within the alloy to stabilise austenite, the exclusion of alloying elements that possess a strong tendency to form carbides is an important consideration.

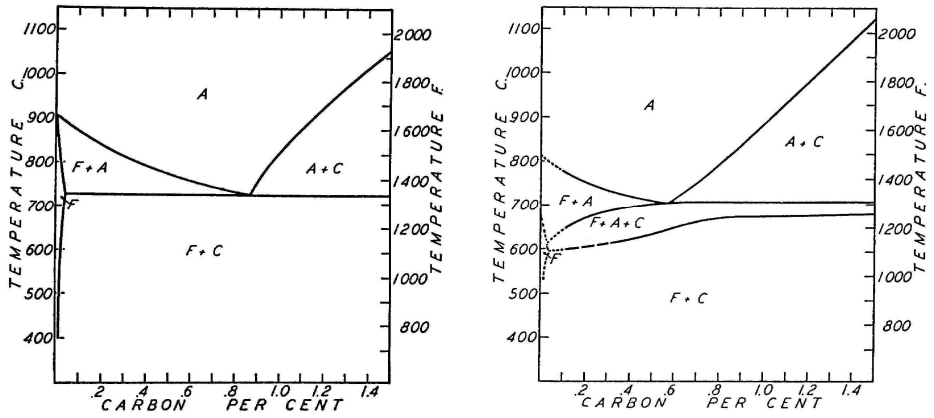

Figure 2.1 –The iron-carbon equilibrium diagram for 0 wt% Manganese (left) and 3.8 wt% Manganese (right) (Bain, Davenport et al. 1932).

The effect of manganese on the iron-carbon equilibrium diagram (Figure 2.1) is to lower both the A_{e1} and A_{e3} points (Andrews 1956) (Bain, Davenport et al. 1932) (Hume-Rothery and Christian 1946). Similarly to nickel, a sufficiently large addition of manganese will stabilise austenite to room temperature. This effect is seen in Hadfields steel, a highly wear resistant, fully austenitic steel containing 12-14wt% manganese (Hadfield, Williams et al. 1921) (White and Honeycombe 1962) (Bhattacharyya 1966). The minimal propensity of manganese to form manganese carbide (Mn_3C) is a consequence of the energy of formation of this compound, which is very close to that of cementite (Grobner 1954). The energy of formation influences the free energy of nucleation for a manganese carbide particle (misfit and

interfacial energy are other factors) (Porter and Easterling 1992). Manganese is therefore not known as a strong carbide former, whereas other elements with a much higher energy of carbide formation such as titanium and vanadium are deserving of this reputation.

With respect to inhibiting equilibrium carbide (cementite) formation, two reasons exist for selecting silicon as the alloying element of choice for this application. Firstly, the discovery of this characteristic of silicon is not new and consequently some studies and hypotheses exist for the mechanism by which silicon acts in this capacity (Hobbs, Lorimer et al. 1972) (Burke and Owen 1954) (Gordine and Codd 1969) (Saito, Abiko et al. 1993) (Apayev, Yakovlev et al. 1961) (Kenneford and Williams 1957). Secondly, the TRIP steel production process is also dependant upon effective inhibition of cementite formation and so some useful research involving silicon alloying has already been published (Jun, Park et al. 2004) (Luzginova, Zhao et al. 2007) (Choi, Kim et al. 2002). Other prospective cementite inhibition alloying elements include aluminium and phosphorous (Traint, Pichler et al. 2002).

The question of exactly what proportion of silicon should be added to the experimental steel was resolved through the research of Saleh and Priestner. In their work, eight iron-manganese-carbon-silicon dual phase steels with silicon contents ranging from 0.26wt% to 1.96wt% were investigated (all other alloying additions kept constant). A dual phase structure was obtained using a typical intercritical-anneal/bainitic-hold heat treatment process; retained austenite was then quantified. The results showed no further gains in austenite volume fraction for silicon compositions above 1.44wt% (Saleh and Priestner 2001).

A carbon composition close to eutectoid is desirable because the temperature required for austenitisation is a minimum at the eutectoid composition. Using the binary iron-carbon phase diagram for this purpose is slightly inaccurate as the experimental alloy contains other elements besides iron and carbon; however, this was done to simplify matters. After considering all of the above, the chemical composition for the experimental alloy was set at 0.7wt% C, 5wt% Mn and 1.5wt% Si.

2.1.2 Melting and casting of the experimental steel

Electrolytic iron, electrolytic manganese, high purity carbon and high purity silicon were weighed in the correct proportions and loaded into a bowl-shaped impression in the water-cooled copper hearth of an arc furnace. The furnace was then evacuated and purged with argon five times before melting the raw materials under a partial pressure of argon. To ensure adequate mixing of the individual elements of the alloy, the resulting small ingot was flipped over once-solidified and then re-melted; this process was repeated twice. The steel was then melted into a trough in the copper hearth; this gave a final sample size of approximately 10mm diameter and 70-90mm in length (Figure 2.2). The limitations of the furnace constrained the sample mass to 45-50 grams. Steel produced by this method was observed to be bright, and free from all but the most minor oxidation.

Figure 2.2 – Sample 27 pictured after melting and casting

Out of necessity, during the course of the research project some refinements were made to the process by which steel was produced, and the method of operation of the arc furnace. In the first few samples produced and tested it was observed that carbon content was subject to significant variations. This was thought to be due to the behaviour of the carbon particles in the electric arc. During the melting process the fine carbon particles can become charged by the arc and repel each other. This phenomenon presents as a visible scattering of carbon dust across the copper hearth when the furnace is cooled and opened for sample retrieval. Efforts were made to minimise this effect by covering the carbon with large pieces of electrolytic iron, however, the problem could not be completely eliminated by this method. Therefore, of the first few melts made, a few had to be set aside as the carbon variation was considered too great. To overcome the variability in carbon content between melts it was decided to prepare batches of four melts together. Before final melting, each melt was cut into four pieces and then remelted with a piece from each of the other three melts. Carbon analysis results showed that this technique was highly successful in reducing carbon content variability to insignificant levels.

A later development in the operation of the arc furnace involved varying the arc current during the course of the melting process. During initial melting the arc current was kept relatively low to minimise carbon scattering until a small amount of iron had been melted, sufficient to cover all the raw material. Once a small pool of molten material had been established the arc current was then increased to a higher level to melt all of the remaining solid material. The four-sample batch production process described previously was also applied and so the end result was higher carbon contents with low melt-to-melt variability.

2.1.3 Homogenisation

The samples as produced in the arc furnace possessed a highly dendritic microstructure. Therefore, to improve the uniformity, a homogenisation heat treatment was carried out. To prevent decarburisation and oxidation the small ingots were first sealed in fused silica glass tubing under approximately one quarter of an atmosphere of argon (Figure 2.3). Prior to ultimate sealing off, the tube atmosphere was evacuated and purged with argon five times using a rotary vacuum pump. Homogenisation was completed with a soak at 1200ºC for 96 hours in a tube furnace. The soak time and temperature was comparable to that used by others for alloys of similar composition (Bhadeshia 1979).

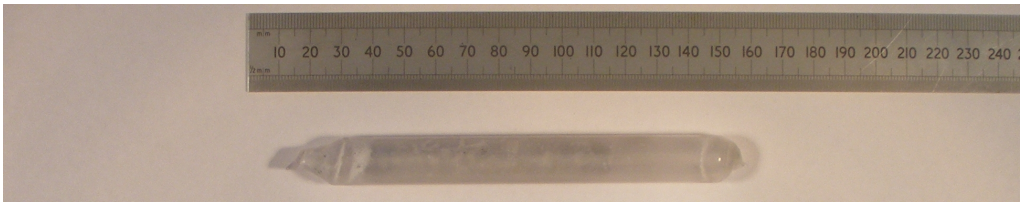

Figure 2.3 – Sample 27 pictured after sealing off and homogenisation in fused silica tubing

2.2 Sectioning of steel samples

2.2.1 Light Optical Microscopy and X-Ray Diffraction

The samples as produced in the arc furnace were of a rough cylindrical shape and so disc format specimens were obtained by sectioning samples transverse to their length. The samples were cut under conditions of flood lubrication; disc thickness was around 2.5mm to 3mm (Figure 2.4). In some cases, where the rapid solidification of the sample in the arc furnace had caused a highly irregular shape (Figure 2.5) it was necessary to discard short lengths of the sample.

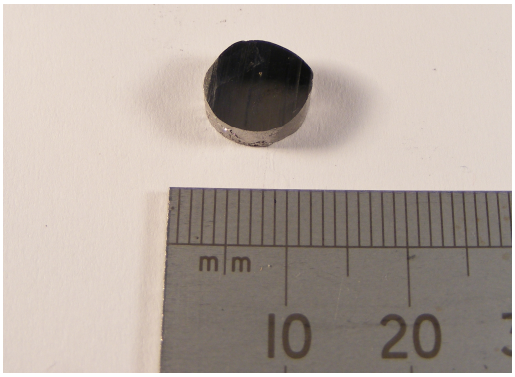

Figure 2.4 –A specimen obtained after sectioning sample 19

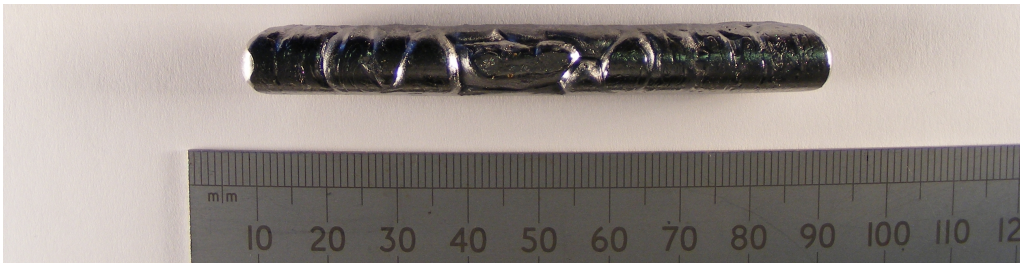

Figure 2.5 - Irregular profile on sample 27 caused by rapid solidification upon contact with the water cooled copper hearth

2.2.2 Neutron diffraction

Specimens for neutron diffraction were sized to make best use of the neutron beam cross section while also conforming to the mounting system used on the instrument. Exposing specimens to the highest possible flux of neutrons maximises the statistics of the data produced by the diffractometer detectors. All things considered, it was found appropriate to section each sample into three long specimens, and one very short specimen for carbon analysis; the cutting method was as described in Section 2.2.1.

2.3 Heat treatment of steel specimens

Four different heat treatment methods were used in the course of the research project. The first method employed only air furnaces and was used for the initial scoping studies to ensure that the experimental methods being considered were capable of giving useful results. The second method used both air furnaces and molten salt baths; salt baths were added to the project to enhance the reliability of the partitioning stage by enabling rapid heating to a precise temperature. Accurate measurement of the partitioning time was facilitated by spot welding thermocouples

to each specimen and recording the temperature history using a data logger. The third heat treatment method was used for those specimens which were subject to neutron diffraction measurements. The fourth method involved sub-zero quenching and was introduced to study the effect of partitioning on the thermal stability of retained austenite. Details of all the heat treatment methods are contained in the sections which follow.

2.3.1 Effecting the Q&P heat treatment using only air furnaces (First method)

From the outset of the project it was elected to carry out the air furnace heat treatments by lowering the specimens into the furnace through the furnace exhaust vent. This method has two advantages; firstly the furnace temperature is not subjected to the disturbance that would be caused by opening the furnace door. Secondly, it is possible to effect very rapid placement and removal of a specimen. To derive maximum benefit from this experimental technique some initial investigations were carried out to determine the heating rates that result from this method. Specimen heating rates were established for furnace temperatures between 200 and 1200°C via the method described in the following paragraph.

Type-R (Pt/Pt13%Rh) thermocouple wire of 0.1mm/0.125mm diameter was spot welded to a test specimen. The specimen was then lowered into the furnace via the exhaust vent and suspended at the same level as the integral furnace thermocouple. Insulation of the thermocouple wires from each other was accomplished using twin bore alumina segments threaded onto the wires. The thermocouple wire was connected to a Fluke 2635A Hydralogger using a length of Type-R, temperature compensated cable. The Hydralogger was linked to a PC and Fluke Hydralogger software was used to log temperature data at one second intervals.

Data from the heating rate trials was used to identify suitable heating times and temperatures for both the austenitisation and partitioning stages of the Q&P heat treatment process. On the basis of the heating rate data, the temperature selected for austenitisation was 1000°C. Analysis of thermocouple data (see Section 4.6 and Section 4.8.6) showed that austenitisation would be achieved well below this temperature. Therefore, as the disc specimens were of a small size and low mass a total of 5 minutes at this temperature was considered sufficient to fully austenitise and dissolve any carbides present.

Partitioning times and temperatures were chosen after careful study of work by Gerdemann and co-workers (Gerdemann, Speer et al. 2004). Their work indicates that the most predictable results are obtained using a two step Quenching and Partitioning process with the partitioning time and temperature kept short and high respectively. In particular, Gerdemann had some success using the Koistinen-Marburger equation to predict the austenite fraction following a Q&P heat treatment.

The time taken for a specimen to reach 500°C in an air furnace of the same temperature was found to be relatively slow compared to the anticipated partitioning process timescale, therefore, an alternative method of rapid heating for the partitioning stage was devised. The mean time for the test specimen to reach 500ºC when suspended in a furnace environment of 1000ºC was 13 seconds. Therefore, to bring about a partitioning heat treatment of 500°C the specimen was quickly withdrawn from the furnace after 13 seconds, and then suspended a set distance (known to correspond to 500°C) from the top of the furnace exhaust vent (furnace still at 1000°C). The temperature of the gas flow up the exhaust vent was found to vary according to the distance from the exhaust vent tube wall. Therefore, for consistency it was found to be important to suspend specimens centrally within the exhaust vent.

Following the heating-rate trials, a cradle structure was made to transfer specimens in and out of the furnace and quenching media. The cradle and handle (Figure 2.6) were fabricated from Nickel/Chromium wire of 0.45mm diameter. The specimens were suspended at the same height in the furnace as the integral furnace thermocouple. This was also the same height as used for the heating-rate trials previously described

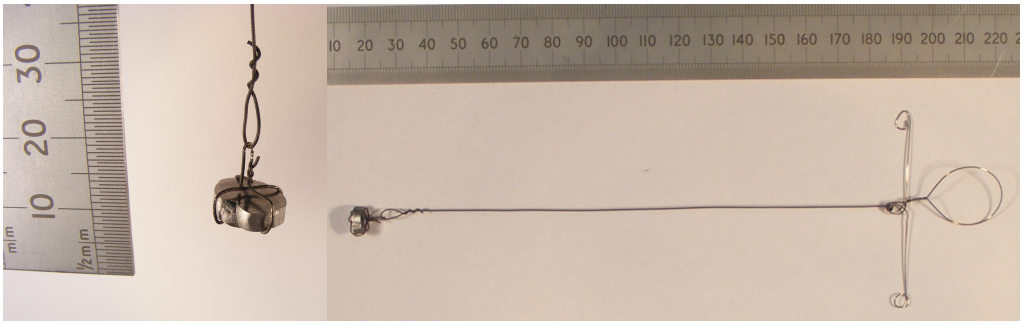

Figure 2.6 –The nichrome wire cradle shown containing a specimen ready for heat treatment (left), and the complete handle assembly used for transferring specimens in and out of the various heat treatment environments (right)

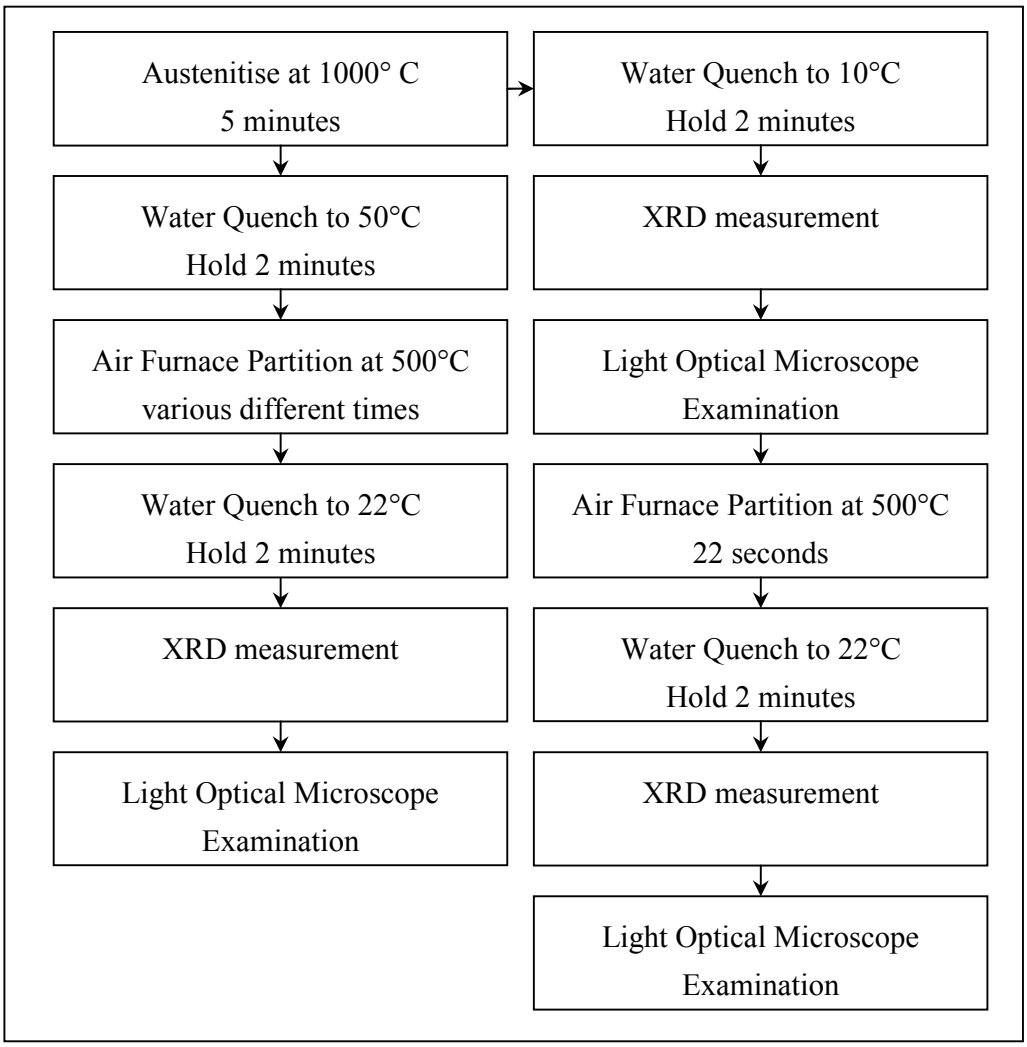

Figure 2.7 - Heat treatment flowchart for air-furnace Q&P experiments

The accuracy of the retained austenite fraction prediction (a combination of an M_s empirical formula and the Koistinen-Marburger relationship) was not known at the outset. Therefore, in order to ensure a significant fraction of retained austenite

for study, a relatively high temperature (50°C) was used for the initial quench following austenitisation. Following partitioning, the specimens were quenched to room temperature (22°C). A smaller number of specimens were initially quenched to 10°C, examined by XRD and LOM, partitioned at high temperature, quenched to 22°C and then finally re-examined with XRD and LOM. For all specimens the quenching medium was water; the quenching water was adjusted to the correct temperature using ice, or a hotplate, as required. A flowchart detailing the sequence of heat treatment stages and characterisation methods is shown in Figure 2.7.

Following the initial round of Q&P heat treatment experiments, further work revealed that the partitioning temperatures actually achieved were probably lower than 500°C. At the time of determining the heating rates, the significance of sample mass (i.e. heat capacity) and sample finish (i.e. radiative heat transfer rate) were not fully appreciated. Therefore, for this heat treatment method only, it is considered that the partitioning temperatures actually achieved were not quite as high as intended. However, while accepting the possibility of an inaccuracy here, the most important consideration is that all of the specimens used for actual Q&P experiments were alike (i.e. approximately the same mass and exactly the same surface finish). Therefore, the results show a valid progression in terms of the effect of partitioning time on microstructural evolution.

2.3.2 Effecting the Q&P heat treatment using air furnaces, salt baths and thermocouples (Second method)

The original intent was to record the entire Q&P heat treatment temperature/time history by spot welding a Type-K thermocouple to each specimen and then using the thermocouple as a handle to lower the specimens into the various furnace environments and quenching media. However, attempts to do this were thwarted by thermocouple degradation at 1000°C. By necessity, the thermocouples that can be readily attached by spot welding must be of relatively fine wire. Unfortunately, such small diameter thermocouples degrade relatively quickly at the chosen austenitisation temperature of 1000°C. Therefore, following 5 minutes austenitisation at 1000°C it was found that the temperatures recorded in the partitioning salt bath were inaccurate. Precious metal thermocouples were considered to be too expensive and fragile to use for every specimen. Consequently, it was elected to record the temperature history for the partitioning stage only, using Type-K thermocouples. Although this situation was a slight compromise on that originally envisaged, the amount of information lost is small as the austenitisation heat treatments are highly similar. At the partitioning temperatures of 400 and

500°C, Type-K thermocouples were found to give reliable results even after repeated exposure to these temperatures.

The procedure for administering the austenitisation heat treatment was exactly the same as for the first method (see Section 2.3.1). As previously intimated, the partitioning stage was accomplished using molten salt baths. A survey of the available literature showed that various salts could be used to achieve partitioning temperatures of 400 and 500°C (Totten, Bates et al. 1993) (Nelson 1940) (Becherer 1991) (Barber 1963) (USDOD 1977). For this particular application a 50:50 mixture of the salts potassium nitrate and sodium nitrate was considered appropriate. Suitable crucible furnaces were bought in for the project, however, as the crucibles supplied with the furnaces were fabricated from graphite, they were unsuited for use with nitrate salts. In terms of nitrate salt compatibility, nickel is a suitable crucible material as it is highly resistant to corrosion from nitrate salts over the entire range of feasible partitioning temperatures. Therefore, some appropriately sized nickel crucibles were acquired and the crucible furnace top openings were enlarged slightly to suit.

In performing the actual partitioning heat treatments, Type-K thermocouples were spot welded to the specimens and the temperature/time history of the partitioning and quench stages was collected and recorded in much the same way as detailed for the heating rate trials previously described (see Section 2.3.1). Initial trials showed that the heating rate could be significantly increased by gently agitating the specimen while in the salt bath. Decreasing the heating time is a significant advantage in achieving very low partitioning times and so the decision was taken to gently agitate all specimens. The rate of temperature increase in a specimen becomes progressively lower as the specimen approaches salt bath temperature; therefore, the following protocol was deemed appropriate when determining total partitioning time from the temperature/time datalogger records. For partitioning at 400°C the partitioning time was arbitrarily considered to include all those datapoints at or above 390°C. Likewise, for partitioning at 500°C, the partitioning time was considered to include all those datapoints at or above 490°C. With the assistance of gentle agitation, the times to heat to 390°C and 490°C were approximately 9 seconds and 13 seconds respectively. Thermocouple traces typical of partitioning heat treatments at 400°C are shown in Figure 2.8.

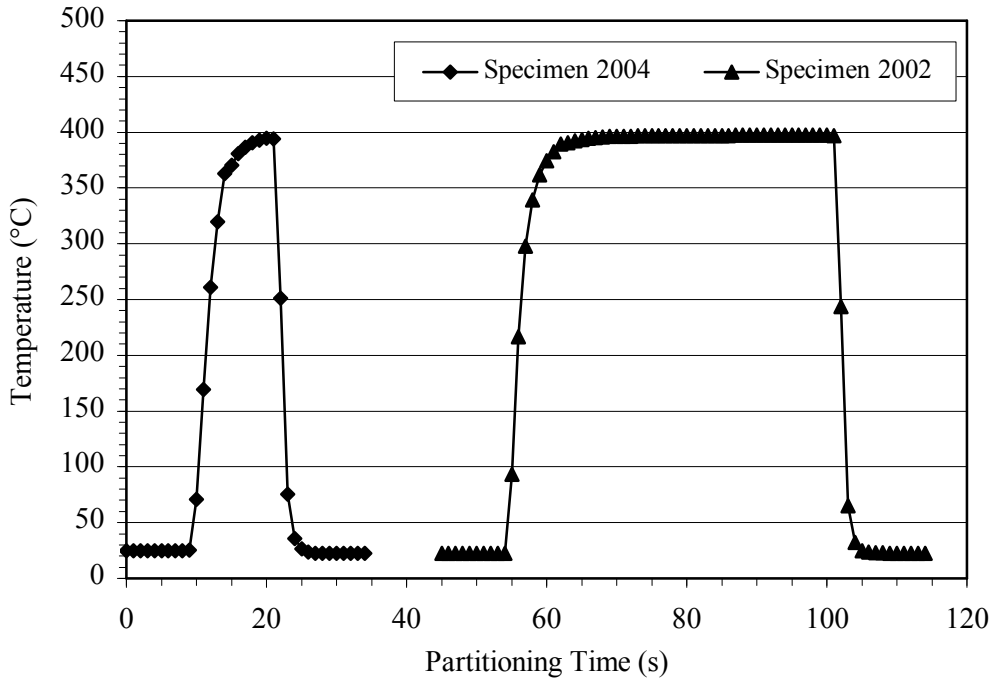

Figure 2.8 – Partitioning temperature/time histories recorded for specimen 2004 and 2002 (3 seconds and 38 seconds partitioning time respectively)

For partitioning times of 180 seconds or more, the use of a thermocouple spot welded to the specimen to precisely measure partitioning time was considered superfluous; consequently, the heating times of 9 and 13 seconds were used in conjunction with a stopwatch to determine total partitioning time. A flowchart detailing the sequence of heat treatment stages and characterisation methods is shown in Figure 2.9.

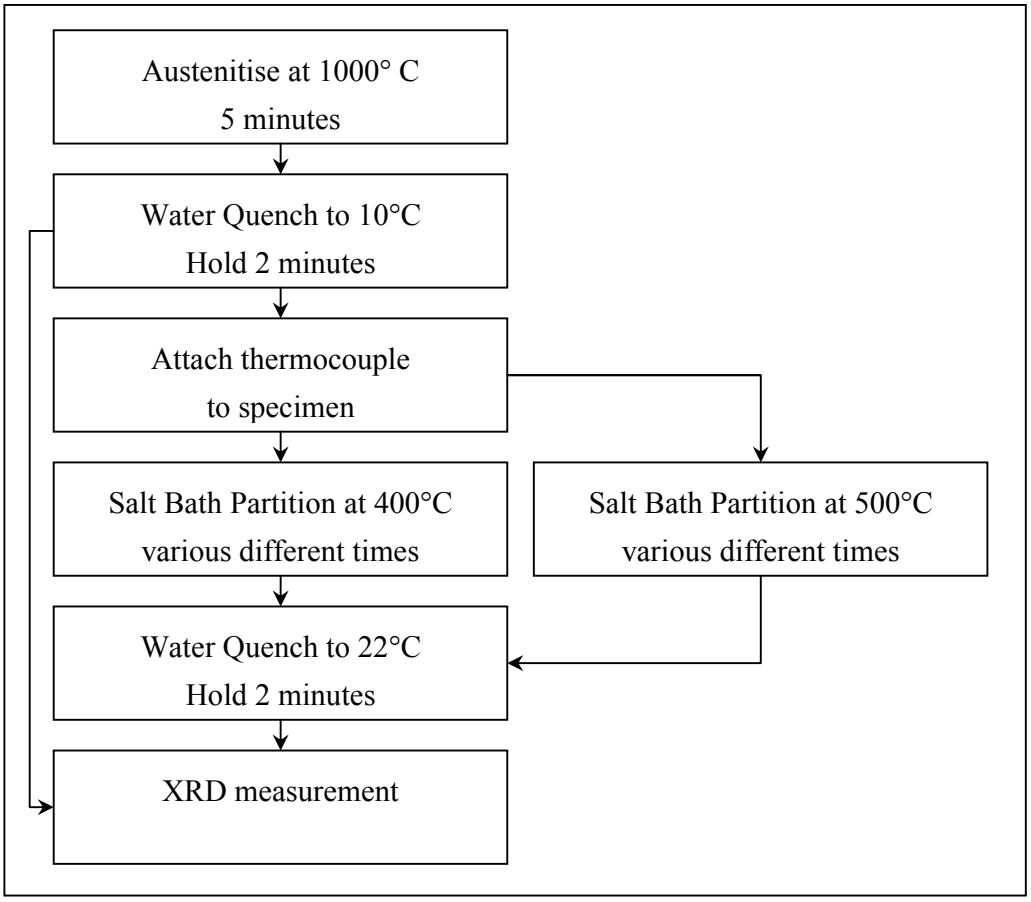

Figure 2.9 - Heat treatment flowchart for Q&P experiments utilising air-furnaces and salt baths.

2.3.3 Heat treatment of specimens for neutron diffraction measurements (Third method)

Utilising neutron diffraction, each specimen was subject to in-situ measurements during the partitioning (heating) stage of the Q&P process. Hence, the specimens were presented to the instrument in their as-quenched state having received only the initial austenitise and quench stages of the Q&P heat treatment. The specimens for neutron diffraction were cylinders rather than the disc format used for other experiments in the project. Therefore, it was necessary to identify a suitable austenitisation time for the different specimen format to allow for the increase in mass. Heating rate trials were performed using Type-R thermocouple wire spot welded to a representative test specimen. To achieve an austenitising heat treatment similar to that performed on the disc type specimens it was found necessary to extend the austenitisation period from 5 minutes to 7.5 minutes. Austenitisation temperature was unchanged at 1000°C and quenching was into water at 10°C as before. A smaller number of cylinder format specimens were austenitised, quenched to 10°C, and then immediately quenched into liquid methanol at -61°C.

This was done to investigate the effect of retained austenite fraction on partitioning response. Cooling of the methanol from ambient to -61°C was carried out in a vacuum flask using liquid nitrogen. Prior to neutron diffraction measurements, surface oxides formed during austenitisation were removed using a solution of distilled water, hydrofluoric acid and hydrogen peroxide.

As the cylinder format specimens were of a much higher mass than the disc format specimens the heat effect at the point of austenitisation was more pronounced. Therefore, the data collected during these austenitisation and quench heat treatments provided a clearer indication of the A_1 and A_3 temperatures than data gathered using the disc format specimens.

2.3.4 Sub-zero quenching (Fourth method)

A small number of specimens were subjected to sub-zero quenching. The objective of sub-zero quenching was to measure the stability of retained austenite against decomposition to martensite. This experiment was carried out for specimens that had previously received austenitise-quench, or austenitise-quench-partition-quench heat treatments as described in Section 2.3.2. The partitioning time and temperature employed was 20 seconds at 400°C.

Sub-zero quenching was carried out in a vacuum flask using liquid nitrogen, and methanol cooled with liquid nitrogen. As the freezing point of methanol is -98°C it was considered convenient to use a mixture of liquid and solid methanol for the first sub-zero quench, and liquid nitrogen (-196°C) for the second sub-zero quench. Specimens were introduced to the sub-zero quench media using a nichrome wire cradle as previously described and used for other heat treatment procedures. Sub-zero quenching was 2 minutes at -98°C, and 10 minutes in liquid nitrogen. The longer period of quenching in liquid nitrogen was necessary to allow for the Leidenfrost effect. A flowchart detailing the experimental procedure is shown in Figure 2.10.

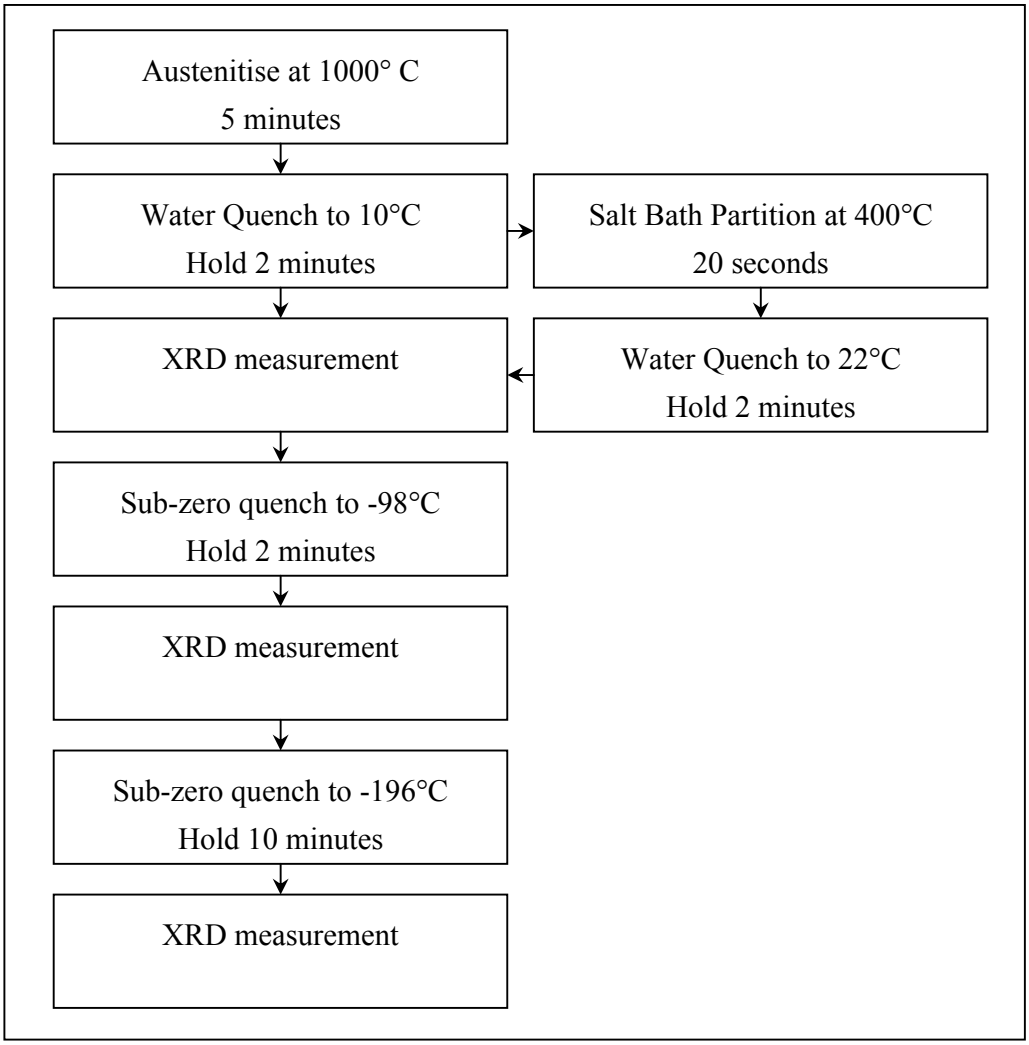

Figure 2.10 – Heat treatment flowchart for sub-zero quenching experiments.

2.4 Grinding and polishing

Following heat treatment and prior to Light Optical Microscopy and X-ray diffraction measurements, approximately 0.5mm of material was removed using coarse silicon carbide paper in a wet grinding process. This was done to mitigate against decarburised surface layers. Wet grinding was continued on sequentially finer grades of silicon carbide paper, finishing with p1200 grade. Polishing was carried out using cloth wheels impregnated with 6 micron and 1 micron diamond paste.

2.5 Light Optical Microscopy (LOM)

Examination using Light Optical Microscopy was carried out following the preparation route detailed in Section 2.4. Etchants used to reveal the microstructure were standard Nital and Sodium Meta-bisulphite solutions, as described in

metallographic preparation manuals (VanderVoort 2004). Etching times were from a few seconds to two minutes in duration.

2.6 Scanning electron microscopy (SEM)

A limited amount of SEM was undertaken using a Philips XL30 Environmental Scanning Electron Microscope (ESEM). Preparation of specimens was generally the same as described for LOM (see Section 2.4), although it was found that etch times needed to be increased significantly compared to the LOM preparation procedure. Some specimens were also examined in an un-etched, as polished state in order to observe artefacts of the steel production method. Specimens were attached to SEM aluminium mounting stubs using double-sided self-adhesive conductive carbon pads.

2.7 Carbon content analysis

A suitable process for accurate determination of carbon content was not available in-house, consequently all carbon analyses were conducted by an external contractor. The method used by the contractor involved infra-red analysis of the gases produced by combustion of a specimen. For one sample only, a larger number of specimens were investigated; this was done to determine the level of elemental homogeneity that is characteristic of the material production method used.

2.8 Manganese and silicon content analysis

Two different techniques were used to quantify the concentration of manganese and silicon in the samples prepared for experimentation. Measurements were initially made using Energy Dispersive X-Ray (EDX) instrumentation attached to a Scanning Electron Microscope. Later on, the services of an external analysis laboratory were also employed; measurements made there were completed using traditional wet-chemistry techniques. A description of the EDX procedure used is given in the following paragraphs.

Unfortunately, EDX on its own cannot provide an absolute quantification of chemical composition as the count rate of X-rays received by the EDX detector can be affected by other elements that are also present in the specimen. For example, in the case of metallurgical analysis it is important to be aware that the EDX system may have been calibrated using materials such as manganese oxide, or silicon oxide,

rather than manganese or silicon in steel. Therefore, to allow more accurate measurements to be made, a series of chemical standards were fabricated. Two British Chemical Standards (BCS) were available, BCS No. 401 and BCS No. 403. These consisted of steel turnings and documentation indicating chemical composition analyses as determined by 16 separate laboratories. As the BCS standards contained only relatively low levels of the elements of interest (manganese and silicon), two more standards were fabricated via the arc furnace route; accurate determination of the elemental composition of these two standards was contracted out to an external analysis laboratory. The BCS turnings were mounted via a hot press method, utilising a mixture of Bakelite powder and copper powder, grinding and polishing was as described for LOM with the exception of the etching step which was omitted as it was not required. All of the standards were mounted for EDX analysis using the same method as described for SEM (see Section 2.6).

The instrument used for EDX measurements was a Philips XL30 Environmental Scanning Electron Microscope (ESEM) fitted with an Oxford Instruments INCA 250 EDX analysis system. A total of 24 spectra were collected for each standard using the spot-analysis function, the data acquisition time for each spectrum collected was 60 seconds (live time). Prior to making any measurements, the quantification-optimisation part of the EDX analysis program was run using a pure cobalt specimen provided by the electron microscopy department. The average silicon and manganese contents, as measured by EDX, and as determined by laboratory chemical analysis procedures were plotted against each other. Regression analysis was then employed to determine the constants of the linear equation that relate the two measurements to each other.

For each sample prepared using the arc furnace, two specimens were selected for EDX elemental composition measurements. Each specimen was subjected to 12 measurements using the same method as described for the standards. For one sample only, a larger number of specimens were investigated; this was done to determine the level of elemental homogeneity that is characteristic of the material production method used. The linear equation extracted from measurement of the standards was then used to accurately determine chemical composition.

2.9 X-Ray diffraction measurements (XRD)

X-ray diffraction was used to obtain measurements of the lattice parameter, phase fractions, and lattice strain. These measurements are of assistance in

identifying and quantifying the various solid state transformations that occur during the Q&P heat treatment process. In the initial stages of the project, the evaluation of diffraction data was undertaken in a relatively manual way. Peak fitting software was used to obtain the positions and the integrated-intensities of the peaks. These outputs were then used in a series of calculations to determine lattice parameters and phase fractions. Later on in the project, use was made of Rietveld refinement to extract lattice strain from the diffraction patterns, quantify additional phases such as carbides, and improve on the manual calculations previously used for lattice parameter and phase fraction. Although all of the data presented in the results sections was derived via the Rietveld process, the manual process is described here for two reasons; firstly, it was used for all of the initial analysis that was influential in steering the research project, secondly, much of the theory is common to both manual analysis, and Rietveld analysis.

2.9.1 Specimen preparation for X-ray diffraction

It is well known that austenite may transform to martensite under suitable conditions of applied stress or strain (see Sections 1.2.6 and 1.12). Hence, various publications (Jatczak, Larson et al. 1980) (ASTM 2008) recommend that preparation of specimens for X-ray diffraction measurement is undertaken with great care so as not to induce transformation of austenite to martensite. However, in this project the transformation of austenite to martensite during mechanical polishing is used to advantage to investigate the effect of the partitioning stage on the mechanical stability of retained austenite. A benchmark measurement of the as-quenched state was obtained by electropolishing a specimen to remove deformed material prior to X-ray diffraction measurements. Additional benchmark measurements were acquired by the measurement of a number of as-quenched specimens using a neutron diffractometer (see Section 2.10).

2.9.2 The XRD instruments used and their operating parameters

X-Ray diffraction measurements were acquired using conventional Bragg-Brentano diffractometers. In this design of diffractometer the X-Ray source is stationary, the specimen, at the centre of the diffraction circle is tilted while the detector moves around the outside of the diffractometer circle. Due to refurbishments of laboratories it was at times necessary to source XRD measurement services from the School of Earth and Environment (SEE). Fortunately the SEE machine was of the same design and produced results that, for the purposes of most of the measurements being made in this project were indistinguishable from those generated using the Institute for Materials Research (IMR) machine. Therefore, the

data of the two machines could be plotted on the same graphs without encountering disparities.

Specimens measured within the IMR X-ray diffraction laboratory were mounted on a glass microscope slide in a standard aluminium XRD 'window' using plasticine. Those specimens measured in the SEE X-ray laboratory were also mounted using plasticine, but with the addition of a low-background silicon plate between the specimen and a standard aluminium holder. Typical operating parameters for the XRD machines were an acceleration voltage of 40kV and a current of 30mA. In all cases the radiation was produced by an X-ray tube featuring a copper target, a monochromator was used to reduce X-ray fluorescence from the specimen. Relatively low measurement speeds were used e.g. 8 seconds per step, with 2 theta step sizes of 0.025 degrees, for some measurements these settings were slowed down even further to improve the detection of carbides.

2.9.3 Fitting peaks to the diffraction patterns

Data for diffraction peak matching was taken from the database within the HighScore XRD analysis software package, a printed source (McClune, Maguire et al. 1982), the Chemical Database Service (Fletcher, McMeeking et al. 1996), and from published work on the evaluation of retained austenite (Jatczak 1980) (Jatczak, Larson et al. 1980).

Manual analysis of diffraction data was carried out using peak fitting software (Wojdyr 2007) (Wojdyr 2010). Within this software the background count was removed by inserting a series of points 'by eye'. Peak fits were then achieved by appropriate location of Voigt function curves in the diffraction pattern, and running the fit function until convergence was achieved. The outputs from the curve fitting process were the centre point and area for each peak. Although some sources advise that overlapping peaks cannot be used (Jatczak 1980) (Jatczak, Larson et al. 1980) it was found that using modern curve fitting software it was possible to achieve a stable fit with up to three overlapping peaks.

2.9.4 Measuring the lattice parameter

The research by Bragg published in 1912 (Bragg 1912), and other follow up papers in subsequent years represent the origins of using X-rays to study crystal structures. The resulting equation, which is known as the Bragg equation or Bragg

law (Equation 2.1) may be found in all X-ray diffraction textbooks e.g. those written by Cullity (Cullity 1956), and Suryanarayana (Suryanarayana and Norton 1998).

$$n\lambda = 2d'Sin\theta$$

Equation 2.1

where n is the order of reflection, λ is the wavelength of the radiation and d′ is the lattice plane spacing (Cullity 1956).

Through knowledge of the crystal structure, the locations of the peaks are used to determine lattice plane spacings, and ultimately, the lattice parameter of the unit cell for a given phase. In the diffraction patterns obtained, the level of peak broadening precluded identification of separate peaks for $K\alpha_1$ and $K\alpha_2$ radiation. Hence, for manual calculations a weighted average of the $K\alpha_1$ and $K\alpha_2$ wavelengths was used to determine structural information via the Bragg equation.

2.9.5 Using XRD to determine phase fractions in steel

Several techniques have been developed to deduce the austenite to martensite ratio depending upon which diffraction lines are available and the expected level of preferred orientation (Miller 1964) (Dickson 1969) (Gullberg and Lagneborg 1966) (Giamei and Freise 1967). The type of radiation used has a significant bearing on which lines are available and while some types of radiation give good dispersion and poor intensity the opposite is true for other types of radiation; in this respect Arnell believes that Copper radiation offers a good compromise (Arnell 1968). The first and most simple method (Equation 2.2 and Equation 2.3) uses a comparison between adjacent martensite and austenite peaks. If only one pair of peaks are compared then this method is prone to inaccuracy in materials which have preferred orientation, although this risk can be mitigated against by averaging over two or more peak comparisons:

$$\frac{I_\gamma}{I_\alpha} = \frac{R_\gamma \times c_\gamma}{R_\alpha \times c_\alpha}$$

Equation 2.2

$$c_\gamma + c_\alpha = 1$$

Equation 2.3

where (I) is observed Intensity, (R) is Relative Intensity, (c_α) and (c_γ) are the actual fractions of martensite and austenite respectively (Cullity 1956)

The method that is most suited to situations where a number of martensite and austenite peaks are available for comparison utilises the actual intensity and relative intensity of all peaks in one equation (Equation 2.4). When a sufficient number of peaks are available for comparison this method is reported to account for the effects of preferred orientation (Jatczak 1980) (Jatczak, Larson et al. 1980):

$$V_A = \frac{\frac{1}{n_A}\sum_0^n (I_A^{hkl} / R_A^{hkl})}{\frac{1}{n_M}\sum_0^n (I_M^{hkl} / R_M^{hkl}) + \frac{1}{n_A}\sum_0^n (I_A^{hkl} / R_A^{hkl}) + V_c}$$

Equation 2.4

where V_A and V_c are austenite volume fraction and carbide volume fraction respectively (V_c is zero if no diffraction lines are present for carbides) and n_A and n_M are the number of (hkl) lines for which the integrated intensities have been measured (Dickson 1969) (Jatczak 1980) (Jatczak, Larson et al. 1980).

In this project, prior to using Rietveld refinement the method used to evaluate phase fractions was the summation formula (Equation 2.4).

2.9.6 The Rietveld refinement method

The Rietveld method presents a completely different approach to interpretation of XRD data. Before use of the Rietveld method became commonplace, the standard method of interpreting powder diffraction data involved processing diffraction peaks one at a time (as described in Sections 2.9.4 and 2.9.5). While this was sufficient for simple structures, the heavily overlapping peaks caused by more complicated crystal structures acted as a catalyst for higher resolution instruments and new analytical methods (Young 1993). The creation of the Rietveld method (Rietveld 1969) marked

the first occasion that it was possible to process the entire diffraction profile one intensity measurement at a time, rather than breaking it down into individual peaks or groups of peaks. For this project, where the structures of the main phases are well known, the Rietveld method not only improves the accuracy of results but also saves a great deal of time in tasks such as subtracting the background, fitting peaks to data, and performing all the calculations such as those for scattering factor, multiplicity, temperature factor, and ultimately, the relative intensities and phase fractions.

2.9.7 Rietveld refinement software and procedure

The General Structure Analysis System (GSAS) written by Larson and Von Dreele (Larson and Von Dreele 2004) was used for Rietveld refinement. This software was used in conjunction with EXPGUI, the Graphical User Interface (GUI) developed for GSAS by Toby (Toby 2001). Refinements were carried out on a PC running a Windows XP operating system and the parameters refined consisted of, background profile, unit cell dimensions (lattice parameters), temperature factors (atomic displacement parameters), phase fractions, phase lattice strain, and the specimen displacement parameter. In order to maintain the specimen displacement parameter at the same value for all phases it was necessary to insert some appropriate constraints. Crystallite size was not expected to vary significantly from specimen to specimen, or during partitioning. Therefore, in view of the fact that the crystallite size parameter and lattice strain parameter can interact strongly with each other, the decision was taken not to refine the crystallite size parameter. Hence, the lattice strain measurements in the experimental results sections are presented without any corrections for crystallite size effects. The peak shape chosen for fitting the data was based on the work of Howard, Thompson et al, and Cagliotti et al (Howard 1982) (Thompson, Cox et al. 1987) (Caglioti, Paoletti et al. 1958). Within GSAS, this peak shape was embodied as Constant-Wavelength Profile Type 2.

2.9.8 Strategy for developing the Rietveld structural models

The greatest difficulty encountered when interpreting diffraction data from quenched steel entails the treatment of peaks originating from the body-centred-tetragonal martensite structure. These peaks typically exhibit a high level of broadening due to strain, crystallite size, and instrumental effects, resulting in significant overlap of the individual peaks. In this project, Rietveld refinements of X-ray diffraction data reveal that a disparity sometimes exists between observed and theoretical intensities for peaks such as BCT martensite 200 and 002. Figure 2.11 and Figure 2.12 illustrate Rietveld refinements carried out between the angles of 60 and 70° 2Θ for two specimens of similar chemical composition, both austenitised at

1000°C and quenched to 10°C. These results represent two extremes, those of relatively poor and relatively good fit, and indicate that the observed diffraction pattern cannot always be satisfactorily explained by the presence of only a single BCT martensite phase (and accompanying retained austenite phase).

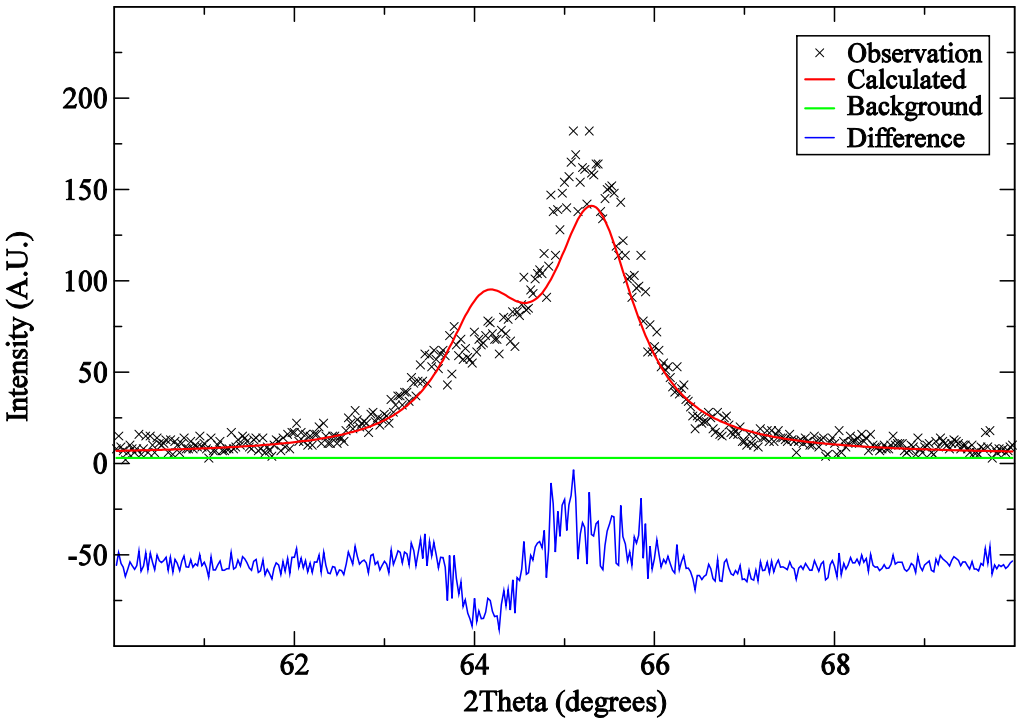

Figure 2.11 – Rietveld fit for martensite 200 (right) and 002 (left) reflections calculated on the basis of a single phase of BCT martensite (specimen 0510)

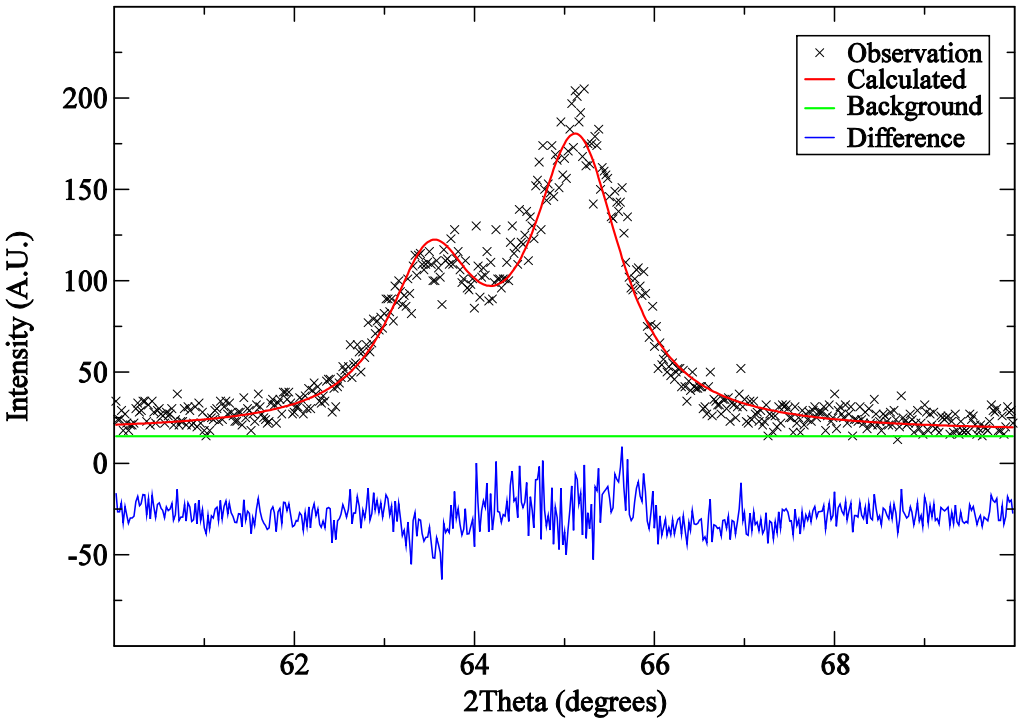

Figure 2.12 – Rietveld fit for martensite 200 (right) and 002 (left) reflections calculated on the basis of a single phase of BCT martensite (specimen 0914)

It is known that quenched martensite is a metastable phase, and also, that significant diffusion of interstitial carbon may occur in body-centred structures, at ambient, or even sub-zero temperatures (De Cristofaro and Kaplow 1977) (Chen, Hall et al. 1980) (Chen and Winchell 1980). Given the nature of quenched martensite (see also Section 1.10.5), it is not unreasonable to propose that in this research project, some of the carbon in BCT martensite is able to diffuse at room temperature into more energetically favourable locations or configurations (clusters). Various factors are hypothesised to control the rate and extent to which room temperature tempering of BCT martensite occurs; metallographic polishing not only introduces plastic deformation, thus boosting the number of energetically favourable locations (cryatallographic defects) able to accommodate carbon, but also raises the temperature of the specimen, aiding diffusion. The length of time between quenching of a specimen and measurement is also believed to be a variable, as is the temperature of the laboratory in which specimens are stored prior to measurement. Unfortunately, during the course of performing the experiments and measurements reported herein, it was not possible to secure X-ray measurement resources prior to conducting a quenching experiment. Consequently, the variable of time (between quenching and measuring) could not be controlled. Although it might have been possible to refrigerate specimens between quenching and x-ray measurement to

reduce carbon diffusion, this was not done, as it was thought that refrigeration could affect the measurement of retained austenite phase fraction.

The process of martensite decomposition upon tempering has been studied by many researchers (see Section 1.10.3). Roberts, Averbach, and Cohen postulated that the first stage of tempering consists of the formation of low-carbon (~0.25wt% carbon) tetragonal martensite 'at the expense of the primary martensite' (Roberts, Averbach et al. 1953). Carbon rejected during this transformation was considered to be consumed by the formation of epsilon carbide (in meta-stable equilibrium with the low carbon martensite). During this transformation, primary martensite is hypothesised to remain at its as-quenched carbon content until it actually transforms; i.e. small areas of primary martensite continually transform, rather than the entire volume of primary martensite progressively losing carbon. The findings of Roberts, Averbach et al are supported by x-ray diffraction studies on single crystals which show splitting of the 002 martensite spot during tempering between room temperature and 100°C (Kurdjumov and Lyssak 1947). Later research suggests that during the early stages of tempering, an equilibrium distribution of carbon between epsilon carbide and dislocations is established (Kalish and Roberts 1971) (Maalekian and Kozeschnik 2008). Hence, it is not hard to envisage the occurrence of solid-state transformations that could give rise to significant local variations in carbon concentration (and therefore variations in lattice parameter) after relatively short periods of holding at room temperature. Therefore, as X-ray diffraction measurements are a high-level average of all the structures present in the specimen, it may not be possible to achieve a good Rietveld fit to diffraction data using a structural model which contains only a single BCT martensite phase.

When considering the possible outcomes of low-temperature tempering, it is worth noting that the formation of low-carbon tetragonal martensite has always been in some doubt (Kurdjumov and Lyssak 1947). In the earliest lattice parameter versus carbon plots, such as those published by Ohman in 1931 (Figure 2.13), the low-carbon region was derived by extrapolation back to the lattice parameter of pure iron, approximately 2.866Å. Since low carbon steels exhibit relatively high M_s temperatures, the lack of a clearly discernible tetragonal-doublet in the diffraction pattern of quenched samples has often been attributed to a mixture of auto-tempering during the quench, and peak broadening from strain and size effects. However, more recent research has questioned whether low-carbon tetragonal martensite can exist at all. The work of Liu and Zhong (Liu, Zhong et al. 1995) (Zhong, Liu et al. 1995) presents a case for a cut off point at ~0.18wt% carbon, below which, an isotropic

rather than anisotropic distortion of the body-centred lattice is the most energetically favourable way to accommodate an above-equilibrium carbon concentration. Therefore, the well known lattice parameter versus carbon content plot for martensite is modified as per Figure 2.14; in Figure 2.15 it is seen that the axial ratio (c/a ratio) is unity at low-carbon contents.

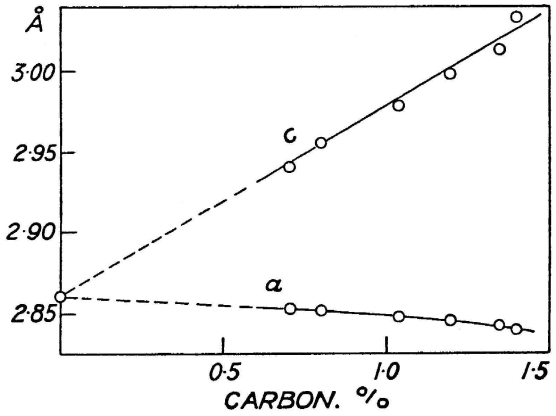

Figure 2.13 – Lattice dimensions of the tetragonal martensite phase as functions of the carbon content (Ohman 1931)

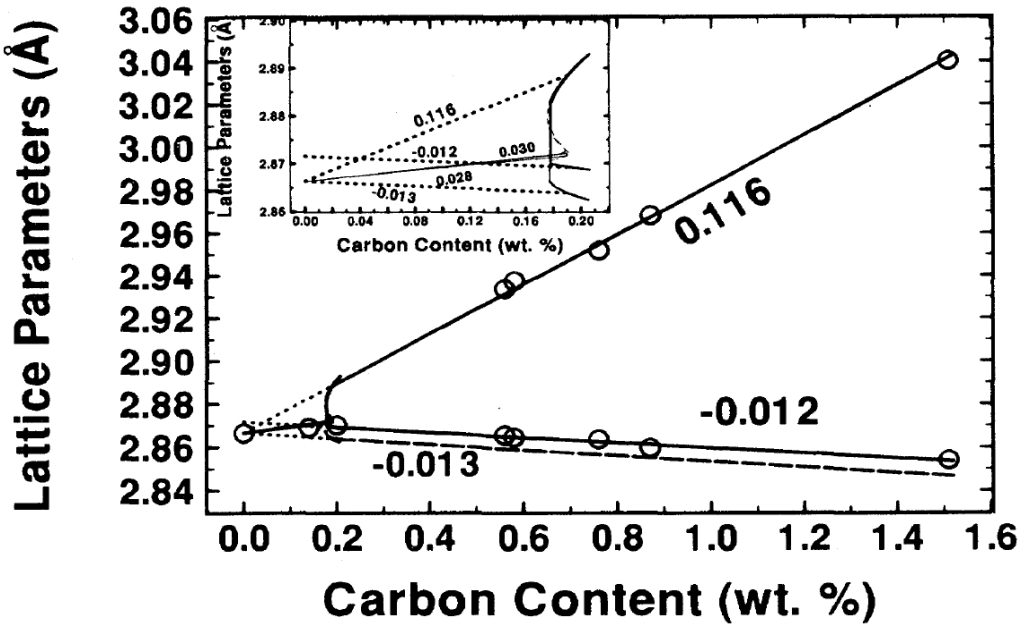

Figure 2.14 – Lattice parameter versus carbon content; solid lines are theoretical lines, dotted lines are unphysical extrapolations, circles denote experimental points, numbers indicate gradients, inset shows detail at the low-carbon end of the plot (Zhong, Liu et al. 1995)

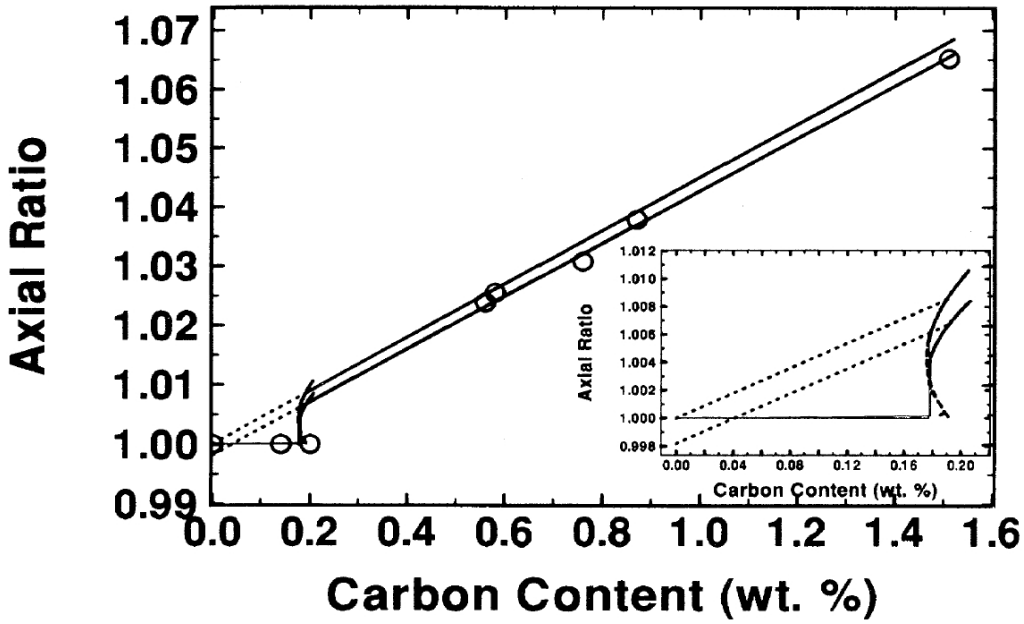

Figure 2.15 – Axial ratio (c/a ratio) of tetragonal martensite versus carbon content; lines and symbols are as for Figure 2.14 (Zhong, Liu et al. 1995)

Prior to the arrival of the Rietveld method, consideration of more than one body-centred (BCC or BCT) phase would have been somewhat difficult; however with Rietveld refinement the introduction of an additional phase is relatively straightforward. In practical terms, the choices for carrying out Rietveld refinements on diffraction data from quenched steel specimens is limited to two options; refining with BCT martensite, or refining with a mixture of BCT and BCC martensite. Refining with two BCT martensite phases (e.g. high c/a, and low c/a) is not an option as the structural model is not stable and will not converge to a best fit. Hence, in the case that a specimen contains mainly high and low axial ratio BCT martensite (but very little true BCC phase), an improvement in fit can only be achieved by approximating low-axial-ratio martensite to a BCC phase. Figure 2.16 and Figure 2.17 illustrate the fits achieved, with, and without an additional BCC martensite phase. The residuals are slightly lower when a BCC martensite phase is included, indicating a slightly better fit. After careful consideration, data from XRD measurements on specimens in the as-quenched state was refined with 3 phases (BCT, BCC and FCC); following partitioning two phases (BCC and FCC) was found to be sufficient, even at the lowest partitioning times.

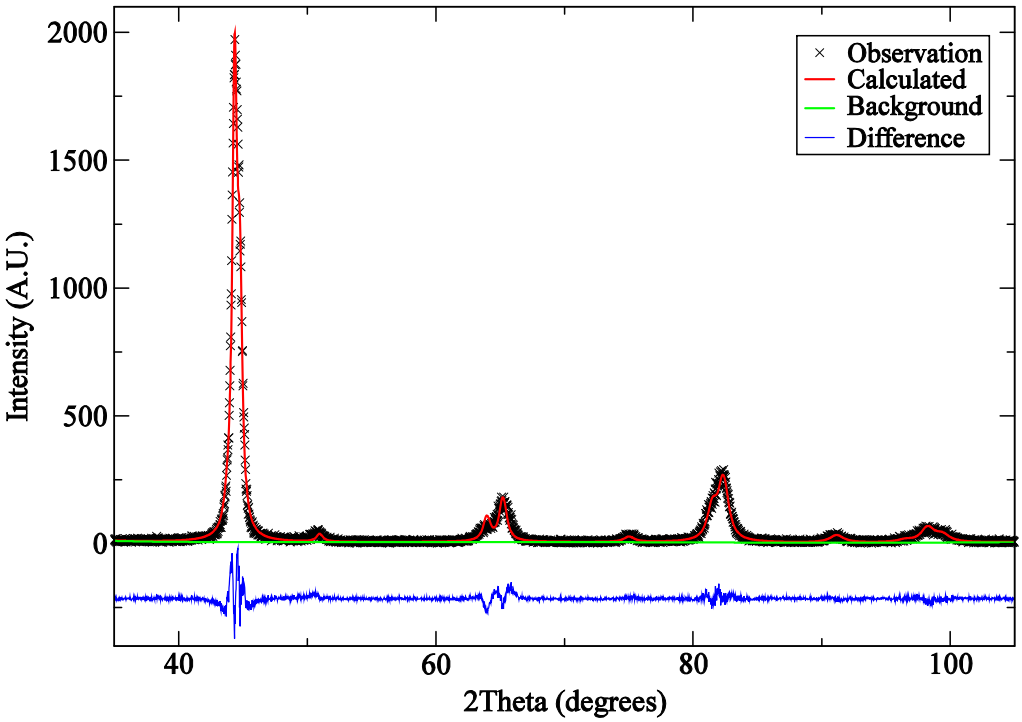

Figure 2.16 – Diffraction data from specimen 0510 fitted with the phases BCT martensite and FCC austenite

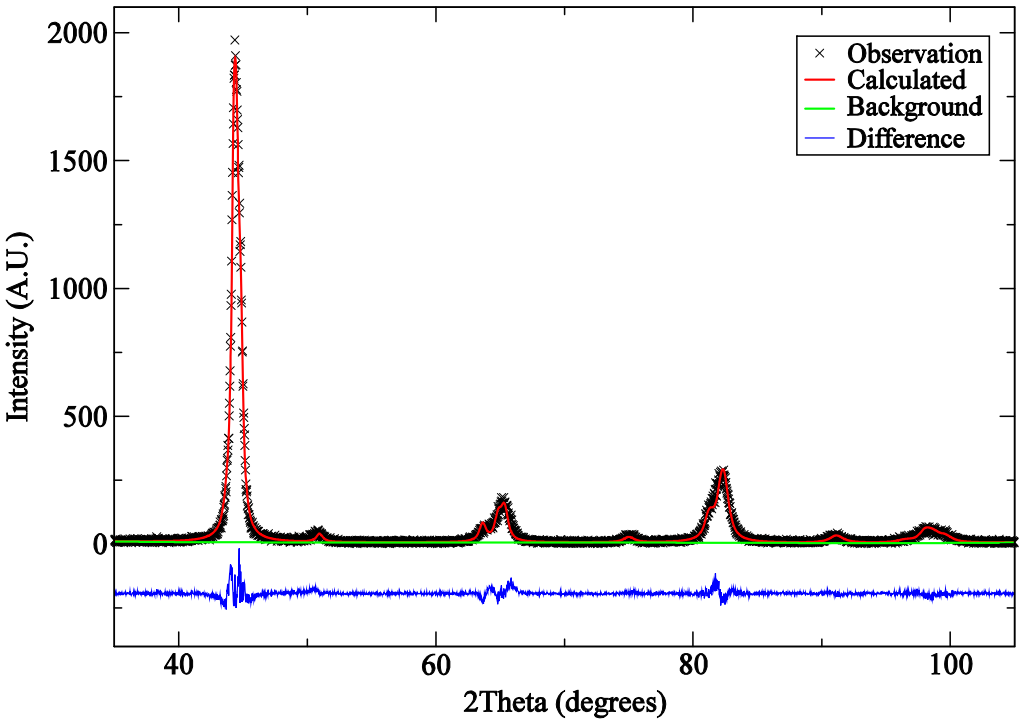

Figure 2.17 - Diffraction data from specimen 0510 fitted with the phases BCT martensite, BCC martensite and FCC austenite

Some of the diffraction patterns obtained from quenched and partitioned specimens exhibited evidence of carbide precipitation. However, unfortunately the use of more than one diffractometry set-up to measure specimens introduced variability into the ability to detect carbides (see Section 7.4 for a fuller discussion). Therefore, all diffraction data was initially refined on the basis of no-carbides-present. The effect of this approach is that, for those specimens which contained carbides, the phase fractions of austenite and martensite are slightly inflated and a significant quantity of carbon may be unaccounted for. At a later stage, additional refinements were performed for those diffraction patterns containing clear evidence of carbides, the results of this are reported separately.

2.9.9 Method of estimating carbon concentration from lattice parameter data

There is no shortage of published data concerning the correlation of carbon concentration with lattice parameter for as-quenched mixtures of martensite and retained austenite (e.g. Figure 2.18 and Figure 2.19).

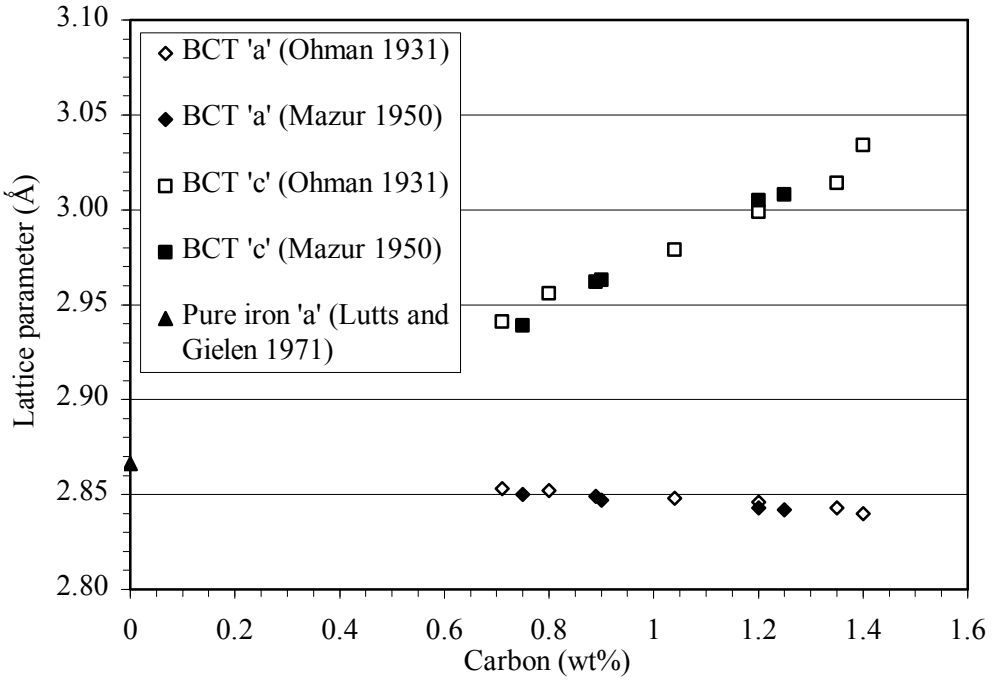

Figure 2.18 - Correlation of carbon content with lattice parameters for quenched martensite, plotted from published data (Ohman 1931) (Mazur 1950) (Lutts and Gielen 1971)

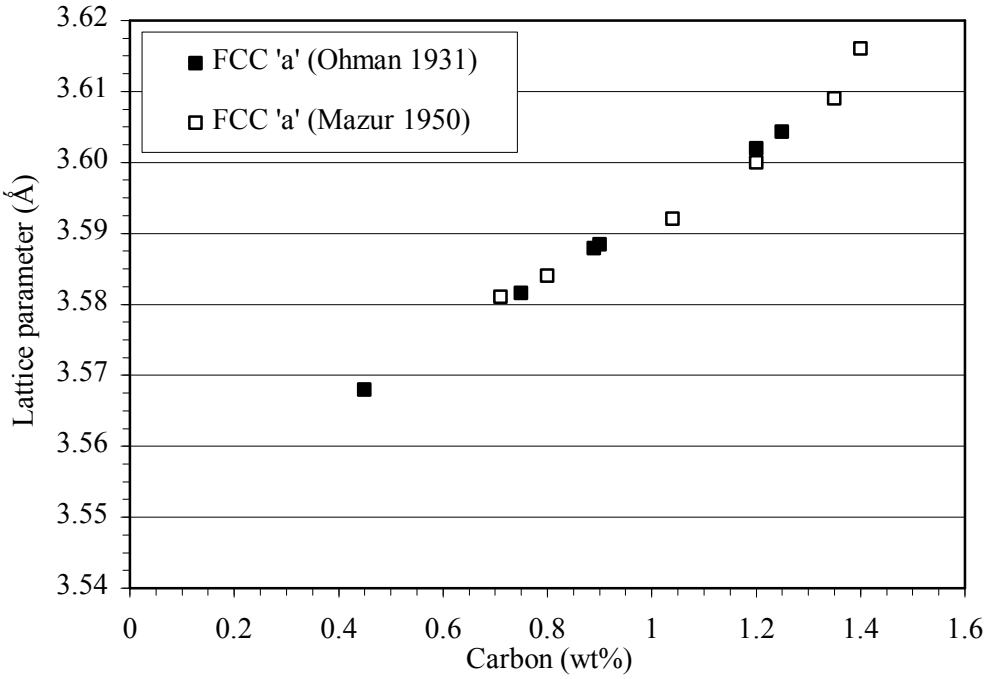

Figure 2.19 - Correlation of carbon content with lattice parameters for retained austenite, plotted from published data (Ohman 1931) (Mazur 1950)

For quenched martensite, lattice parameter measurements can be compared with published data such as that shown in Figure 2.18 after suitable consideration of the issues described in Section 2.9.8. Alternatively, it is reasonable to simply assume that as-quenched martensite possesses the same carbon concentration as that determined during chemical composition measurements of the alloy.

Similarly to as-quenched martensite, austenite measured in as-quenched specimens can also be assumed to possess the full carbon concentration of the alloy. For partitioned specimens, although much data (Figure 2.20) on carbon concentration versus austenite lattice parameter exists, the application of a mathematical relationship to derive an estimation of austenite carbon concentration is not without complications. In the laboratory, the effect of carbon concentration on austenite lattice parameter can be measured by various methods; quenching to obtain retained austenite (and martensite), high alloying (e.g. manganese or nickel) to stabilise austenite to room temperature, or measurements on the iron-carbon system at an elevated temperature such that austenite is the most stable phase. Data from each of these methods must be used with caution; in the case of quenched steel, austenite lattice parameter measurements may be affected by the dilatational nature of martensite formation (Ridley, Stuart et al. 1969) (Yershov and Oslon 1968), high alloying causes adjustments to the lattice parameter (Dyson and Holmes 1970) and

measurements at high temperatures must be extrapolated to obtain data at ambient temperatures. Other methods have been reported, for example, the work of Scott and Drillet employed Electron Energy Loss Spectroscopy (EELS) and XRD to evaluate lattice parameter with respect to carbon content (Scott and Drillet 2007); although their results contained a lot of scatter, and suggest that the relationship is non-linear, this methodology is arguably less vulnerable to unwanted secondary effects. The data assembled by Scott and Drillet (Figure 2.20) shows that although the carbon concentration versus lattice parameter gradients established by different researchers are quite similar, the carbon conconcentration constants (y-intersects) are, in some cases, quite different.

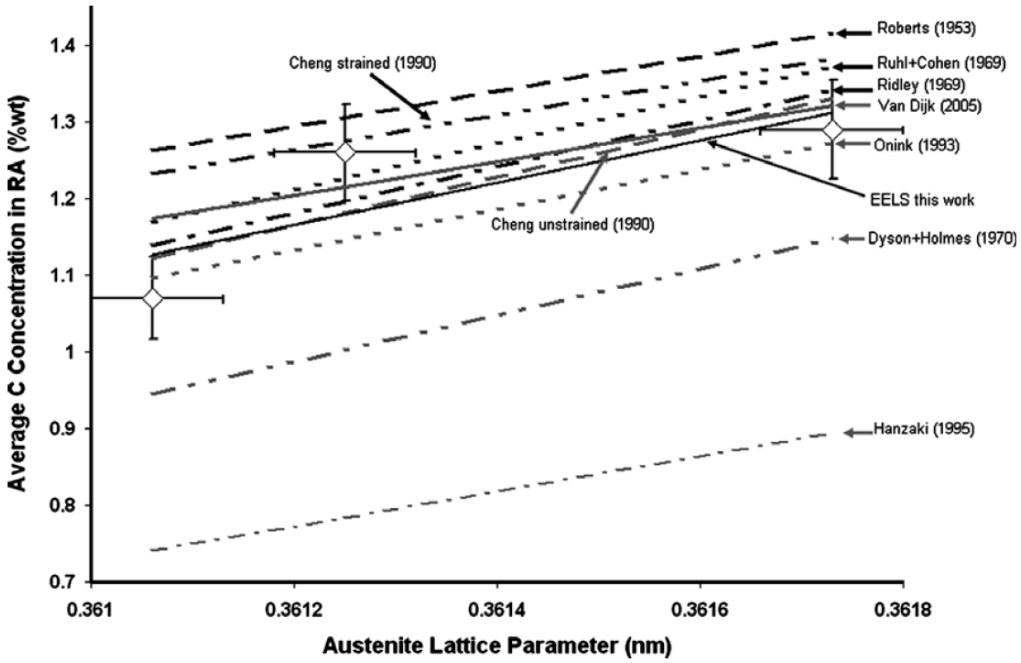

Figure 2.20 – Austenite lattice parameter variation with carbon content, 'EELS this work' refers to the work of Scott and Drillet (Scott and Drillet 2007), all other datasets are as labelled (Roberts 1953) (Ruhl and Cohen 1969) (Ridley, Stuart et al. 1969) (Dijk, Butt et al. 2005) (Onink, Brakman et al. 1993) (Dyson and Holmes 1970) (Hanzaki, Hodgson et al. 1995a) (Hanzaki, Hodgson et al. 1995b) (Cheng, Bottger et al. 1990)

Establishing the relationship between lattice parameter and ferrite carbon concentration raises even greater problems than for austenite; the presence of even relatively small amounts of carbon in ferrite represents a non-equilibrium condition and so it is hypothesised that any results obtained could be adversely affected by rapid precipitation of carbon to low energy areas or metastable carbides. Hence, studies of alpha iron published by Onink and co-workers show that varying carbon

content from 0 to 0.8 wt% has very little effect on ferrite lattice parameter (Onink, Brakman et al. 1993). Nevertheless, at least one hypothetical relationship has been published that can be used for the estimation of ferrite carbon concentration from lattice parameter measurements. Kurdjumov and Lyssak proposed that the rate at which the lattice parameter of supersaturated cubic iron varies with carbon concentration can be estimated from the well known tetragonal variation as per Equation 2.5 (Kurdjumov and Lyssak 1947). Figure 2.21 illustrates the result of plotting Equation 2.5 with published data for BCT martensite. The gradient of the BCC martensite relationship shown in Figure 2.21 is approximately 0.024Å/wt%C; it is interesting to note that this value is quite similar to the gradients of 0.028 and 0.030Å/wt%C given in the inset plot of Figure 2.14.

$$a_{cubic} = \sqrt[3]{a^2_{tetragonal} \cdot c_{tetragonal}}$$

Equation 2.5

where a_{cubic} is the theoretical lattice parameter of supersaturated (cubic) ferrite, $a_{tetragonal}$ and $c_{tetragonal}$ are the lattice parameters of tetragonal martensite as published

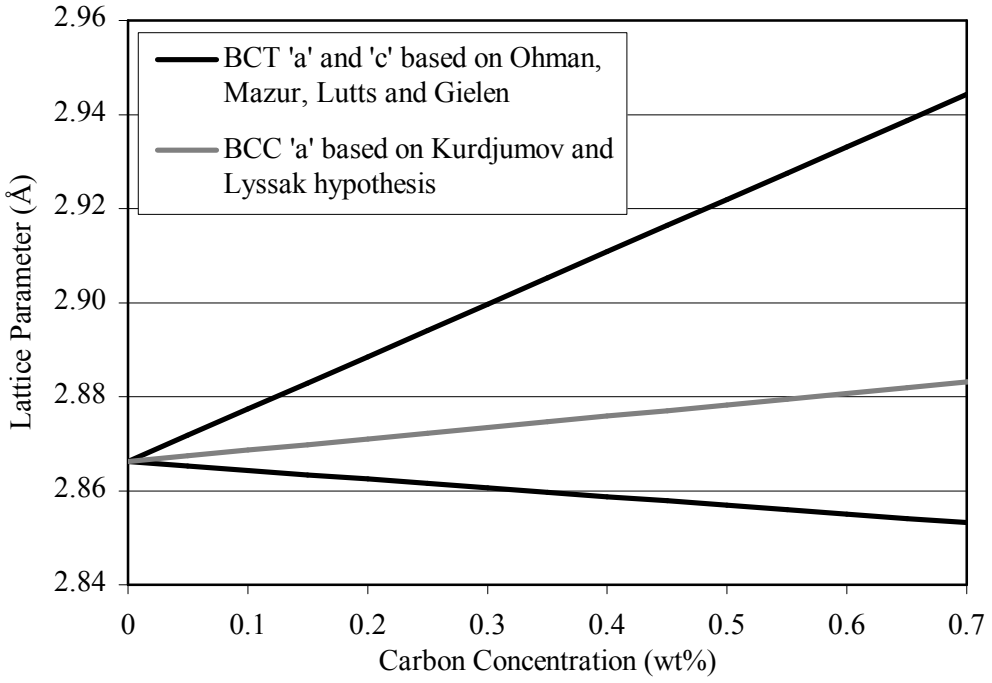

Figure 2.21 – Theoretical BCC martensite lattice parameter versus carbon concentration relationship, as proposed by Kurdjumov and Lyssak (Kurdjumov and Lyssak 1947)

Taking all of the above into account, the approach used to estimate carbon concentration in the different phases was as follows: For BCT martensite in as-quenched specimens, carbon concentration was calculated from the lattice 'c' parameter. The equation used to do this was derived by creating a least-squares fit to the data of Ohman and Mazur, while forcing the constant in the equation to equal the lattice parameter for pure iron reported by Lutts and Gielen (see Figure 2.18). For BCC martensite (in both as-quenched and partitioned specimens), the hypothetical relationship proposed by Kurdjumov and Lyssak (Equation 2.5) was used in conjunction with the lattice parameter versus carbon relationship already described for BCT martensite (see Figure 2.21). Austenite carbon concentration was estimated by assuming that the austenite lattice parameter measured in the as-quenched condition was representative of the carbon concentration as determined for each individual sample by the external analysis laboratory. The gradient from the carbon concentration versus lattice parameter relationship of Seki and Nagata was then employed to calculate the variations in austenite carbon concentration during partitioning. (Seki and Nagata 2005).

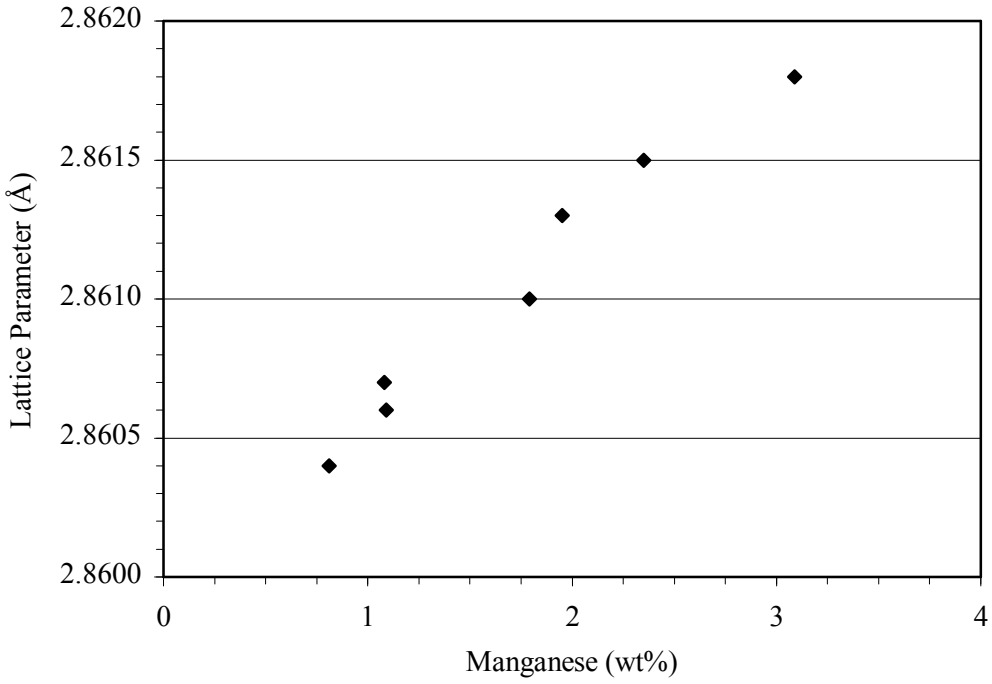

Figure 2.22 - Variation of lattice parameter in iron alloyed with manganese, plotted using published data (Sutton and Hume-Rothery 1955)

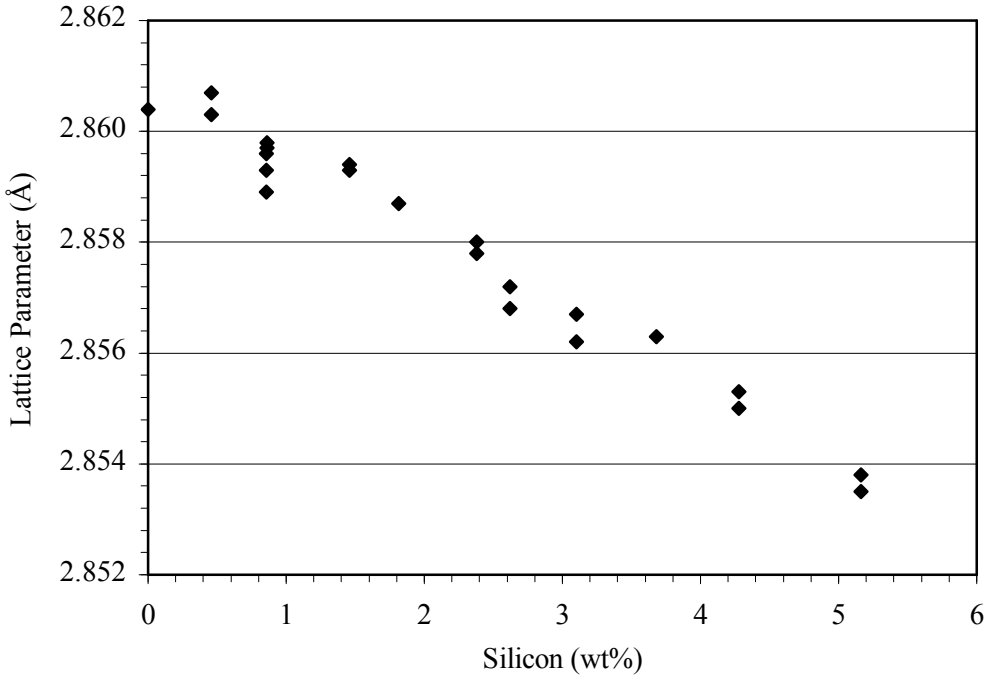

Figure 2.23 - Variation of lattice parameter in iron alloyed with silicon, plotted using published data (Jette and Greiner 1933)

When using lattice parameter measurements to estimate carbon insterstitial occupancy, it is appropriate to consider the effects of substitutional alloying in the case that constrained-carbon-equilibrium does not apply and partitioning of substitutional alloying elements takes place during partitioning. Figure 2.22 and Figure 2.23 indicate that the effect of Manganese and Silicon on the lattice parameter of BCC iron is relatively low. Determination of the effect of substitutional alloying elements on austenite lattice parameter is subject to similar difficulties as already described for the interstitial alloying element carbon. In Figure 2.24, room temperature measurements on highly alloyed, fully austenitic alloys show that the relationships sometimes exhibit dependency on the composition of the base alloy in which the alloying effect is being measured. Fortunately, phase equilibria predictions at the partitioning temperatures of interest (see Section 2.11.1) suggest that the equilibrium concentrations of manganese and silicon in ferrite and austenite are relatively close to that of the overall alloy composition. Therefore, even if partitioning of substitutional alloying elements does occur, the effect on lattice parameter measurements is not expected to be of any consequence.

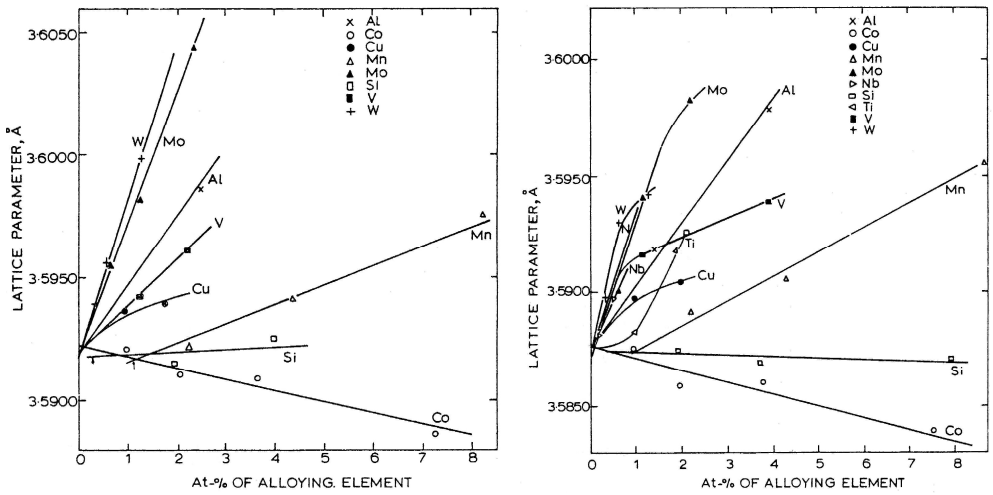

Figure 2.24 – Effect of substitutional alloying elements on austenite lattice parameter for base alloy compositions (in wt%) of 18Cr-10Ni (left) and 16Cr-25Ni (right) (Dyson and Holmes 1970)

2.10 Neutron diffraction measurements

The High Resolution Powder Diffractometer (HRPD) instrument at ISIS, Rutherford Appleton Laboratory, UK was used to make measurements on as-quenched specimens before, during, and after the partitioning stage of the Q&P heat treatment process. Neutron diffraction using HRPD offers significant advantages over the XRD technique. Firstly, neutron diffraction is a whole-volume technique and so is able to make measurements that are largely free from surface effects. Secondly, HRPD is a time-of-flight instrument, therefore, together with a recent upgrade to the HRPD neutron guide tube, this enables rapid collection of data from a specimen that is undergoing solid state transformations during an in-situ heat treatment. Thirdly, the high resolution capability of the instrument is well suited to measurements involving the relatively small lattice parameter changes that take place during solid state transformations in steel. Fourthly, the high resolution is also useful in terms of determining the lattice strains via line broadening measurements. Lastly, neutron diffraction is more sensitive to 'light' elements than x-ray diffraction. This characteristic opens up the possibility of detecting carbon located within interstitial sites.

2.10.1 HRPD instrument setup

Prior to submitting a proposal for beamtime on HRPD, two specimens were subject to trial measurements, one quenched, and one quenched and partitioned. These measurements established the viability of using the HRPD instrument to make

measurements that would be useful to the project, and also enabled determination of optimum instrument settings prior to more comprehensive experiments.

Specimens were mounted in the HRPD beamline using thin wall vanadium cans. Two different pieces of hardware were used to position the vanadium can in the beamline. Initially, the furnace environment was in place to enable in-situ measurements to be made at elevated temperatures. Therefore, most of the measurements made on as-quenched specimens and all of the measurements made at elevated temperatures were completed in this configuration, which also included the ability to hot-change specimens at up to 300°C. Following the measurements made at high temperature, the furnace environment was removed from the beamline to improve the signal to background count ratio during room temperature measurements on partitioned specimens. The standard hardware for room temperature measurements was then used to position the vanadium cans in the beamline; this hardware incorporated a boron compound to absorb stray neutrons and reduce the part of the background count that is caused by neutron scattering from materials other than the specimen being measured.

Two sets of jaws control the cross section of the neutron beam which irradiates the specimen. Optimum setting of the jaws ensures maximum count rates at the detectors while minimising background count rate. The setting used for the jaws was 15mm * 20mm; for most of the specimens measured this was sufficient to expose the entire specimen to neutrons. As the HRPD instrument is situated almost 100 metres from the neutron spallation source, the range of wavelengths and times-of-flight produced by the liquid methane moderator results in overlap between the ‘slowest’ neutrons from the current cycle and the ‘fastest’ neutrons from the next cycle (ISIS operates at 50 cycles per second). Therefore, two disc choppers situated approximately 6, and 9 metres from the moderator are installed to control the window of wavelengths that are seen by the specimen being measured. For all specimens the neutron times-of-flight admitted to the specimen were constrained by the disc choppers to 10ms-110ms. For the backscatter bank of detectors on HRPD located at 168.33° 2Θ this gives a d-spacing detection window of approximately 0.2Å-2.2Å.

2.10.2 HRPD furnace environment

A water cooled furnace featuring vanadium and stainless steel construction was provided for the purpose of conducting dynamic measurements during heating of the

as-quenched specimens. Control of the furnace was via a Type-K thermocouple in contact with the upper portion of the vanadium can (so as not to form part of the diffraction measurements). A tubular vanadium heating element surrounded the vanadium can; in the evacuated environment required for neutron diffraction, heat was transmitted to the vanadium can solely by radiative means, consequently heating rates were relatively slow compared to normal laboratory heat treatment conditions. Cooling was also slow as heat transfer was limited to radiation onto the vanadium heating element and conduction of heat through the mounting hardware. As beamtime comes at a high premium, two options were available to offset the low cooling rate. Injection of helium could be used to provide a convective medium for accelerated cooling; alternatively, it was possible to remove and insert specimens at temperatures of up to 300°C using an air-lock system. Photos of the furnace environment sample holder arrangement are presented in Figure 2.25 and Figure 2.26.

Figure 2.25 – A vanadium can shown attached to the furnace environment sample holder, cylindrical specimens occupied the right hand (lower) portion of the can, the thermocouple is just visible on the lower left side of the can

Figure 2.26 – The lower part of the furnace environment sample holder, this part of the sample holder can be retracted into the tubular top section of the sample holder (out of view to the left) during a hot-change operation, the thermocouple is visible as a loop of wire between the vanadium can and the sample holder

2.10.3 Post processing of HRPD data

The diffraction peaks caused by the vanadium can were subtracted from each diffraction pattern using software at the ISIS facility. The subtraction process was not perfect and so small deviations in the background count are visible at the locations where vanadium peaks have been removed. The software also applied a correction to compensate for the intensity versus wavelength variation that is characteristic of the neutron spallation source and the liquid methane moderator (Figure 2.27).

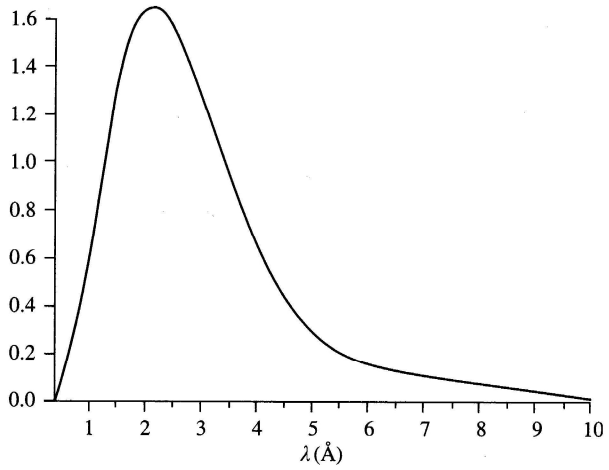

Figure 2.27 – Typical neutron wavelength distribution for a diffractometer situated on a neutron guide at a spallation source, the Y axis is neutron flux, taken from Kisi and Howard, after ISIS (Kisi and Howard 2008) (ISIS website)

2.10.4 Rietveld refinement software and procedure used to interpret HRPD data

The diffraction data from the HRPD instrument was refined using the GSAS and EXPGUI software already described in Section 2.9.7. The parameters refined were in the main, the same as already listed for the XRD diffraction data. The peak shape selected for fitting the data was developed by W.I.F. David and R.B. Von Dreele (Unpublished) based on the work of Ikeda and Carpenter (Ikeda and Carpenter 1985). This peak shape is incorporated into GSAS as Time-of-Flight Profile Type 2. For reasons previously described (see Section 2.9.7), the lattice strain measurements in the experimental results sections are presented as refined (i.e. no corrections have been applied for crystallite size effects).

Prior to conducting any refinements of data from actual specimens, it was necessary to determine the instrument parameters for HRPD. The instrument parameters are unique to each detector bank and relate time-of-flight to a particular d-spacing. These parameters were established through refinement of data gathered from a material with accurately determined unit cell dimensions. Standard Reference Material SRM640c (silicon powder) issued by the National Institute for Standards and Technology (NIST) was used for this. Although the HRPD detection system comprises three banks of detectors situated at 30, 90 and 168.33 degrees to the beamline, only the data from the backscatter bank of detectors was refined. This decision was taken mainly because the backscatter bank offers significantly higher resolution than the other banks; also, having set the time-of-flight window to optimise data collection from this bank of detectors, the other banks are found to contain fewer diffraction peaks that are of lower quality than those from the backscatter bank. Diffraction patterns for the silicon standard are shown for the three separate detector banks in Figure 2.28, Figure 2.29, and Figure 2.30. For highly crystalline materials such as silicon, the excellent resolution of the HRPD instrument enables refinement to very low d-spacings. However, for the specimens being measured, high lattice strains curtailed the range over which the data could usefully be refined. For static (isothermal) measurements the limits were set to 20-109ms; for in-situ, dynamic measurements the limits were 34-109ms.

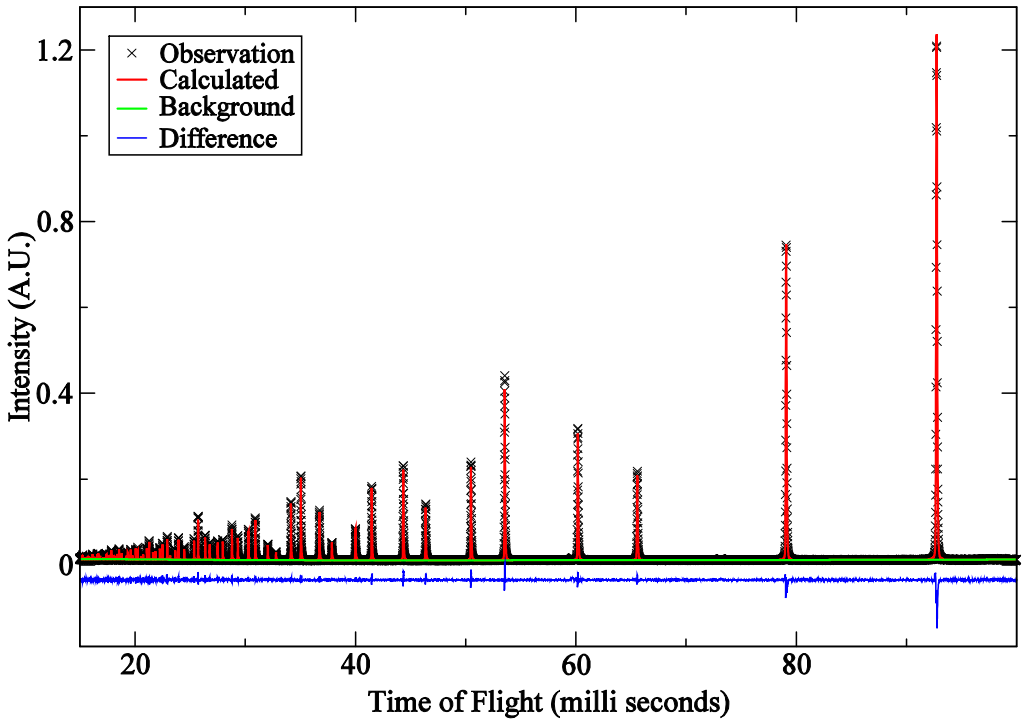

Figure 2.28 – Diffraction pattern from the silicon standard, gathered from detectors in Bank 1 of the HRPD instrument (168.33° to the beamline)

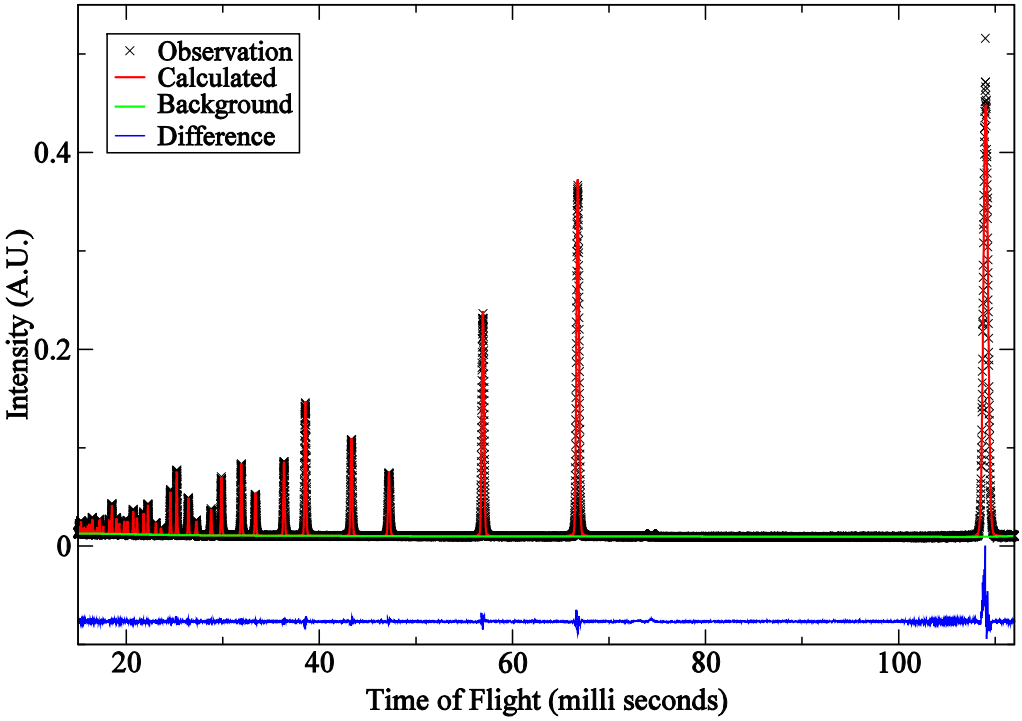

Figure 2.29 – Diffraction pattern from the silicon standard, gathered from detectors in Bank 2 of the HRPD instrument (90° to the beamline)

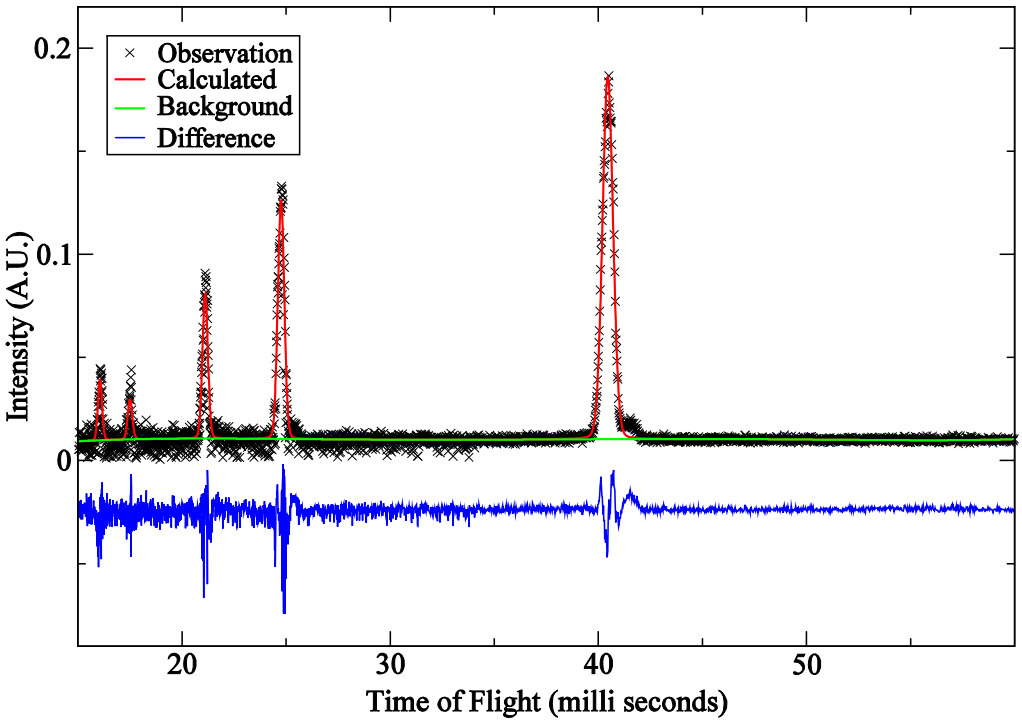

Figure 2.30 – Diffraction pattern from the silicon standard, gathered from detectors in Bank 3 of the HRPD instrument (30° to the beamline)

On time-of-flight instruments such as HRPD, measurements may be converted to wavelengths by use of a modified de Broglie equation as shown in Equation 2.6, where λ is wavelength (m), h is Planck's constant, t is time-of-flight (μs), m is the mass of a neutron (kg), and L is the total neutron flight path (m) (Kisi and Howard 2008)

$$\lambda = \frac{ht}{mL}$$

Equation 2.6

By substituting Equation 2.6 into the Bragg equation and re-arranging, Equation 2.7 results, where d_{hkl} is the d-spacing of crystal planes (Å), h is Planck's constant, t is the time-of-flight, and m is the mass of a neutron (Kisi and Howard 2008)

$$d_{hkl} = \frac{ht}{2mL\sin\vartheta}$$

Equation 2.7

By removing the constants from Equation 2.7, a simplified equation form is obtained as shown in Equation 2.8. In Equation 2.8, the use of microseconds and metres yields d-spacing measurements in Angstroms (Kisi and Howard 2008).

$$d_{hkl} = \frac{t}{505.554L\sin\vartheta}$$

Equation 2.8

The diffraction pattern and instrument parameters are processed by GSAS to compute d-spacings, and ultimately, lattice parameters. A replot of Figure 2.28 showing the diffraction pattern in terms of d-spacings is shown in Figure 2.31. The derivation of phase fractions is much the same as already described for X-ray diffraction and is also computed by GSAS.

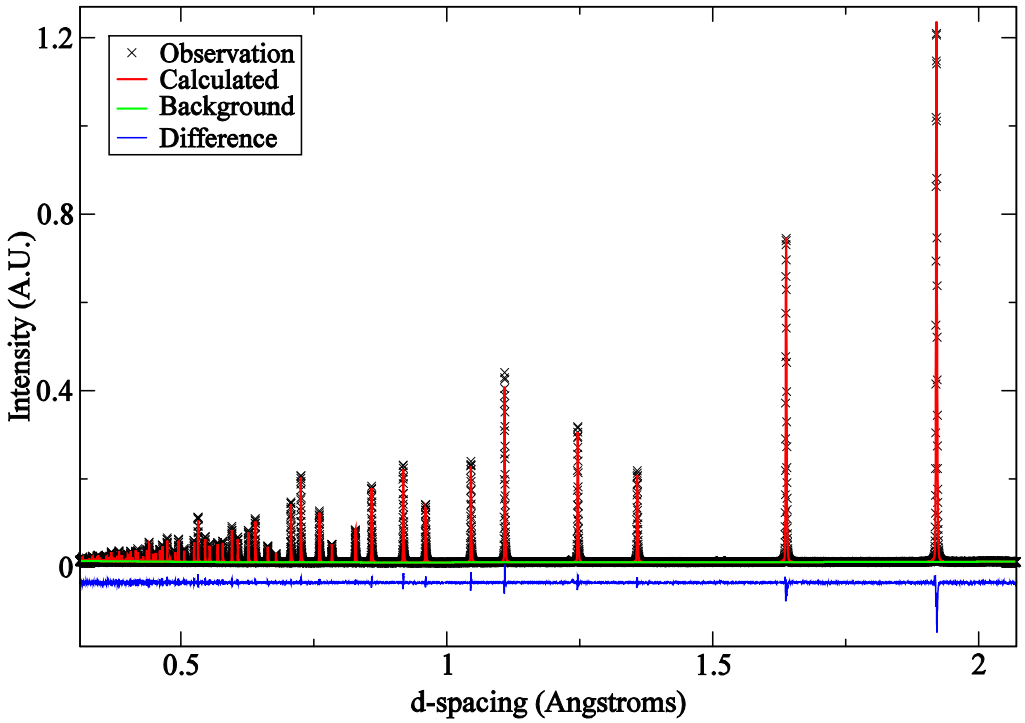

Figure 2.31 – Replot of Figure 2.28, showing d-spacing of the silicon standard (HRPD detector Bank 1)

2.10.5 Development of Rietveld structural models

The analytical process to determine microstructural parameters from neutron diffraction data is subject to much the same complications as have already been described for X-ray diffraction in Section 2.9.8. However, although the situation is simplified by virtue of the fact that the time interval between quenching and measuring was relatively constant for all specimens; a further complication arises due to the dynamic nature of the in-situ partitioning measurements. In the as-quenched condition, as for X-ray diffraction data, refinements may be completed with two phases (austenite and BCT martensite), or with the addition of a third, BCC martensite phase. These two options are illustrated in Figure 2.32 and Figure 2.33 respectively. For those specimens subjected to in-situ partitioning, both options were trialled, i.e. commencing refinements in the as-quenched state with either two or three phases. It was observed that both methods gave very similar results for austenite lattice parameter and phase fraction. Having considered the outcome from each method, it was decided to present in-situ partitioning results for refinements employing two phases in the initial as-quenched state. Although this was different to the approach used for X-ray diffraction data, a change in the method was made for two reasons. Firstly, the specimens were measured only a few days after quenching, secondly, the carbon content of the material used was higher. Due to the higher carbon content a larger quantity of carbon has to be rejected before a BCC structure

can result. The higher carbon content also increases the proportion of twinned martensite, therefore, it is hypothesised that fewer low-energy locations are available to accommodate carbon rejected from the BCT structure.

When data from as-quenched specimens is initially refined with a two phase (FCC and BCT) structural model, at some point during in-situ partitioning a transition to a three phase model (BCC, FCC and BCT) must occur due to tempering of BCT martensite. This transition is illustrated using two consecutive datasets in Figure 2.34 and Figure 2.35. The change can be observed by considering the BCT martensite 200 and 002 peaks located at approximately 69.2 and 71ms respectively, between which an additional BCC peak is present in Figure 2.35 but not in Figure 2.34. Once sufficient partitioning has taken place, the BCT phase becomes indistinct and the three phase structural model must be replaced by a two phase (BCC and FCC) model. This changeover is illustrated from Figure 2.35 to Figure 2.38, the extra BCC peak is visible between the BCT martensite 200 and 002 peaks in the first few datasets, but is the only peak present in Figure 2.38.

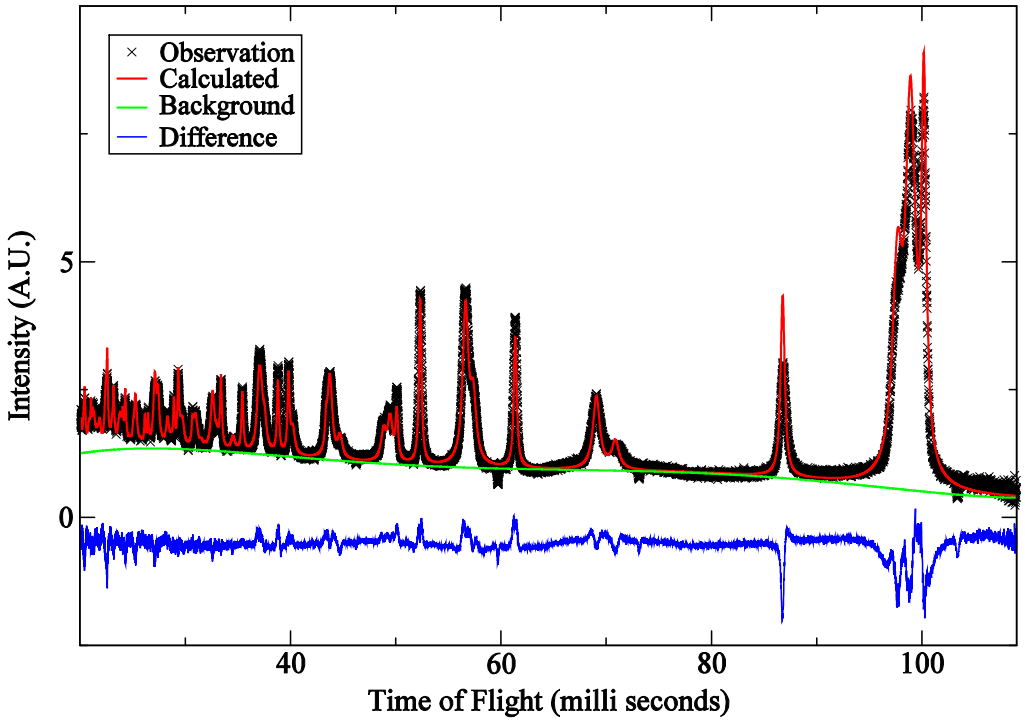

Figure 2.32 – Refinement of as-quenched data from the HRPD instrument with FCC and BCT phases (dataset acquired from specimen 3802)

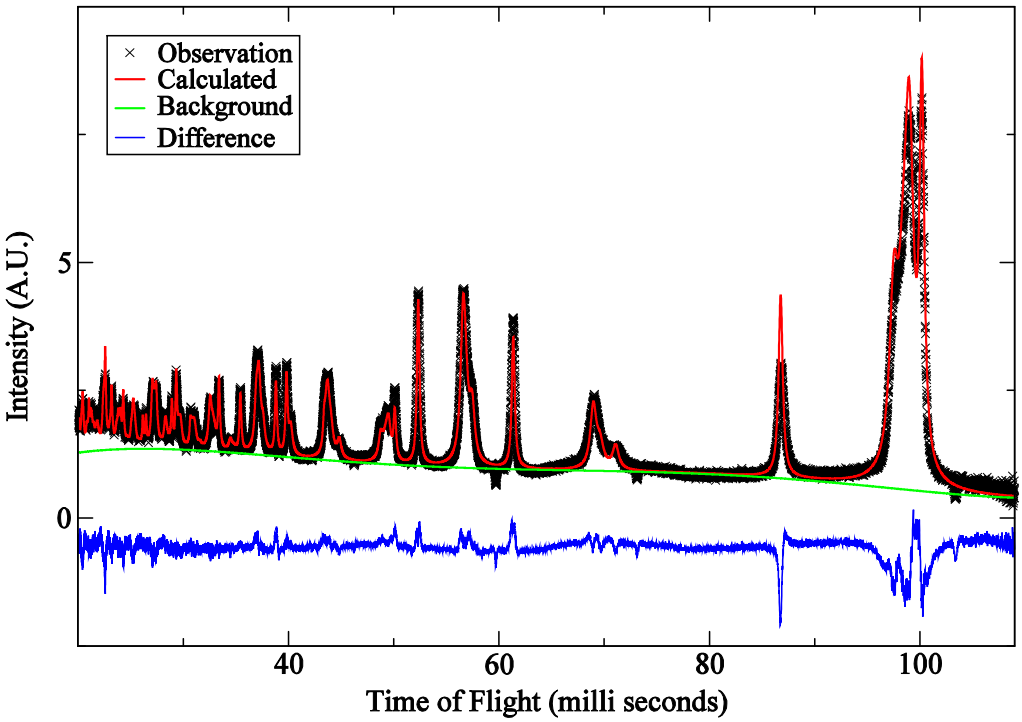

Figure 2.33 - Refinement of as-quenched data from the HRPD instrument with BCC, FCC and BCT phases (dataset acquired from specimen 3802)

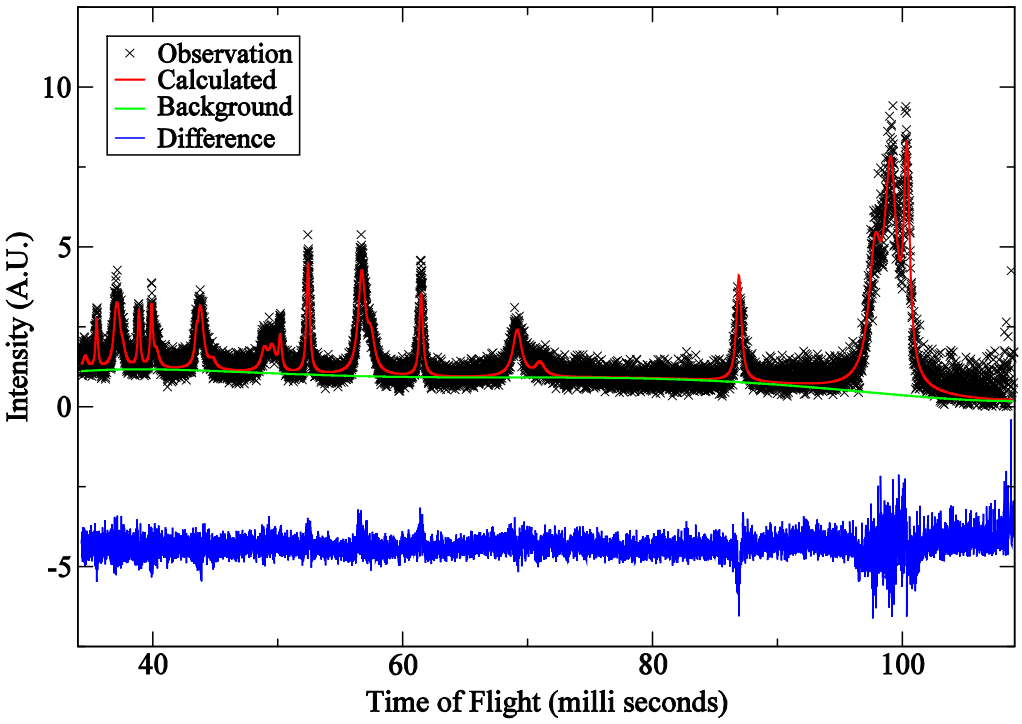

Figure 2.34 – Two phase (FCC and BCT) Rietveld fit to specimen 3802 during in-situ partitioning (dataset 43031 collected at approximately 94°C)

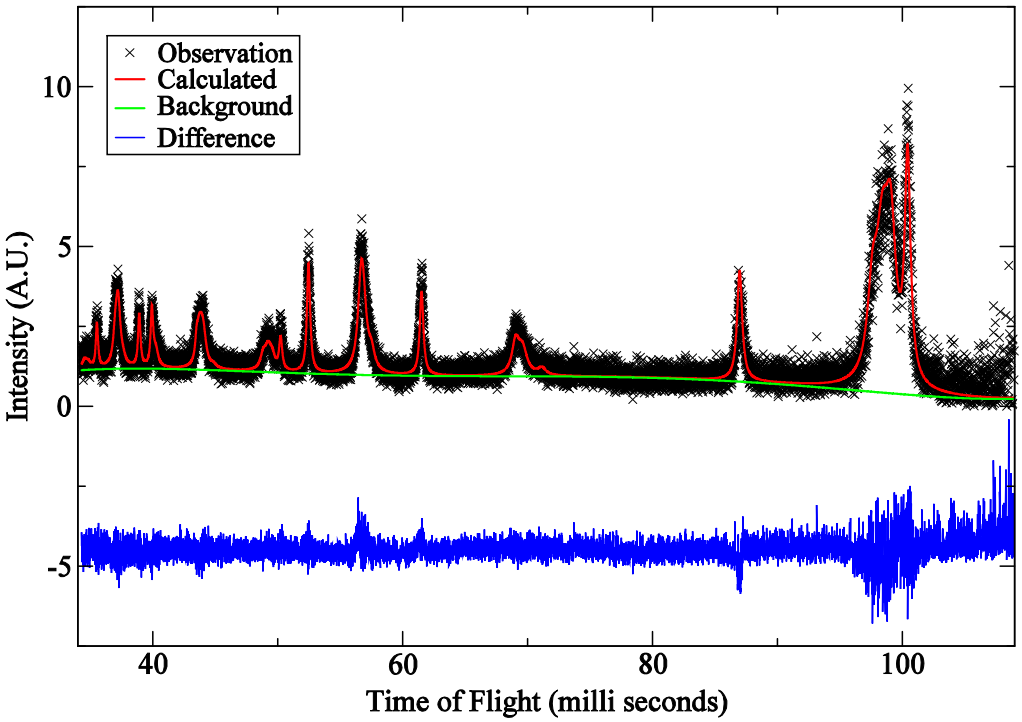

Figure 2.35 – Three phase (BCC, FCC and BCT) Rietveld fit to specimen 3802 during in-situ partitioning (dataset 43032 collected at approximately 136°C)

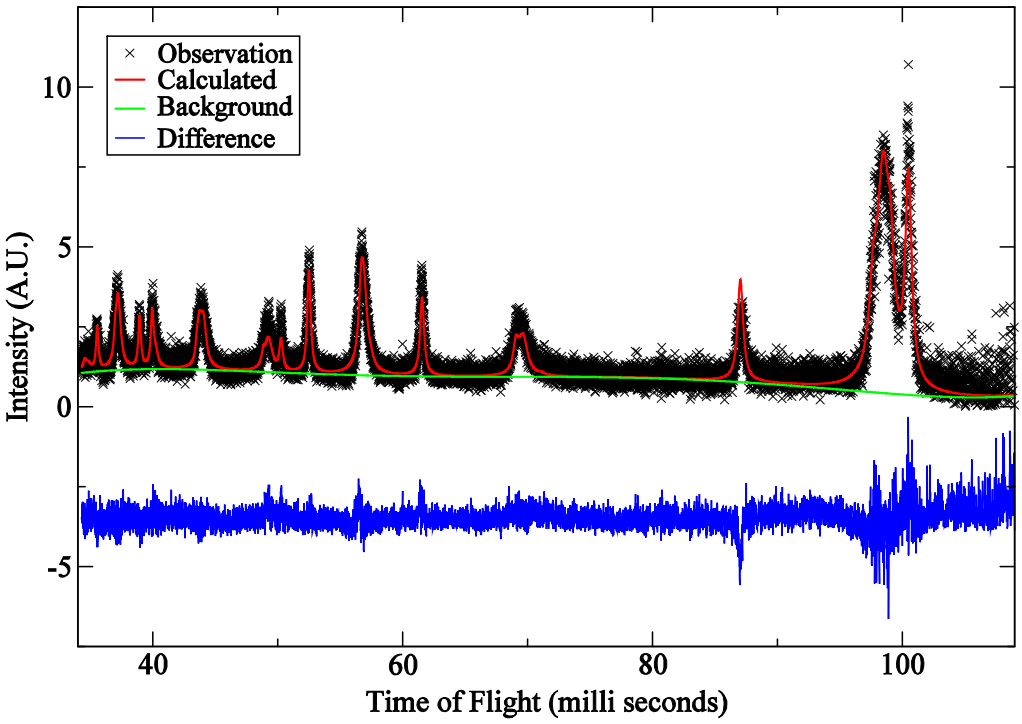

Figure 2.36 – Three phase (BCC, FCC and BCT) Rietveld fit to specimen 3802 during in-situ partitioning (dataset 43033 collected at approximately 184°C)

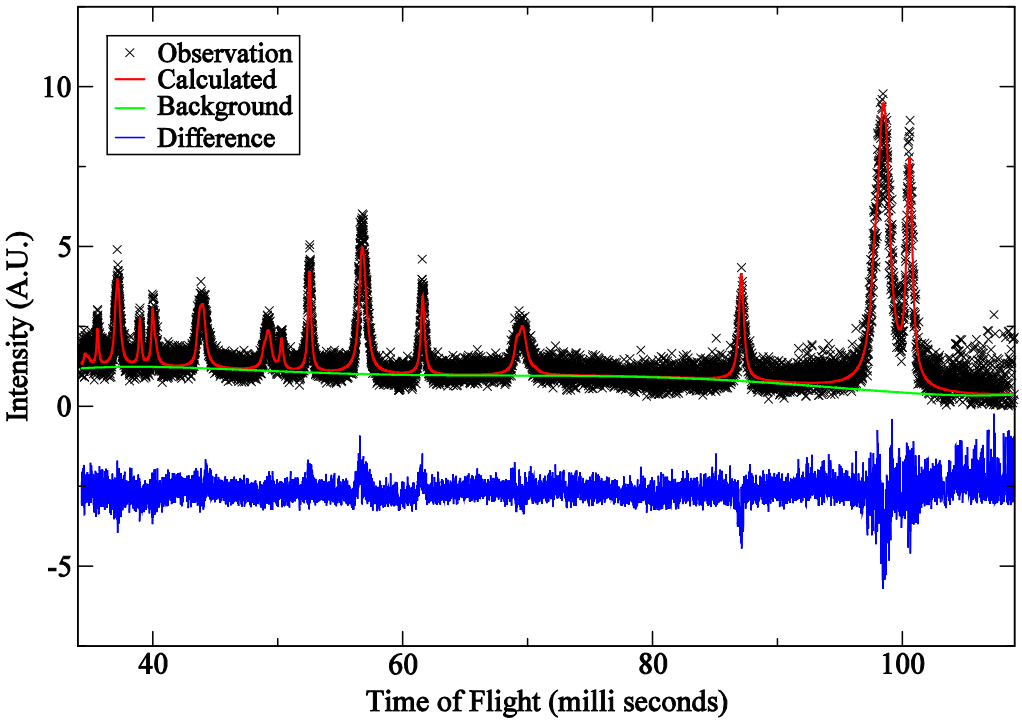

Figure 2.37 – Three phase (BCC, FCC and BCT) Rietveld fit to specimen 3802 during in-situ partitioning (dataset 43034 collected at approximately 224°C)

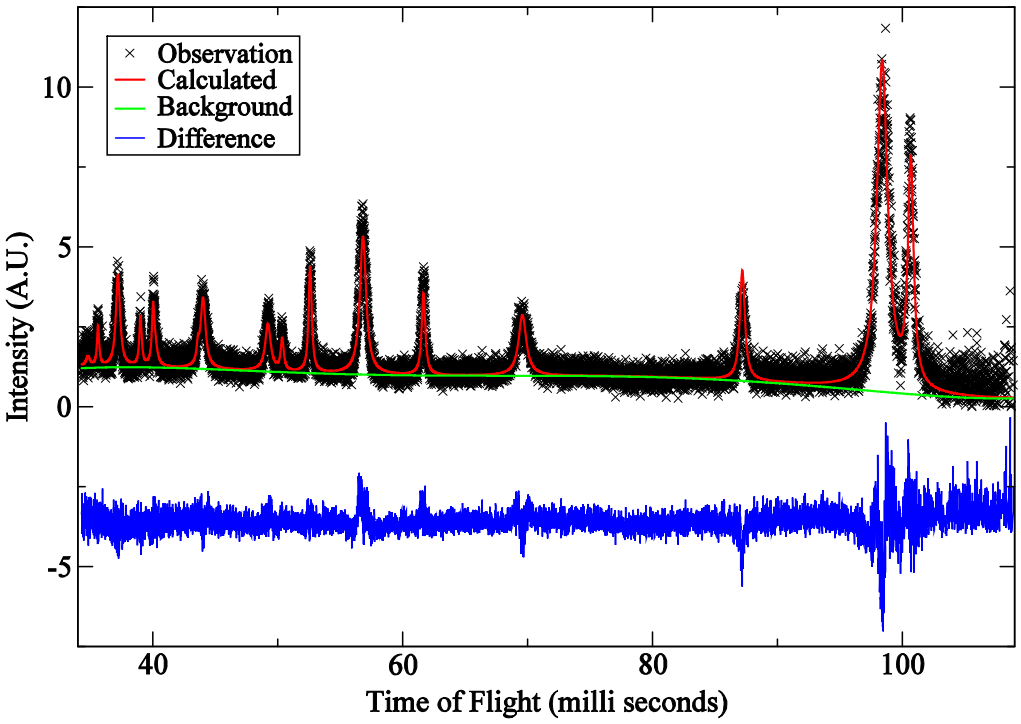

Figure 2.38 – Two phase (BCC and FCC) Rietveld fit to specimen 3802 during in-situ partitioning (dataset 43035 collected at approximately 263°C)

2.10.6 Determination of specimen temperature during in-situ measurements with the furnace environment

The log files generated during HRPD measurements include a record of the temperature of the vanadium can. The temperature was measured using a Type K thermocouple in direct contact with the upper portion of the vanadium can (see Figure 2.25). The same thermocouple also forms part of the closed loop feedback system which connects to the furnace controller and regulates the input power to the furnace element. In order to subtract thermal expansion effects from the lattice parameter data (see Section 2.10.7), it is necessary to determine a reasonably accurate temperature/time history for the specimen during measurement. When using the temperature data from the HRPD run log file to subtract thermal expansion effects it is clear that inaccuracies are present due to the lag in response between heating of the vanadium can, and heat transfer from the vanadium can to the specimen.

No information was available from ISIS to approximate the magnitude of the thermal lag that exists between heating of the vanadium can and heating of the specimen; therefore it was necessary to apply a theoretical correction to the thermocouple data. To reduce the background count, the measurement environment is evacuated to a low pressure; hence, heat transfer by convective means is relatively insignificant. Two other heat transfer methods are possible, radiation and conduction; the vanadium cans had rounded bottoms and so the contact area between the vanadium can and the specimen was relatively small, consequently, the conductance path is expected to present a high thermal resistance to heat transfer (see Figure 2.39)

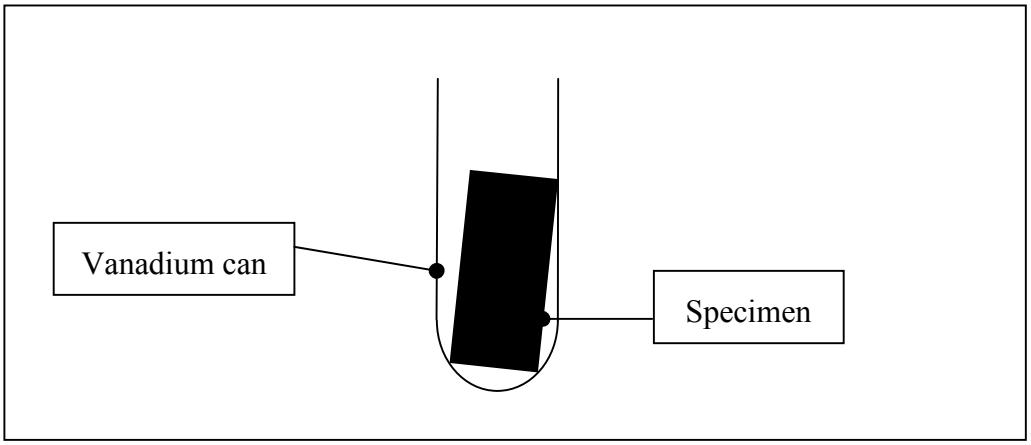

Figure 2.39 – Schematic representation of the minimal contact area between a vanadium can and the specimen inside

Therefore, radiative heat transfer from the vanadium can to the specimen is considered to be the dominant mode of heat transfer. A theoretical temperature correction was applied by assuming that the thermocouple records are an accurate record of the vanadium can temperature. Specimen temperature was then calculated by an iterative process on the basis that the vanadium can radiates heat onto the specimen. Radiative heat exchange was approximated by Equation 2.9 (Holman 2010), the formula for heat transfer between two infinite concentric cylinders; where q is the heat flow from the vanadium can to the specimen, σ is the Stefan-Boltzmann constant, and T_1, T_2, A_1, A_2 and ε_1 ε_2 are the absolute temperatures, areas, and emissivities of the vanadium can and specimen respectively.

$$q = \frac{\sigma A_1 (T_1^4 - T_2^4)}{\frac{1}{\varepsilon_1} + \frac{A_1}{A_2}\left(\frac{1}{\varepsilon_2} - 1\right)}$$

Equation 2.9

Values for the emissivities and areas of the surfaces were not known, however, for the purposes of generating a temperature correction it is acceptable to replace σ, and all values of A and ε with a single factor. Therefore, Equation 2.9 is simplified to Equation 2.10, where 'c' is a constant which was set after careful consideration of data from all seven of the specimens which were subjected to in-situ partitioning. The value for 'c' was chosen such that the BCC martensite lattice parameter is observed to decrease at relatively low temperatures, while the austenite lattice parameter remains stable until higher temperatures are reached. This was done to fit existing knowledge of tempering reactions, and also to match up with the disparate diffusion rates of carbon in ferrite and austenite (e.g. as illustrated in Figure 1.11).

$$q = (T_1^4 - T_2^4) \times c$$

Equation 2.10

2.10.7 Subtraction of thermal expansion from lattice parameters derived during in-situ measurements with the furnace environment

The lattice parameter changes caused by migration of carbon from supersaturated martensite to austenite are relatively small when compared to the

increases encountered due to thermal expansion. Therefore, the published literature was consulted to identify data suitable for subtracting thermal expansion from the lattice parameter measurements. For both the alpha (BCC), and gamma (FCC) phases several sources were reviewed. The data sources and thermal expansion relationships reviewed are given in Table 2.1 and Table 2.2. With two exceptions, the data given in Table 2.1 and Table 2.2 are for pure iron (i.e. no carbon). One of the relationships reported by Seki and Nagata for gamma iron includes a term for the effect of carbon on lattice parameter (denoted by 'C' in the equation). Additionally, the relationship established by Choi, Kim et al was determined for austenite in TRIP steel (austenite carbon content was estimated at 1.39 wt%).

Lattice parameter - Temperature relationship	Temperature range of evaluation and units of T	Reference
$a_0(nm)=8.1593*10^{-6}T+0.35519$	1183-1550K	(Seki and Nagata 2005)
$a_0(nm)=0.35519+8.1593*10^{-6}T+1.7341*10^{-3}C$	1452-1550K	(Seki and Nagata 2005)
$a_0(Å)=3.5832+7.00*10^{-5}T$	900-1070°C	(Gorton, Bitsianes et al. 1965)
$a_0(nm)=0.36155+8.7383*10^{-6}T$	25-330°C	(Choi, Kim et al. 2002)

Table 2.1 – Published thermal expansion data for gamma iron

Lattice parameter - Temperature relationship	Temperature range of evaluation and units of T	Reference
$a_0(nm)=1.602*10^{-9}T^2+2.059*10^{-6}T+0.2860$	295-1183K	(Seki and Nagata 2005)
$a_0(Å)=2.8658+3.747*10^{-5}T+8.59*10^{-9}T^2$	22-900°C	(Gorton, Bitsianes et al. 1965)

Table 2.2 – Published thermal expansion data for alpha iron

After trialling the various lattice parameter/temperature relationships, it was found that the data as published by Gorton, Bitsianes et al offered the best match to room-temperature, as-quenched austenite lattice parameter measurements. Therefore, thermal expansion corrections were computed using the data of Gorton, Bitsianes et al in conjunction with the specimen temperature calculated by the method described in Section 2.10.6. Data from the same publication (Gorton, Bitsianes et al. 1965) was also used to apply a temperature correction to the BCC martensite lattice parameter measurements.

Determination of a suitable correction for thermal expansion of the BCT martensite ‘c’ lattice parameter is significantly more difficult than for the other two phases due to the ease with which tempering occurs. Searches of the available literature did not turn up any suitable data, hence, the measurements collected during this project were inspected to determine whether any useful information was present. Examination of the first few datapoints of those specimens partitioned from room temperature showed that a linear relationship could be extracted. Data from specimens which were hot-changed while the furnace was at high temperature was not used, as the heating rate was much higher, and so the onset of tempering effects was much more rapid. The relationship established is illustrated in Figure 2.40.

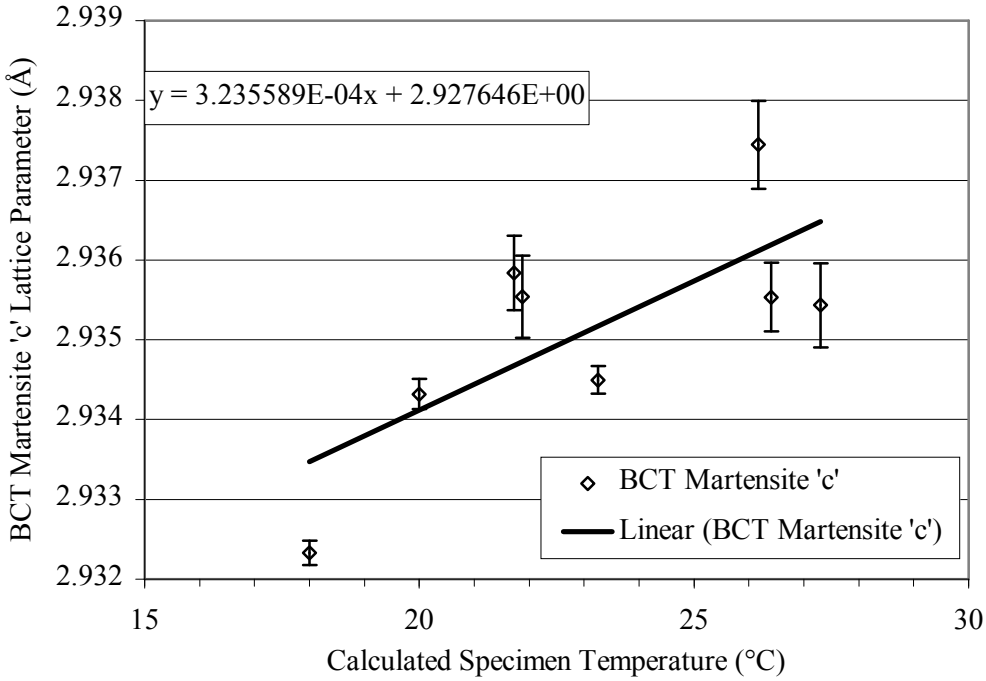

Figure 2.40 – Determination of BCT Martensite thermal expansion coefficient using data from specimens 3802, 3603 and 3803

After applying thermal expansion corrections to the lattice parameter measurements, for each in-situ partitioning experiment, a small correction was determined for each phase, and applied to every measurement in the experiment. The correction was applied such that the lattice parameter measurements in the first dataset (i.e. at room temperature) were unchanged from the uncorrected measurements.

2.10.8 Method of estimating carbon concentration from lattice parameter data

The procedure used to estimate carbon content from lattice parameter measurements was as described in Section 2.9.9 for XRD data. For the FCC austenite lattice parameter only, a correction was applied so that the calculated carbon concentration matched the alloy carbon content; this is essentially the same as already described in Section 2.9.9 for the treatment of XRD data.

2.11 Simulation of carbon partitioning from supersaturated martensite to austenite

The simulation program MAP_STEEL_PARTITION, as available on the Materials Algorithms Project website (MAP website) was used for simulating partitioning dynamics for comparison with Q&P practical experiments. The program is available as computer code written in Fortran, to be compiled by the user before execution. A publication exists describing the basic architecture of the program and examples of some of the results obtained (Mujahid and Bhadeshia 1992).

2.11.1 Program inputs

A summary of the inputs required by MAP_STEEL_PARTITION is presented in Table 2.3, followed by more detailed descriptions and rationale behind the values selected.

Line 1	KTEMP	EQFER	EQAUS	EBAR	TAUS	TFER	IAUS
Line 2	A3	SETIME					
Line 3	W						

Table 2.3 – Summary of MAP_STEEL_PARTITION inputs

KTEMP –Temperature (in Kelvin) at which partitioning takes place

EQFER – Para-equilibrium concentration of carbon in ferrite (expressed as a mole fraction)

EQAUS - Para-equilibrium concentration of carbon in austenite (expressed as a mole fraction)

EBAR – Average mole fraction of carbon present in the alloy

TAUS – Thickness of austenite into which carbon is partitioning (m)

TFER - Thickness of ferrite from which carbon is partitioning (m)

IAUS – Number of segments the austenite slice is divided into

A3 – Division of output (determines how often data is output)

SETIME – Maximum run time of the program (s)

W – Carbon-carbon interaction energy in austenite

The para-equilibrium carbon concentration values for ferrite and austenite, EQFER and EQAUS were derived with the assistance of Dr. Andrew Watson, using the software package MTDATA (National Physical Laboratory 2006) (Davies, Dinsdale et al. 2002). These predictions are presented in Table 2.5 and Table 2.6 for BCC martensite (ferrite) and Table 2.7 and Table 2.8 for FCC austenite; in all cases the predictions were for an alloy containing 0.53wt% carbon, 4wt% manganese, and 1.7wt% silicon (Table 2.4).

	Weight fraction	Atomic fraction
Iron	0.9377000	0.9044123
Manganese	0.0400000	0.0392169
Silicon	0.0170000	0.0326027
Carbon	0.0053000	0.0237681

Table 2.4 – Composition of the alloy used for MTDATA phase equilibrium predictions

	Weight fraction	Atomic fraction
Iron	0.9425923	0.9259650
Manganese	0.0402087	0.0401515
Silicon	0.0170887	0.0333797
Carbon	0.0001103	0.0005038

Table 2.5 – Predicted composition of BCC martensite at 400°C (assuming no carbide formation)

	Weight fraction	Atomic fraction
Iron	0.9425636	0.9258364
Manganese	0.0402075	0.0401459
Silicon	0.0170882	0.0333751
Carbon	0.0001407	0.0006426

Table 2.6 – Predicted composition of BCC martensite at 500°C (assuming no carbide formation)

If carbides are permitted to form then the predicted BCC martensite equilibrium carbon concentrations are lowered to 4.00E-07 and 2.60E-6 (both expressed as weight fractions) for ferrite at 400 and 500°C respectively. For the purposes of this project, the time frame of greatest interest can be measured in seconds rather than minutes. Therefore, the carbide-free predictions were used as simulation inputs.

	Weight fraction	Atomic fraction
Iron	0.9134221	0.8080916
Manganese	0.0389644	0.0350403
Silicon	0.0165599	0.0291306
Carbon	0.0310537	0.1277375

Table 2.7 – Predicted composition of FCC austenite at 400°C (assuming no carbide formation)

	Weight fraction	Atomic fraction
Iron	0.9231824	0.8448328
Manganese	0.0393807	0.0366334
Silicon	0.0167368	0.0304549
Carbon	0.0207001	0.0880789

Table 2.8 – Predicted composition of FCC austenite at 500°C (assuming no carbide formation)

It was considered worthwhile to make some calculations regarding the ability of the retained austenite phase fraction to accommodate all of the carbon rejected from the supersaturated martensite (i.e. as proposed by Speer, Streicher et al. in 2003). Figure 2.41 shows such a calculation based on a carbon content of 0.53wt% for a range of phase compositions. Comparing Figure 2.41 with the MTDATA carbon solubility predictions for austenite (Table 2.7 and Table 2.8), it is apparent that at 400°C a minimum of ~17wt% austenite is required to enable full partitioning of carbon to take place, at 500° the minimum is ~25wt% austenite.

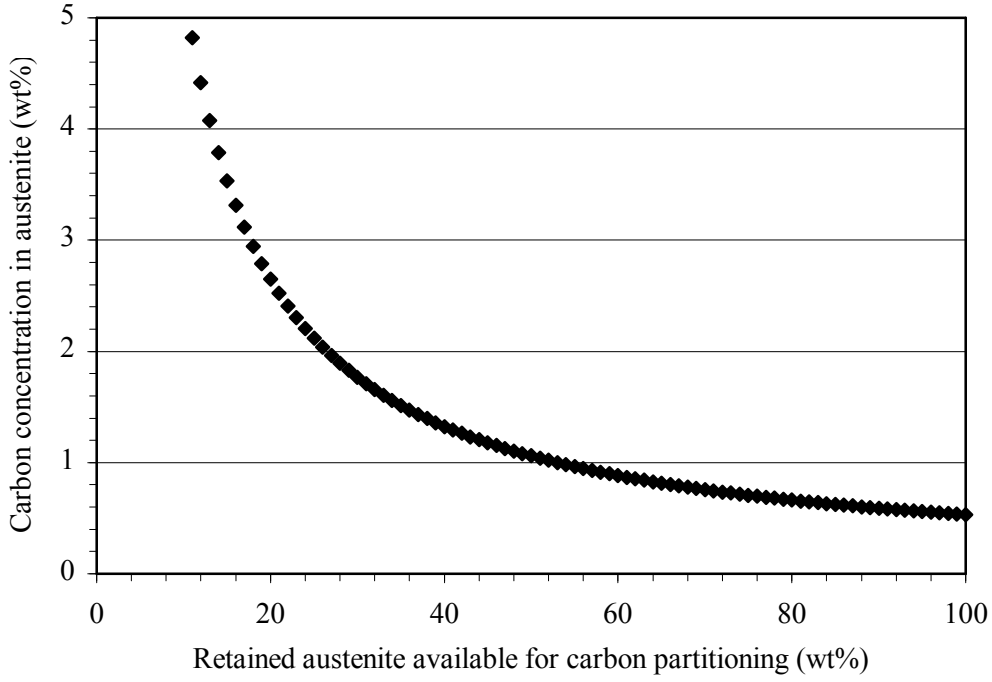

Figure 2.41 – Effect of retained austenite fraction on retained austenite carbon concentration (calculated for an alloy of 0.53wt% carbon)

After considering the theoretical limitations illustrated in Figure 2.41, it was necessary to make some decisions regarding the scenarios that should be modelled. The simulation of partitioning behaviour at 500°C was considered problematical and of limited benefit for two reasons; firstly, ~25% retained austenite is required to accommodate the entire carbon content of the alloy, this is somewhat above the retained austenite quantities measured by diffraction methods (see Chapter 6 and Chapter 7) Secondly, diffraction data suggests that decomposition and decarburisation of retained austenite occurs quite rapidly at 500°C. Therefore, the decision was taken to focus on partitioning behaviour at 400°C.

Representative values for the thickness of martensite laths present in quenched steel were obtained from published literature; Table 2.9 contains a summary of the literature that was consulted, and the values obtained. From Table 2.9 it can be seen that 0.2µm could be considered a reasonable setting for TFER. Austenite thickness (TAUS) was based on the value for TFER, with appropriate factoring to achieve the desired phase fraction ratio. This method of calculating austenite thickness assumes regular spacings of austenite and martensite, and has previously been used by other researchers to simulate the partitioning stage of the Q&P process (Clarke 2006).

A schematic diagram of the partitioning model is shown in Figure 2.42; from this it can be seen that the problem is treated as a one dimensional diffusional coupling. The problem is considered to be symmetrical, consequently, only one half of a martensite lath and adjacent austenite film are considered, hence, the values for TFER and TAUS are halved to take account of this.

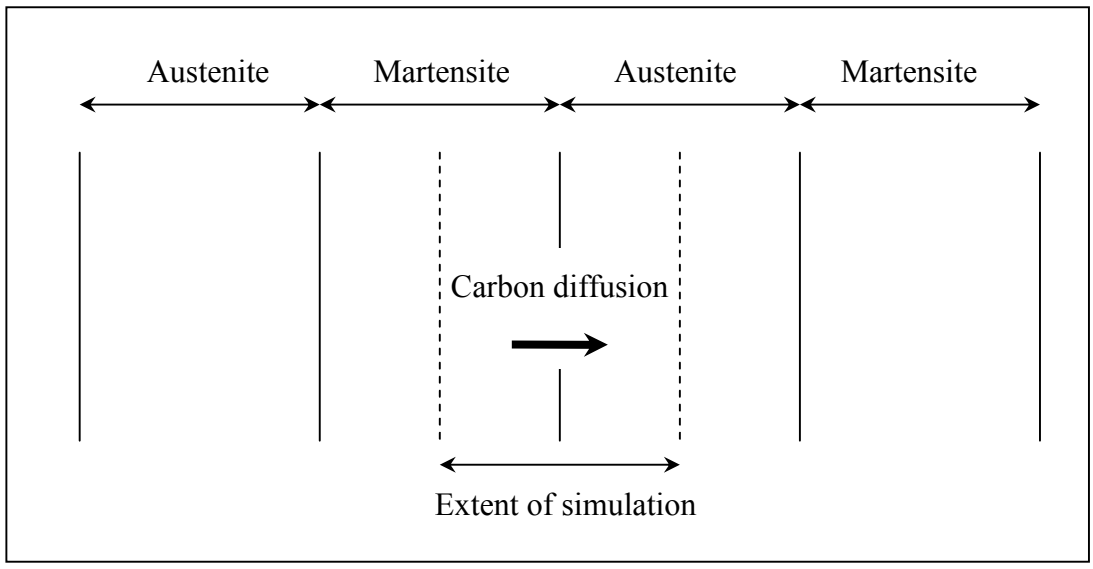

Figure 2.42 – Schematic diagram of the partitioning model

Material	Packet size (μm)	Mean lath width (μm)	Modal lath width (μm)	Distribution range (μm)	Notes	Reference
Fe 17.95Ni 8.78Co 5.01Mo 0.65Ti	-	0.156	0.20-0.25	0.05-1.00	-	(Hossein-Nedjad and Movaghar-Gharabagh 2008)
Fe 0.2C	5-60	-	0.15	-	Quenched	(Swarr and Krauss 1976)
	7-110	-	0.30	-	Quenched and Tempered	(Swarr and Krauss 1976)
Fe 0.065C 0.31Si 0.97Mn 2.32Cr 0.83Ni 0.19Mo	36-76	0.20-0.30	-	-	Water Quench (WQ)	(Naylor and Blondeau 1976) (Naylor 1979)
	30-77	0.55-0.69	-	-	Methyl-Cellulose Quench (MCQ)	
	29-84	0.35-0.42	-	-	WQ and Tempered	
	33-96	0.66-0.71	-	-	MCQ and Tempered	
Fe 0.2C 0.01Mn	-	-	0.15	-	Thin foil sample	(Apple, Caron et al. 1974)
	-	-	0.20	-	Replica of sample	
Fe 0.2C	-	-	0.20	0.10-1.20	-	(Marder and Krauss 1971)

Table 2.9 – Published martensite lath width data

The number of segments (IAUS) into which the simulation is divided has a significant effect on both computation time and the accuracy of the results (Mujahid and Bhadeshia 1992). The setting of IAUS chosen for simulation was 4000, this is identical to the value in the example input file on the MAP website (MAP website). The publication by Mujahid and Bhadeshia describes in detail the way in which the simulation program uses the variable IAUS to set the simulation timestep and the thickness of the ferrite segments (number of ferrite segments) (Mujahid and Bhadeshia 1992).

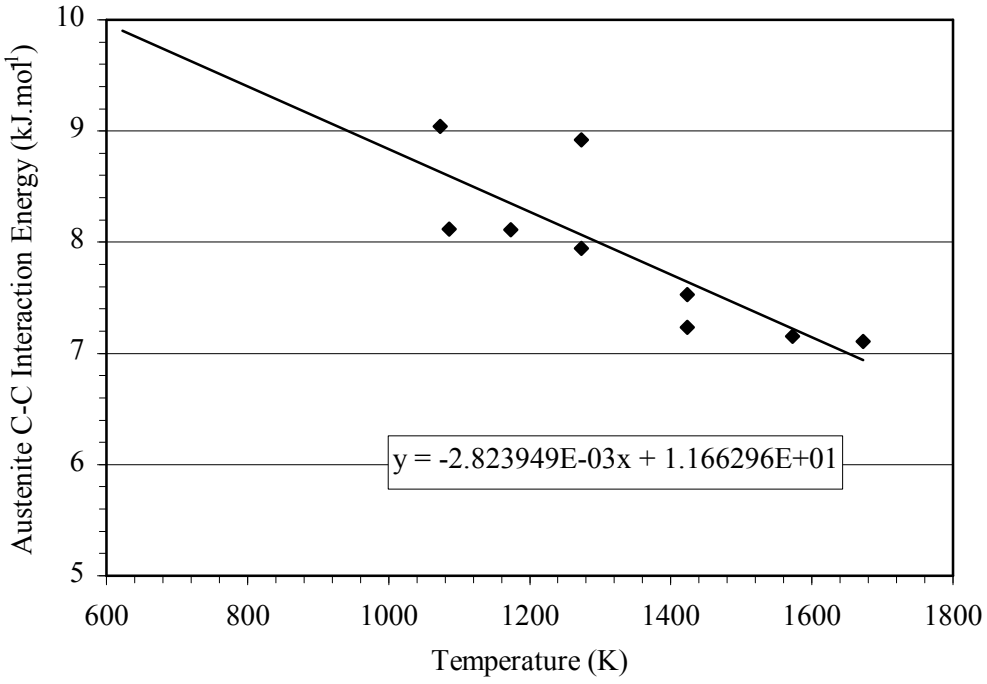

Figure 2.43 – Carbon-carbon interaction energy in austenite

The value for W, the austenite carbon-carbon interaction energy is perhaps the most complex of the inputs required. At the time the simulation code was written the value for W is thought to have been determined by a series of thermodynamics calculations, taking into account alloying effects (Bhadeshia 1981a) (Shiflet, Bradley et al. 1978) (Kinsman and Aaronson 1967) (Uhrenius 1973). However, more recent data indicates that temperature has a significant effect on W (McLellan and Ko 1987); the effect of temperature on W is not believed to have been considered previously. Hence, the data from Mc Lellan and Ko has been plotted (Figure 2.43), and an extrapolation made to the partitioning temperatures of interest. Comparing Figure 1.13 with Figure 2.43 it is apparent that the variation in C-C interaction energy due to temperature appears to be greater than that caused by alloying

additions. Therefore, an extrapolation based on the data plotted in Figure 2.43 has been used in preference to the method previously described by Bhadeshia (Bhadeshia 1981a).

2.11.2 Verification of the compiled simulation code

Prior to using the compiled code for simulation of the partitioning problem, the example input file supplied on the Materials Algorithms Project website (MAP website) was used to ensure that the example output supplied on the same webpage could be faithfully replicated.

2.11.3 Modelling strategy

The partitioning model was initially used to create a comparison with published results obtained using DICTRA (e.g. Figure 1.9 and Figure 1.10), and subsequently to simulate the partitioning behaviour of the alloy prepared for study and reported on herein.

2.12 Accuracy and uncertainty of the experimental measurements

As for all scientific research, the experimental measurements reported herein are subject to inaccuracy and uncertainty. Although every care has been taken to reduce the inaccuracy and uncertainty to the lowest practicable level, it has been considered appropriate to quantify the levels of uncertainty expected to be present.

2.12.1 Carbon concentration measurements

Measurements were normally supplied by the external contractor to either two or three decimal places on the following basis:

0.01-0.099wt% carbon – Measurement to three decimal places

0.1-0.99wt% carbon – Measurement to two decimal places

1.0wt% carbon and greater – Measurement to two decimal places

Occasionally analysis results were supplied to three decimal places for carbon concentrations above 0.099wt%. This was only done in the event that the external contractor had performed additional quality control measurements. The uncertainty in the carbon concentration measurements was stated to be ±5% of the actual value present.

2.12.2 Silicon and manganese concentration measurements

Specimens measured by the external contractor were automatically compared with quality control standards by the X-ray fluorescence (XRF) system software. If for any reason the system was not set up for automatic comparison, the analyst was required to ensure that the measurement results for quality control standards fell within the inter-laboratory uncertainty data for the quality control standards used. When inter-laboratory uncertainty data was not available, the measurement of the quality control standard was required to be correct to a function of 0.04 multiplied by the square root of the reported composition of the quality control standard used ($0.04*\sqrt{c}$).

Those samples measured by EDX were subject to the same uncertainty as described above (EDX measurements were calibrated against samples measured by the external contractor, or in the case of the BCS standards, against the same sample measured by a number of different analysis laboratories).

2.12.3 X-ray and neutron diffraction measurements

The Rietveld refinement software used to process X-ray and neutron diffraction data (GSAS) provides uncertainty data expressed in terms of standard deviation. The level of uncertainty is unique to each data point, and is included in graphs as error-bars indicating plus and minus one standard deviation ($\pm 1\sigma$). Where estimations have been derived from the primary measurements (e.g. carbon concentration from lattice parameter measurements), the standard deviation from the primary measurement has been used to generate error-bars for the estimations. In many cases, and particularly for static measurements, the uncertainty is relatively small and the error-bar is sometimes difficult to distinguish from the symbol marking the position of the datapoint.

Chapter 3
Calibration of EDX standards

Prior to using EDX methods to evaluate the manganese and silicon content of the steel samples which had been prepared, it was considered necessary to calibrate the measurement system. In this chapter the results of the calibration exercise are presented and discussed.

3.1 Experimental results

The data used to correct EDX measurements of manganese and silicon in steel are shown in Figure 3.1 and Figure 3.2 respectively. The silicon dataset has one less datapoint than the manganese dataset; this situation arose because one of the BCS standards did not contain any silicon. The linearity of the relationship between the two methods of measurement is seen to be good in both cases. For manganese, the EDX measurement method is observed to overmeasure, while for silicon, the opposite is true.

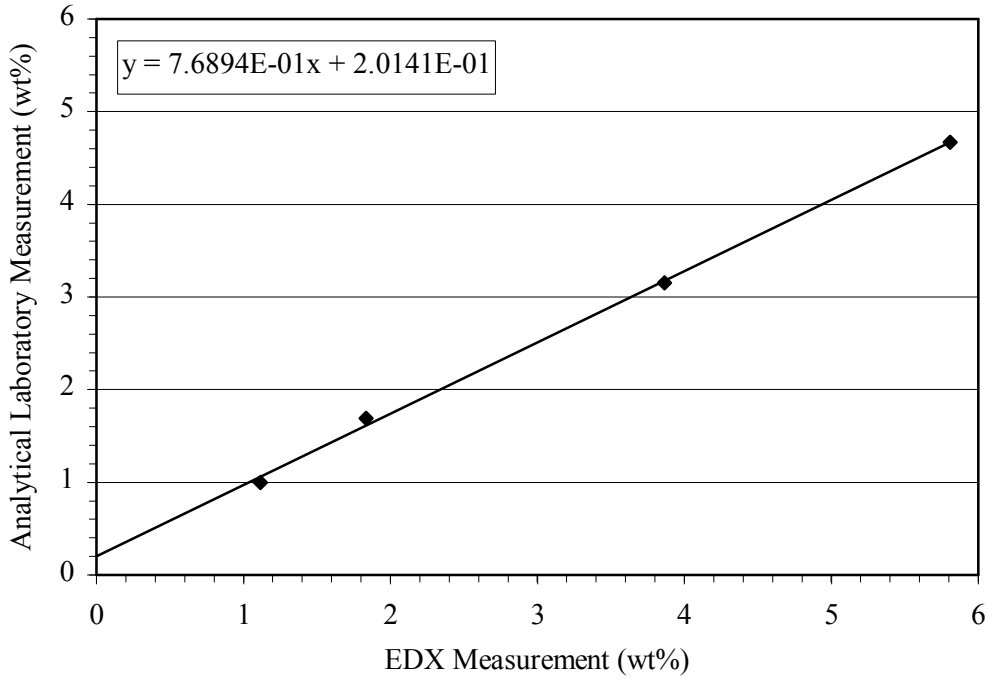

Figure 3.1 – EDX calibration plot for manganese in steel

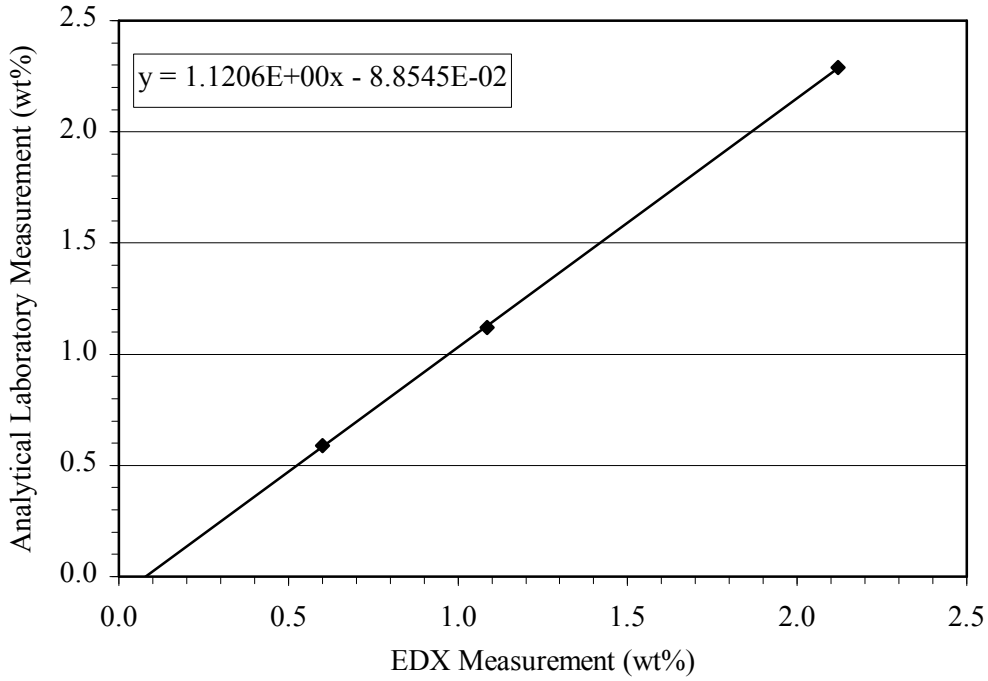

Figure 3.2 – EDX calibration plot for silicon in steel

3.2 Discussion of EDX standard calibration results

For both manganese and silicon, the linearity of the relationships established covers the entire compositional range of interest. The linearity of the relationships gives confidence that the EDX-correction method is capable of producing reliable results.

Chapter 4
Characterisation of the material produced for experimentation

Within this chapter can be found results and discussion of the various materials characterisation procedures which were carried out on the steel produced for Q&P experimentation.

4.1 Chemical analyses of samples

4.1.1 Variation in chemical composition along the length of a sample

Chemical homogeneity along the length of sample 05 is shown in Figure 4.1. All specimens were measured after Q&P heat treatment, except for specimen 0503 (sample slice 3), which was never used for a Q&P experiment and so was measured directly after homogenisation. Homogeneity within sample 05 is observed to be good, hence the material preparation procedures are considered to be adequate for conducting robust and repeatable Q&P experiments.

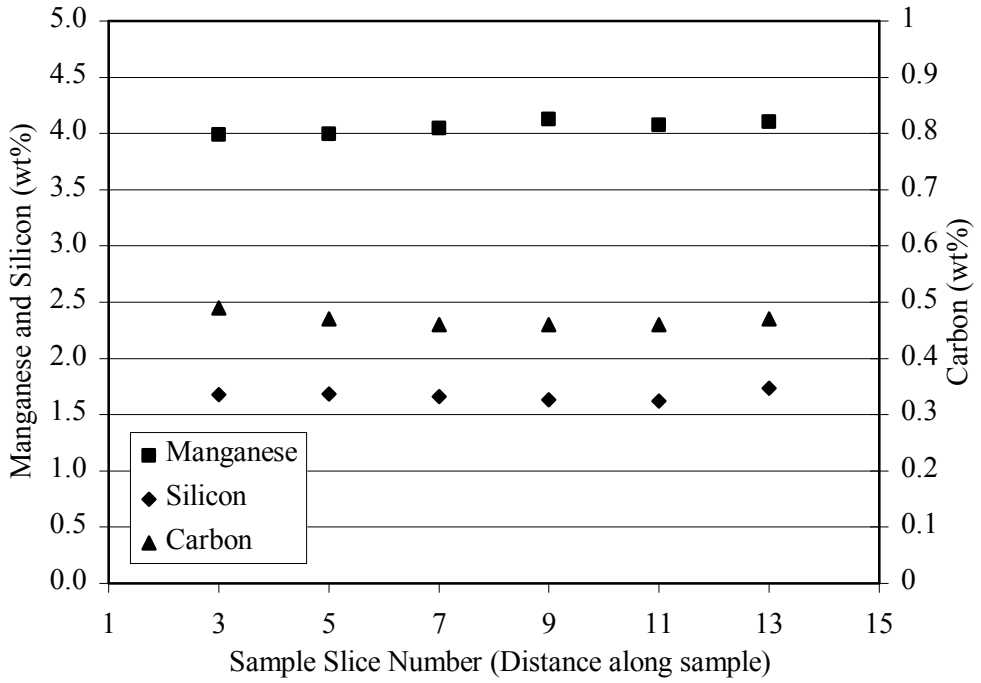

Figure 4.1 – Variation of manganese, silicon and carbon along the length of sample 05.

4.1.2 Chemical composition of samples used for Q&P experimentation

Results for the chemical analyses performed on samples are given in Table 4.1 (full composition determination was only completed for those samples actually used for Q&P experiments). The effect of slight variations in the material preparation procedure (see Section 2.1.2) on chemical composition and sample-to-sample variability is evident e.g. those samples produced as a batch of four have a lower sample-to-sample variation in carbon concentration. One sample was reported to contain a much higher carbon content than any of the other samples (0.935wt%), this was thought to be due to a mistake at the external analysis laboratory.

Sample ID	C (wt%)	Si (wt%)	Mn (wt%)	Production method
05	0.47†	1.67♦	4.06♦	Produced individually
08	0.64†	*	*	
09	0.54†	1.73♦	3.90♦	
12	0.59†	*	*	
19	0.52†	1.34†	4.53†	Produced in a batch of four
20	0.53†	1.73♦	3.96♦	
21	0.55†	*	*	
22	0.53†	1.69♦	3.96♦	
27	0.628†	0.00†	4.53†	Produced in a batch of four
28	0.610†	0.00†	4.63†	
29	0.623†	*	*	
30	0.935†	*	*	
35	0.623†	*	*	Produced in a batch of four
36	0.626†	1.35†	4.63†	
37	0.651†	*	*	
38	0.640†	1.30†	4.57†	

Table 4.1 – Chemical composition of samples for Q&P experimentation († external analysis laboratory measurement, ♦ EDX measurement, * not measured)

4.2 Predicted retained austenite fraction based on chemical composition

Using the chemical composition data in Section 4.1.2, the calculation method of Speer and co-workers (Speer, Streicher et al. 2003) previously described in Section 1.11.1, and illustrated in Figure 1.17 was used to calculate the retained austenite fraction theoretically expected to be present after a Q&P heat treatment. Predictions are presented showing variation in austenite fraction versus initial

quench temperature, assuming full austenitisation and a final quench temperature of 22°C. Figure 4.2 shows calculations for two chemical compositions; the prediction for 0.53wt% carbon and 4wt% manganese is intended to be representative of the earlier samples used for Q&P experimentation (e.g. samples 05 and 09). The second prediction is similar, but with the carbon content increased to 0.63wt% and the manganese content increased to 4.5wt% to reflect the slightly higher alloying content of the later samples (e.g. samples 27 and 38). The linear-formula of Andrews (Andrews 1965) was used to provide martensite start temperatures for input to the Koistinen-Marburger equation. Table 4.2 lists the phase fractions of retained austenite predicted to be present after initial quenching to selected temperatures of interest.

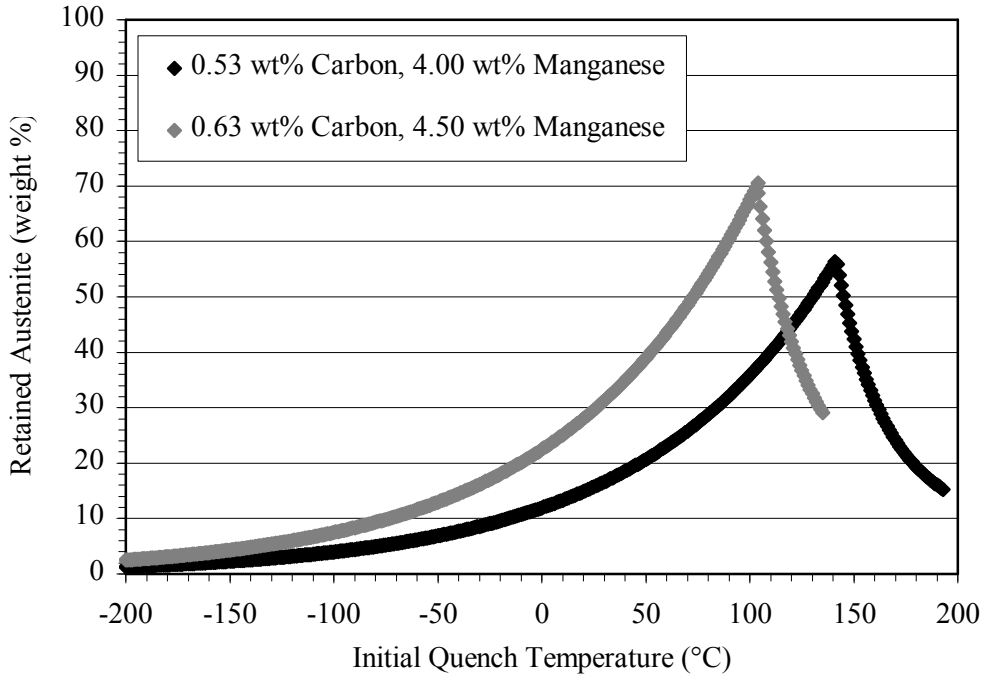

Figure 4.2 – Predicted Q&P behaviour of the steels produced for experimentation

	Predicted Retained Austenite (wt%)	
Initial Quench Temp.	0.53 wt% Carbon	0.63 wt% Carbon
50°C	20.7	39.0
10°C	13.3	25.0
-61°C	6.1	11.5

Table 4.2 – Predicted retained austenite for selected initial quench temperatures (as calculated for Figure 4.2)

4.3 Pre-homogenisation microstructure

The dendritic microstructure of samples as produced in the arc-furnace (i.e. pre-homogenisation) is shown in Figure 4.3. Sample 03 was produced during equipment familiarisation and was of a very similar chemical composition to those samples used for the Q&P experiments reported herein (sample 03 was not actually used for any Q&P heat treatments).

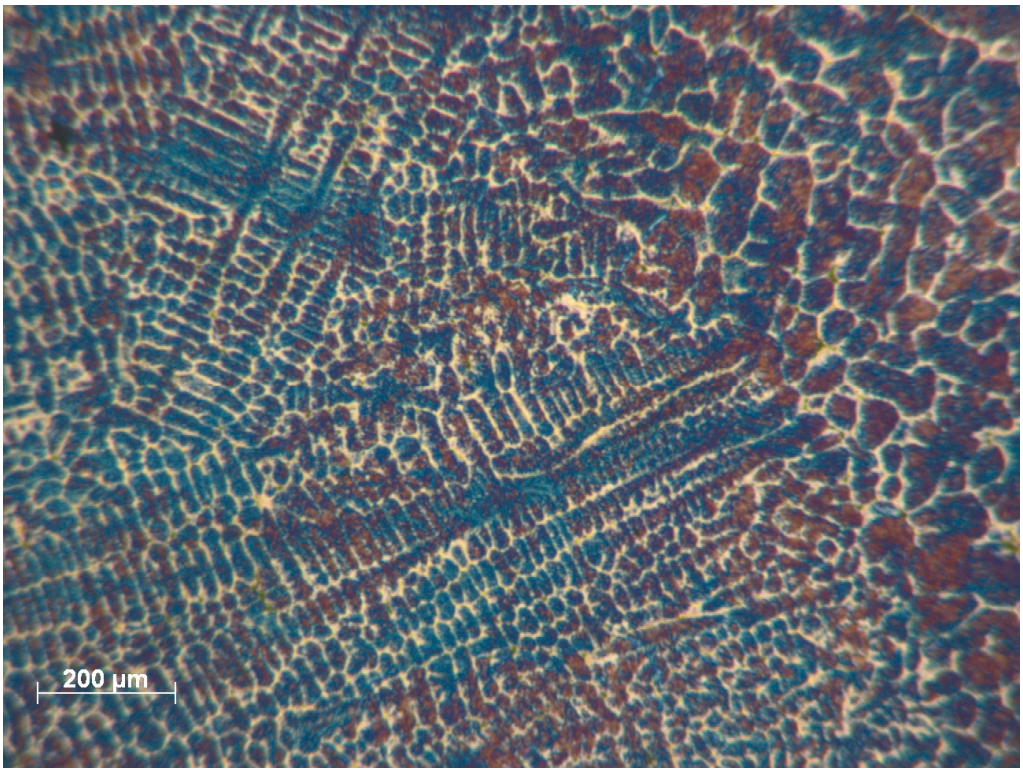

Figure 4.3 – Sample 03, polished and etched in sodium-metabisulphite, showing dendritic structures

4.4 Post-homogenisation microstructure

Light Optical Microscopy (LOM) was utilised to reveal the microstructure of the material prior to application of the experimental Q&P heat treatments. Figure 4.4 and Figure 4.5 illustrate aspects of the structure revealed by LOM. The use of Scanning Electron Microscopy (SEM) has identified the numerous black spots visible in the LOM micrographs as being due to gas porosity (Figure 4.6).

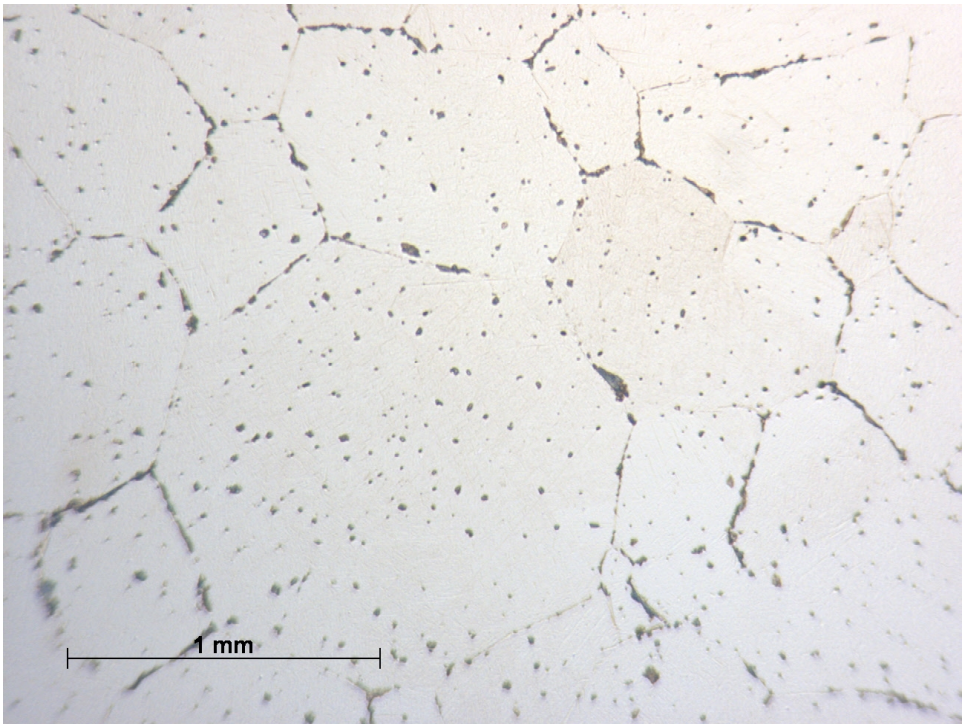

Figure 4.4 – Specimen 2012, lightly etched with Nital to reveal prior austenite grain boundaries

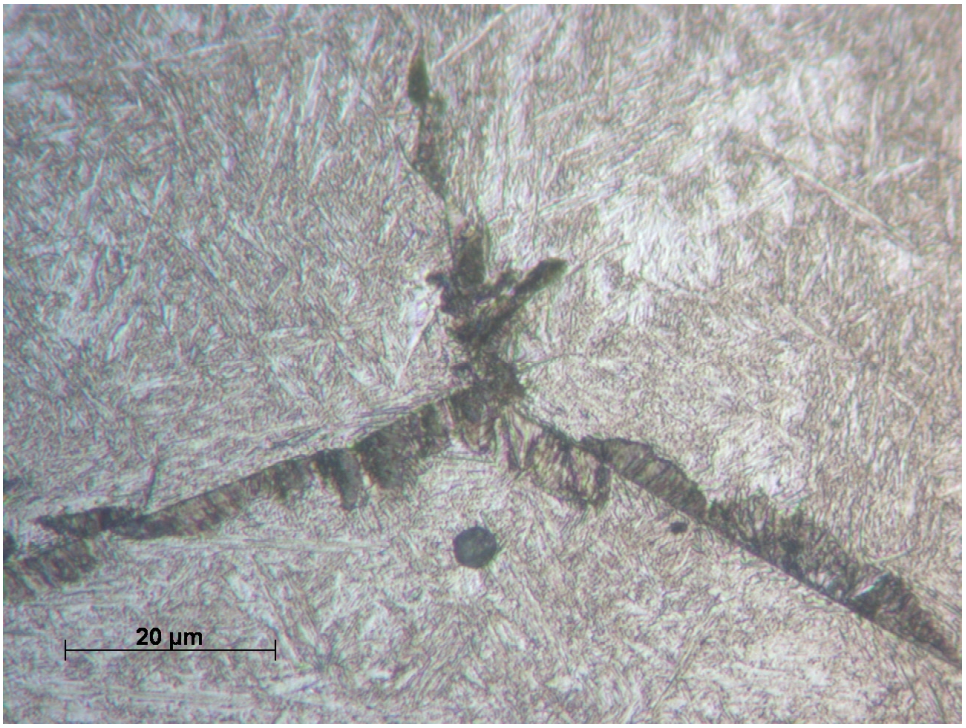

Figure 4.5 – Specimen 2012, etched with Nital to show martensitic microstructure and the triple-point of three prior-austenite grain boundaries

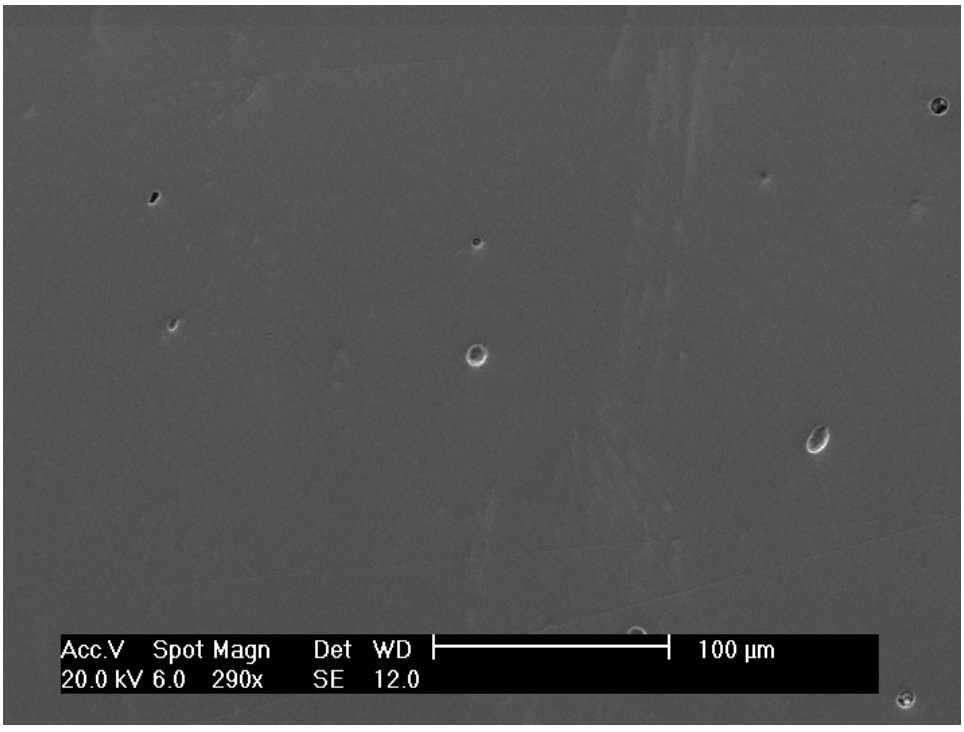

Figure 4.6 – Specimen 2213, polished and examined by SEM to identify the existence of gas porosity.

4.5 Post homogenisation X-Ray Diffraction (XRD) measurements

Two specimens were measured post-homogenisation to investigate the starting microstructure to which the experimental Q&P heat treatment processes would be applied. The diffraction pattern obtained from specimen 0503, together with corresponding Rietveld fit is shown in Figure 4.7.

In an effort to determine whether any carbide structures could be detected in the post-homogenised material, a much 'slower' XRD measurement was carried out on specimen 2012 with the use of a low-background silicon mounting plate to reduce the background count. Although the counting time per data point was approximately five times that used for specimen 0503, inspection of the 2Θ range where carbide peaks would be expected to be at their most prominent (Figure 4.8) did not reveal any evidence of carbides.

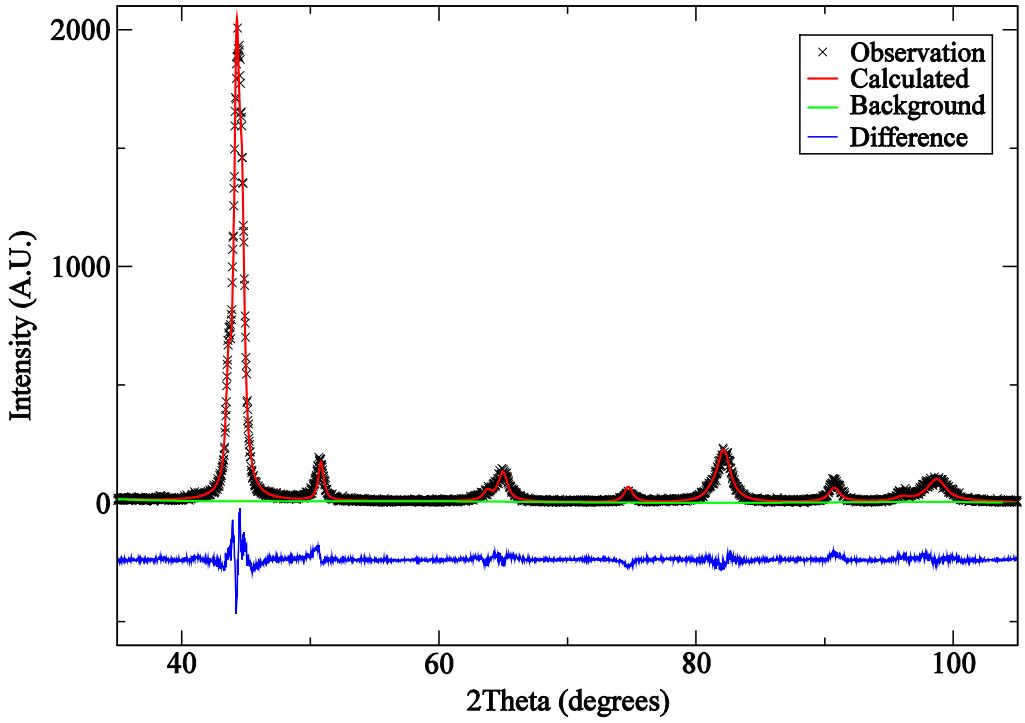

Figure 4.7 – XRD pattern and Rietveld fit for specimen 0503, as homogenised, before any Q&P heat treatment

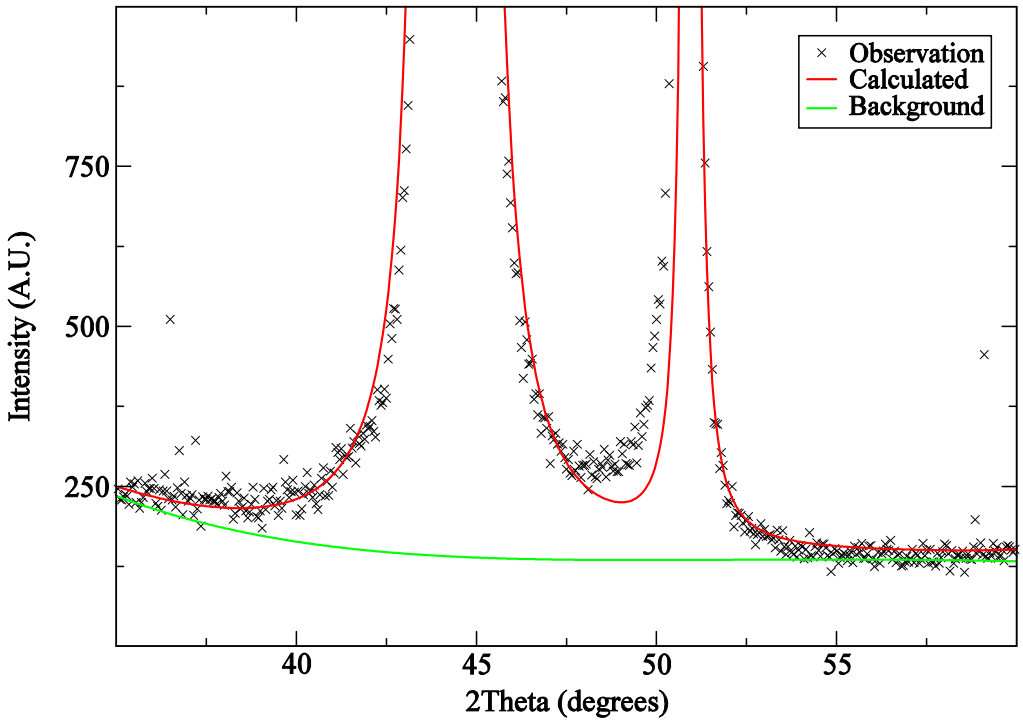

Figure 4.8 – XRD pattern and Rietveld fit for specimen 2012, as homogenised, before any Q&P heat treatment

The lattice parameters and phase fractions for the two specimens in their as-homogenised condition are given in Table 4.3 and Table 4.4 respectively.

Specimen	BCC 'a' (Å)	FCC 'a' (Å)	BCT 'a' (Å)	BCT 'c' (Å)
0503	2.873386	3.592081	2.867791	2.918914
2012	2.876810	3.593503	2.859260	2.936370

Table 4.3 – Structural parameters of specimens in the as-homogenised state

Specimen	BCC martensite fraction	FCC austenite fraction	BCT martensite fraction
0503	0.026604	0.073281	0.900120
2012	0.228360	0.431670	0.339970

Table 4.4 – Phase fractions of specimens in the as-homogenised state

Table 4.3 and Table 4.4 reveal that significant microstructural differences are present between the two as-homogenised specimens. These differences are postulated to have been caused by a slight variation in the homogenisation heat

treatment. Sample 05 was sealed in silica tubing and homogenised on its own while sample 20 was homogenised as a batch of 4 sealed off samples. This difference in the homogenisation heat treatment would be expected to influence the cooling rate after the furnace was switched off by changing the thermal inertia of the system.

4.6 Austenitisation temperature (A_1 and A_3 temperatures)

Upon examining data collected during the heating rate trials (see Section 2.3.1), it became apparent that the heating curves contain useful information with respect to the austenite transformation temperature. Over relatively small temperature ranges the rate of heat transfer from the furnace to the specimen can be considered to be almost constant. Therefore, sudden deviations in the recorded heating rate indicate that the specimen is absorbing or releasing heat internally. An example of this in the form of an inflexion in the heating curve is shown in Figure 4.9.

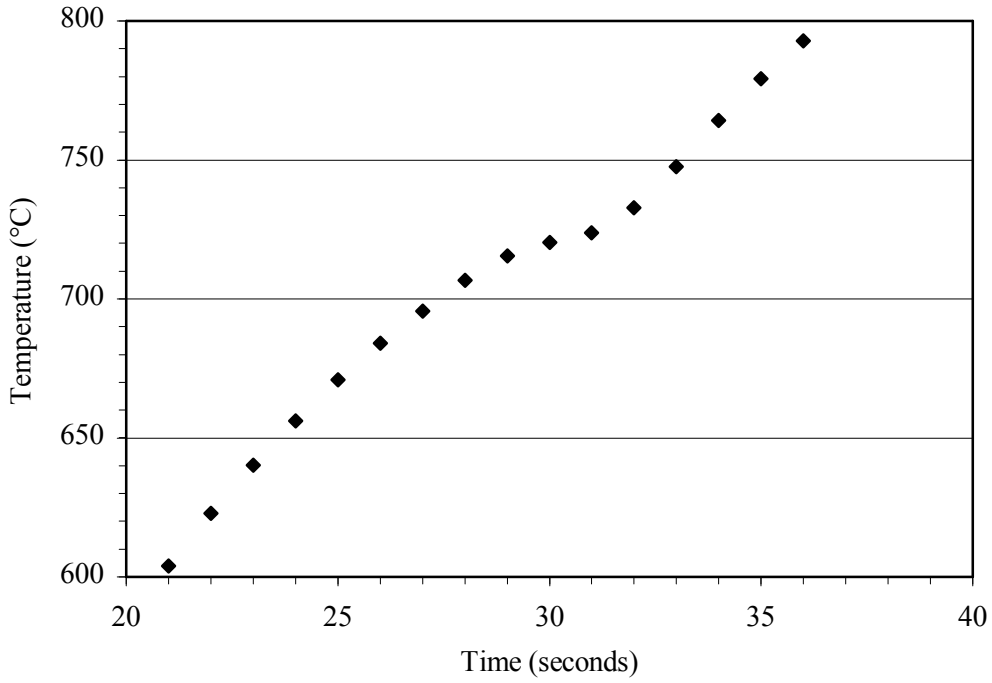

Figure 4.9 – Data from a heating rate trial using specimen 0502 showing the inflexion caused by the alpha to gamma phase change, furnace temperature was 1000°C

The explanation for this observation is that the specimen is undergoing a phase change from the alpha (body centred cubic) structure to the gamma (face centred

cubic) structure. Initially the heating rate falls, this corresponds to the start of the transformation when the free energy of the sample must temporarily increase to overcome the activation energy for the transformation. As the transformation completes, the free energy reduction enabled by the phase transformation causes a rise in the heating rate. Following transformation the heating rate then stabilises to a rate similar to that existing before the transformation.

The effect of the phase change on the specimen heating rate is made more apparent by computing the derivative of specimen temperature with respect to time, and plotting this against specimen temperature. A plot of this type is shown in Figure 4.10 for heating rate trials on specimen 0502 in furnace environments of 800, 1000 and 1200°C.

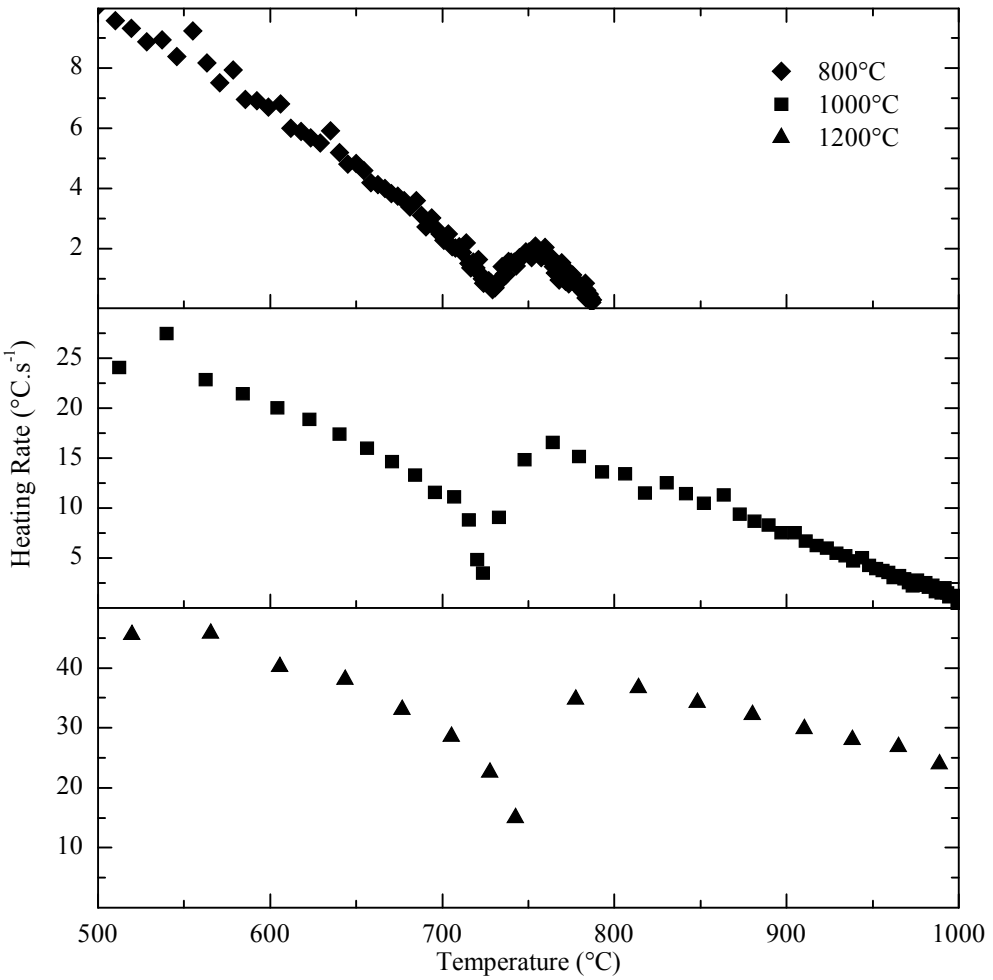

Figure 4.10 – Heating rate data for specimen 0502 showing the difference in response for furnace environments of 800, 1000, and 1200°C

From Figure 4.10 it is observed that for a furnace temperature of 800°C the A_1 point is indistinct; for furnace temperatures of 1000°C and 1200°C austenitisation is estimated to commence at approximately 700°C. The temperature at which austenitisation is complete (the A_3 temperature) is estimated at 760-770°C for furnace temperatures of 800 and 1000°C, and 800°C for a furnace temperature of 1200°C.

Heating rate measurements were also carried out on cylinder format specimens during the austenitise-quench heat treatments carried out prior to neutron diffraction experiments (see Section 2.3.3). The difference in response between the silicon and silicon-free alloy is shown in Figure 4.11; other specimens of both silicon, and silicon-free composition were observed to display the same response. For both of the alloys, a slight upturn in heating rate occurs at around 400°C, and continues up to the point of austenitisation. During austenitisation a significant difference is evident between the two alloys, the silicon-free alloy undergoes a much more abrupt change in heating rate at the point of austenitisation.

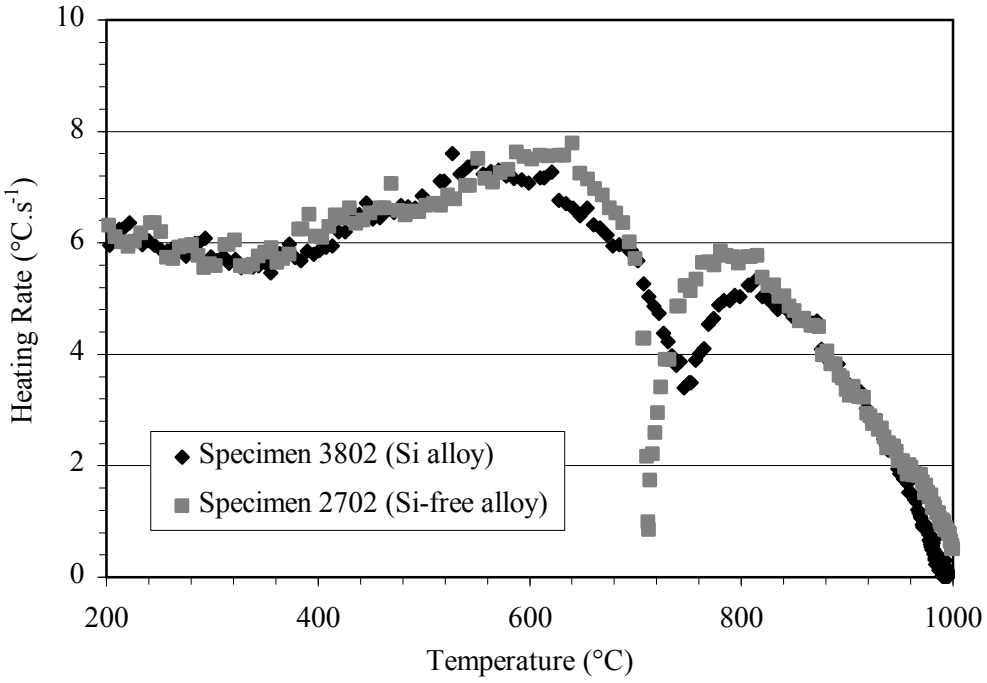

Figure 4.11 – Heating rate comparison for Silicon and Silicon-free material derived during austenitisation of cylindrical specimens for neutron diffraction experiments

4.7 Oxide formation during austenitisation

During the heating rate trials and Q&P heat treatments it was normal for an oxide film to form on specimens during austenitisation at 1000°C. Typically the oxide film formed was relatively thin and parted from the sample during water quenching. Although the temperature selected for austenitisation was 1000°C, some higher temperatures were also investigated during the initial heating rate trials. At a furnace temperature of 1200°C the oxide layer formed on the specimen was significantly changed, a thick, glass-like layer of oxide formed; thermocouple records showed that when this occurred specimen temperature significantly exceeded furnace temperature (Figure 4.12).

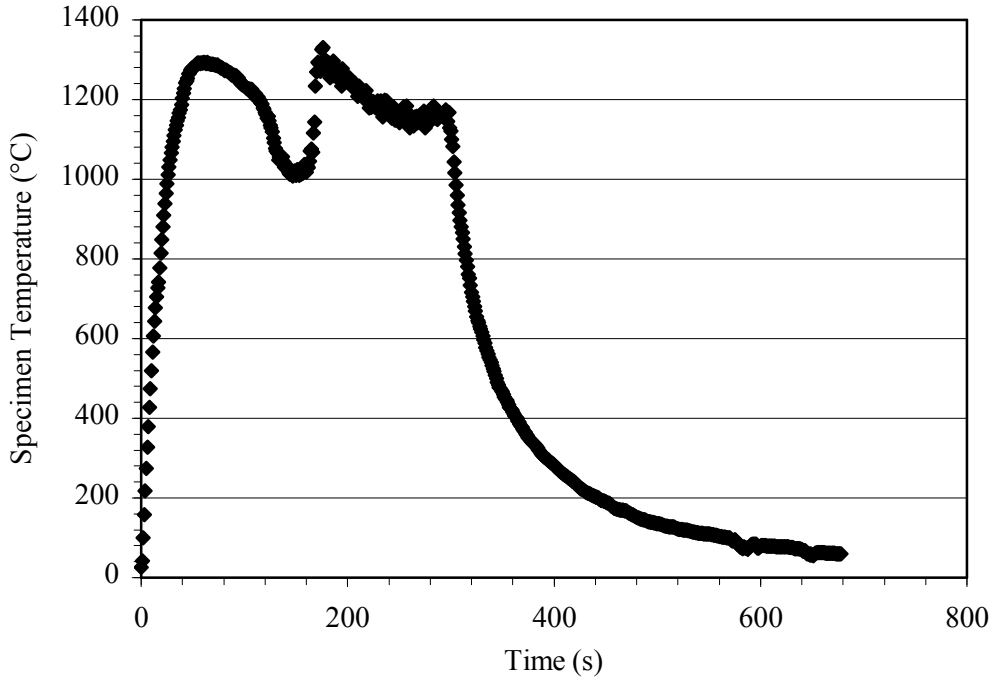

Figure 4.12 – Temperature/time history of specimen 0502 during heating rate trials in a furnace environment of 1200°C

The oxide formed on specimen 0502 during the heating rate trial illustrated in Figure 4.12 was collected and subjected to XRD measurement in order to characterise the oxidation reaction products. As the quantity of oxide available was relatively small, counting statistics were enhanced by mounting on a low-background silicon plate and measuring overnight. Candidates for peak matching were selected from the Chemical Database Service (Fletcher, McMeeking et al. 1996), a structural model for the phases present was then assembled within GSAS (see Section 2.9.7). A Rietveld fit to the XRD pattern is given in Figure 4.13; phase

fractions and original source references for the crystallographic data used in the structural model are listed in Table 4.5.

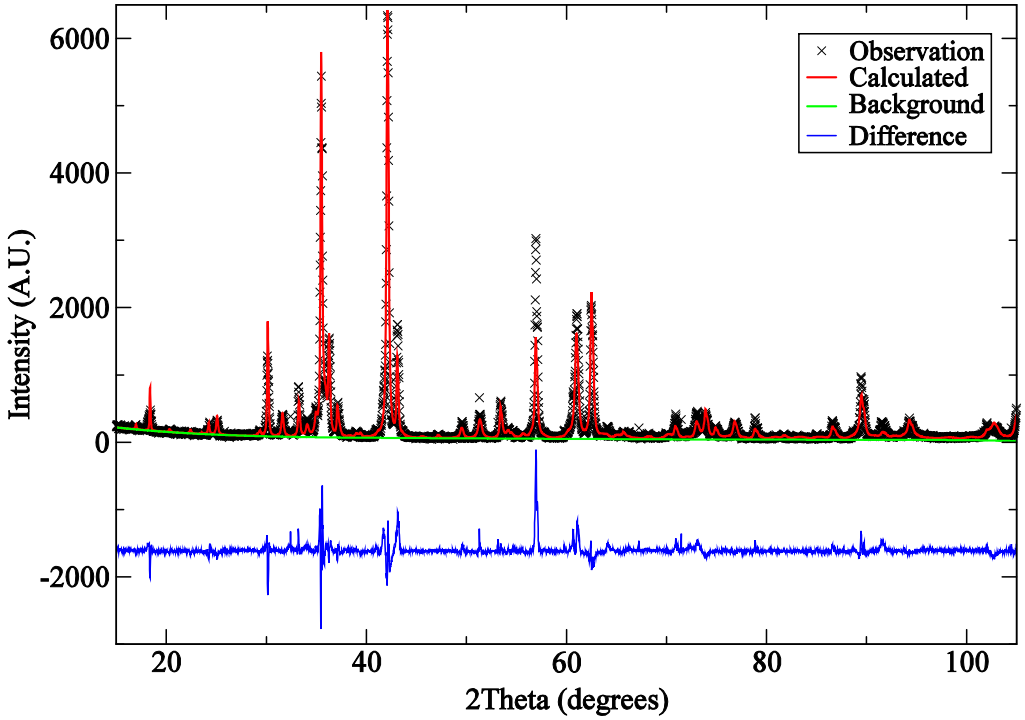

Figure 4.13 – Rietveld fit to the XRD pattern of the oxides formed at 1200°C

Phase	Phase Fraction	Original source of crystallographic data
FeO	0.72476	(Willis and Rooksby 1953)
Fe_3O_4	0.17357	(Okudera and Toyara 1998)
Fe_2O_3	0.036515	(Sadykov, Isupova et al. 1996)
Fe_2SiO_4	0.065154	(Lottermoser, Steiner et al. 2002)

Table 4.5 – Phase fractions in the oxide collected from specimen 0502

4.8 Discussion of characterisation results

4.8.1 Chemical analyses of samples

Measurements along the length of sample 05 found only small variations in chemical composition. This demonstrates that the process of flipping and remelting samples within the arc-furnace, combined with homogenisation in fused silica tubing is effective in equilibrating the distribution of alloying elements throughout a

sample. Therefore, it is considered that the procedures used for material production are sufficiently rigorous to enable robust, repeatable results to be obtained.

All of the samples measured displayed a manganese concentration somewhat below that intended (~4-4.5wt% measured versus 5wt% intended). This disparity is attributed to the high vapour pressure of manganese (compared to iron). During melting the ingot sits in an indentation in a water cooled copper hearth, hence, a large heat input is required at the top surface to completely melt the ingot. Following melting in the arc-furnace, it was frequently observed through the viewing glass that the sample was fuming, therefore, evaporation during melting is thought to be the origin of the manganese shortfall. Silicon concentration measurements varied from approximately 1.3 to 1.7wt% (1.5wt% intended). Samples measured using EDX were consistently found to have higher silicon concentrations than those measured using an external analysis laboratory. A similar but opposite effect is evident for the manganese measurements; this suggests that an inaccuracy could be present in one or both of the measurement methods.

All but one of the samples contained less carbon than intended (0.7wt%); this situation is believed to have arisen as a result of electrostatic scattering of graphite powder by the arc during the initial melting process. The samples used for Q&P experimentation can be divided neatly into two groups; those with ~0.53wt% carbon and those with ~0.63wt% carbon. The difference, 0.53 to 0.63 was probably due to a slight improvement to the arc furnace operational procedure whereby the arc current was kept low until a small pool of molten iron had formed (see Section 2.1.2). By keeping the arc current low until a small pool of molten iron was covering the alloying additions, the electrostatic dispersion of powdered graphite was minimised and the carbon content of the sample was raised. Comparing the earliest melts with later melts it is clear that the practice of cutting up and mixing together four melts, rather than producing melts completely independently of each other has a beneficial effect on the sample to sample variability of carbon. Sample 30 was reported as having a much higher carbon content than any of the other samples, it is considered that this could be due to an error at the external analsysis laboratory. However, no follow up measurement was conducted and so as a precaution this sample was not used for any Q&P experiments.

In summary, chemical composition measurements within a sample and between individual samples have revealed that deviations in chemical composition

exist. However, the differences are relatively small and are considered unlikely to complicate the interpretation of results. The difference in carbon content between earlier and later samples (i.e. ~0.53wt% versus ~0.63wt%) was accommodated by using the lower carbon samples mainly for X-Ray diffraction experiments, and the higher carbon samples exclusively for neutron diffraction experiments.

4.8.2 Predicted retained austenite fraction based on chemical composition

Retained austenite fraction predictions were carried out for comparison with experimental data, discussion relating to these predictions is contained in Chapter 6.

4.8.3 Pre-homogenisation microstructure

The pre-homogenisation microstructure displayed in Figure 4.3 illustrates the importance of applying a homogenisation heat treatment to remove the as-solidified dendritic structure and its associated variations in chemical composition. The dendritic structure is characteristic of a cast ingot in which a significant chilling effect is applied via a mould wall.

4.8.4 Post-homogenisation microstructure

The post-homogenisation microstructure (Figure 4.4) is seen to possess a relatively large grain size after soaking for 96 hours at 1200°C. The homogenisation parameters were chosen to allow diffusion of substitutional solutes during the homogenisation process; a large grain size and the breakdown of the dendritic structure suggests that diffusion of iron (and substitutional atoms) has occurred. The thermodynamic driving force for grain growth comes in the form of reduction of grain boundary area. By reducing grain boundary area the material minimises the amount of free energy that is expended as interfacial energy between adjacent grains. In Figure 4.5, the martensitic appearance of a post-homogenisation furnace-cooled specimen illustrates the high hardenability brought about by the manganese alloying additions. The presence of gas porosity, as identified by SEM in Figure 4.6 explains the appearance of specimen 2012 in Figure 4.4. The source of porosity is considered to have most probably originated from the raw materials. The iron and manganese used were both labelled as having been produced via electrolytic means. Microscopy of the raw materials (not presented here) has revealed that both of these raw materials contained fissures and pockets which could have been a source of gas porosity during the material production process. Gas porosity is not expected to

affect diffraction measurements, however, it could prove troublesome if polishing thin foils for Transmission Electron Microscopy (TEM).

4.8.5 Post homogenisation X-Ray Diffraction (XRD) measurements

Of the two post-homogenisation specimens measured, significant differences in lattice parameters and phase fractions were observed. These differences can most likely be attributed to a detail of the homogenisation heat treatment. Sample 20 (the source of specimen 2012) was homogenised as a batch of four sealed-off samples, while sample 05 was homogenised individually. It is hypothesised that the thermal inertia of having 4 sealed off samples in the tube furnace together was sufficient to significantly alter the measured microstructural parameters. At slower cooling rates it would be expected that some auto-tempering is able to occur. The effects of auto tempering could include stabilisation of austenite by carbon enrichment (as for the one-step Q&P process), an increase in BCC martensite fraction (at the expense of BCT martensite), and relaxation of quenching stresses. The measurements given in Section 4.5 represent an interesting outcome as they suggest that in the alloy being studied it could be possible to achieve a microstructure similar to Q&P simply by austenitisation followed by furnace-cooling. Particularly notable is the retained austenite fraction of well over 40% obtained in specimen 2012 after slow cooling from the austenite field.

4.8.6 Austenitisation temperature (A_1 and A_3 temperatures)

The variation in the A_3 temperature (Figure 4.10) recorded during the heating rate trials has two possible explanations. Firstly, it is well known that at higher heating rates the austenitisation behaviour of steel can be subject to diffusional constraints. This phenomenon is known as criticality, and occurs when the temperature of the specimen increases too fast for equilibrium conditions to be maintained. Hence, when criticality occurs the observation is that completion of austenitisation is retarded relative to the equilibrium austenitisation temperature. The suffixes ‘c’ (critical) and ‘e’ (equilibrium) may be used to denote the conditions under which the A_1 and A_3 temperatures were measured. The second possible explanation for the variation in A_3 temperature concerns the order in which the heating rate trials were carried out. As the trials were carried out in order of increasing furnace temperature it also seems possible that progressive decarburisation of the specimen was responsible for this observation. According to the iron-carbon equilibrium diagram, decarburisation would cause an increase in A_3 temperature.

For the cylindrical specimens (i.e. Figure 4.11) the mass of material was greater than for the disc specimens previously described, consequently the sensitivity to solid state transformations during the heating process was increased. For both the silicon and silicon-free alloy, the upturn in heating rate at approximately 400°C (Figure 4.11) denotes the onset of a solid state transformation which is reducing the free energy of the system, and releasing that energy as heat. This observation could be explained by the formation of carbides, which is an exothermic process and so manifests as a release of heat. At the point of austenitisation a pronounced difference is observed between the silicon and silicon-free alloy. The effect of excluding silicon on the austenitisation behaviour is to cause a much more abrupt internal heat effect at the point of austenitisation. A possible explanation for this difference is that the silicon addition retards the alpha to gamma transformation by increasing the carbon-carbon interaction energy. This effect of silicon, which is illustrated in Figure 1.13, retards diffusional processes by increasing the repulsion between adjacent carbon atoms in the austenite lattice.

4.8.7 Oxide formation during austenitisation

The increase in specimen temperature recorded over and above the furnace temperature could be interpreted as evidence of an exothermic reaction, the oxidation of iron is highly exothermic and so this would seem a likely explanation. The compounds identified in the oxide collected from specimen 0502 shows that iron oxides are the principal constituents, although evidence also exists in the XRD pattern for a reaction product containing silicon. However, while other researchers (Mahieu, Maki et al. 2002) have reported the presence of manganese silicate (Mn_2SiO_4); this investigation has found that iron silicate (Fe_2SiO_4) is the silicon containing phase that is produced when the surface of a silicon-manganese steel is oxidised. By consulting a reducibility diagram (Ellingham 1944), it becomes apparent that at a temperature of 1200°C, manganese is able to reduce FeO and Fe_2O_3 to iron. Therefore, it might reasonably be assumed that manganese oxide and manganese silicate would form in preference to the corresponding iron compounds. However, preferential oxidation of manganese would require diffusion of manganese through the bulk of the steel, a relatively slow process, even at 1200°C. Therefore, for relatively short periods of intense oxidation the formation of iron oxide is logical, as the iron content of the steel is much greater than the manganese content.

Chapter 5
Light Optical Microscopy and Scanning Electron Microscopy of Quenched and Quench and Partitioned samples

This chapter contains details of the examination of as-quenched and quench and partitioned specimens, as assessed by Light Optical and Electron Microscopy (LOM and SEM) methods.

5.1 Experimental results

Light Optical Microscopy (LOM) was one of the first investigative techniques used during the course of the research project. Consequently, most of the LOM work was carried out on specimens processed by the first heat treatment method, using only air furnaces (see Section 2.3.1). LOM micrographs are presented at three different magnifications for specimens that have undergone various different austenitise-quench, and full Q&P heat treatments.

The first set of LOM micrographs show the microstructure of specimen 0509 following austenitisation at 1000°C and quenching to 10°C (Figure 5.1 to Figure 5.3). The same specimen was then partitioned at 500°C for 22 seconds, re-polished and re-etched for further LOM examination (Figure 5.4 to Figure 5.6). Micrographs are also presented for uninterrupted Quench and Partition heat treatments carried out using the same parameters as described for specimen 0509, but for different partitioning times. Specimen 0512 was partitioned for 2 seconds (Figure 5.7 to Figure 5.9), specimen 0514 was partitioned for 92 seconds (Figure 5.10 to Figure 5.12).

Two micrographs are presented for specimens examined using Scanning Electron Microscopy (SEM). Figure 5.13 shows specimen 0914 following austenitisation at 1000°C and quenching to 10°C, a nital deep etch was used to reveal the microstructure. In Figure 5.14, specimen 2212 is depicted following austenitisation at 1000°C, quenching to 10°C and partitioning in a molten salt bath at 500°C for 900 seconds, final quench was to 22°C (also nital deep etched).

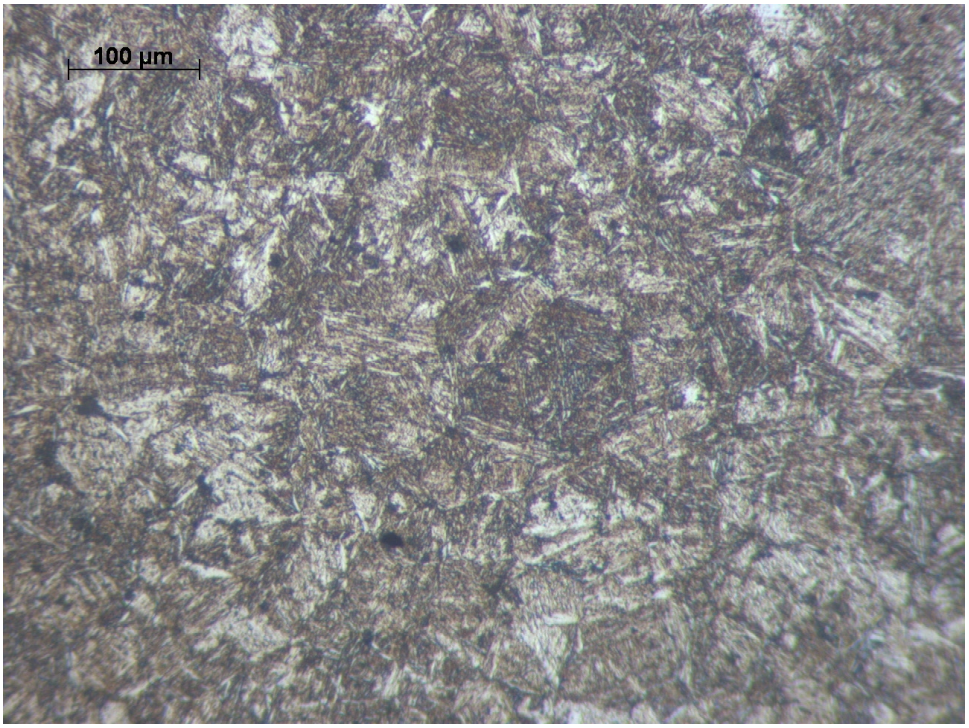

Figure 5.1 - Specimen 0509 following austenitisation at 1000ºC and quenching to 10ºC

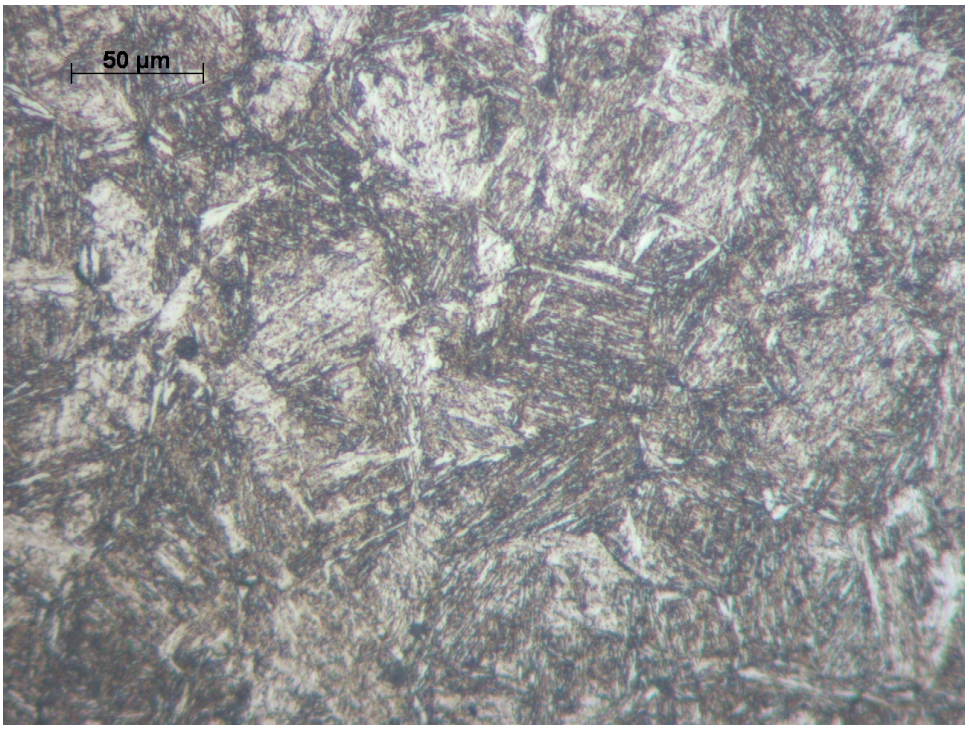

Figure 5.2 - Specimen 0509 following austenitisation at 1000ºC and quenching to 10ºC

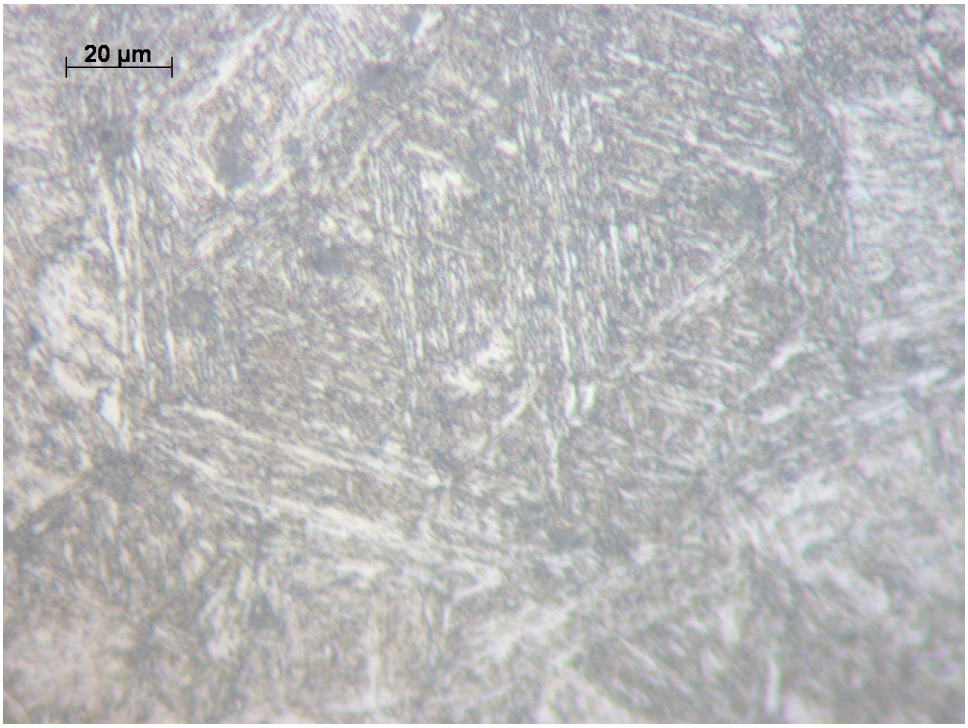

Figure 5.3 - Specimen 0509 following austenitisation at 1000ºC and quenching to 10ºC

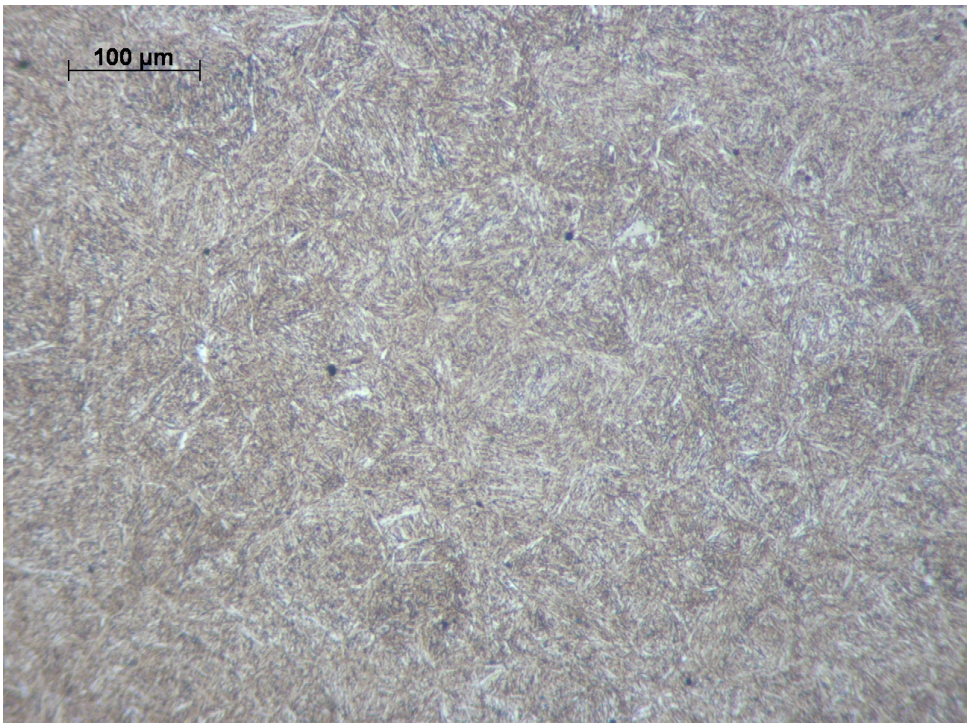

Figure 5.4 - Specimen 0509 following quenching (see Figure 5.1 caption) and partitioning at 500ºC for 22 seconds

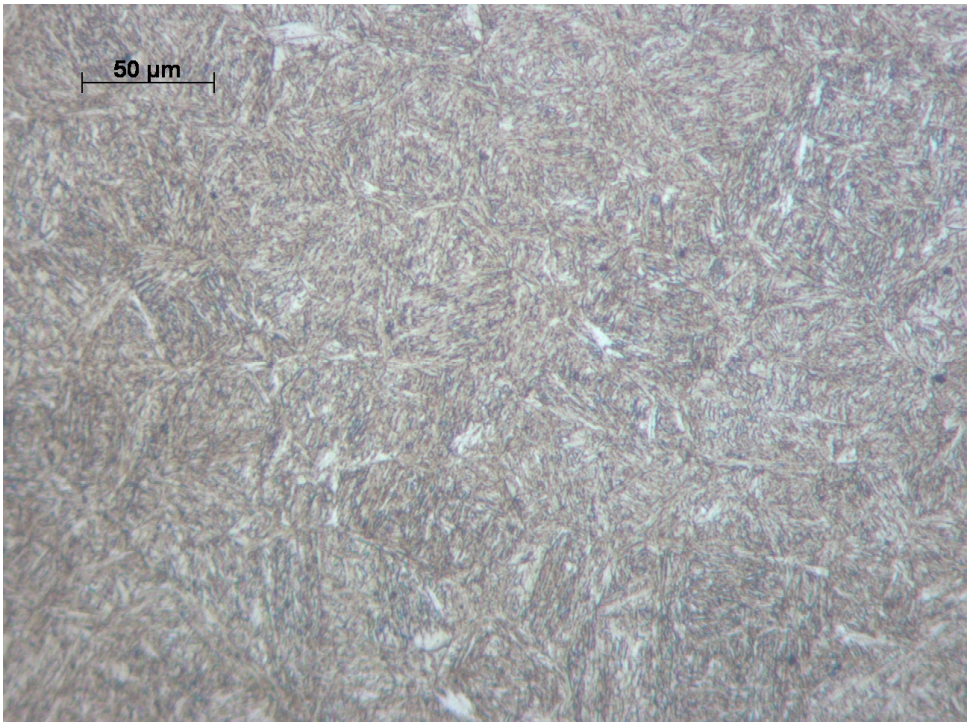

Figure 5.5 - Specimen 0509 following quenching (see Figure 5.1 caption) and partitioning at 500ºC for 22 seconds

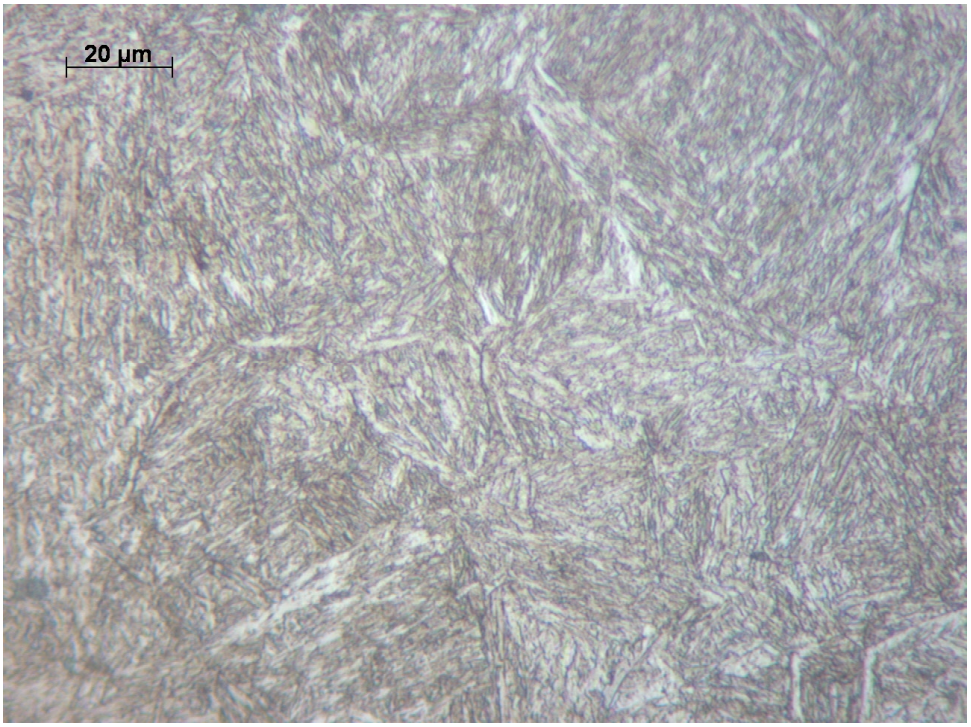

Figure 5.6 - Specimen 0509 following quenching (see Figure 5.1 caption) and partitioning at 500ºC for 22 seconds

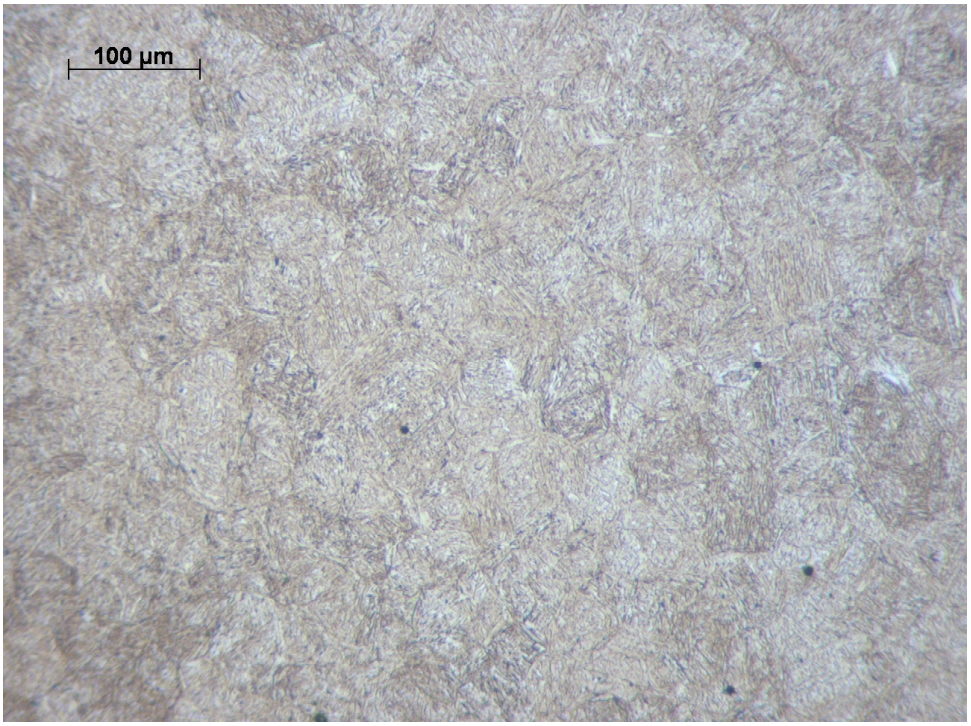

Figure 5.7 - Specimen 0512 following austenitisation at 1000ºC, quenching to 50ºC and partitioning at 500ºC for 2 seconds

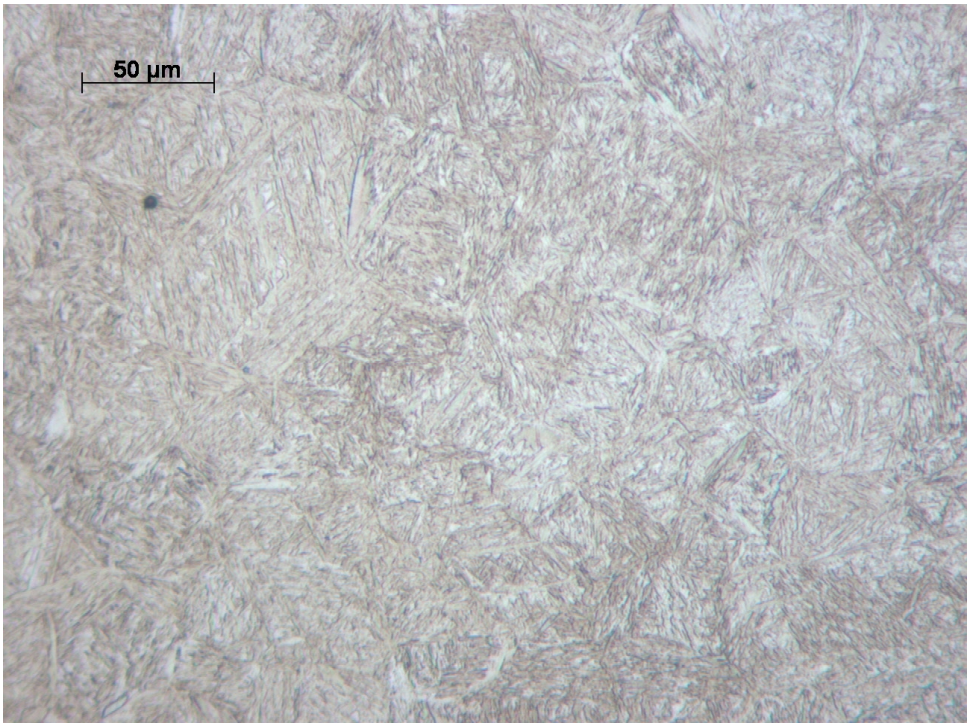

Figure 5.8 - Specimen 0512 following austenitisation at 1000ºC, quenching to 50ºC and partitioning at 500ºC for 2 seconds

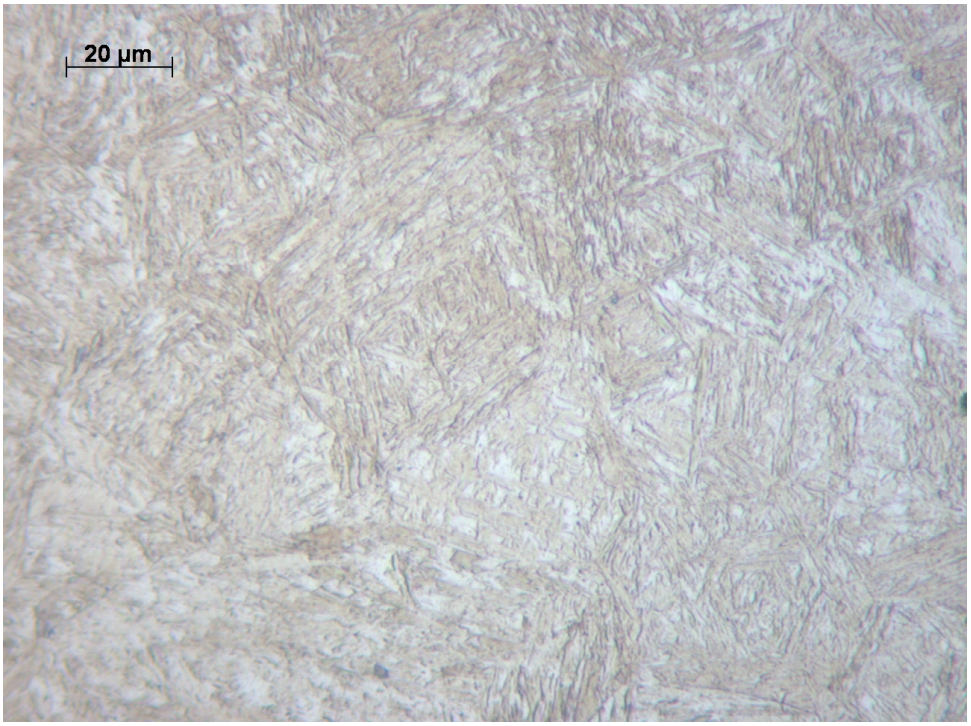

Figure 5.9 - Specimen 0512 following austenitisation at 1000ºC, quenching to 50ºC and partitioning at 500ºC for 2 seconds

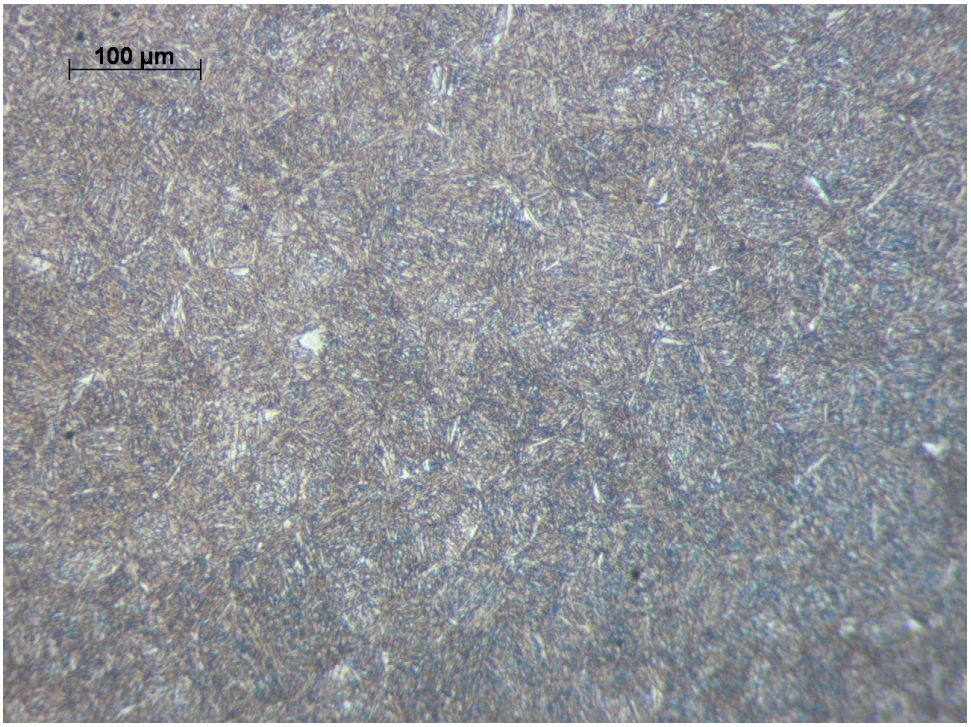

Figure 5.10 - Specimen 0514 following austenitisation at 1000ºC, quenching to 50ºC and partitioning at 500ºC for 92 seconds

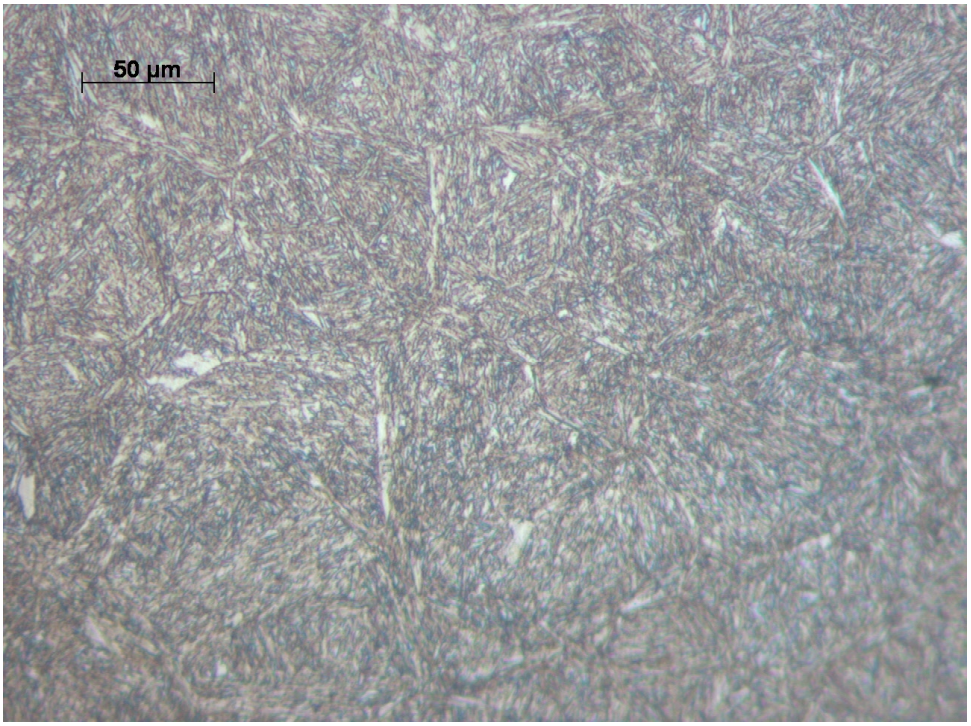

Figure 5.11 - Specimen 0514 following austenitisation at 1000ºC, quenching to 50ºC and partitioning at 500ºC for 92 seconds

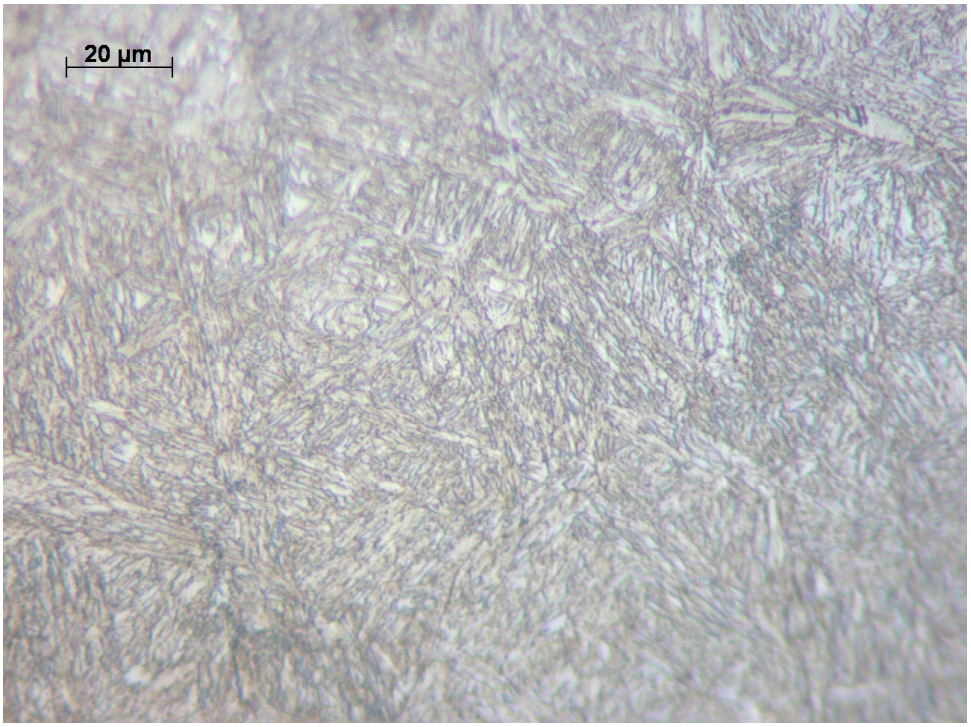

Figure 5.12 - Specimen 0514 following austenitisation at 1000ºC, quenching to 50ºC and partitioning at 500ºC for 92 seconds

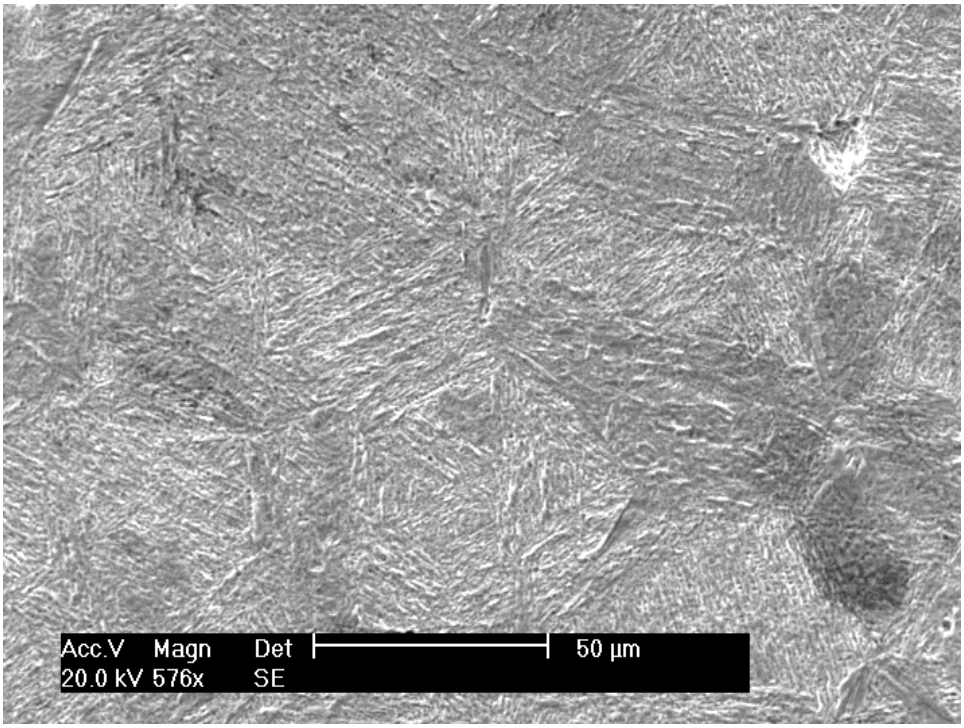

Figure 5.13 - Specimen 0914, austenitised at 1000°C for 300 seconds, quenched to 10°C; nital deep etch

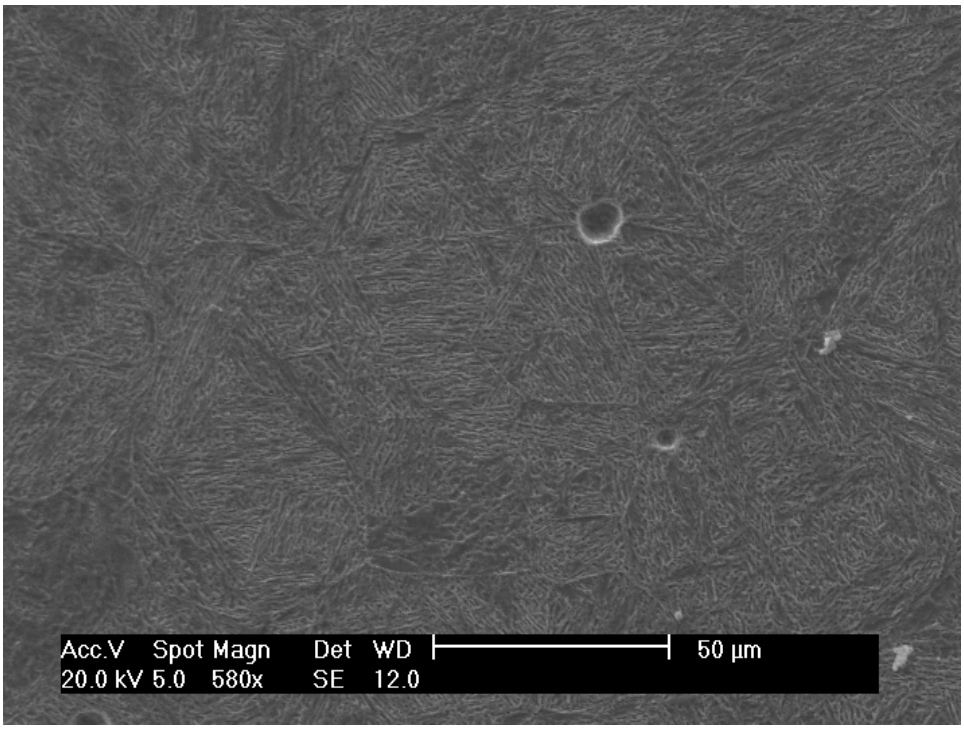

Figure 5.14 – Specimen 2212, austenitised at 1000° for 300 seconds, quenched to 10°C, and partitioned at 500°C for 900 seconds, nital deep etch

5.2 Discussion of results

Comparing the micrographs in this chapter to those of the previous chapter (e.g. Figure 4.4 in Section 4.4), it is apparent from the prior austenite grain boundaries that a significant reduction in grain size has occurred during the course of the experimental austenitise-quench and Q&P heat treatments. The change in prior austenite grain size provides evidence that re-austenitisation has occurred, followed by fresh martensite formation during quenching.

The micrographs of austenitise-quench specimens have a martensitic appearance while those of partitioned specimens appear similar, but with a lightly tempered look. In the LOM micrographs, some of the specimens pictured had been quenched to 50°C and some to 10°C. The difference in quenching temperature should logically result in a change in phase fractions (see Figure 4.2 and Table 4.2 in Section 4.2); however, such a difference is not readily apparent in the micrographs. As polishing is essentially a process involving cold work, it is considered that the observed austenite phase fraction may have been modified by a TRIP effect (the effect of polishing on austenite phase fraction is comprehensively discussed in Chapter 6). No carbides are visible in any of the micrographs, however, except at very long partitioning times, carbides would be expected to be relatively fine, and so may not be visible except by techniques such as Transmission Electron Microscopy.

Chapter 6
Diffraction measurements on quenched specimens

In this chapter, the results obtained using X-ray and neutron diffractometry techniques are presented and discussed for specimens which were measured in the as-quenched state. The results are compared to previously published data and theories; some complications pertaining to interpretation of diffraction data from quenched steel are also discussed.

6.1 X-ray diffraction measurements

6.1.1 Lattice parameters

Results are presented for specimens austenitised at 1000°C for 5 minutes and quenched into water at 10°C; specimens were cut from samples 05, 09, 19 and 20. Figure 6.1 illustrates issues already described in Section 2.9.8, whereby an additional BCC phase may be inserted into the structural model to account for room temperature tempering. Lattice parameter measurements for austenite are shown in Figure 6.2.

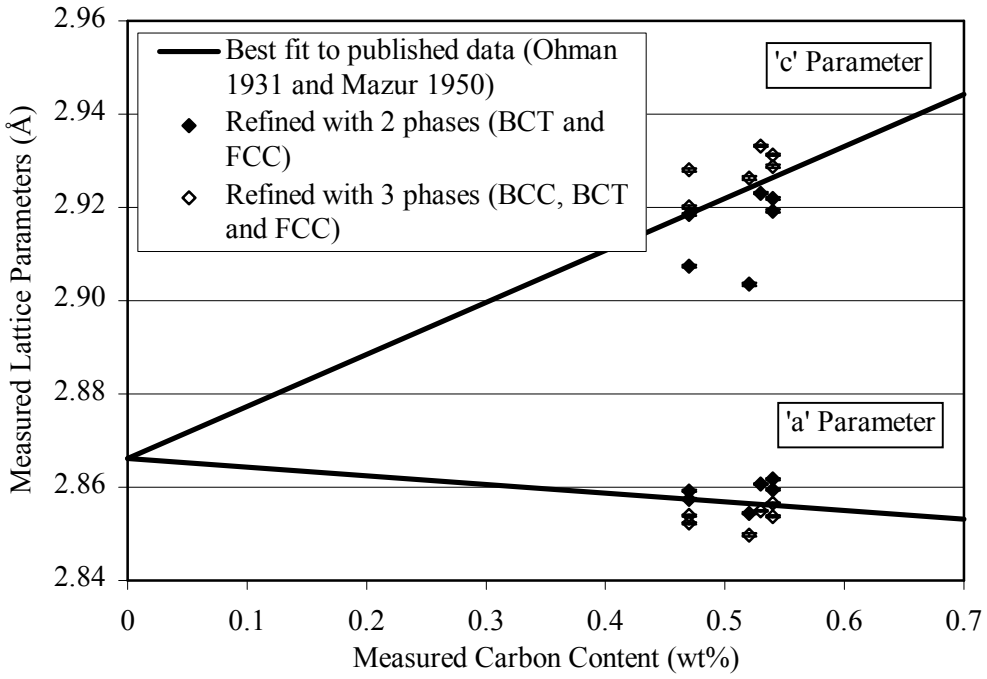

Figure 6.1 – Comparison of X-ray diffraction measurements of martensite lattice parameters with published data (see Figure 2.18)

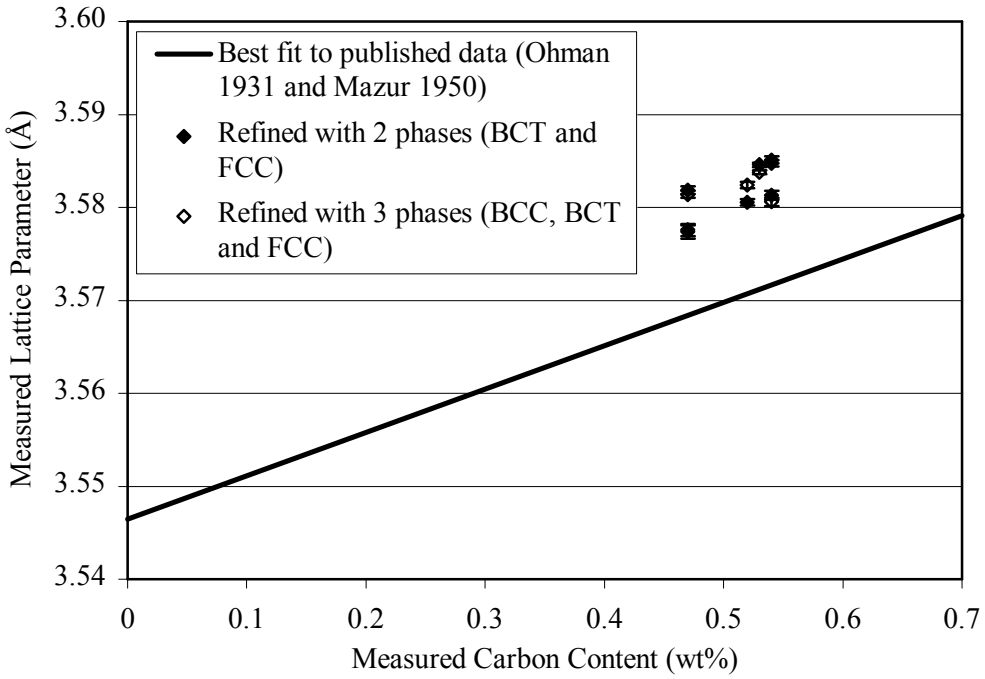

Figure 6.2 – Comparison of X-ray diffraction measurements of retained austenite lattice parameter with published data (see Figure 2.19)

Lattice parameter measurements for retained austenite (Figure 6.2) differ from the published data of Ohman and Mazur, although unlike the measurements for martensite, the structural model used to interpret the diffraction data (two phases or three phases) has little effect on the values obtained.

6.1.2 Retained austenite fraction

Figure 6.3 illustrates the differences between retained austenite fraction as measured by X-ray diffraction, and predictions made using the Koistinen-Marburger formula (see Section 4.2). Austenite phase fraction is observed to vary significantly between the different specimens measured, and in all cases is below the prediction. However, the shortfall in measured austenite phase fraction is not unexpected as the specimen preparation method is anticipated to result in transformation of austenite to martensite under certain conditions (see Section 1.12 and 2.9.1). To investigate the effect of specimen preparation (i.e. mechanical polishing) a series of measurements were made on specimen 0914 following mechanical and electropolishing (Figure 6.4). The order in which the measurements were made is as indicated in the graph legend (top to bottom), the results suggest that removal of some or all of the deformed surface layers increases the measured austenite phase fraction.

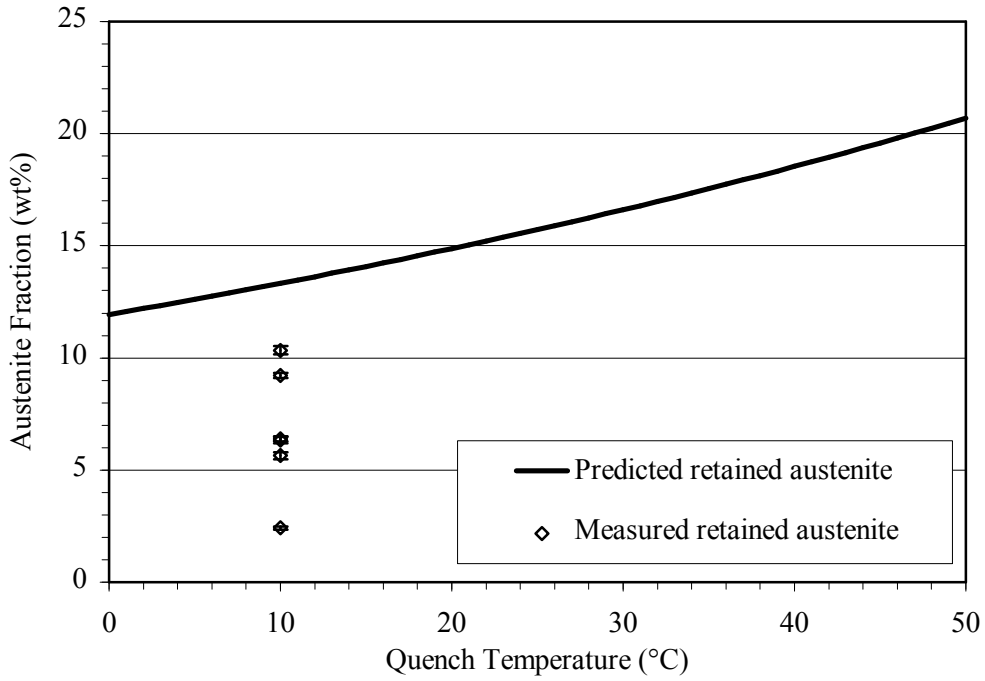

Figure 6.3 – Predicted versus measured retained austenite fraction for several different specimens polished to 1μ and measured using X-ray diffraction

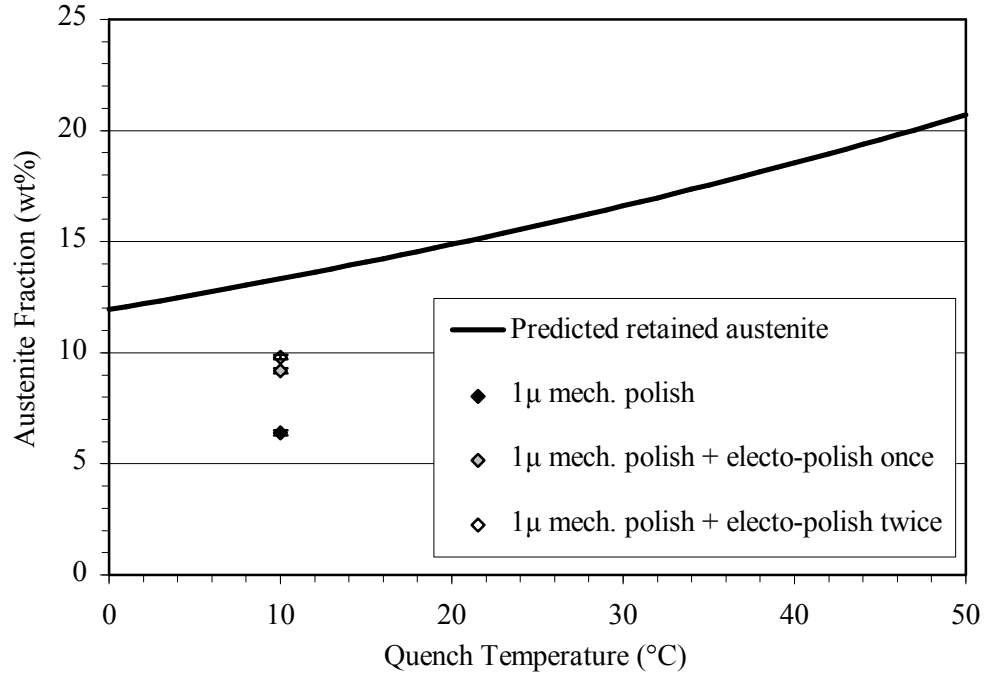

Figure 6.4 – Predicted versus measured retained austenite fraction for specimen 0914 polished to 1μ, electropolished and measured using X-ray diffraction

6.2 Neutron diffraction measurements

Most of the results presented are for specimens austenitised at 1000°C and quenched into water at 10°C, although in two cases an additional quench to -61°C in methanol was applied immediately after the 10°C water quench (see Section 2.3.3). Specimens were cut from samples 09, 22, 27, 28, 36, and 38; the specimens cut from samples 09 and 22 were of disc format, the remainder were all of cylindrical format (see Section 2.2 and 2.3 for details of the sectioning process and heat treatment methods applied to the different specimen formats).

6.2.1 Lattice parameters

Lattice parameter measurements for martensite and retained austenite are compared with published data in Figure 6.5 and Figure 6.6 respectively. For the two-phase structural model, scatter in the martensite ‘c’ lattice parameter measurements is reduced compared to the X-ray diffraction results presented in Figure 6.1.

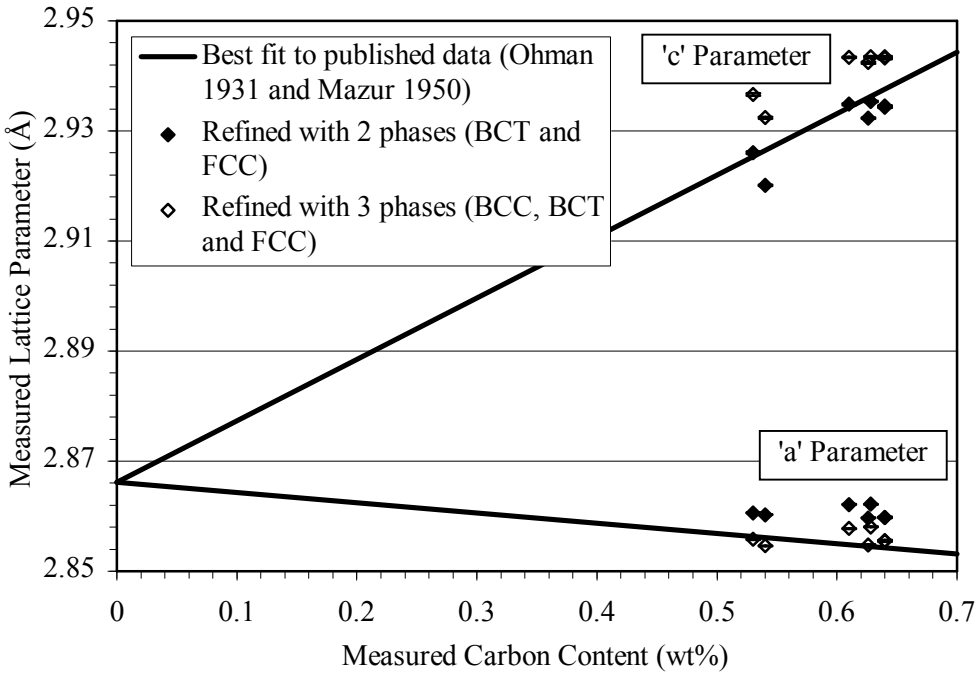

Figure 6.5 – Comparison of HRPD measurements of martensite lattice parameters with published data (see Figure 2.18)

The addition of a BCC phase (i.e. a total of three phases) gives a similar level of scatter in the martensite measurements, but has the effect of increasing the differential between the martensite ‘a’ and ‘c’ lattice parameter values compared to

the two-phase structural model. In common with the X-ray diffraction results, retained austenite lattice parameter measurements are somewhat higher than previously published values, and are unaffected by the choice of structural model (i.e. two or three phases).

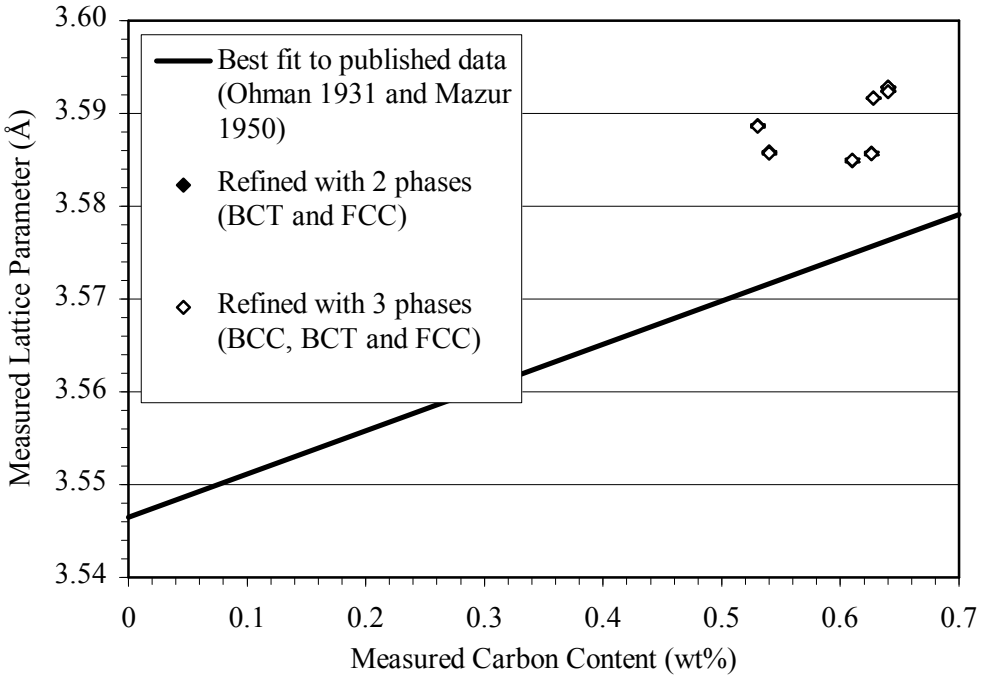

Figure 6.6 – Comparison of HRPD measurements of retained austenite lattice parameter with published data (see Figure 2.19)

6.2.2 Retained austenite fraction

Retained austenite fraction measurements for two slightly different compositions are compared with predictions (see Section 4.2) in Figure 6.7 and Figure 6.8. For both of these comparisons, the measurements are somewhat closer to the predictions than for the X-ray diffraction data presented in Section 6.1.2. Figure 6.9 replicates the data already presented in Figure 6.4, but with the addition of a neutron diffraction measurement. As for Figure 6.4, the measurements were completed in the order indicated in the graph legend (top to bottom). The results presented in Figure 6.9 suggest that surface effects (i.e. transformation from austenite to martensite) are present in X-ray diffraction measurements even after electropolishing.

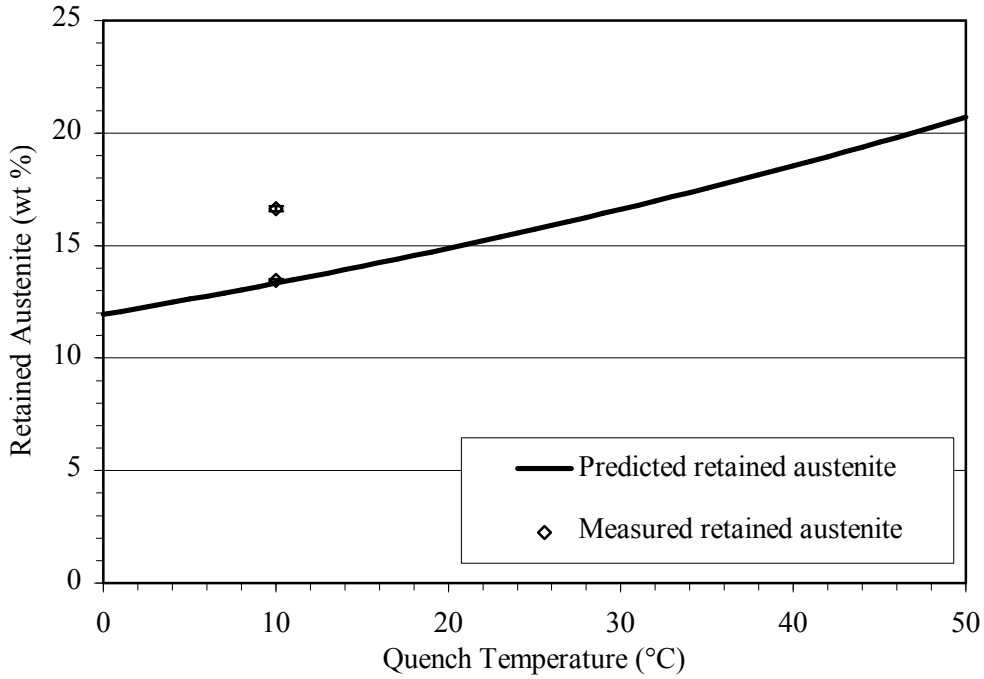

Figure 6.7 – Predicted versus measured austenite fraction for two different specimens of nominal composition 0.53C-4.00Mn measured using HRPD

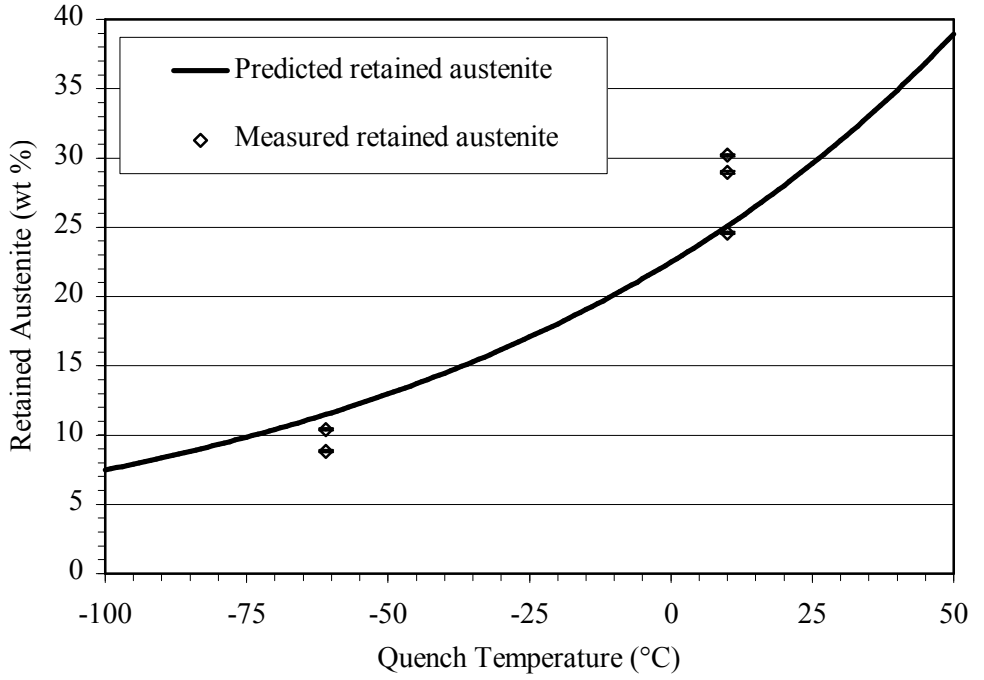

Figure 6.8 – Predicted versus measured austenite fraction for several different specimens of nominal composition 0.63C-4.50Mn measured using HRPD

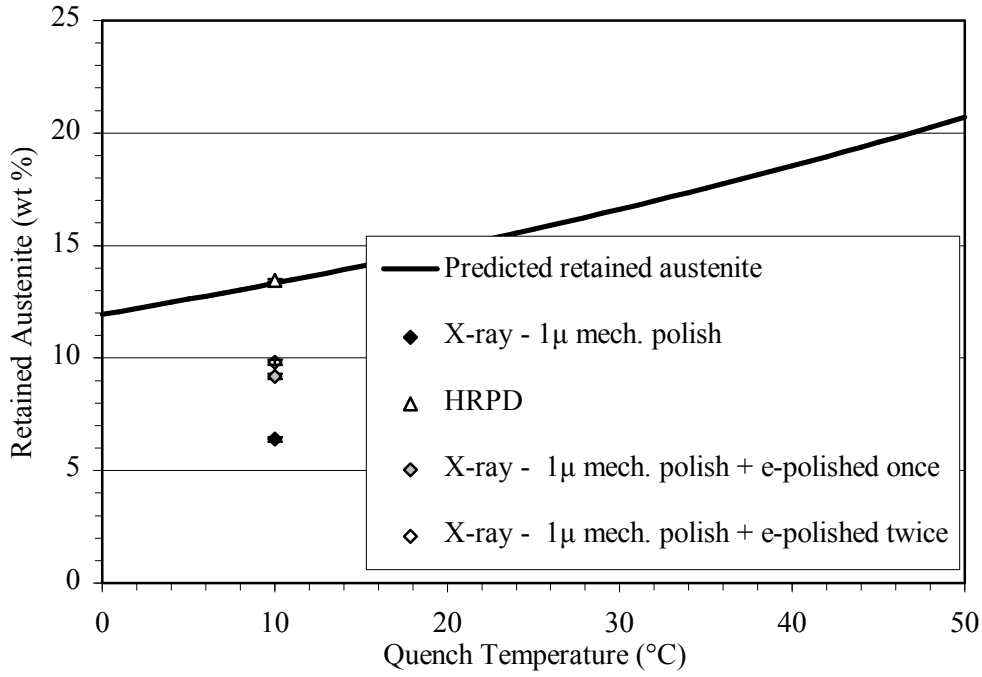

Figure 6.9 – Predicted versus measured retained austenite fraction for specimen 0914 measured using X-ray and neutron diffraction techniques

6.2.3 Relationships between austenite fraction, austenite lattice parameter and lattice strain

In this project, the martensite transformation process is observed to produce relationships between untransformed austenite fraction, austenite lattice parameter and lattice strain. The correlations between untransformed austenite fraction, austenite lattice parameter and austenite lattice strain are illustrated in Figure 6.10 and Figure 6.11 respectively. In Figure 6.12 it is seen that a similar relationship also applies to untransformed austenite fraction and martensite lattice strain. By including an additional BCC phase in the structural model, it is hypothesised that the variability caused by room temperature tempering of martensite is 'absorbed'. Hence, Figure 6.13 shows a similar correlation to Figure 6.12, but with significantly reduced scatter in the results. In Figure 6.12 and Figure 6.13, one specimen (0914) was initially subjected to polishing and X-ray diffraction measurement, a delay of around one month then occurred before this specimen was measured using HRPD. The lower lattice strain in this specimen suggests that the as-quenched structure is relatively sensitive to low-level heating (during polishing) and standing time at room temperature.

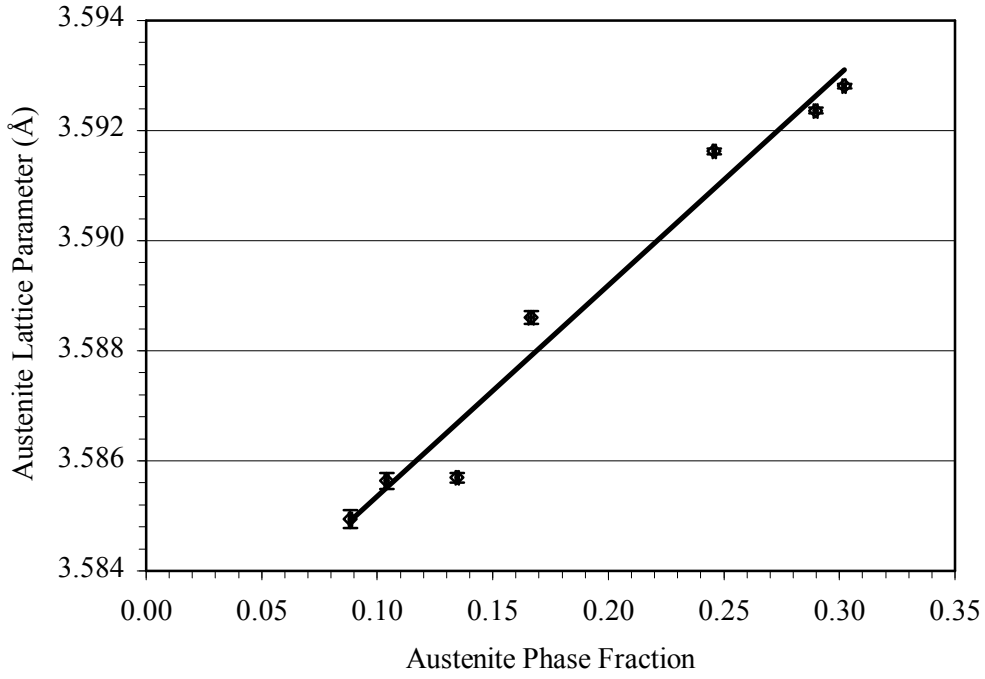

Figure 6.10 – Correlation between austenite lattice parameter and untransformed austenite fraction determined using HRPD

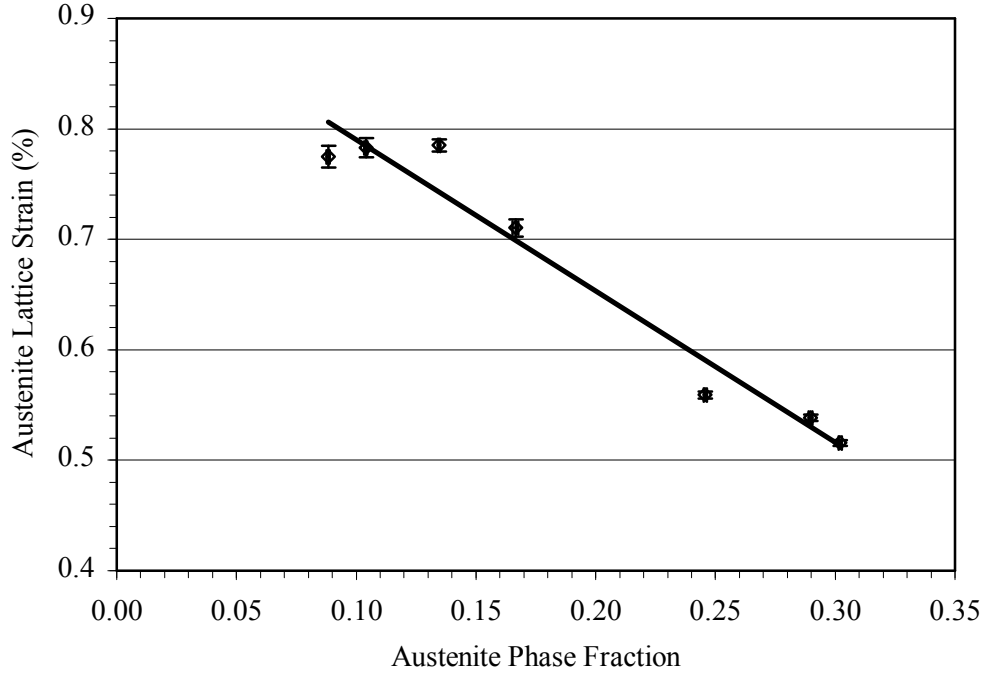

Figure 6.11 – Correlation between austenite lattice strain and untransformed austenite fraction determined using HRPD

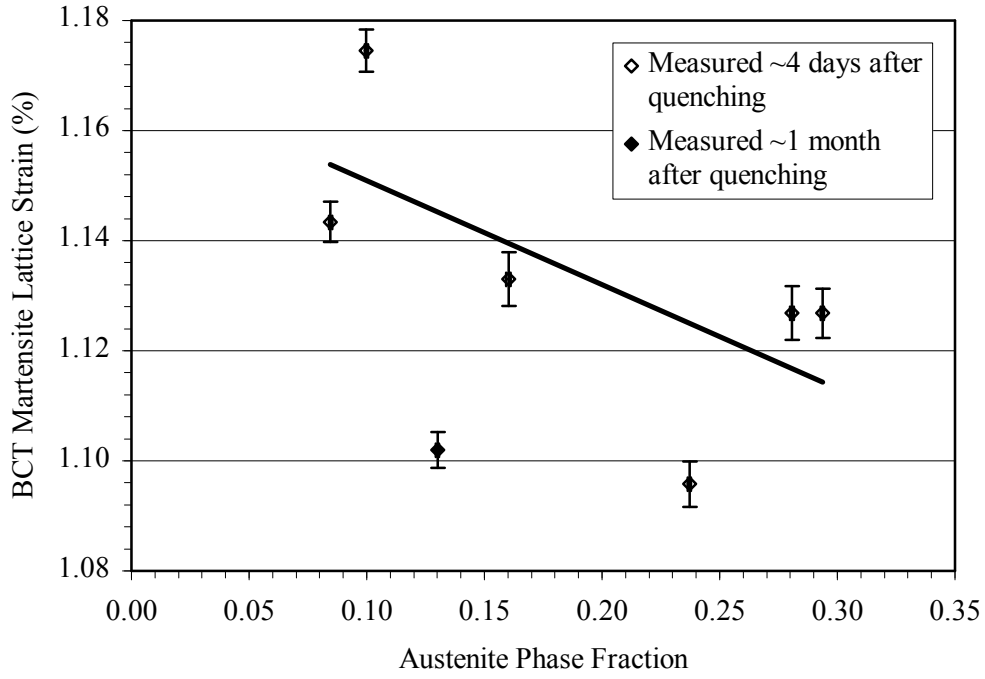

Figure 6.12 – Correlation between martensite lattice strain and untransformed austenite fraction determined using HRPD data with a structural model consisting of 2 phases (BCT martensite and FCC austenite)

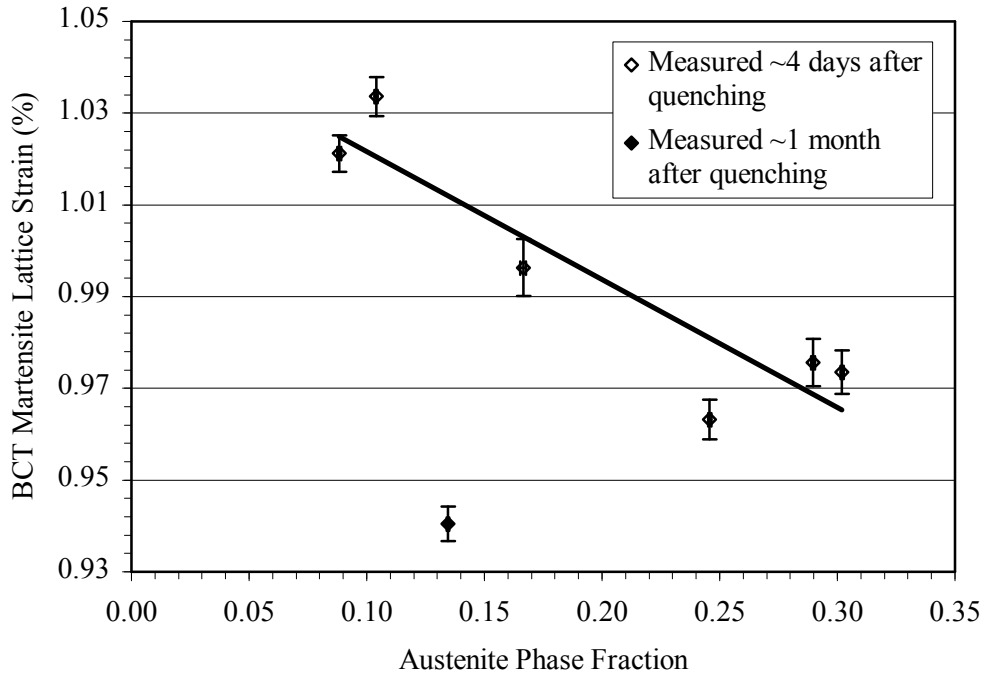

Figure 6.13 – Correlation between martensite lattice strain and untransformed austenite fraction determined using HRPD data with a structural model consisting of 3 phases (BCC martensite, BCT martensite and FCC austenite)

6.3 Discussion of diffraction measurements on quenched specimens

6.3.1 Lattice parameters

X-ray diffraction measurements of the martensite ‘c’ lattice parameter (Figure 6.1) are observed to contain less scatter when an extra BCC phase is included in the structural model for Rietveld refinement. As previously postulated in Section 2.9.8, the additional BCC phase is capable of accounting for ‘true’ BCC martensite, approximating low axial ratio martensite, or a combination of the two. Therefore, it is believed that the additional BCC phase reduces scatter by enabling the separation of as-quenched, high-axial-ratio martensite from martensite which has undergone tempering during polishing or holding at room temperature (for the purposes of this discussion, ‘tempering’ means any change to the as-quenched BCT structure, rather than complete decomposition of the BCT phase). X-ray diffraction is a surface/near-surface measurement technique, hence, polishing is thought to contribute to tempering via two mechanisms. Firstly, by cold working the material the number of energetically favourable locations (lattice defects) where carbon can reside is boosted. Secondly, the mechanical work performed on the specimen causes heating which raises the diffusion rate.

Besides reducing scatter in the martensite ‘c’ measurement, a further effect of introducing an additional BCC phase is that the differential between the martensite ‘a’ and ‘c’ lattice parameters is increased, such that the X-ray diffraction measurements are slightly more representative of published data. It is considered that this occurs by the same mechanism as already described for the reduction of scatter in the martensite ‘c’ lattice parameter. Although austenite lattice parameter measurements are unaffected by the choice of structural model chosen for Rietveld refinement, the values (Figure 6.2) are slightly higher than those published. Complications pertaining to the relationship between carbon concentration and austenite lattice parameter have been previously discussed in Section 2.9.9 and are subject to further deliberation in Section 6.3.3, where the subject is raised again with respect to neutron diffraction measurements.

Neutron diffraction measurements of the martensite ‘c’ lattice parameter show significantly less scatter than their XRD counterparts. The reduction in scatter is thought to be due to the absence of two variables from the neutron diffraction data. Firstly, neutrons penetrate and diffract from the entire specimen, hence any surface

effects that may be present form a relatively low proportion of the measurement. Secondly, all but one of the measurements on HRPD were made the same fixed time period after quenching. For the measurements determined using a two-phase structural model (i.e. BCT and FCC) one datapoint is slightly further removed from the published-data best fit line than any of the other datapoints. As illustrated in Figure 6.14, it is interesting to note that this particular datapoint was derived from specimen 0914, which had already been prepared for and measured by X-ray diffraction, and was then left standing at room temperature for a month prior to being measured on HRPD. This observation is considered to be an effect of low temperature tempering, further deliberations on this subject are made in Section 6.3.3.

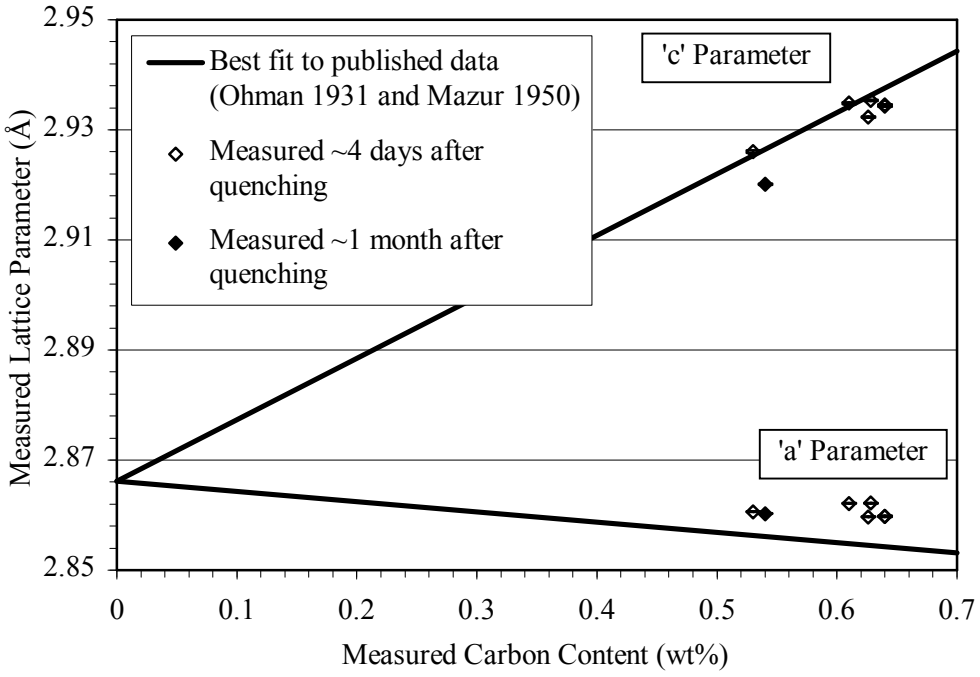

Figure 6.14 – HRPD measurements of lattice parameters in quenched specimens illustrating the effect of time interval between quenching and measurement

6.3.2 Retained austenite fraction

X-ray diffraction measurements of specimens in the as-quenched, mechanically polished condition display significant specimen to specimen variation, and fall below the values predicted by the Koistinen-Marburger relationship (Figure 6.3). In contrast, the neutron diffraction measurements (Figure 6.7 and Figure 6.8), although also containing some variation, are relatively close to the predicted values. An increase in austenite phase fraction (relative to the mechanically polished condition)

was obtained when an electropolished specimen was measured by the X-ray diffraction method (Figure 6.4).

These results are logical when one considers the attributes of the different measurement methods. Neutron diffraction is a whole-volume measurement technique, whereas X-ray diffraction is a surface/near-surface measurement method. Therefore, in those specimens measured by neutron diffraction, the surface of the specimen forms only a relatively small proportion of the measurement. In specimens measured by X-ray diffraction, a TRIP effect causing transformation of retained austenite to martensite is thought to occur when specimens are subjected to elastic and plastic deformation, as is assumed to occur during mechanical polishing. By removing some of the deformed surface layers via electropolishing, an increase in austenite phase fraction as measured by X-ray diffraction is observed, although Figure 6.9 suggests that some surface effects still remain.

Various publications have been made on the nature of the grinding and polishing process, and on the thickness of the deformed layer that is formed in metals during grinding and polishing (Samuels 1985) (Turley and Samuels 1985) (Samuels 1957) (Samsonov and Gaevskaya 1976) (Lihl and Mayer 1960). From these publications it is apparent that the depth of disturbance can extend from less than 1 micron to 10s of microns from the surface, depending on the severity of the grinding or polishing, and the material being prepared. However, even in the case of a 0.1μ polish a deformed layer is still present. A calculation of X-ray penetration using the method described by Cullity (Cullity 1956) is shown in Figure 6.15. It is apparent from this calculation that, depending on the severity of the grinding and polishing process, much of the material measured by X-ray diffraction could be affected by surface deformation caused by specimen preparation. It is also interesting to note that the type of X-ray radiation has a significant effect on the depth of X-ray penetration into the material, with ‘harder’ radiation (e.g. molybdenum) penetrating to a much greater depth than ‘softer’ radiation (e.g. copper).

As the grinding and polishing operation was carried out by hand, some natural variability is expected in the process. Also, abrasives can degrade with usage reducing the efficiency with which the material is ‘cut’, thereby affecting the depth of deformation. Therefore, much of the specimen to specimen variation in the retained austenite fraction as measured by X-ray diffraction (Figure 6.3) can probably be attributed to differences during the grinding and polishing process, with

the remainder being due to small differences during austenitisation and quenching, and slight variations in the concentration of alloying elements.

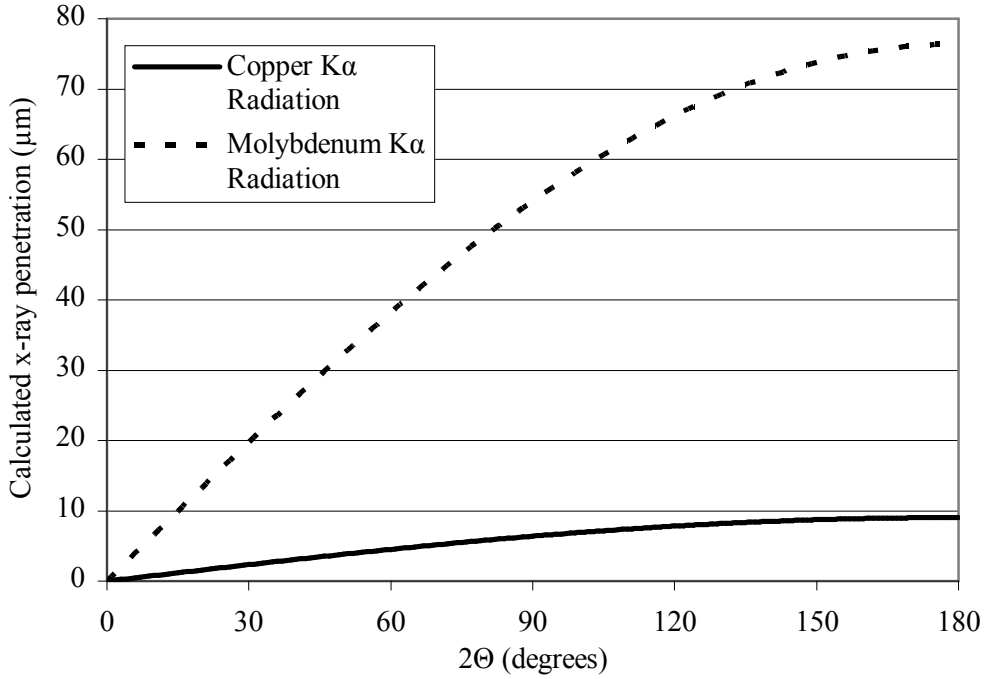

Figure 6.15 –X-ray penetration calculated on the basis of a pure iron specimen and an attenuation factor of 100

6.3.3 Relationships between austenite fraction, austenite lattice parameter and lattice strain

A strong correlation exists between austenite lattice parameter and untransformed austenite fraction (Figure 6.10). Although similar effects have been reported in the literature, this type of outcome has been subject to more than one explanation. Yershov and Oslon observed that discontinuities occur in the linear expansion coefficient of austenite during the martensite transformation process (Yershov and Oslon 1968). For martensite fractions below about 0.4-0.5 the austenite lattice parameter was increased relative to 'free' austenite, this was considered to be due to a combination of the expansive nature of the martensite transformation and coherency between the two phases. At martensite fractions higher than 0.4-0.5 the 'framework' of martensite was believed to compress the austenite, resulting in austenite lattice parameters below those of 'free' austenite. In this research project, all of the measurements involve martensite fractions well above 0.4-0.5, hence the observation that austenite lattice parameter decreases with austenite phase fraction agrees with the findings of Yershov and Oslon.

Ridley and co-workers (Ridley, Stuart et al. 1969) studied austenite lattice parameter dependency on carbon for both retained austenite (obtained by quenching) and ‘equilibrium austenite’ (extrapolations of high temperature data). Their research found that the lattice parameter of retained austenite varies more steeply with carbon content than that of ‘equilibrium austenite’. Two explanations were put forward for this difference in behaviour; compressive stresses generated via the austenite to martensite transformation, and precipitation of carbon at dislocations. In Figure 6.11 it is seen that martensite transformation does have a significant impact on lattice strain measurements and so the concentration of dislocations is expected to increase with decreasing retained austenite fraction. Although it is known that room temperature and sub-zero tempering of martensite occurs; in austenite the jump-frequency of carbon is thought to be significantly lower (see Figure 1.11), and in this project the martensite start temperature is sufficiently low that redistribution of carbon in austenite during quenching is less likely than for a 0.2wt% carbon steel (for example). Therefore, the ‘compressive stresses’ explanation seems more probable in this case, and also agrees with the hypotheses of Yershov and Oslon.

Interpretation of the lattice strain measurements must be undertaken with caution, bearing in mind the assumptions made in Section 2.9.7 and Section 2.10.4 regarding the relative contribution of lattice strain, crystallite size and instrumental effects to the peak profile. However, in view of the relationship between austenite lattice parameter and untransformed austenite fraction previously described, it may not be unreasonable to regard lattice strain as the dominant or main contributor to peak broadening. If one considers that the observed peak broadening is almost entirely the result of lattice strain effects, correlations between untransformed austenite fraction and lattice strain for both austenite and martensite are unsurprising. The austenite to martensite transformation is known to be expansive and dislocation formation (which results in higher lattice strain measurements) represents a means of accommodating the dilatation through plastic deformation. However, it is as well to remember that sub-division of retained austenite via martensite formation could also contribute to peak broadening via a reduction in the size of the average austenite crystallite; this could lead to the observation of increased austenite ‘strain’ at lower austenite phase fractions.

Scatter in the BCT martensite strain versus austenite fraction relationship is significantly reduced when an additional BCC phase is included in the structural

model. The reduction in scatter is thought to occur via the take-up of martensite which has tempered to BCC martensite or low-axial-ratio BCT martensite (where the meaning of 'tempering' is as described in Section 6.3.1). However, even after the introduction of an additional BCC phase, a disparity is observed between specimens measured ~4 days after quenching and a single specimen measured ~1 month after quenching (this specimen was also subject to polishing and XRD measurement prior to assessment on HRPD). This situation can be explained by considering that whereas those specimens measured after ~4 days contain both tempered and untempered martensite, the specimen measured after ~1 month contained only tempered martensite. Such an explanation is in agreement with the reduced martensite 'c' lattice parameter for this specimen (0914) illustrated in Figure 6.14.

In terms of studying the Q&P process, all of the effects described in this section are inconvenient. When attempting to estimate carbon concentration based on lattice parameter measurements, one must be aware that relaxation of elastic strains during partitioning could be mistaken for an increase in austenite carbon concentration. High lattice strains are also undesirable as they result in increased broadening and overlapping of diffraction peaks.

Chapter 7
X-ray diffraction measurements of quenched and partitioned specimens

This chapter contains results of X-ray diffraction measurements on quenched and partitioned specimens. In all cases, the effect of partitioning on various microstructural parameters is plotted as a function of partitioning time. In Figure 7.1, lattice parameter, austenite fraction and lattice strain measurements are presented for those experiments carried out using only air furnaces and water quenching baths (see Section 2.3.1). These experiments were carried out to ensure that the methods being considered were capable of delivering useful results. Due to the experimental techniques used, the data obtained contained a relatively high level of specimen to specimen variability, consequently, only minimal interpretation of the measurements was undertaken.

Following the experiments reported in Figure 7.1, the use of molten salt baths and thermocouples spot welded to the specimens enabled much greater precision in carrying out the partitioning stage of the Q&P heat treatment (see Section 2.3.2). Consequently, specimen to specimen variability was reduced compared to the results presented in Figure 7.1. Therefore, lattice parameter and phase fraction measurements were used to estimate the concentration and distribution of carbon during the Q&P process. Experimental results for partitioning at 400°C are presented in Figure 7.2 to Figure 7.5, while those for partitioning at 500°C are given in Figure 7.6 to Figure 7.9. For each partitioning temperature, the measurements of lattice parameter, lattice strain and phase fraction are plotted with respect to partitioning time. These are followed by plots of carbon concentration and carbon distribution versus partitioning time. Data from as-quenched specimens is plotted at partitioning time equal to zero to illustrate the changes brought about by partitioning (i.e. some of the measurements from Chapter 6 are repeated here).

Finally, additional analysis is presented pertaining to the presence of carbides in partitioned specimens. As for the results described in the previous paragraph, estimations of carbon concentration and carbon distribution were performed. Hence, phase fraction (Figure 7.19), carbon concentration (Figure 7.20) and carbon distribution (Figure 7.21) are all plotted with respect to partitioning time for those specimens which could be assessed for carbides.

7.1 Partitioned using an air furnace

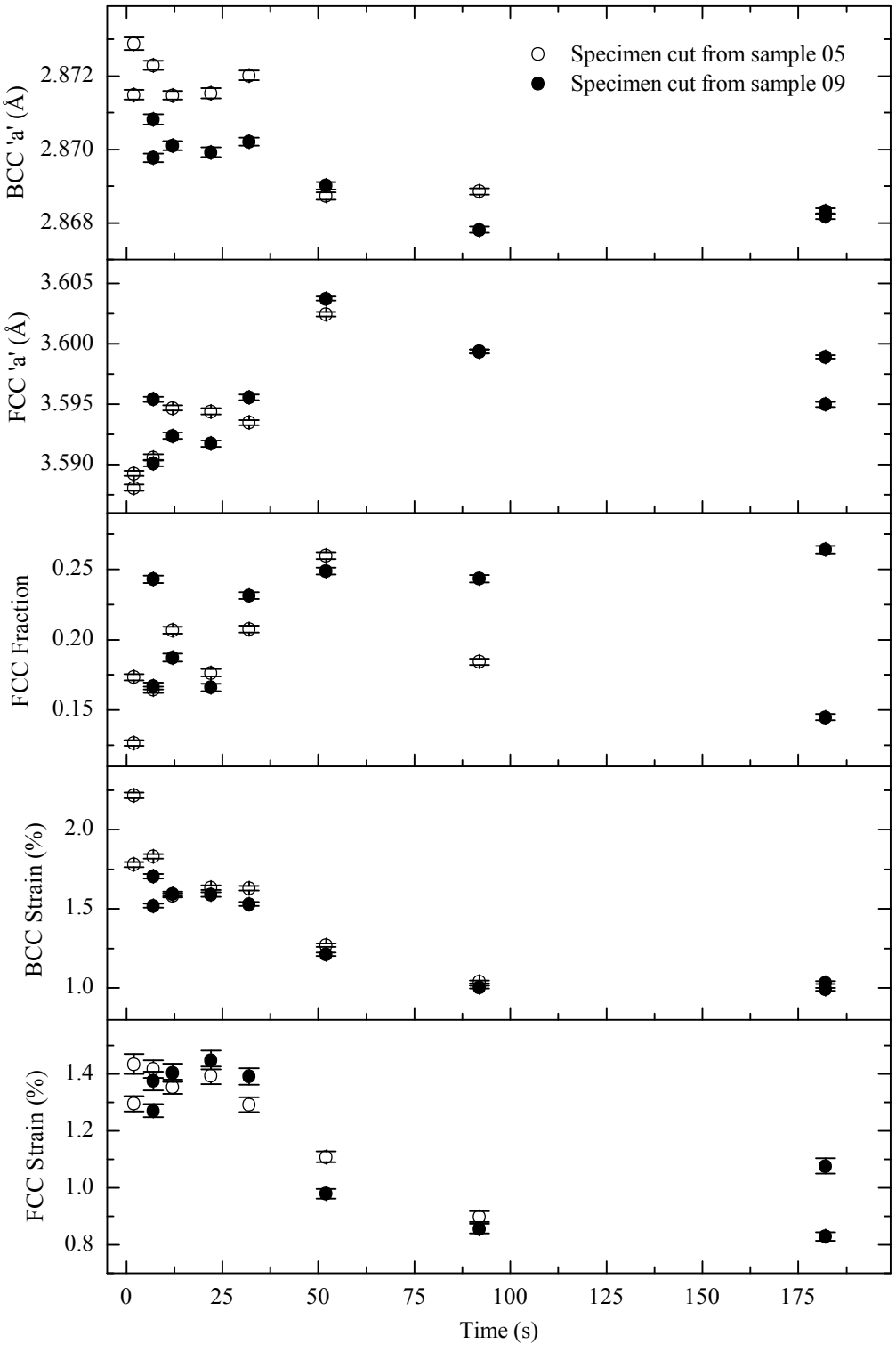

Figure 7.1 – Evolution of microstructural parameters with respect to partitioning time following quenching to 50°C and partitioning at 500°C

7.2 Partitioned at 400°C using a molten salt bath

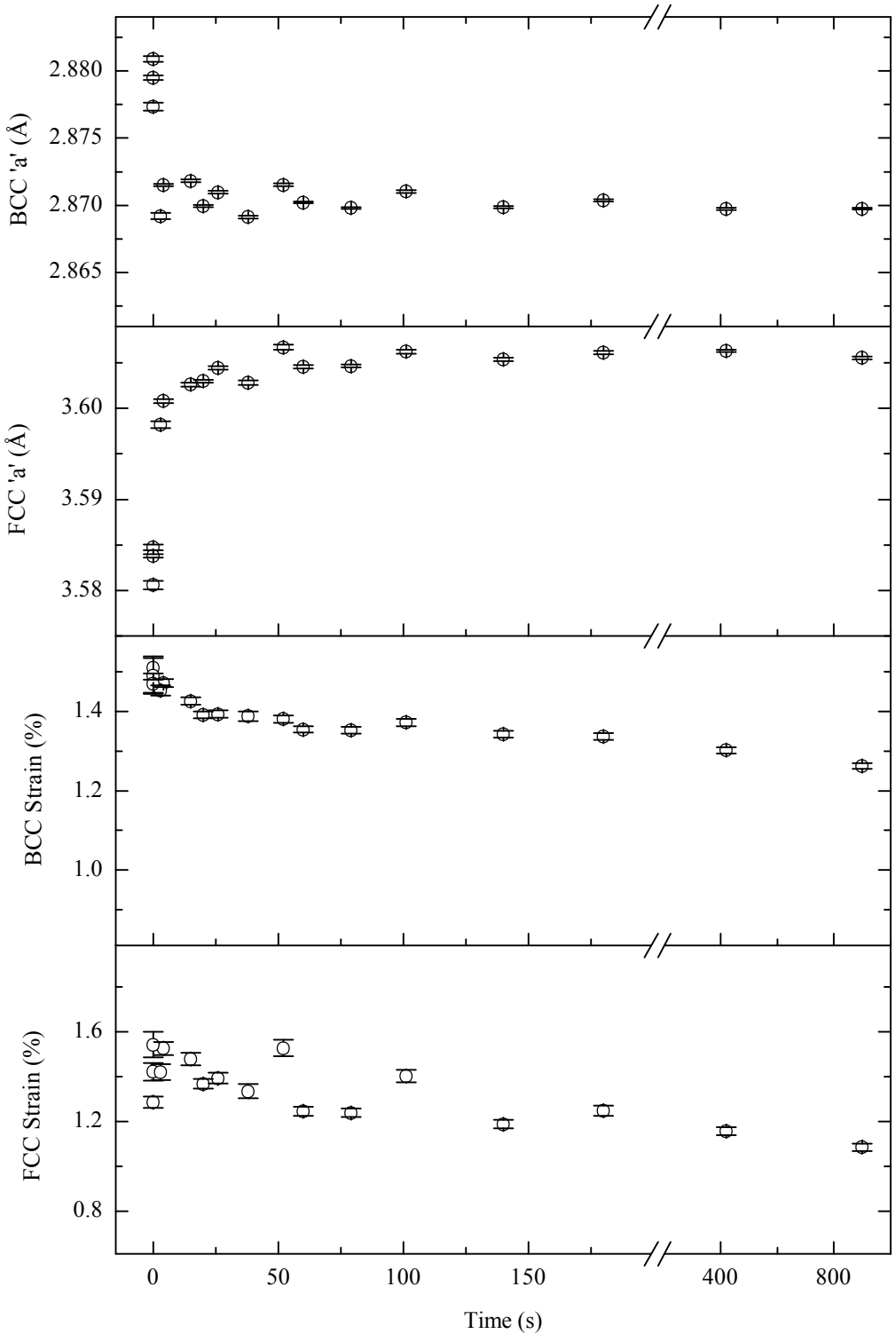

Figure 7.2 – Evolution of lattice parameters and lattice strains, with respect to time, in specimens quenched to 10°C and partitioned at 400°C

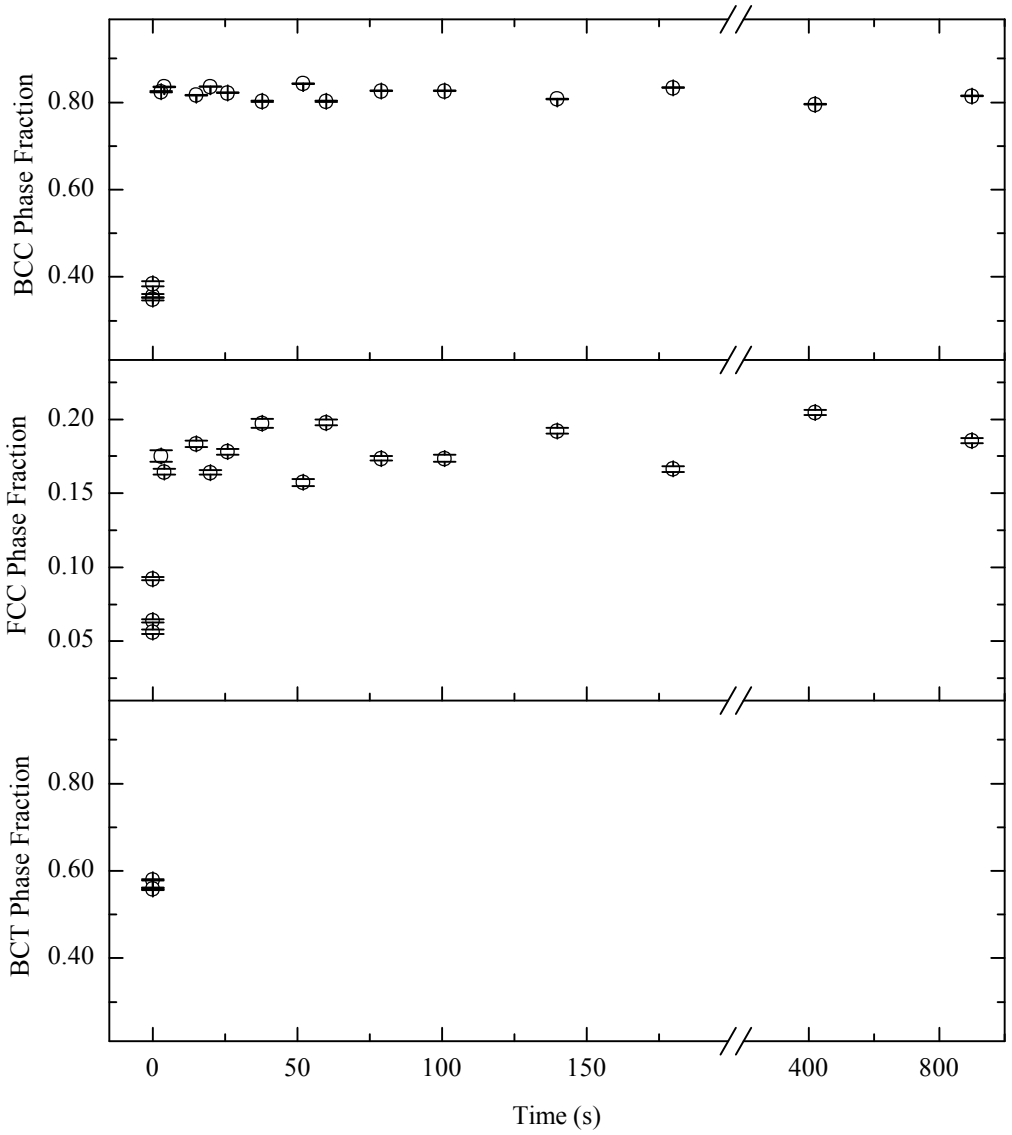

Figure 7.3 - Evolution of phase fractions with respect to time, in specimens quenched to 10°C and partitioned at 400°C

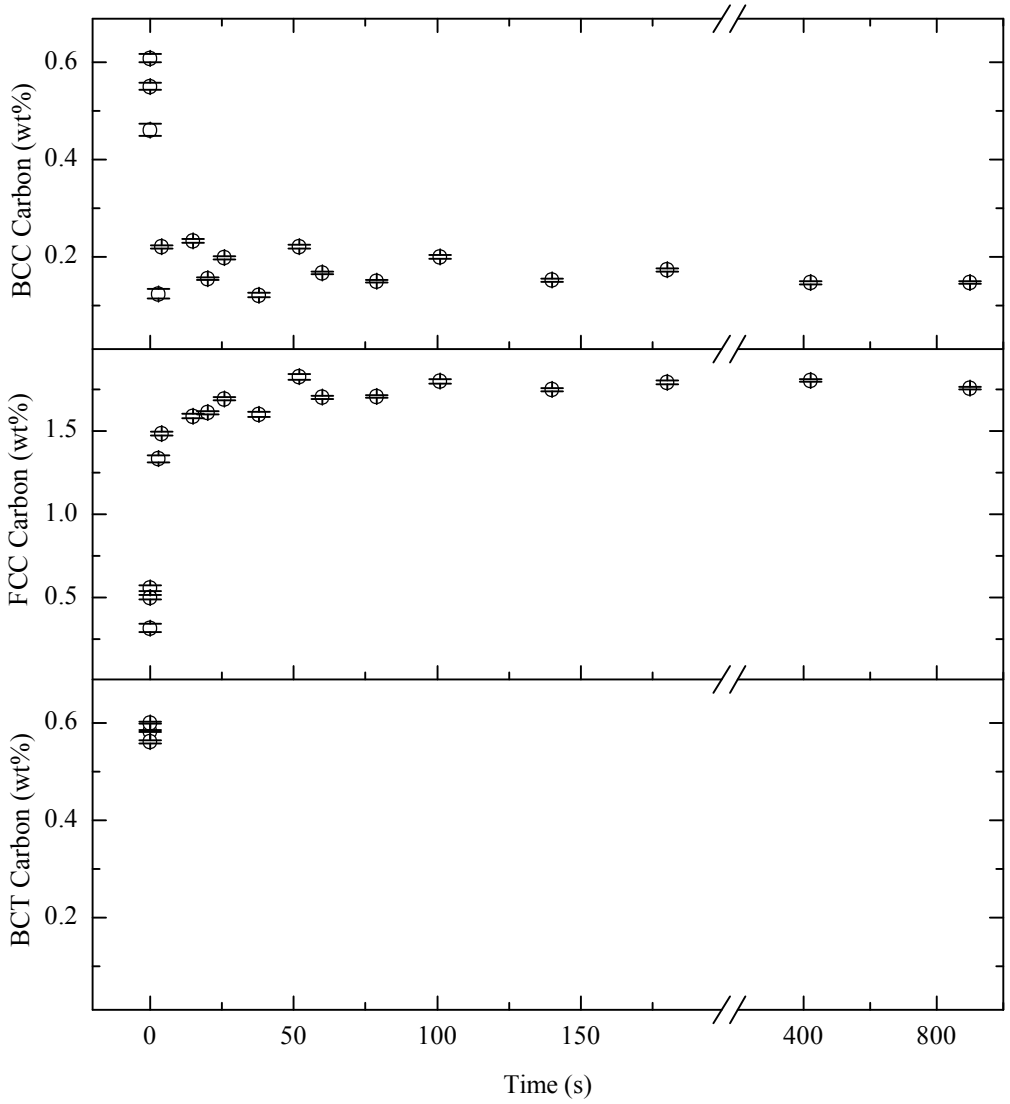

Figure 7.4 - Evolution of individual phase carbon concentrations with respect to time, in specimens quenched to 10°C and partitioned at 400°C

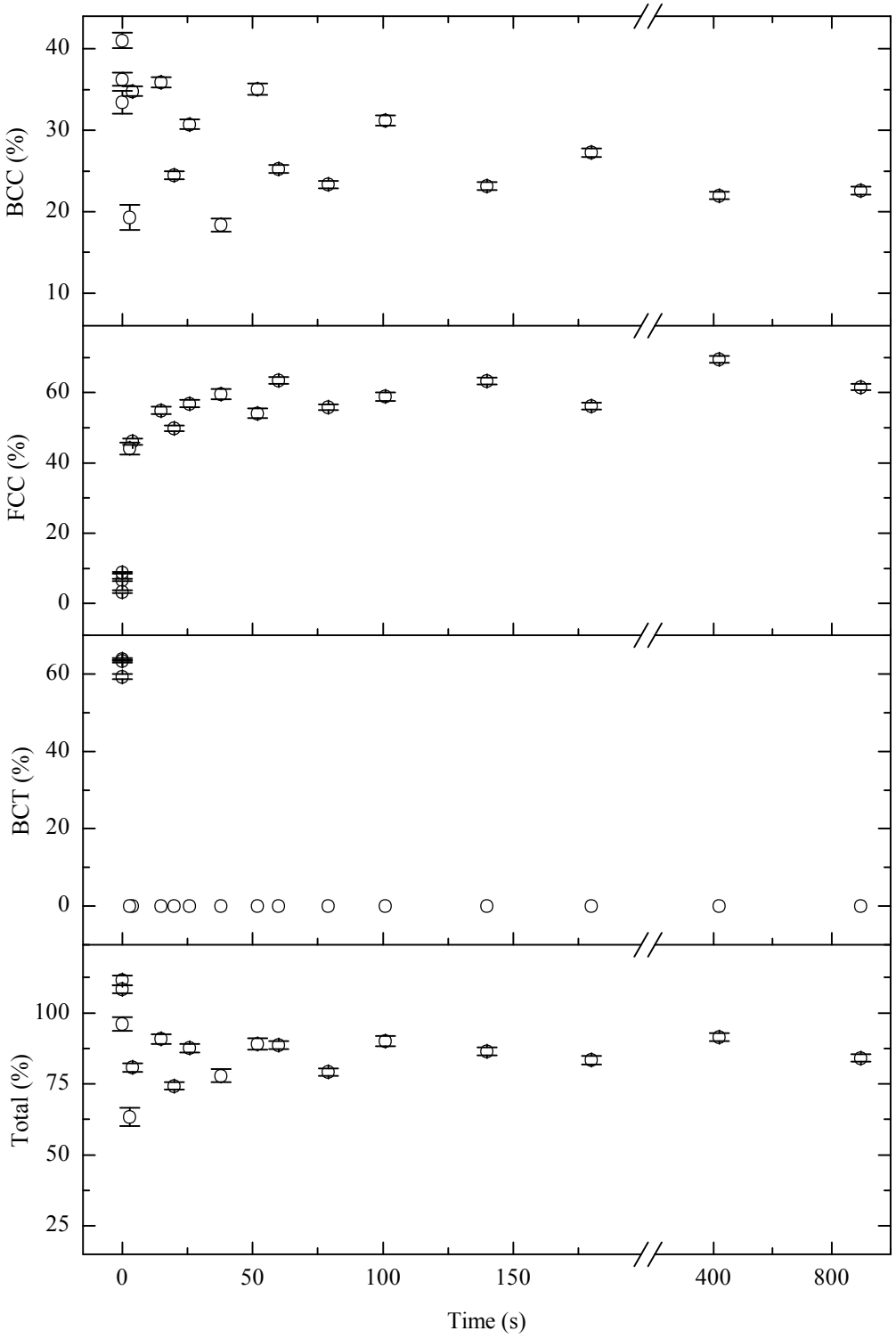

Figure 7.5 - Evolution of carbon distribution with respect to time, in specimens quenched to 10°C and partitioned at 400°C (expressed as a percentage of a total nominal alloy content of 0.53wt% carbon)

7.3 Partitioned at 500°C using a molten salt bath

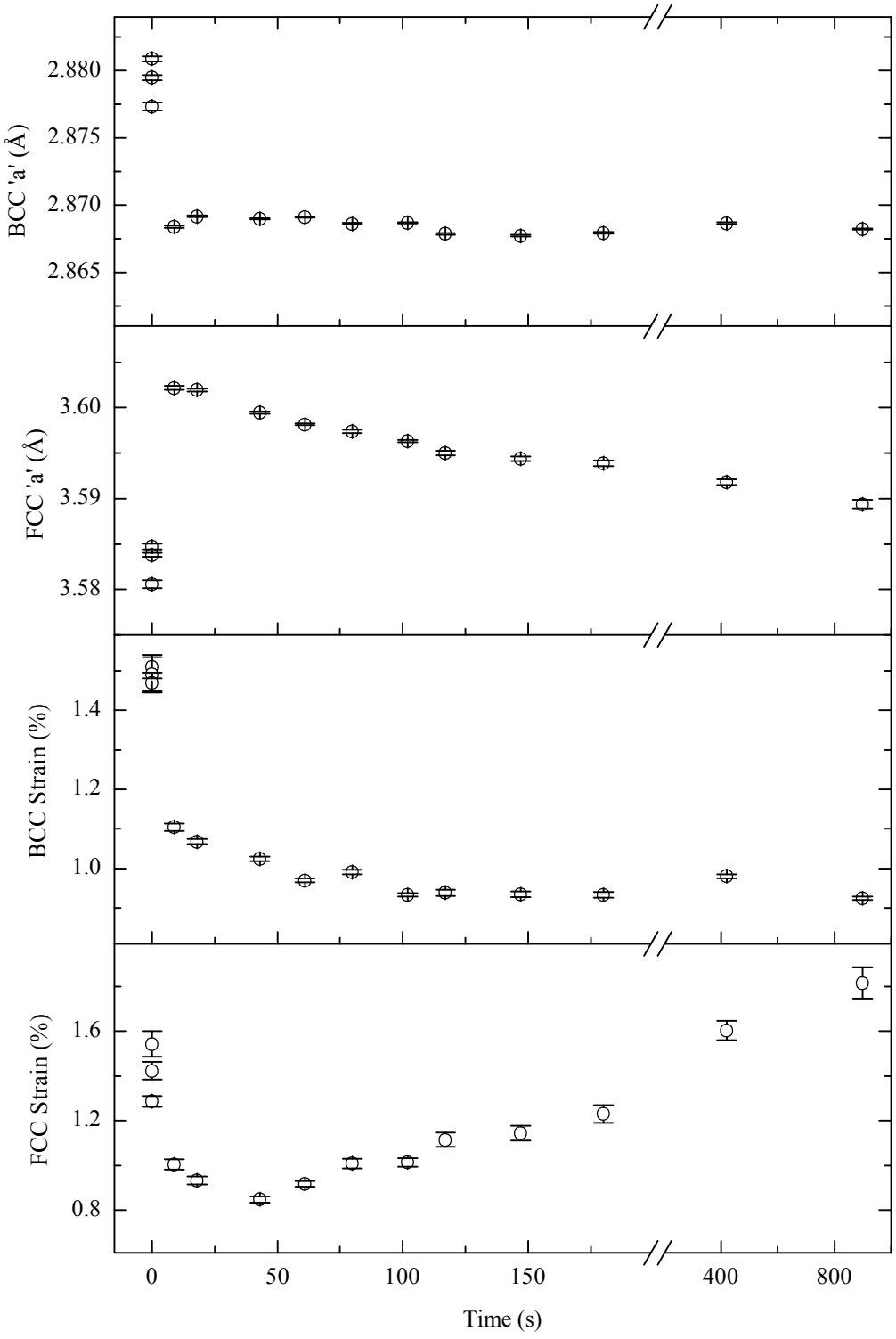

Figure 7.6 – Evolution of lattice parameters and lattice strains, with respect to time, in specimens quenched to 10°C and partitioned at 500°C

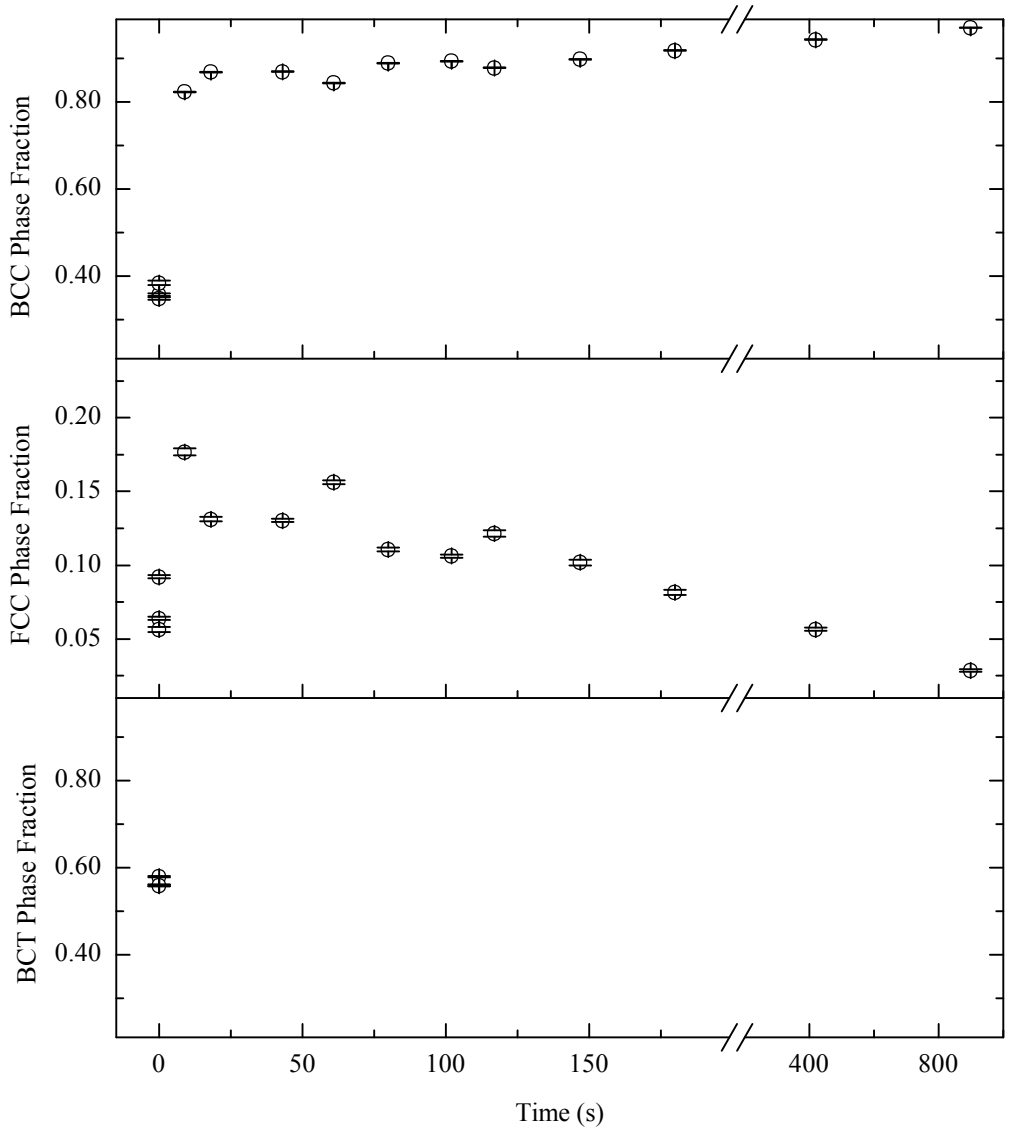

Figure 7.7 - Evolution of phase fractions with respect to time, in specimens quenched to 10°C and partitioned at 500°C

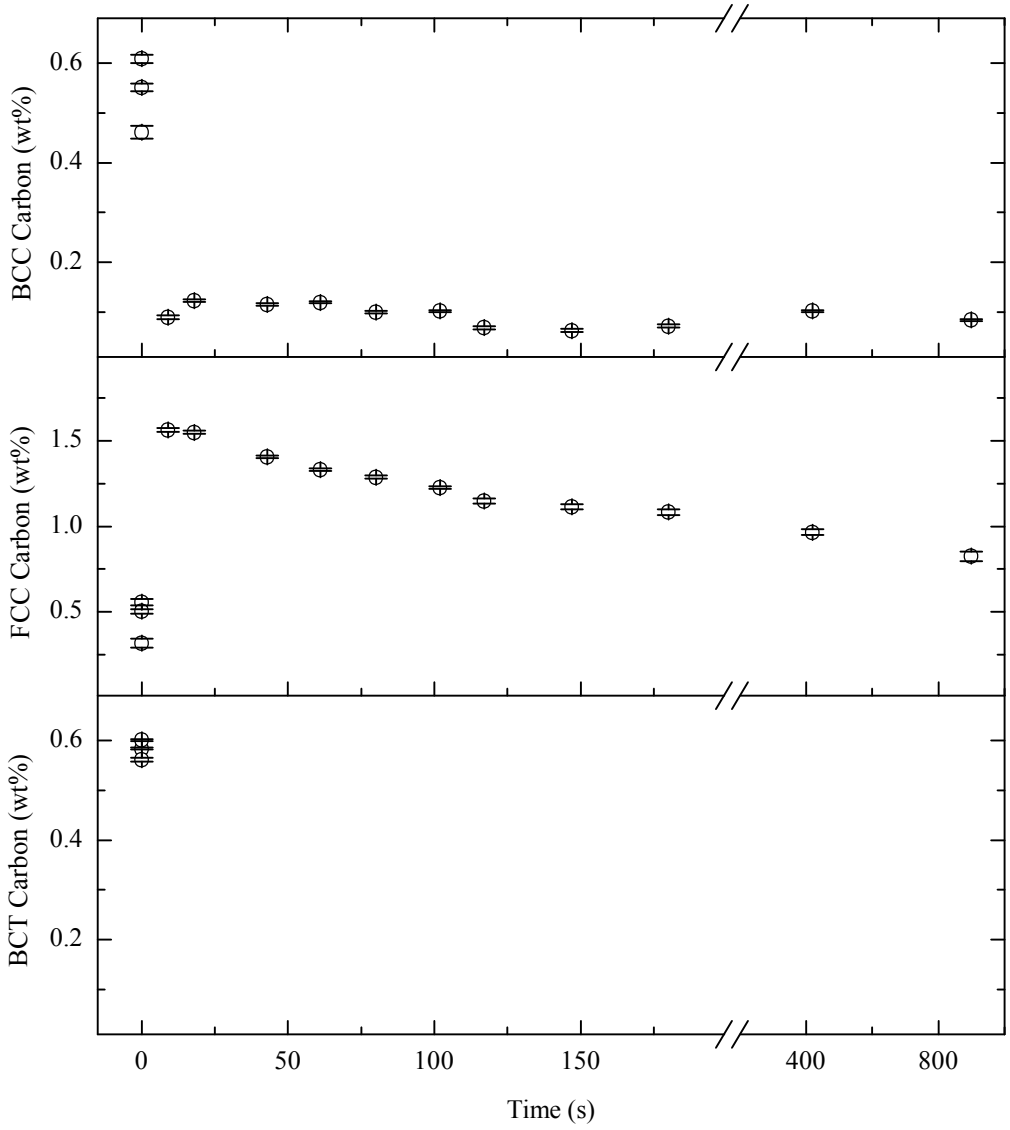

Figure 7.8 - Evolution of individual phase carbon concentrations with respect to time, in specimens quenched to 10°C and partitioned at 500°C

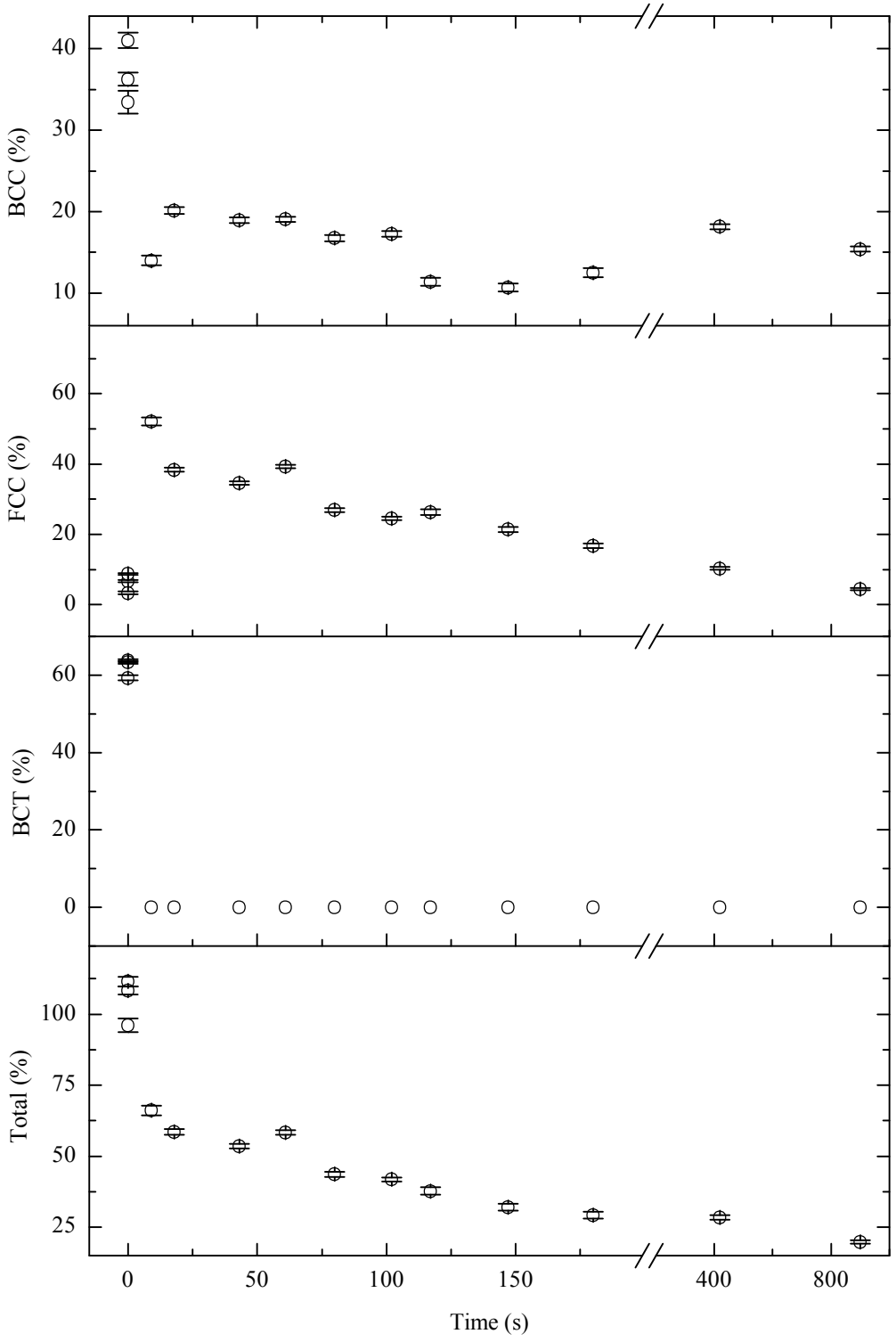

Figure 7.9 - Evolution of carbon distribution with respect to time, in specimens quenched to 10°C and partitioned at 500°C (expressed as a percentage of a total nominal alloy content of 0.53wt% carbon)

7.4 Interpretation of carbide peaks

Examination of the X-ray diffraction patterns reveals that in some cases evidence exists for the presence of a third phase (Figure 7.10). A differential is observed here between measurements made using the SEE instrument and those made using the IMR instrument. The additional peaks produced by an extra phase were readily visible in data from the SEE diffractometer (Figure 7.10), but not in data from the IMR diffractometer (Figure 7.11). After comparing various datasets from both diffractometers, the disparity was deduced to originate from a combination of two factors.

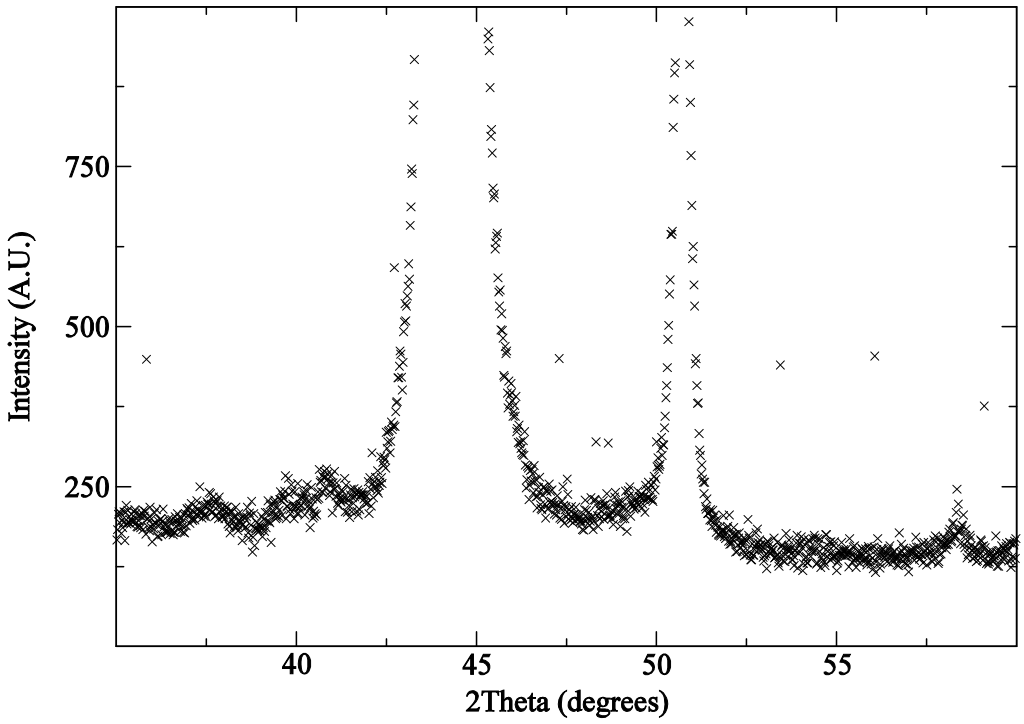

Figure 7.10 – XRD pattern from specimen 2208 measured on the SEE diffractometer following a Q&P heat treatment (partitioned for 102 seconds at 500°C)

The measurements which gave the most intense third-phase peaks were conducted on the SEE diffractometer using longer counting times than were used for any of the measurements on the IMR diffractometer. However, as some of the third-phase peaks appeared in SEE measurements that were carried out at very similar counting times as those used at IMR, this explanation does not fully account for the differences observed between the two instruments. The second difference concerns the mounting system used for each instrument; while the IMR system uses a glass microscope slide for mounting specimens, the SEE system uses a low-background-

count silicon plate. The silicon plate, which is aligned with a specific crystal plane exposed to the X-rays, has the effect of significantly reducing the background count relative to the diffracted intensities; this improves the signal to noise ratio of the instrument so that peaks of very low intensity are visible above the background count.

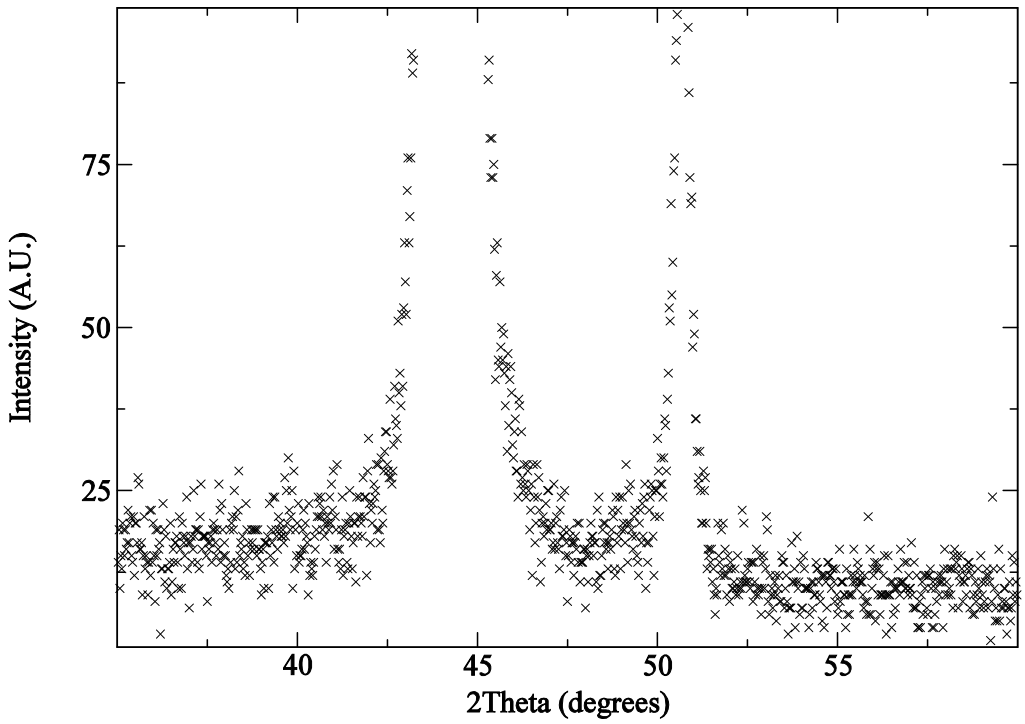

Figure 7.11 - XRD pattern from specimen 2206, measured on the IMR diffractometer following a Q&P heat treatment (partitioned for 117 seconds at 500°C)

The literature available indicates that a variety of carbides are able to form within the Fe-C and Fe-Mn-C systems. Examples of carbides reported by other researchers include Fe_2C, Fe_4C, Fe_3C, Fe_5C_2, $Mn_{23}C_6$, Mn_5C_2, Mn_7C_3, Mn_3C, $Mn_{15}C_4$, $(Fe,Mn)_3C$, $(Fe,Mn)_5C_2$ (Hirotsu and Nagakura 1972) (Nagakura and Toyoshima 1979) (Herbstein and Smuts 1964) (Duggin and Hofer 1966) (Duggin, Cox et al. 1966) (Lipson and Petch 1940) (Hume-Rothery, Raynor et al. 1942) (Fasiska and Jeffrey 1965) (Karen, Fjellvag et al. 1991) (Bouchaud 1967) (Tanaka and Shimizu 1981) (Ma, Ando et al. 1983) (Speich 1969).

A smaller number of researchers have published on the topic of phase equilibria within Fe-Mn-C and Mn-C systems (Kuo and Persson 1954) (Benz, Elliott et al. 1973a) (Benz, Elliott et al. 1973b). Although thermodynamic stability of Mn_3C

is reported to be limited to the temperature range 950-1050°C (Figure 7.12), the two carbides of Fe_3C and Mn_3C are isostructural and so manganese carbide readily dissolves in cementite (Bain, Davenport et al. 1932) (Duggin, Cox et al. 1966). Hence, in Figure 7.13 it is seen that the phase M_3C features in the Fe-rich corner of the Fe-Mn-C ternary phase diagram at 600°C. At temperatures below 600°C it might reasonably be expected that the M_3C phase remains stable, i.e. a similar response to that observed in the Fe-C system. Therefore, at the partitioning temperatures of 500 and 400°C it is postulated that M_3C will be the most stable carbide phase.

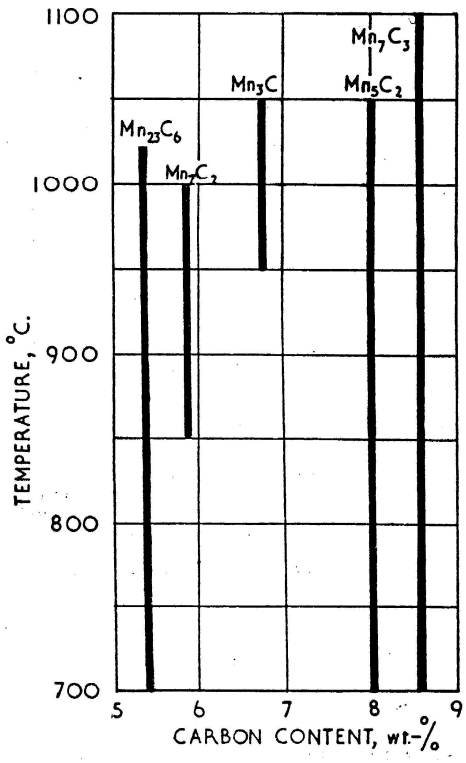

Figure 7.12 – Stability range of manganese carbides (Kuo and Persson 1954)

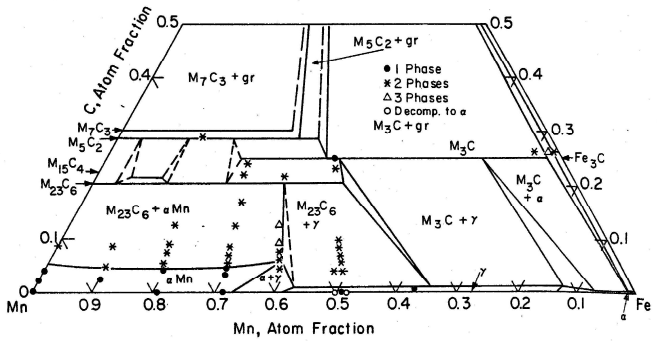

Figure 7.13 – Ternary phase diagram for the system Fe-Mn-C at 600°C (Benz, Elliott et al. 1973b)

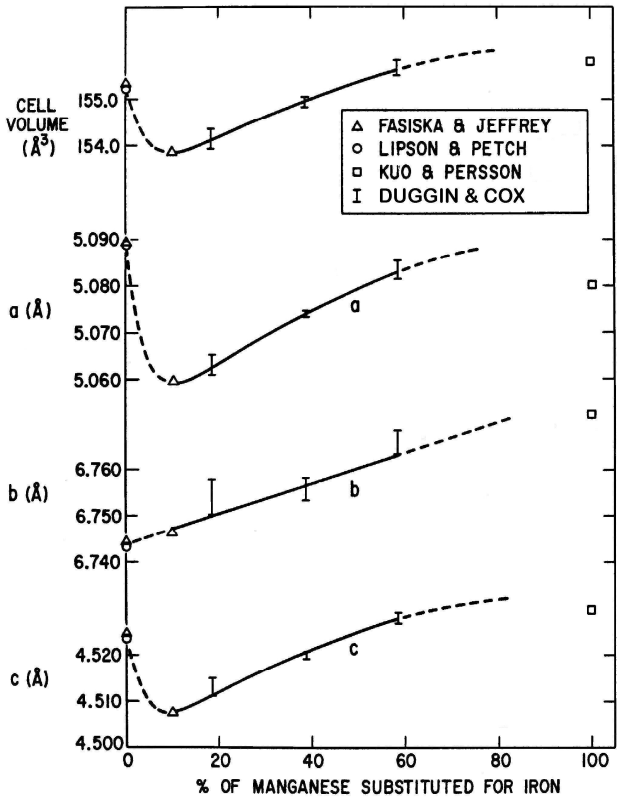

Figure 7.14 – The variations in lattice parameters and cell volume of some Fe-Mn carbides with the cementite structure, with increasing substitution of manganese for iron, after Duggin and Cox (Duggin, Cox et al. 1966) (Fasiska and Jeffrey 1965) (Lipson and Petch 1940) (Kuo and Persson 1954)

Rietveld refinements were initially performed on the diffraction dataset containing the most prominent carbide peaks (specimen 2212, partitioned at 500°C for 900 seconds). For the purposes of this investigation, it would have been useful to refine the lattice parameter of the carbide phase and make comparisons with Figure 7.14. However, the structural model was found to be unstable when lattice parameters were refined for the carbide phase. Contributory factors to the instability are believed to include the relatively low carbide phase fraction, corresponding weak intensities, heavy overlaps of the carbide peaks, and low atomic scattering factor of carbon (Figure 7.18). Therefore, Rietveld refinements were run for three carbides of the same crystal structure but with differing unit cell dimensions. The carbides trialled were pure Fe_3C (Herbstein and Smuts 1964), $Fe_{1.8}Mn_{1.2}C$ (Duggin, Cox et al. 1966), and pure Mn_3C (Kuo and Persson 1954); lattice parameters for these are as listed in Table 7.1.

	Lattice Parameter (Å)		
	a	b	c
Fe_3C	5.090	6.748	4.523
$Fe_{1.8}Mn_{1.2}C$	5.074	6.757	4.521
Mn_3C	5.080	6.772	4.530

Table 7.1 – Lattice parameters of the various carbide structures trialled in the Rietveld refinement of specimen 2212

The Rietveld fits achieved are illustrated in Figure 7.15, Figure 7.16 and Figure 7.17. In all cases, fitting of the structural model to diffraction data was slightly improved by refining XYZ positions of the metal atoms. XYZ for carbon atoms was not refined due to the low scattering factor of this element. A related problem occurs when refining the atomic displacement parameter (temperature factor) for carbon, in that the parameter is observed to converge to the maximum allowable value allowed by the software.

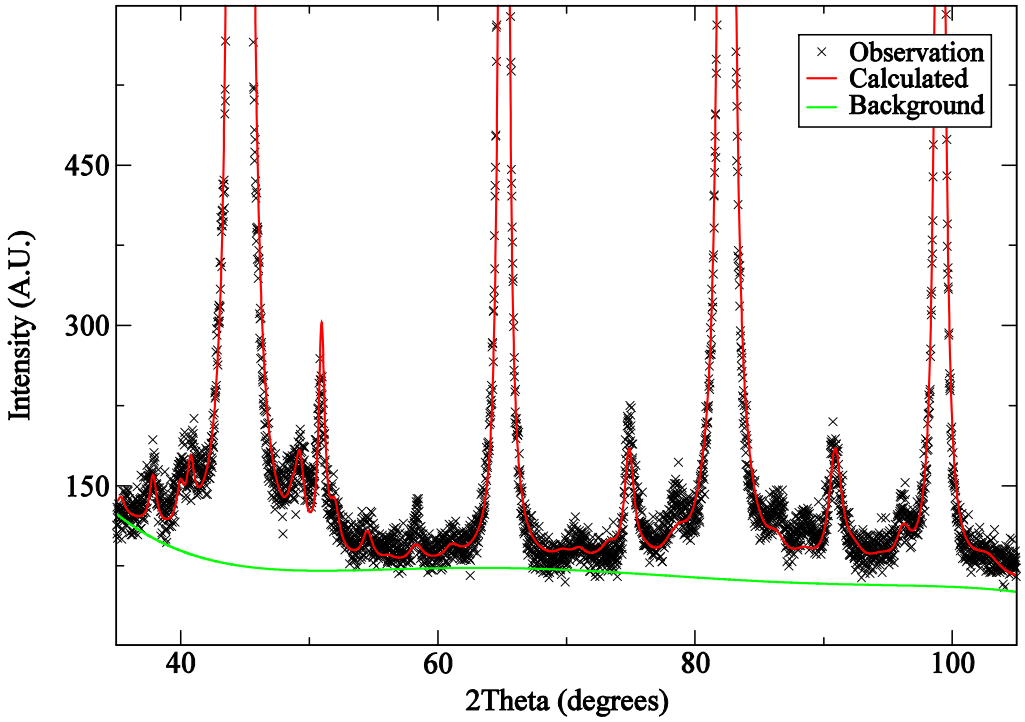

Figure 7.15 – Fitting Fe_3C to additional peaks observed in data from specimen 2212 (partitioned for 900 seconds at 500°C)

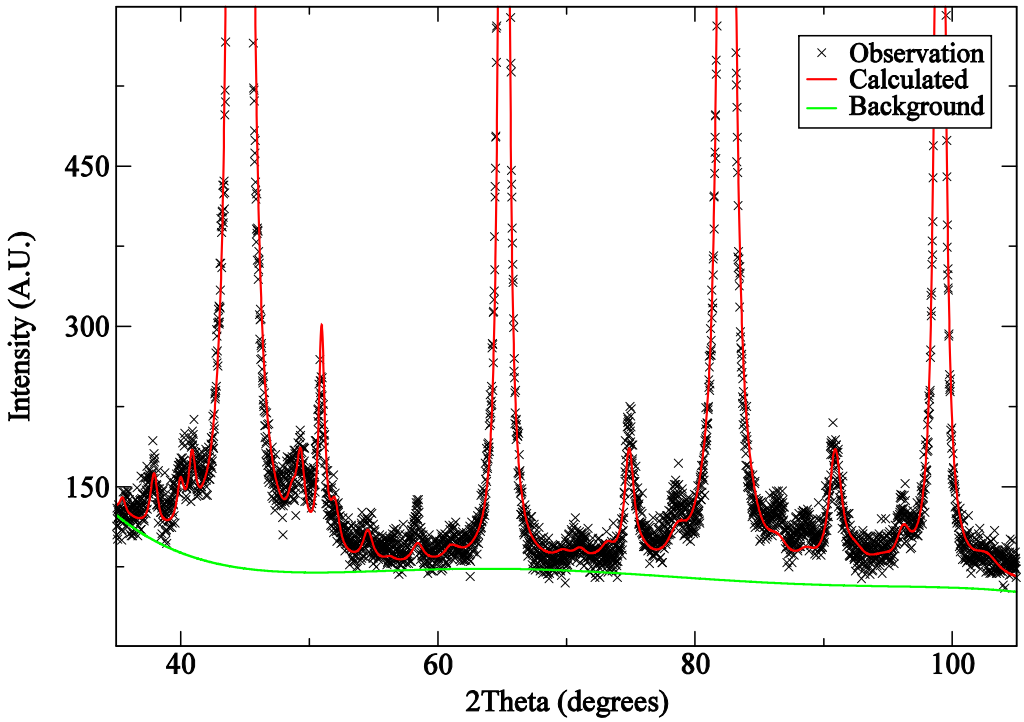

Figure 7.16 – Fitting $Fe_{1.8}Mn_{1.2}C$ to additional peaks observed in data from specimen 2212 (partitioned for 900 seconds at 500°C)

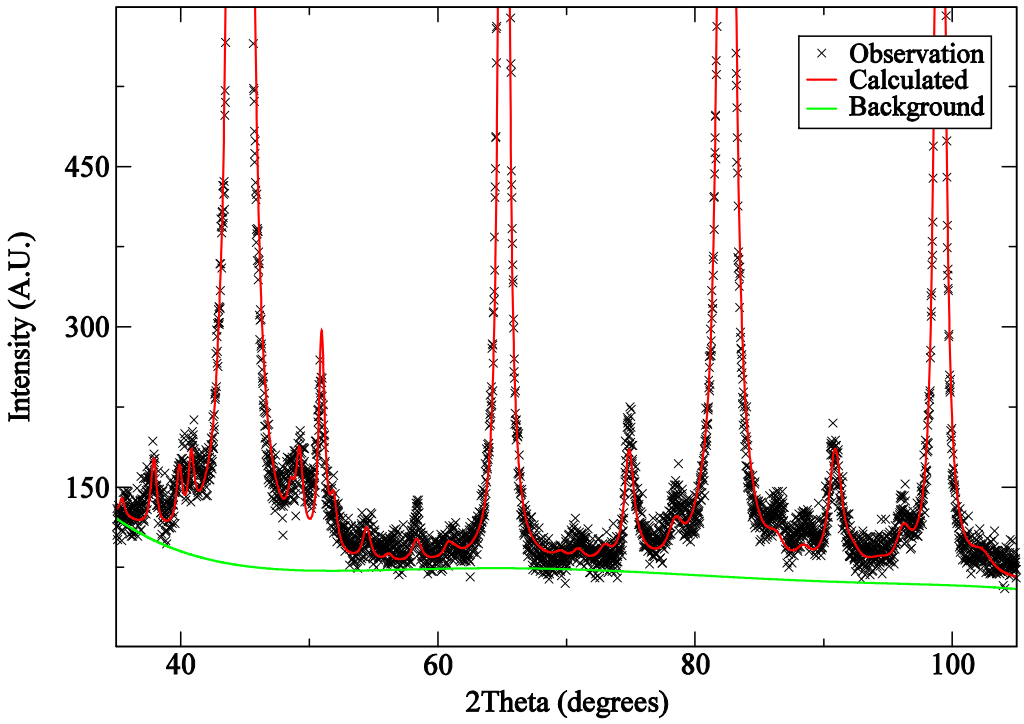

Figure 7.17 - Fitting Mn_3C to additional peaks observed in data from specimen 2212 (partitioned for 900 seconds at 500°C)

Of the three structural models trialled, the Mn_3C model gave slightly lower residuals than the Fe_3C and $Fe_{1.8}Mn_{1.2}C$ models, thus indicating a higher quality of fit. The quality of the Rietveld fit is relatively important, as poorer fits give lower carbide phase fractions, leading to an underestimation of the quantity of carbon consumed by carbide formation. Carbide fractions for the three models, Fe_3C, $Fe_{1.8}Mn_{1.2}C$, and Mn_3C were 4.21wt%, 4.73wt% and 5.05wt% respectively. Consequently, it was decided to refine all datasets with an Mn_3C model for the carbide phase fraction, and using the XYZ atomic coordinates determined from the refinement presented in Figure 7.17. The XYZ atomic coordinates are listed in Table 7.2; comparing these to the values published by Herbstein and Smuts and listed in Table 7.3, it is apparent that the refined values have not strayed significantly from that of the Fe_3C structure.

	Atom coordinates		
	x	y	z
Mn1	0.168631	0.060679	0.333231
Mn2	0.063504	0.250000	0.733131
C	0.890000*	0.250000*	0.450000*

Table 7.2 – Atomic coordinates for Mn_3C determined by Rietveld refinement of diffraction data from specimen 2212 (* denotes not refined)

	Atom coordinates		
	x	y	z
Fe1	0.186	0.063	0.328
Fe2	0.036	0.250	0.852
C	0.890	0.250	0.450

Table 7.3 – Atomic coordinates for Fe_3C as published by Herbstein and Smuts

Although the Mn_3C structural model was found to give the best fit to X-ray diffraction measurements, it is important to note that this does not constitute evidence that the carbides measured are of that chemical composition. Since the atomic scattering factors of Iron and Manganese are very similar (Figure 7.18), almost the same outcome could have been obtained by using a structural model with

the same lattice parameters and atomic XYZ coordinates, but with the Manganese atoms replaced by Iron atoms (i.e. Fe_3C). Similarly, there is no advantage in refining for the fraction of Manganese and Iron on the metal atom sites as the difference in atomic scattering factor between the two atoms is relatively small. Therefore, conclusions are limited to the carbide being of an Fe_3C type structure. However, in view of the Manganese alloying, it would be reasonable to assume that some sharing of metal atom sites between Iron and Manganese probably takes place.

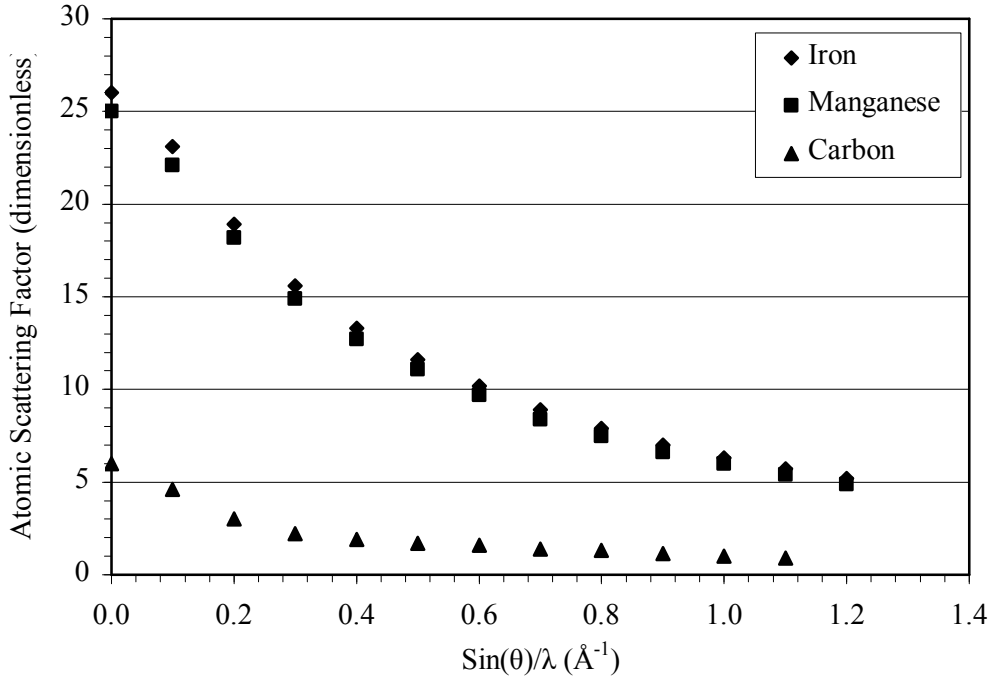

Figure 7.18 – Atomic scattering factors for Iron, Manganese, and Carbon, plotted using data from Cullity (Cullity 1956)

7.5 Reassessment of diffraction data taking account of carbides

In view of the shortfall in carbon that was identified in the lowermost frames of Figure 7.5 and Figure 7.9, diffraction data was re-assessed for carbides. Although some of the specimens partitioned at 400°C displayed evidence of additional peaks, unfortunately they were relatively diffuse and indistinct and so neither identification nor quantification was possible. Therefore, assessments were limited to those specimens partitioned at 500°C, where the additional peaks present could be readily processed by Rietveld refinement. However, of those datasets gathered from specimens partitioned at 500°C, a significant number could not be assessed due to low carbide phase fraction, poor signal to noise ratio or a combination of both (see

Section 7.4 for a full explanation). Those datasets which were suitable for carbide analysis are presented in Figure 7.19, Figure 7.20 and Figure 7.21.

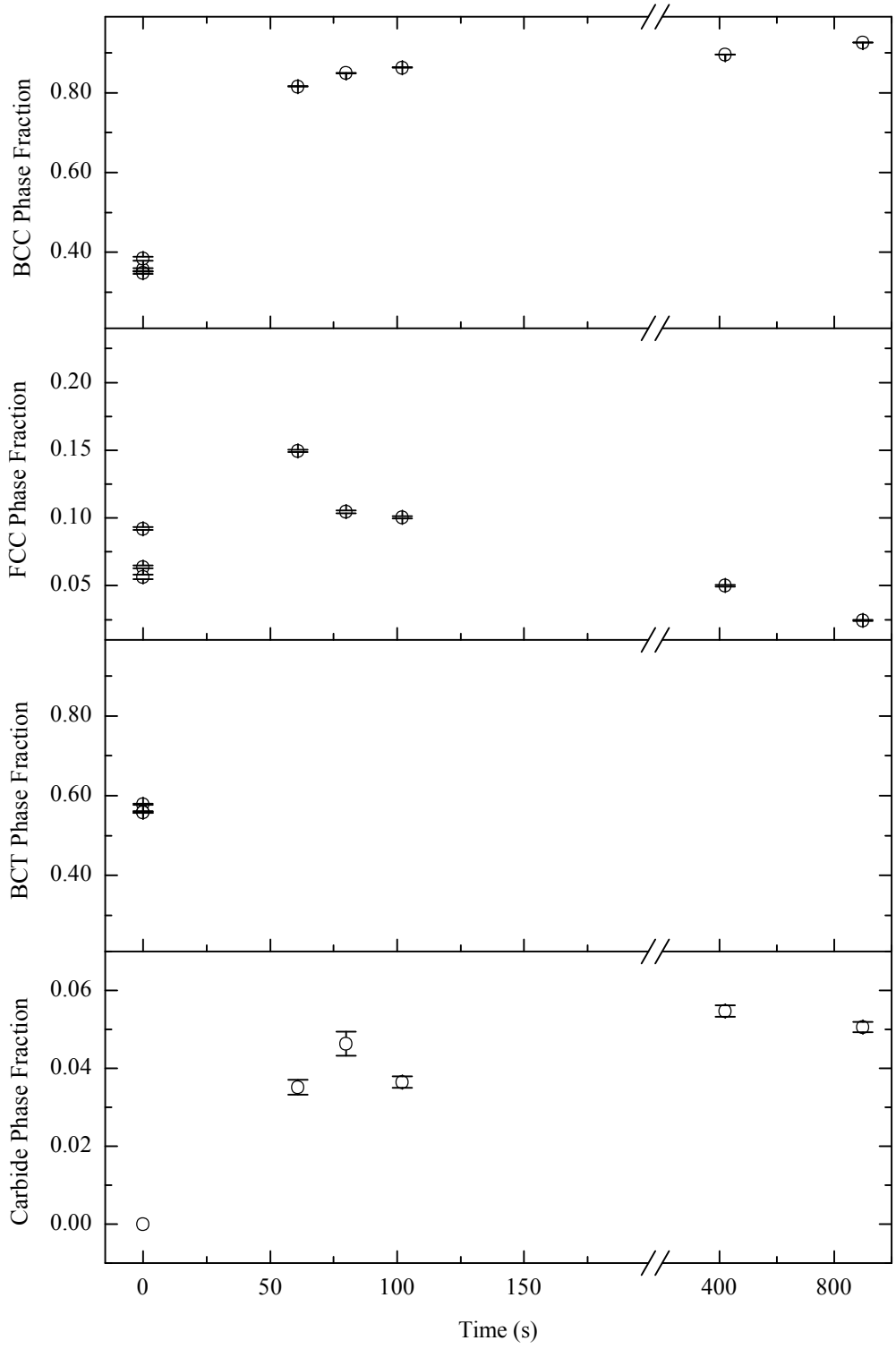

Figure 7.19 - Evolution of phase fractions with respect to time, in specimens quenched to 10°C and partitioned at 500°C (re-assessment including carbides)

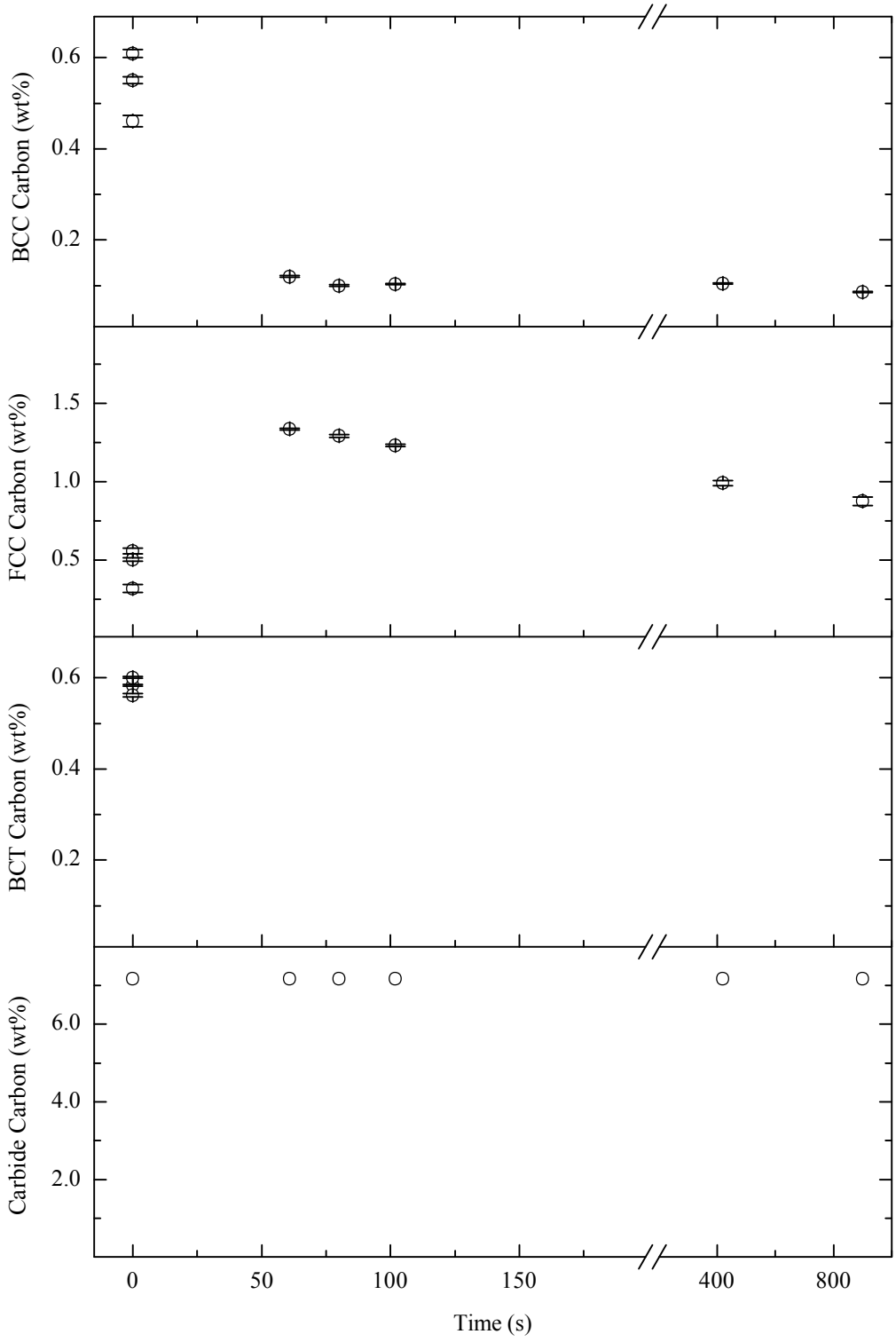

Figure 7.20 - Evolution of individual phase carbon concentrations with respect to time, in specimens quenched to 10°C and partitioned at 500°C (re-assessment including carbides)

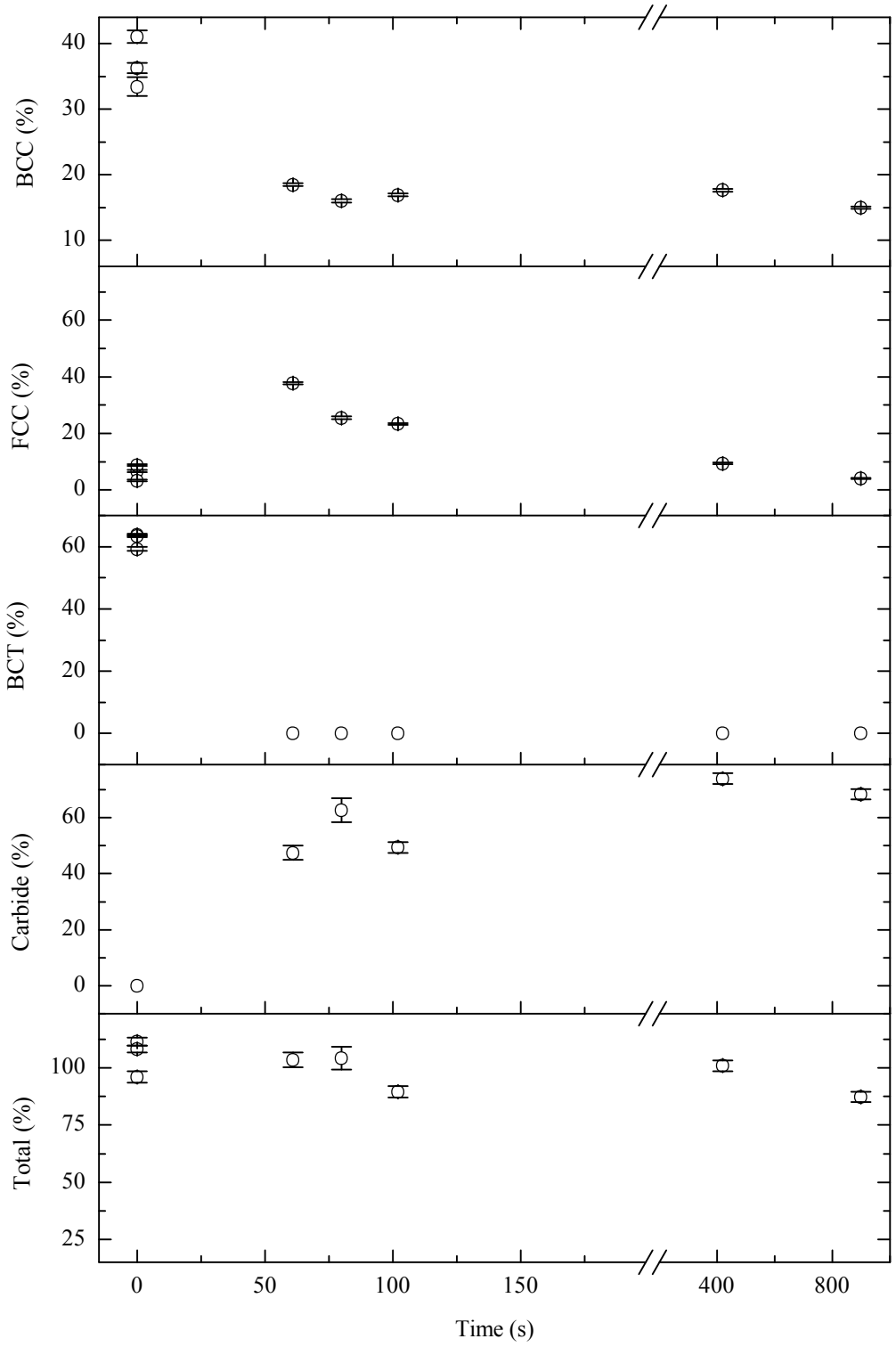

Figure 7.21 - Evolution of carbon distribution with respect to time, in specimens quenched to 10°C and partitioned at 500°C (expressed as a percentage of a total nominal alloy content of 0.53wt% carbon and re-assessed including carbides)

7.6 Discussion of diffraction measurements on quenched and partitioned specimens

7.6.1 Specimens partitioned using an air furnace

The specimens used for these experiments were cut from two different samples of slightly different chemical composition. However, varying carbon concentration from 0.47 to 0.54wt% does not appear to significantly affect the measurements. The scatter in the results is considered to be a consequence of the somewhat imprecise method of performing the partitioning stage of the heat treatment. Despite the scatter, some interesting trends are apparent in Figure 7.1. The lattice parameter of BCC martensite steadily reduces during the first 100 seconds of partitioning. This is believed to correspond to the rejection of carbon from interstitial sites. During the first 50 seconds of partitioning, the austenite lattice parameter is observed to increase, this is thought to signify migration of carbon from martensite into retained austenite. Austenite lattice parameter measurements peak at approximately 50 seconds and then decline slightly, indicating a slight drop in carbon concentration. For both BCC martensite and austenite, lattice strain is observed to decrease over a similar time frame to that of the BCC martensite lattice parameter reductions. The decrease in strain is considered to correspond to a reduction in the number of lattice defects able to act as an energetically favourable 'trap' for carbon, therefore, as partitioning progresses consumption of carbon by carbides is expected to become an increasingly viable competing reaction. Austenite phase fraction is seen to increase with partitioning time, this effect is considered to represent evidence of the stabilisation of austenite by carbon enrichment. As the austenite carbon concentration increases, its martensite start temperature is lowered such that martensitic transformation during the final quench to room temperature (and during mechanical polishing) is reduced. At longer partitioning times there is some evidence of austenite decomposition, however, further datapoints are required to confirm this.

7.6.2 Partitioned at 400°C using a molten salt bath

The measurements obtained by partitioning at 400°C in a molten salt bath share similarities with those described in the previous section. BCC martensite lattice parameter is observed to decrease, while austenite lattice parameter increases. For BCC martensite, it should be remembered that the measurements made at partitioning time equal to zero (i.e. as-quenched) represent an approximation of low axial ratio BCT martensite, BCC martensite, or some combination of the two (see

Section 2.9.8). The decrease in BCC lattice parameter and decomposition of the BCT phase upon partitioning are both associated with rejection of carbon from the supersaturated body-centred lattice. Austenite phase fraction is initially observed to increase sharply upon partitioning; this increase can be accounted for by considering it as a decrease in the amount of austenite that undergoes a TRIP type transformation to martensite during polishing (the effect of metallographic polishing on austenite fraction has already been discussed in Section 6.3.2 and so is not repeated here). An increase in measured austenite fraction suggests that partitioning has conferred additional stability on the retained austenite by carbon enrichment. This confirms that a key objective of the Q&P heat treatment process has been achieved. Austenite fraction measurements of partitioned specimens are in reasonable agreement with the predictions contained within Section 4.2, and the as-quenched measurements shown in Figure 6.7. Therefore, assuming that interface migration does not occur during partitioning, this observation demonstrates that the initial quench is producing a similar quantity of retained austenite to that predicted. During partitioning, after the initial sharp increase, the austenite phase fraction remains stable over the entire range of partitioning times studied. Therefore, if interface migration between martensite and austenite is occurring during partitioning it is not thought to be of a magnitude sufficient to be visible above the scatter in the results.

The combination of molten salt baths and monitoring by spot-welded thermocouples gives much greater precision, and this is evident when comparing these results with those discussed in the previous section. Consequently, lattice parameter and phase fraction measurements have been used to estimate the concentration and distribution of carbon during the partitioning process. As expected, carbon is rapidly rejected from the body-centred phases, resulting in decomposition of BCT martensite to BCC martensite, and reduction of BCC martensite carbon concentration. However, for the duration of partitioning studied, the decrease in body-centred carbon content does not proceed to equilibrium concentration, but remains at approximately 0.15-0.2wt%. Meanwhile, austenite carbon concentration increases from an as-quenched level of ~0.53wt% to around 1.75wt%. By computing the product of carbon concentration and phase fraction, a fuller picture emerges of the partitioning process. In as-quenched specimens, most of the carbon present in the alloy is to be found in the BCT and BCC phases, this is logical as these two phases form a large proportion of the total. During partitioning the situation is reversed, so that austenite, which has a low phase fraction accommodates the majority of the carbon present in the alloy. However, although the total carbon content of the alloy is accounted for in as-quenched specimens, a

shortfall of approximately 12% exists in specimens that have been partitioned. As already mentioned in Section 7.5, in some diffraction patterns evidence exists for the existence of carbides, although unfortunately, for those specimens partitioned at 400°C positive identification or quantification of carbides was not possible. However, in the presence of silicon alloying additions to suppress equilibrium carbide (Fe_3C) formation, it would seem likely that epsilon carbide could be present. A review of the available literature suggests that the observations described above can be explained by an equilibrium distribution of carbon between epsilon carbide and strained interstitial sites in BCC martensite (Kalish and Roberts 1971) (Maalekian and Kozeschnik 2008).

7.6.3 Partitioned at 500°C using a molten salt bath

Partitioning at 500°C is initially observed to proceed very similarly to that discussed in the previous two sections, however, this similarity is relatively shortlived. BCC martensite carbon concentration reduces slightly more than for partitioning at 400°C, austenite carbon content reaches almost the same concentration as for partitioning at 400°C, however, after around 25 seconds of partitioning, decarburisation and decomposition of austenite is observed to commence. Lattice strains undergo a much more pronounced decrease than for partitioning at 400°C, although after around 25 to 30 seconds of partitioning the austenite lattice strain is observed to increase. Three possible explanations exist for the increase in austenite lattice strain. The first explanation is that crystallite size effects succeed lattice strain as the dominant cause of peak broadening. This observation and explanation could fit with an austenite decomposition mode involving continual sub-division of the remaining austenite by ferrite. However, as the increase in strain commences at relatively high austenite fractions this explanation could be considered doubtful. The second explanation is that martensitic transformation is occurring during the final quench, this could cause a genuine increase in austenite lattice strain (e.g. as illustrated in Figure 6.11). However, no evidence for the presence of a BCT structure was observed in any of the diffraction patterns. The third explanation is that as austenite fraction decreases, the austenite lattice strain measurement becomes increasingly sensitive to the placement of the background count level (e.g. if the background is set too low, peak broadening is perceived to have risen, resulting in a false increase in lattice strain). Further work is required to elucidate the exact transformations which occur during austenite decomposition, and the source of the apparent rise in lattice strain. In the situation of austenite decomposition, the only logical location where carbon can reside is carbides. In Section 7.5, a re-assessment of the diffraction data shows that during all

stages of the Q&P process ~100% of the alloy carbon content can be accounted for by introducing a carbide of Fe_3C type structure into the Rietveld analyses.

7.6.4 Consideration of all results

A difference in the partitioning dynamics is apparent between those specimens partitioned using an air furnace and those partitioned using salt baths. For the former, a slow decrease in BCC lattice parameter is evident over a time period of approximately 75 seconds, while for the latter, lattice parameter reduction occurs after much shorter partitioning times (around 2-5 seconds), with no further decrease at longer partitioning times. This behaviour could have more than one origin, firstly, the air-furnace partitioning method was not very precise (see final paragraph of Section 2.3.1) and so it seems possible that specimens partitioned by this method were subjected to a non-isothermal partitioning stage, resulting in a gradual increase of diffusion rate with partitioning time. Secondly, those specimens partitioned using an air furnace were initially quenched to 50°C, rather than the 10°C quench used for those partitioned using molten salt baths. This creates two differences; firstly, the ratio of martensite to untransformed austenite is changed by varying the temperature of the initial quench. Secondly, the re-arrangement of carbon which can occur during two minutes of holding at 50°C is expected to be much greater than for quenching to and holding at 10°C. A higher fraction of untransformed austenite might be expected to increase the rate at which carbon can be rejected from supersaturated martensite, hence this does not seem a likely explanation for the difference in partitioning dynamics. Holding at 50°C for two minutes following the initial quench could be expected to result in a greater proportion of carbon in low-energy, strained interstitial sites than for specimens quenched to 10°C. Hence, once the actual partitioning stage of the heat treatment commences a significant proportion of carbon may already have undergon ‘internal’ partitioning to low-energy locations, thus retarding partitioning of carbon to austenite.

For those specimens initially quenched to 10°C and partitioned at 400°C, the increase in austenite lattice parameter is very rapid for the first few seconds of partitioning, and then continues at a lower rate for a further 50 seconds. It is not known if this effect occurs in those specimens initially quenched to 50°C, as measurement was not possible in an as-quenched state. In those specimens initially quenched to 10°C and partitioned at 500°C, diffusion is expected to be much more rapid than for specimens partitioned at 400°C. Additionally, austenite decarburisation and decomposition occurs very soon after partitioning commences in those specimens partitioned at 500°C, consequently, although a very rapid rise in

austenite lattice parameter was evident, a slower secondary increase was not observed. Therefore, the specimens quenched to 10°C and partitioned at 400°C are unique in displaying the two-stage increase in austenite lattice parameter. The two-stage nature of austenite lattice parameter increases can be explained by three different hypotheses. Firstly, relief of hydrostatic elastic stresses (originally introduced by the expansive nature of martensitic transformation) during tempering could allow the rapid expansion of the austenite lattice; followed by a slower increase due to carbon migration from supersaturated martensite to austenite. Secondly, if retained austenite is assumed to consist of both thin, inter-lath, and granular morphologies, the response could be attributed to the diffusion of carbon into different austenite morphologies; e.g. the initial rapid increase is caused by diffusion of carbon into the thin, inter-lath austenite, while the slower secondary increase corresponds to carbon diffusion and equilibration in granular austenite. The third possible explanation is that this observation is a direct consequence of the way in which the diffusional process of partitioning and equilibration actually occurs (e.g. as illustrated in Figure 1.9 and Figure 1.10). As X-ray diffraction is a measurement technique which averages a colossal number of unit cells, it is not possible to determine which of these hypotheses applies, however, Transmission Electron Microscopy and Electron Diffraction, or Atom-Probe techniques could prove to be useful for further research in this area.

Lattice strain measurements show more pronounced reductions for those specimens partitioned at higher temperature (i.e. 400°C versus 500°C). If it is accepted that lattice strain is an approximate measure of defect density (e.g. dislocations), and that interstitial alloying elements (carbon and nitrogen) prefer to reside in strained interstitial sites in and around dislocations, rather than unstrained interstitial sites, then it is logical that lattice strain can influence partitioning behaviour. Various publications have been made on the subject of interstitial site occupancy in BCC metals (e.g. carbon in ferrite), and the binding energy which applies when atoms occupy strained interstitial sites such as those situated in and around dislocations (Cottrell and Bilby 1949) (Cochardt, Schoek et al. 1955) (Thomas and Leak 1955) (Sarrak and Suvorova 1969) (Kalish and Cohen 1970) (Gavrilyuk and Yagodzinskiy 1986). Similarly to carbon in ferrite, a binding energy between interstitial alloying elements (carbon or nitrogen) and lattice defects in austenite has also been determined (Gavrilyuk, Duz et al. 1987). Hence, a reduction in the density of lattice defects in either ferrite or austenite can be expected to result in increased vulnerability of carbon to competing reactions such as carbide precipitation.

For those specimens partitioned in molten salt baths at 500°C, after only a few seconds of partitioning, both austenite lattice parameter, and austenite phase fraction begin to decrease. In silicon alloyed steels, austenite decomposition during isothermal holding often results in the formation of a low carbon ferrite known as carbide-free-bainite, and carbon enriched austenite. In Figure 7.6, the lattice parameter measurements for austenite are the opposite of what would be expected if carbide-free-bainite was forming. Hence it must be concluded that the silicon alloying addition is ineffective at 500°C. This was confirmed in Sections 7.4 and 7.5 by a smaller number of diffraction measurements which clearly showed carbides of an Fe_3C type structure. Carbon concentration calculations have shown that precipitation of equilibrium carbides can account for ~100% of the alloy carbon content during the austenite decarburisation and decomposition process at 500°C. This contrasts with the behaviour seen at a partitioning temperature of 400°C, at which the austenite carbon concentration and phase fraction is seen to be highly stable. Therefore, stability of austenite at 400°C can probably be attributed to the effectiveness of the silicon alloying addition in preventing equilibrium carbide formation. In the absence of equilibrium carbide formation during partitioning at 400°C, the carbon present in the alloy is thought to form an equilibrium distribution between retained austenite, strained interstitial sites in ferrite (and austenite), and epsilon carbide.

Although the inclusion of an additional BCC phase in the structural model for as-quenched specimens is observed to result in values for BCT martensite lattice parameters that are in better agreement with previously published data, some complications are introduced by this method. In particular, estimations of carbon concentration in the additional BCC phase are observed to be somewhat higher than might be expected in martensite that has reverted from an as-quenched BCT structure to a BCC structure as a result of room temperature tempering (see Section 2.9.8 and Figure 2.14). However, the estimation of carbon concentration within the various phases present in as-quenched specimens is not critical to the study of the Q&P process, since it can reasonably be assumed that in as-quenched specimens the carbon concentration in both martensite and austenite is the same as the measured alloy composition. The redistribution of carbon within as-quenched martensite during room temperature tempering is acknowledged here, however, until partitioning is commenced the overall carbon concentration in martensite is considered to remain unchanged (i.e. little or no carbon migrates across a phase boundary).

Chapter 8
Sub-zero quenching of quenched, and quenched and partitioned specimens

Sub-zero quenching was used to evaluate the Q&P process in terms of thermodynamic stabilisation of austenite. Two specimens were measured by X-ray diffraction before and after sub-zero quenching, one specimen having received only an initial quench, and the other having been quenched and partitioned. A detailed description of the experimental procedure is to be found in Section 2.3.4.

8.1 Sub-zero quenching results

X-ray diffraction measurements are presented in Figure 8.1; for consistency, the same instrument was used to obtain all diffraction patterns.

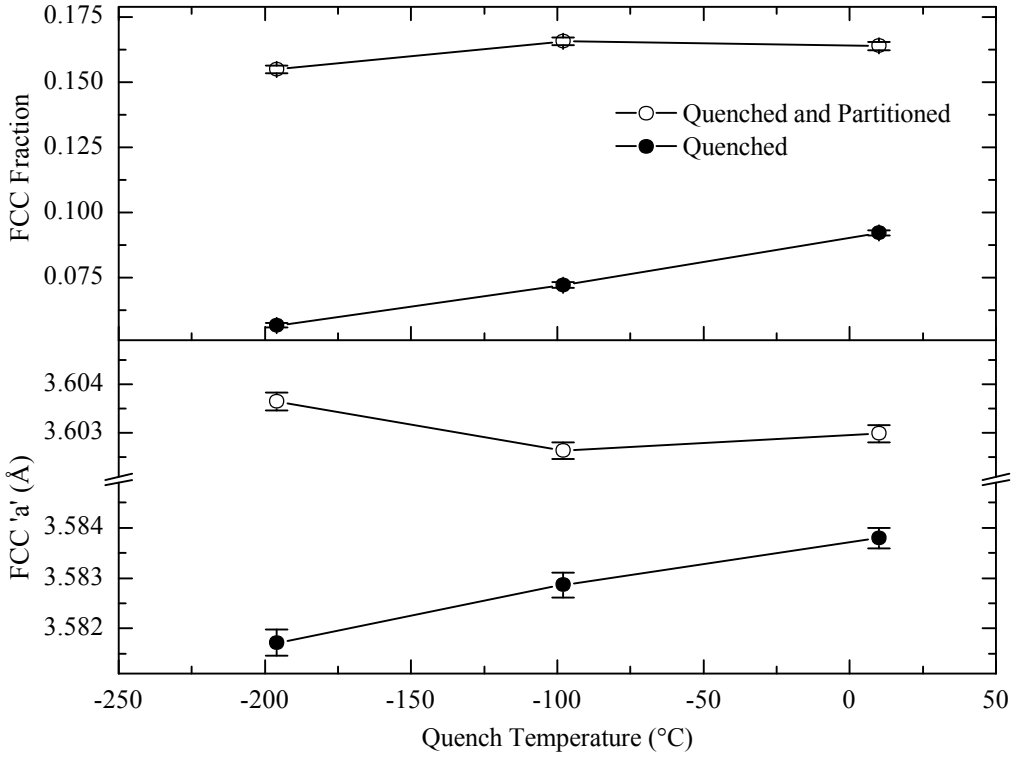

Figure 8.1 – Effect of sub-zero quenching on two specimens, one quenched, one quenched and partitioned

Predictions and measurements of retained austenite fraction after the initial quench to 10°C, and sub-zero quenching are given in Table 8.1 and Table 8.2. The austenite carbon concentration of the un-partitioned specimen was assumed to be

equal to that of the alloy composition, while that of the partitioned specimen was calculated from the austenite lattice parameter measurement using the procedure described in Section 2.9.9. Austenite carbon concentrations were then used with the formula of Andrews (Equation 1.3) to estimate martensite start temperatures.

			Quench Temperature (°C)		
			10	-98	-196
	Austenite Carbon (wt%)	Martensite Start Temperature (°C)	Predicted Retained Austenite (wt%)		
Quenched	0.53	193	13.3	-	-
Un-partitioned	0.53	193	-	4.1	1.4
Partitioned	1.61	-263	-	13.3	13.3

Table 8.1 – Predicted retained austenite fractions for initial quench and sub-zero quenching

			Quench Temperature (°C)		
			10	-98	-196
	Austenite Carbon (wt%)	Martensite Start Temperature (°C)	Measured Retained Austenite (wt%)		
Un-partitioned	0.53	193	9.2	7.2	5.7
Partitioned	1.61	-263	16.4	16.6	15.5

Table 8.2 – Measured retained austenite fractions for initial quench and sub-zero quenching

8.2 Discussion of sub-zero quenching results

For the unpartitioned specimen, the measured austenite phase fraction is lower than predicted after the initial quench to 10°C, but higher than predicted after both sub-zero quenches. The anomaly of lower than expected austenite phase fractions in specimens measured via X-ray diffraction after quenching to 10°C has already been discussed in Section 6.1.2 and 6.2.2, and so is not revisited here. The higher than expected austenite phase fractions after sub-zero quenching to -98 and -196°C must

be attributed to stabilisation of the retained austenite in between each quench. Various examples of stabilisation during holding at room temperature have been reported, a study by Banerjee (Figure 8.2) illustrates the dramatic effect of holding between 0 and 24 hours at room temperature prior to sub-zero quenching (Banerjee 1984).

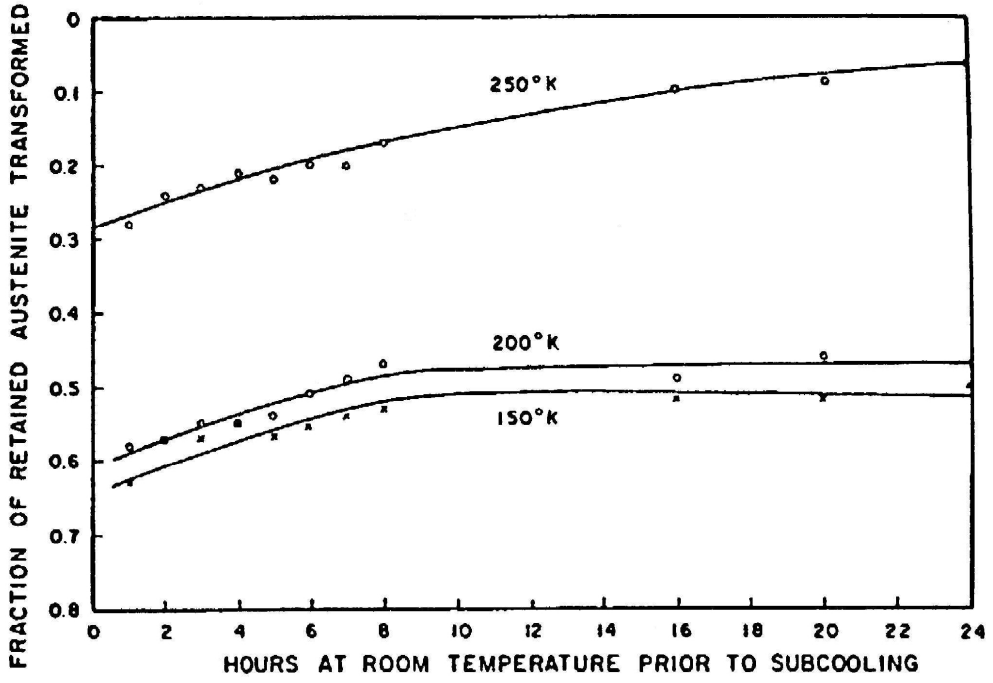

Figure 8.2 – Subatmospheric transformation chart of a low alloy steel (SAE 52100), oil quenched from 955°C; showing the fraction of the retained austenite that transforms after room temperature aging and subcooling to the indicated temperatures (Banerjee 1984), note the position of zero on the y-axis

As predicted by the Koistinen-Marburger equation, the retained austenite fraction in the partitioned specimen remains stable during sub-zero quenching to -98°C. However, despite the estimated martensite start temperature of -263°C, a small amount of retained austenite transforms during sub-zero quenching in liquid nitrogen at -196°C. This transformation can be explained by hypothesising the existence of retained austenite morphologies and volumes which were unable to equilibrate fully during 20 seconds of partitioning at 400°C; such areas could have a lower carbon concentration and therefore possess a martensite start temperature higher than -196°C. Incomplete partitioning may also explain previously reported austenite fraction variations such as those published by Matlock and co-workers (reproduced in Figure 1.24).

Austenite lattice parameter is observed to decrease with austenite phase fraction in the un-partitioned specimen. This agrees with the theory of Yershov and Oslon, who hypothesised that at martensite phase fractions above around 40-50%, the expansive nature of the martensite transformation exerts a compressive effect on retained austenite (Yershov and Oslon 1968). This observation is also in agreement with the correlation between austenite lattice parameter and austenite phase fraction presented in Figure 6.10.

In the partitioned specimen, the austenite lattice parameter increases upon a small fraction of the retained austenite transforming to martensite. Two possible explanations exist for this observation; firstly, although the partitioned specimen contains rather more than 40-50% martensite, only 'fresh' martensite is considered to have an effect on austenite lattice parameter. Therefore, this observation also agrees with the theory of Yershov and Oslon who hypothesised that martensite fractions below around 40-50% result in an elastic extension of the austenite lattice due to coherency between the martensite and austenite lattices (Yershov and Oslon 1968). The second explanation is that the increase in austenite lattice parameter could be due to martensitic transformation of those regions of austenite with the lowest carbon concentration (and therefore the highest martensite start temperature). Carbon concentration variations are hypothesised to exist in post-partitioned specimens for various reasons (e.g. incomplete equilibration of austenite due to insufficient partitioning time, and variations in the size or morphology of retained austenite). Those regions with the lowest carbon concentration would also be expected to have a lower lattice parameter, therefore, if they are removed from the X-ray diffraction measurement via transformation to martensite, the austenite lattice parameter, which is an average of all the unit cells measured, is observed to increase. The relevant diffraction pattern was inspected for evidence of additional tetragonal peaks, but none was found. However, as the change in phase fraction was relatively small, it is thought that detection of a small quantity of 'fresh' martensite may not be possible.

Chapter 9
In-situ neutron diffraction measurements of partitioning

This chapter contains results obtained during in-situ partitioning on the High Resolution Powder Diffractometer (HRPD) beamline at ISIS. The main partitioning variables assessed were partitioning temperature, and the presence or absence of silicon in the alloy. Three separate partitioning temperatures were studied, 300, 400 and 500°C. The effect of silicon content was examined by carrying out experiments on both silicon and silicon-free specimens. A single sub-zero quenched specimen was also subjected to in-situ partitioning measurements to gain some insight into the effect of austenite phase fraction on partitioning behaviour (all other specimens were quenched to 10°C prior to in-situ partitioning).

For each specimen, results are presented illustrating the evolution of lattice parameter, phase fraction and lattice strain with respect to partitioning time. These are followed by estimations of carbon concentration and carbon distribution. Carbon distribution is expressed as a percentage of the total alloy carbon content. In all plots, vanadium can temperature (measured) and specimen temperature (calculated) are also shown. The first set of results is presented in its entirety to illustrate the processing undertaken on the outputs from the Rietveld structural models; results for subsequent specimens are given in a slightly more condensed format. Specimen IDs with the prefix 36 or 38 contain silicon, while those with the prefix 27 are silicon free (chemical analyses may be found in Section 4.1.2 on page 129).

In a few of the datasets presented, gaps are observed to exist in the measurements. These gaps were caused by unpredictable temporary outages of the neutron spallation source and so unfortunately were unavoidable. During the early stages of partitioning, microstructural changes occured relatively quickly and so consecutive datasets were processed and plotted. At longer partitioning times transformations were observed to be somewhat slower, consequently it was considered acceptable to omit some datasets. All data was initially processed by both of the methods described in Section 2.10.5 (i.e. commencing refinements in the as-quenched state with either two or three phases in the structural model). Having tried both methods, it became apparent that starting the Rietveld refinements with a two phase model and then switching to a three phase model when tempering became apparent was the most suitable method. This differs from the treatment of the X-ray diffraction data, where the variability in the length of time between quenching and

measurement, and the effect of mechanical polishing meant that a three phase model for as-quenched specimens was preferable. For those specimens that were subjected to a static measurement in the as-quenched condition prior to in-situ partitioning, this data is also included and appears on plots at partitioning time equal to zero.

The experimental results commence with specimen 3802, this specimen was cut from a silicon alloyed sample and the temperature selected for partitioning was 500°C, heating (partitioning) of the specimen was initiated from room temperature. Figure 9.1 illustrates the lattice parameters, as recorded and corrected for thermal expansion. Phase fraction, lattice strain, carbon concentration and carbon distribution are shown in Figure 9.2 to Figure 9.5. It is interesting to note that the total carbon accounted for (lowermost pane in Figure 9.5) undergoes an inflection.

The results for specimen 3802 are followed by two more silicon alloyed specimens, 3803 and 3804, partitioned at 400 and 300°C respectively. Partitioning of specimen 3803 was started from room temperature, partitioning of specimen 3804 commenced with the furnace still warm following the previous experiment. Specimen 3803 was affected by an unexpected outage of the neutron spallation source. Therefore, a gap of approximately 10 minutes is present during the early stage of partitioning, unfortunately this is also the time period when the most rapid microstructural changes are expected to take place. Results for specimen 3803 appear in Figure 9.6 to Figure 9.10, while those for specimen 3804 can be found from Figure 9.11 to Figure 9.15. The final experiment reported for silicon alloyed material concerns a sub-zero quenched specimen (3603) partitioned at 500°C. This experiment was started with the furnace at room temperature, the results are to be found in Figure 9.16 to Figure 9.20, a short (~3.5 minutes) neutron spallation source outage occurred during the early stages of this experiment.

The remaining datasets presented were all collected from silicon free specimens, in each case the experiment was commenced with the furnace still warm from the previous experiment. The first dataset presented is for specimen 2704 partitioned at 500°C (Figure 9.21 to Figure 9.25), it is notable that the austenite lattice parameter versus time history for this experiment appears erratic compared to other datasets (possible explanations for this appear in the discussion section). Results for specimen 2703, partitioned at 400°C appear in Figure 9.26 to Figure 9.30, while those for specimen 2702, partitioned at 300°C are to be found in Figure 9.31 to Figure 9.35.

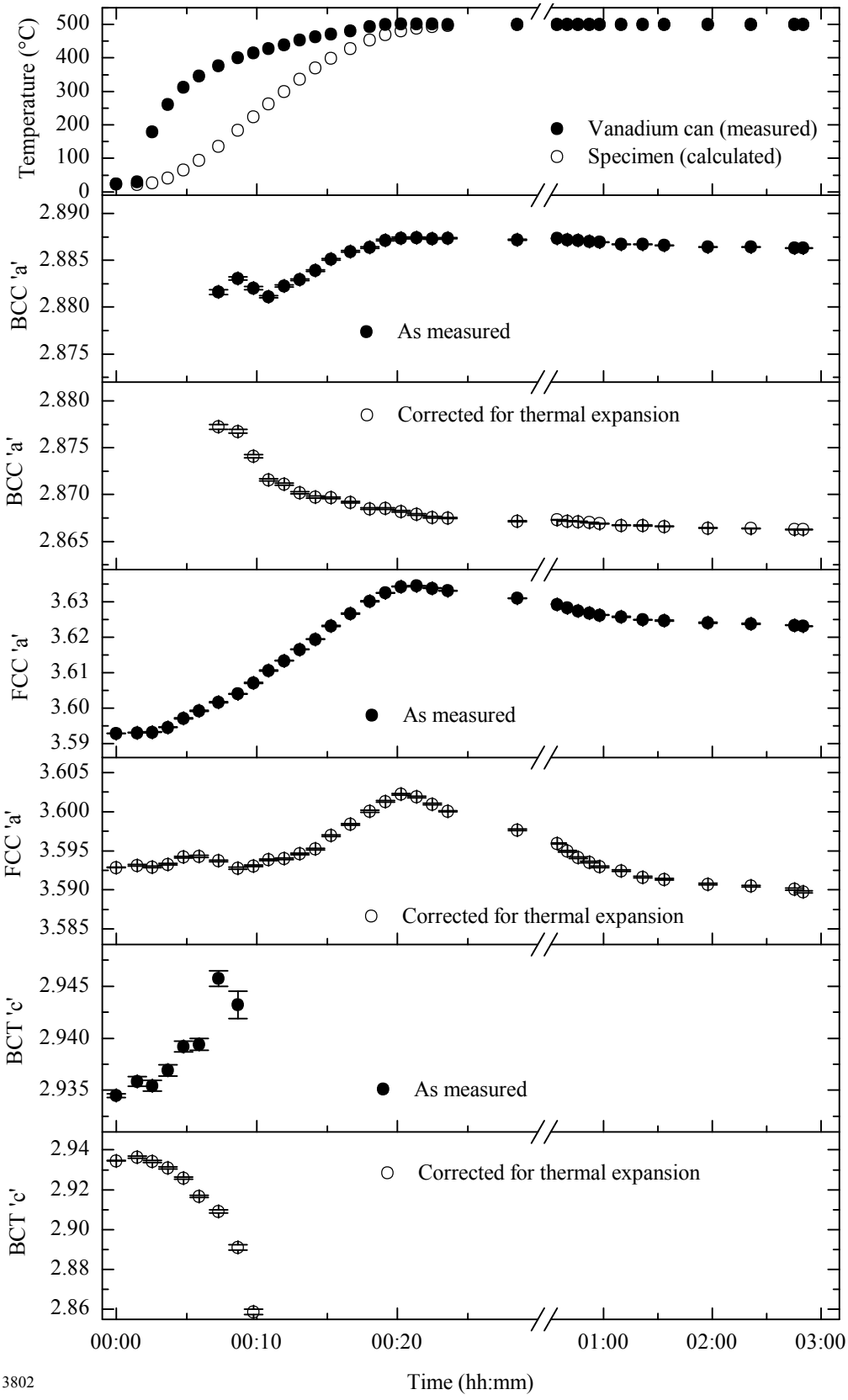

Figure 9.1 – Lattice parameters as measured and corrected for thermal expansion, for a Si-alloyed specimen quenched to 10°C and partitioned at 500°C (specimen 3802)

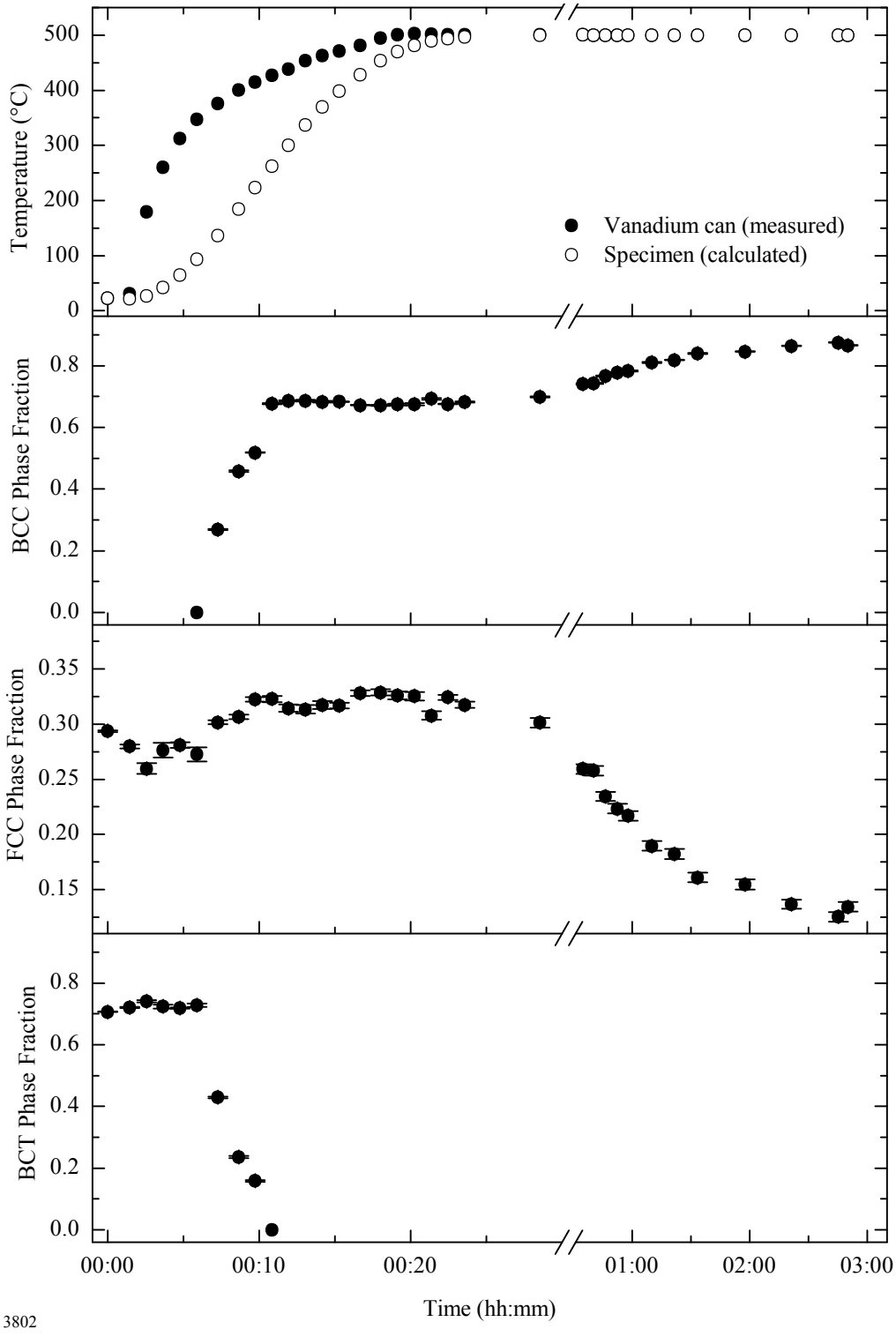

Figure 9.2 – Phase fractions for a Si-alloyed specimen quenched to 10°C and partitioned at 500°C (specimen 3802)

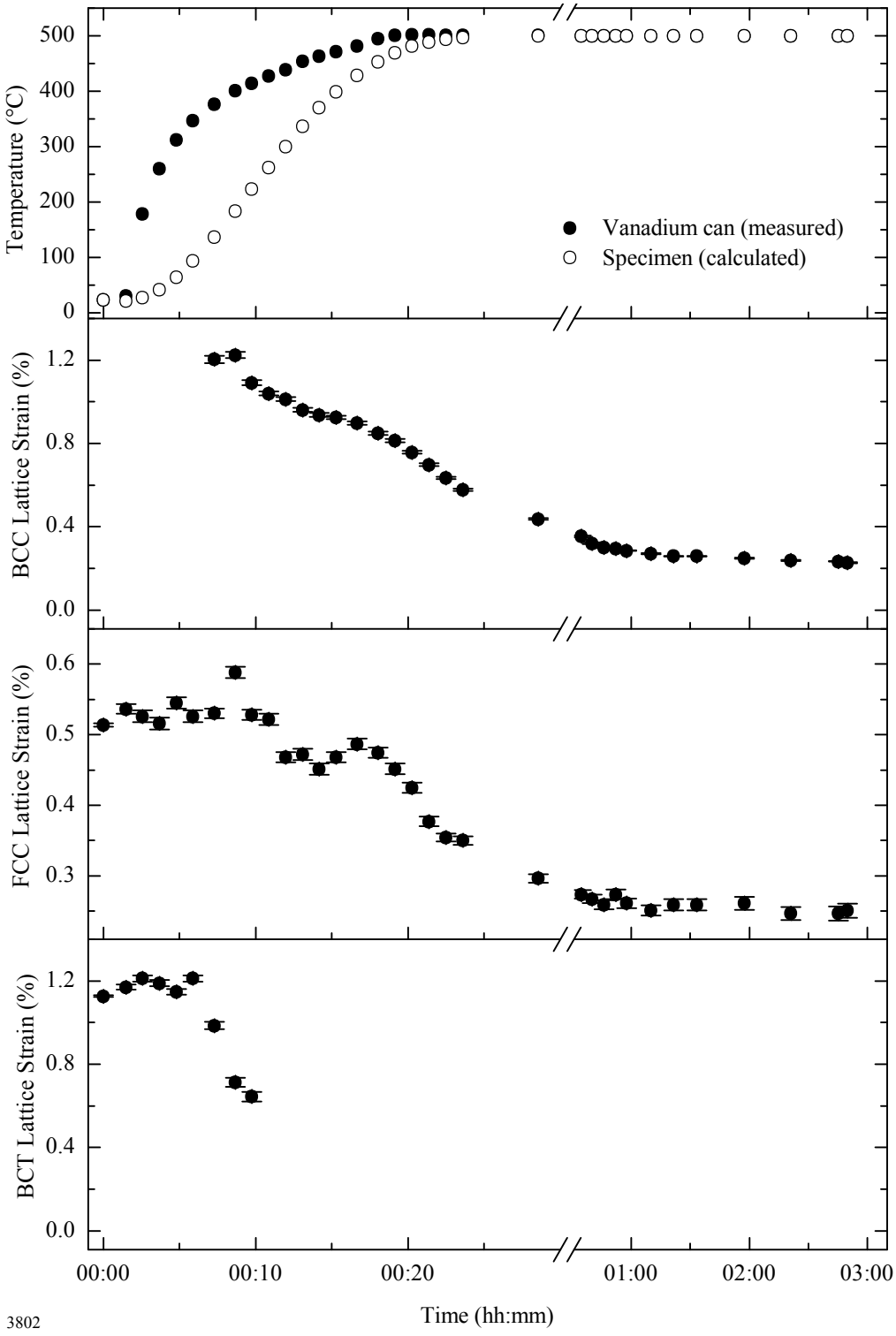

Figure 9.3 – Lattice strains for a Si-alloyed specimen quenched to 10°C and partitioned at 500°C (specimen 3802)

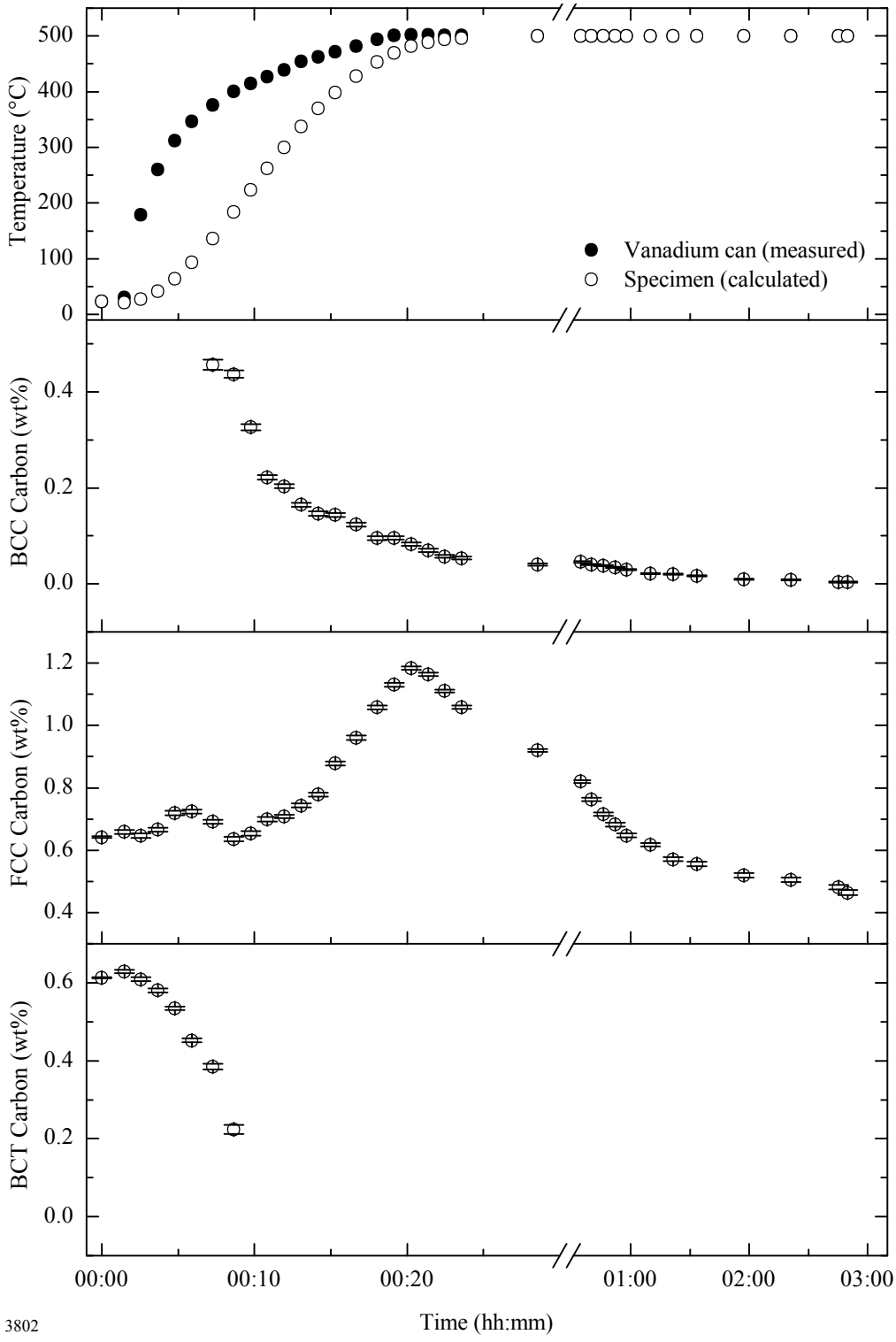

Figure 9.4 – Carbon concentrations for a Si-alloyed specimen quenched to 10°C and partitioned at 500°C (specimen 3802)

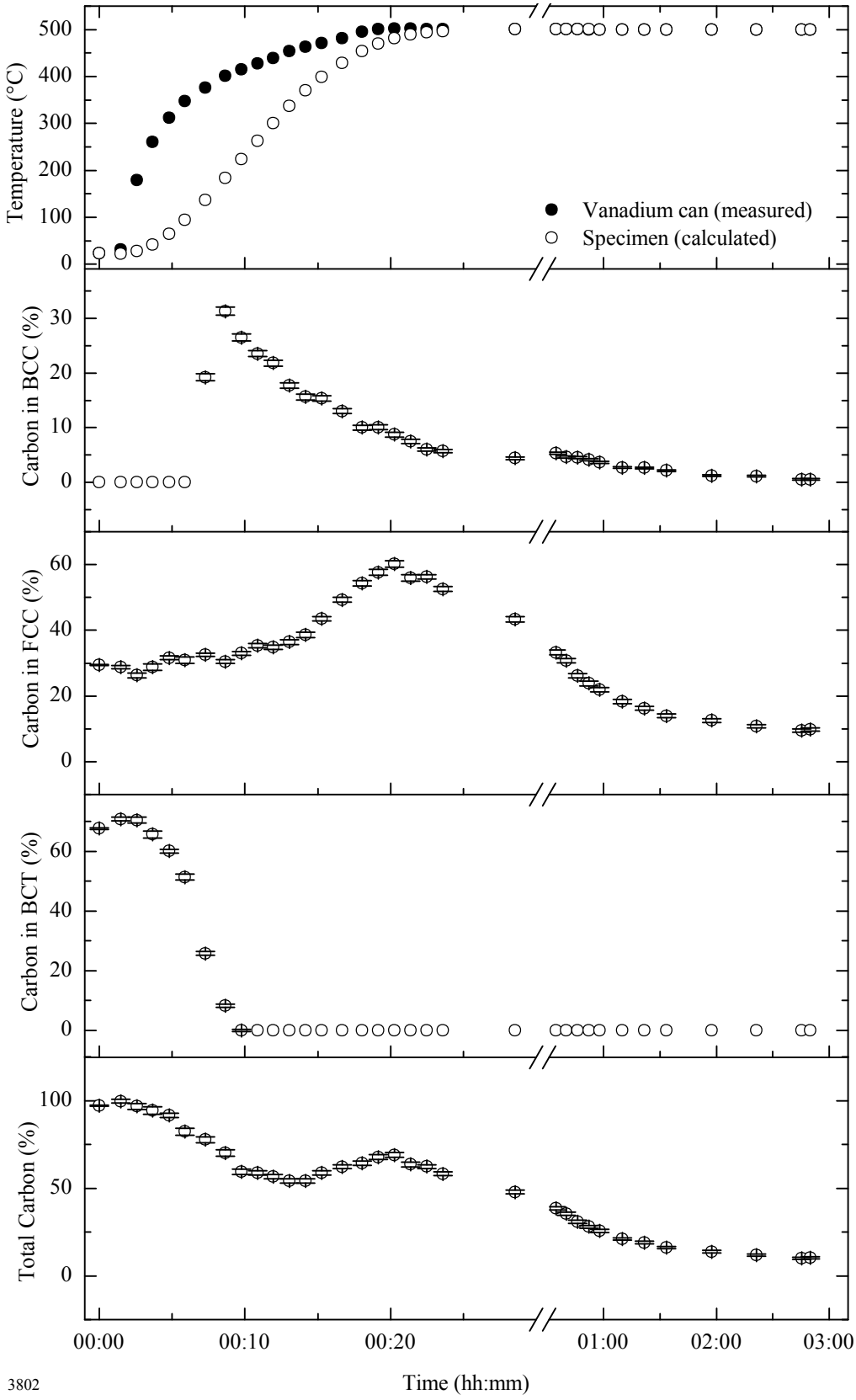

Figure 9.5 – Carbon distribution for a Si-alloyed specimen quenched to 10°C and partitioned at 500°C (specimen 3802)

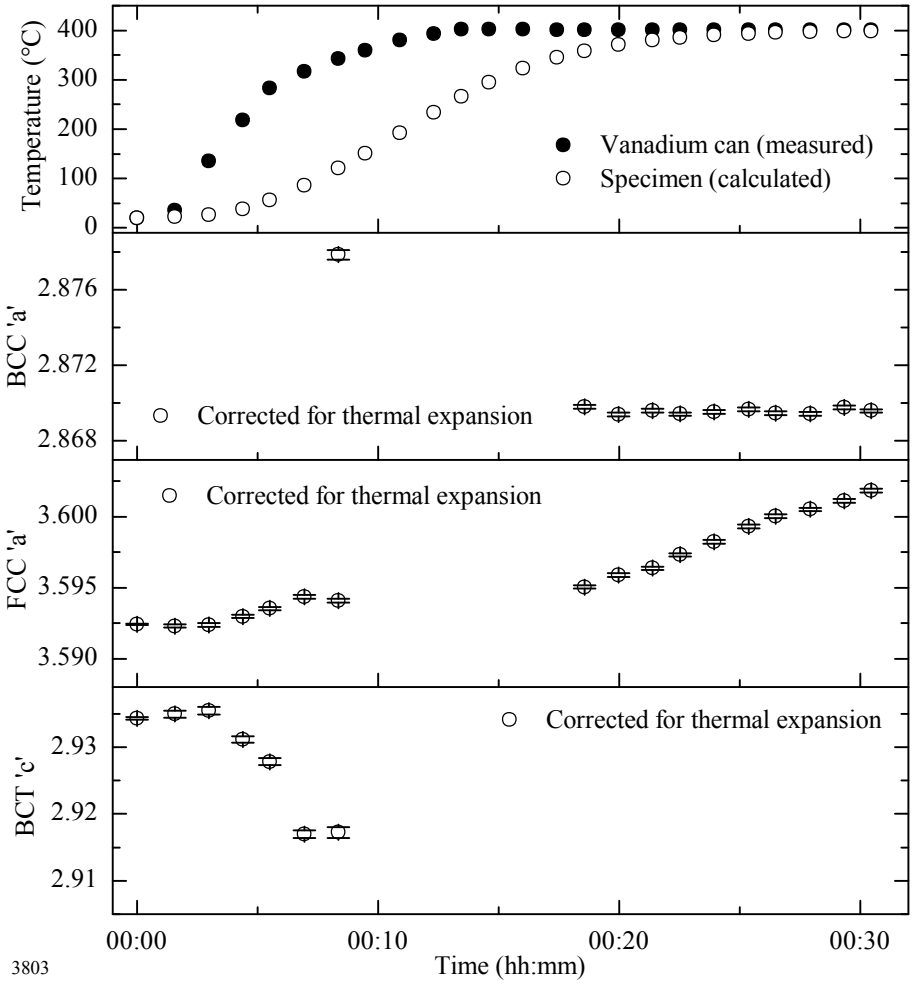

Figure 9.6 – Lattice parameters for a Si-alloyed specimen quenched to 10°C and partitioned at 400°C (specimen 3803)

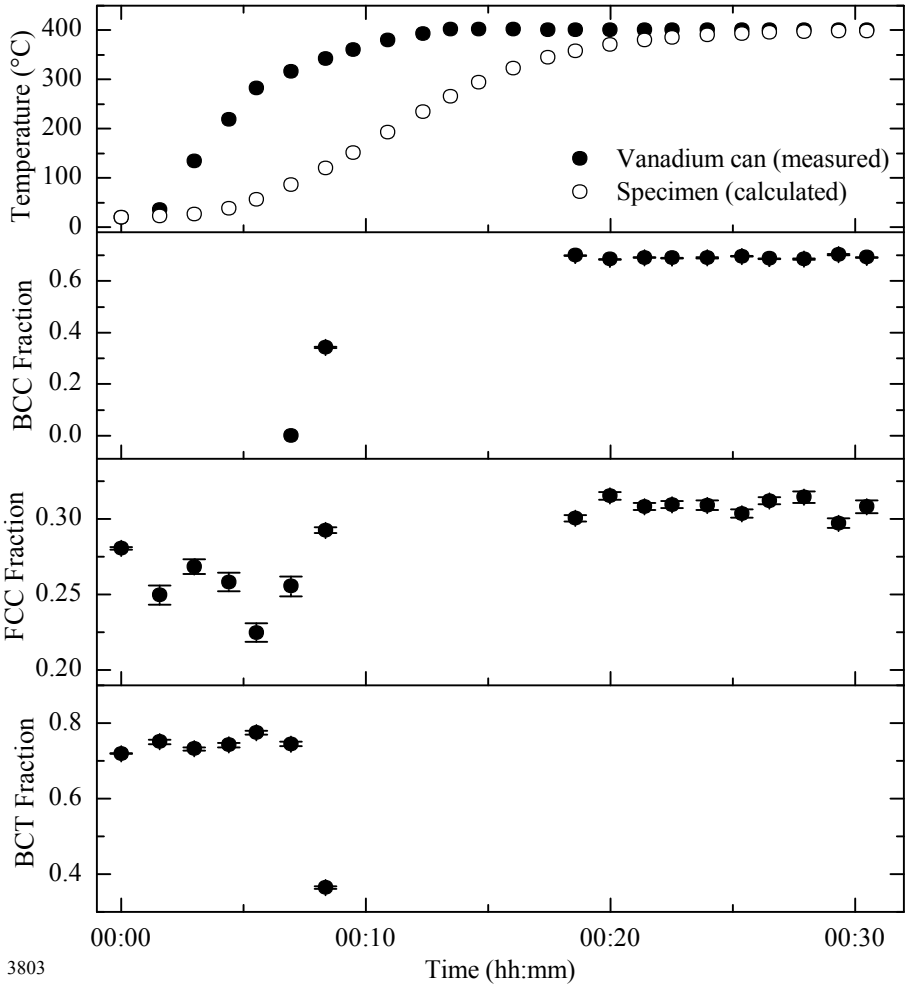

Figure 9.7 - Phase fractions for a Si-alloyed specimen quenched to 10°C and partitioned at 400°C (specimen 3803)

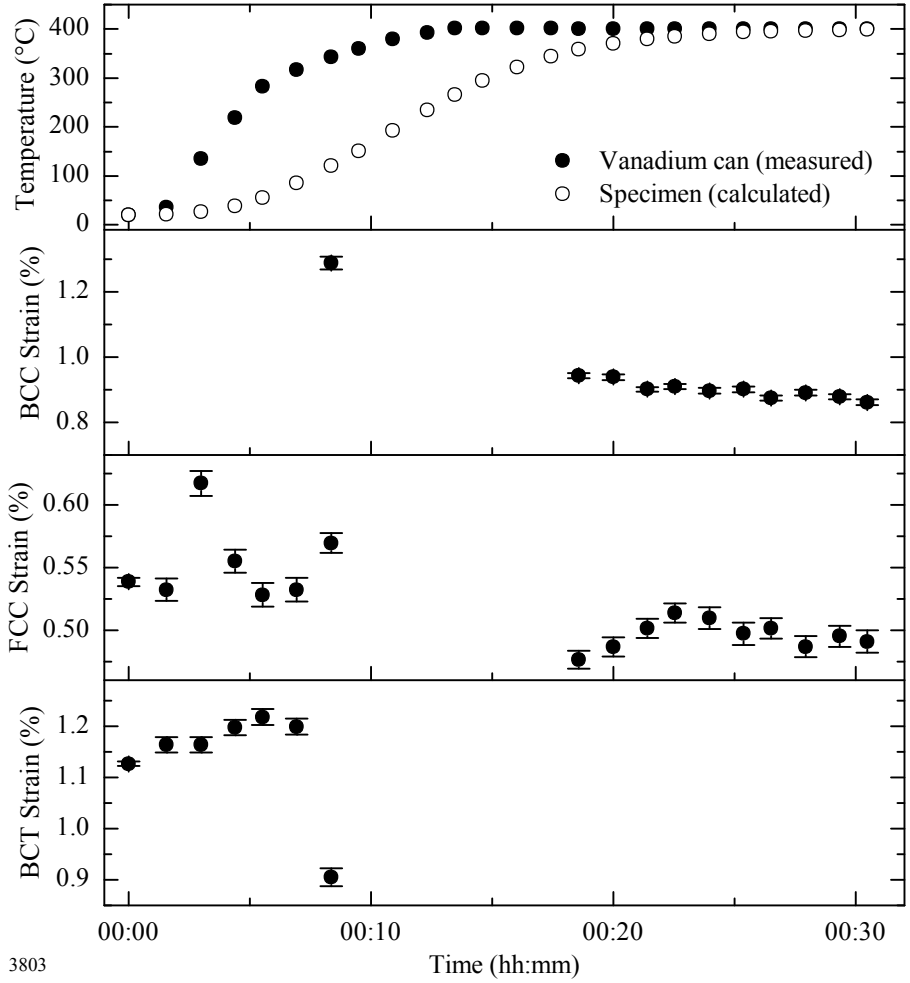

Figure 9.8 – Lattice strains for a Si-alloyed specimen quenched to 10°C and partitioned at 400°C (specimen 3803)

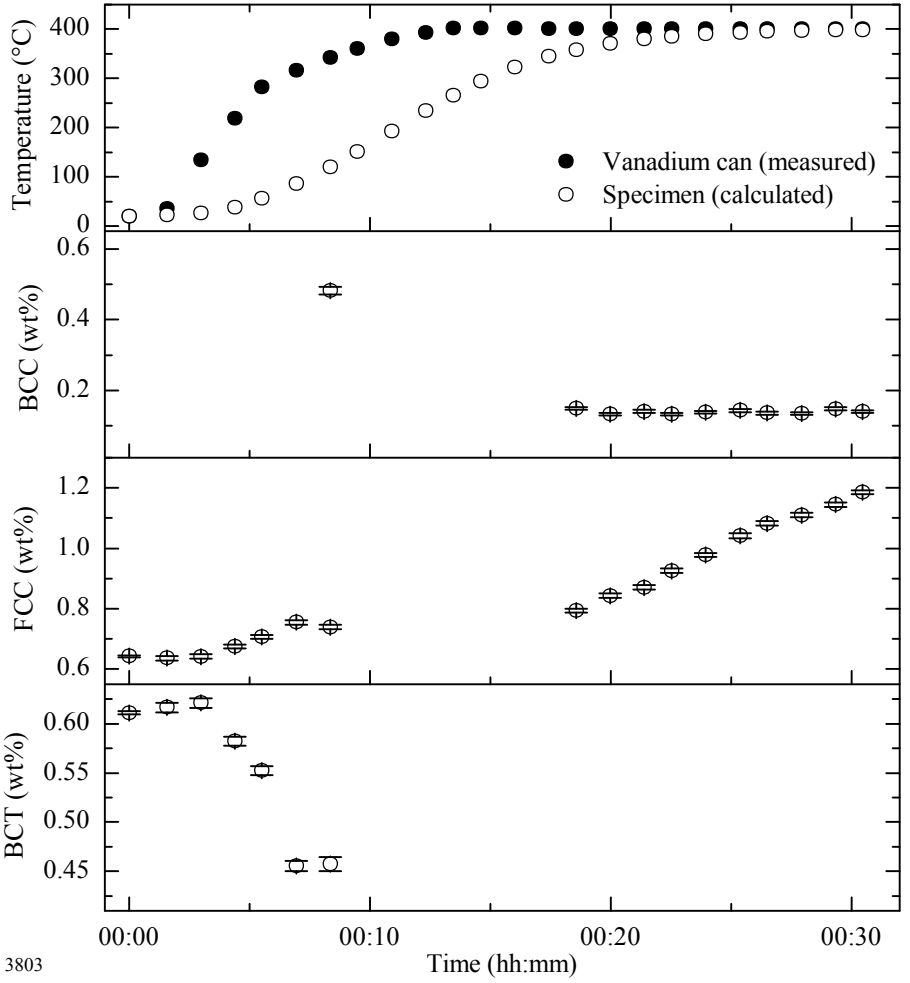

Figure 9.9 – Carbon concentrations for a Si-alloyed specimen quenched to 10°C and partitioned at 400°C (specimen 3803)

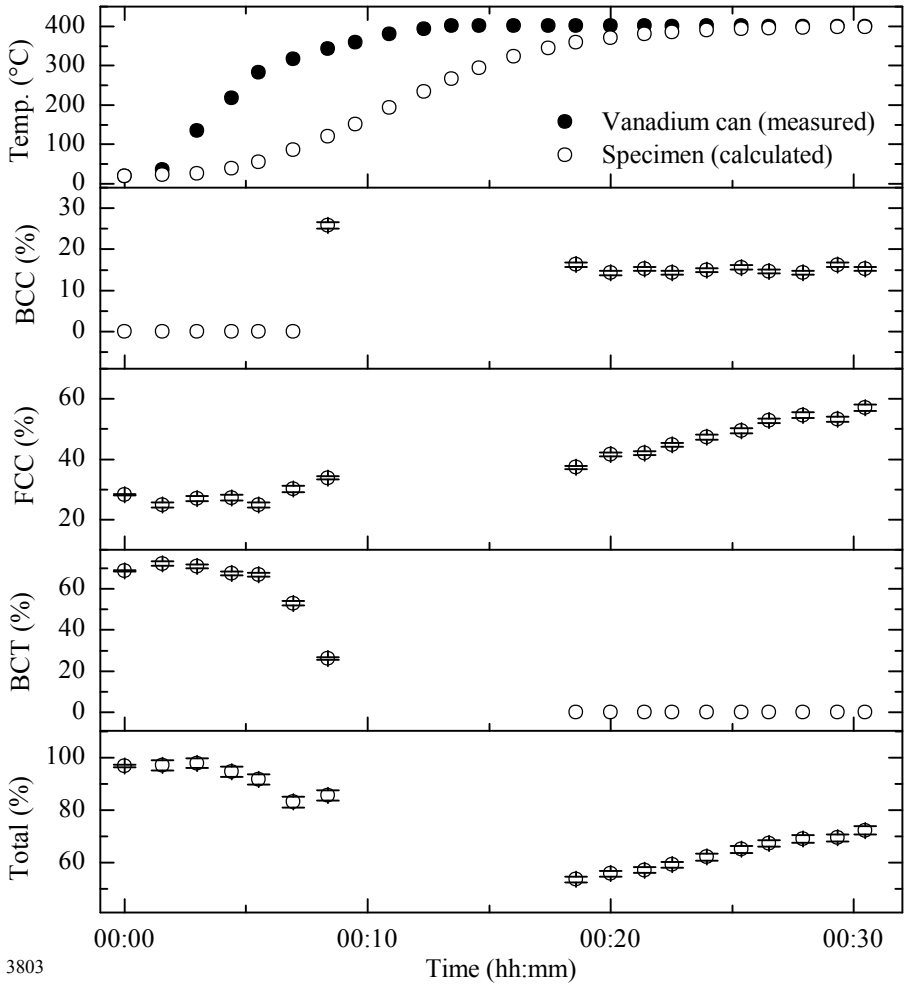

Figure 9.10 – Carbon distribution for a Si-alloyed specimen quenched to 10°C and partitioned at 400°C (specimen 3803)

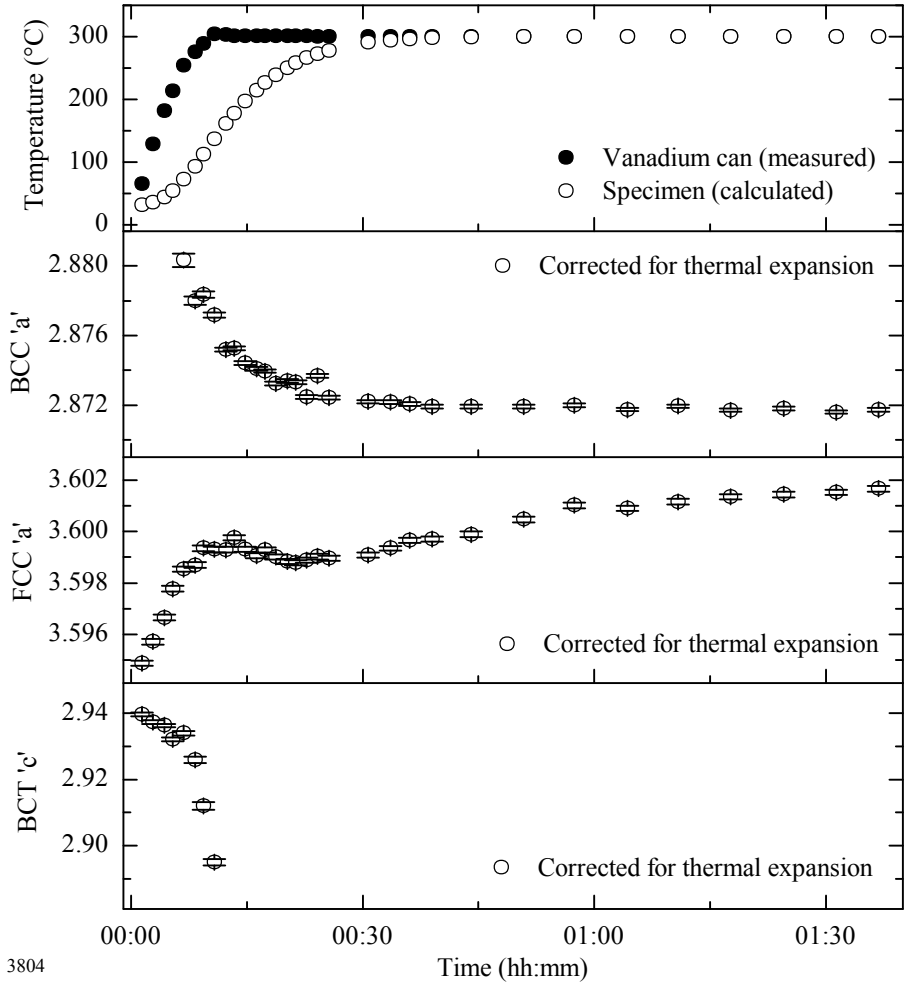

Figure 9.11 – Lattice parameters for a Si-alloyed specimen quenched to 10°C and partitioned at 300°C (specimen 3804)

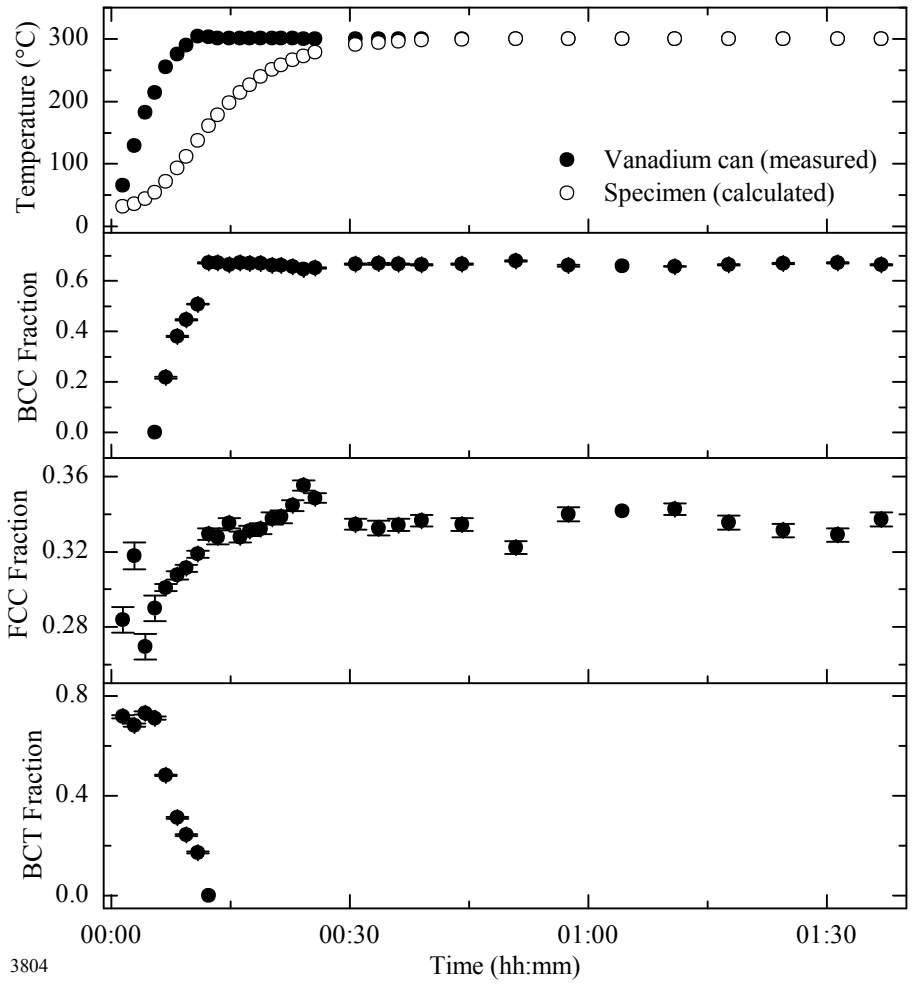

Figure 9.12 - Phase fractions for a Si-alloyed specimen quenched to 10°C and partitioned at 300°C (specimen 3804)

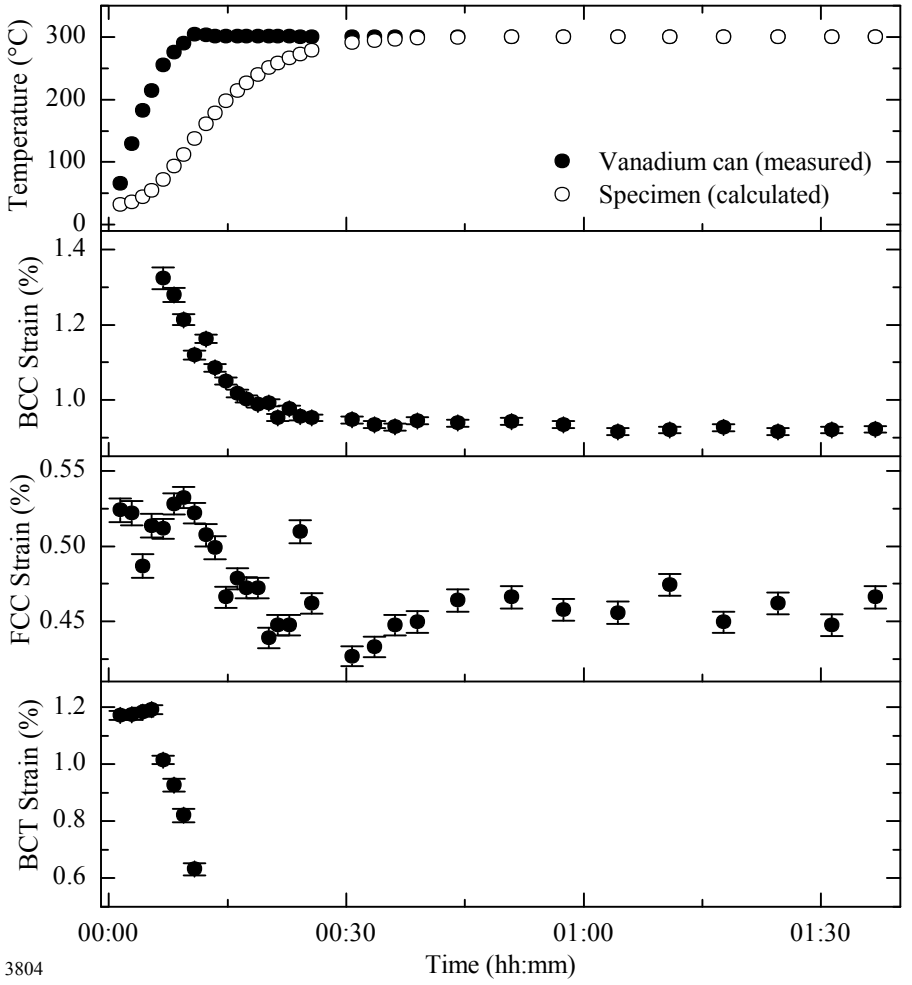

Figure 9.13 – Lattice strains for a Si-alloyed specimen quenched to 10°C and partitioned at 300°C (specimen 3804)

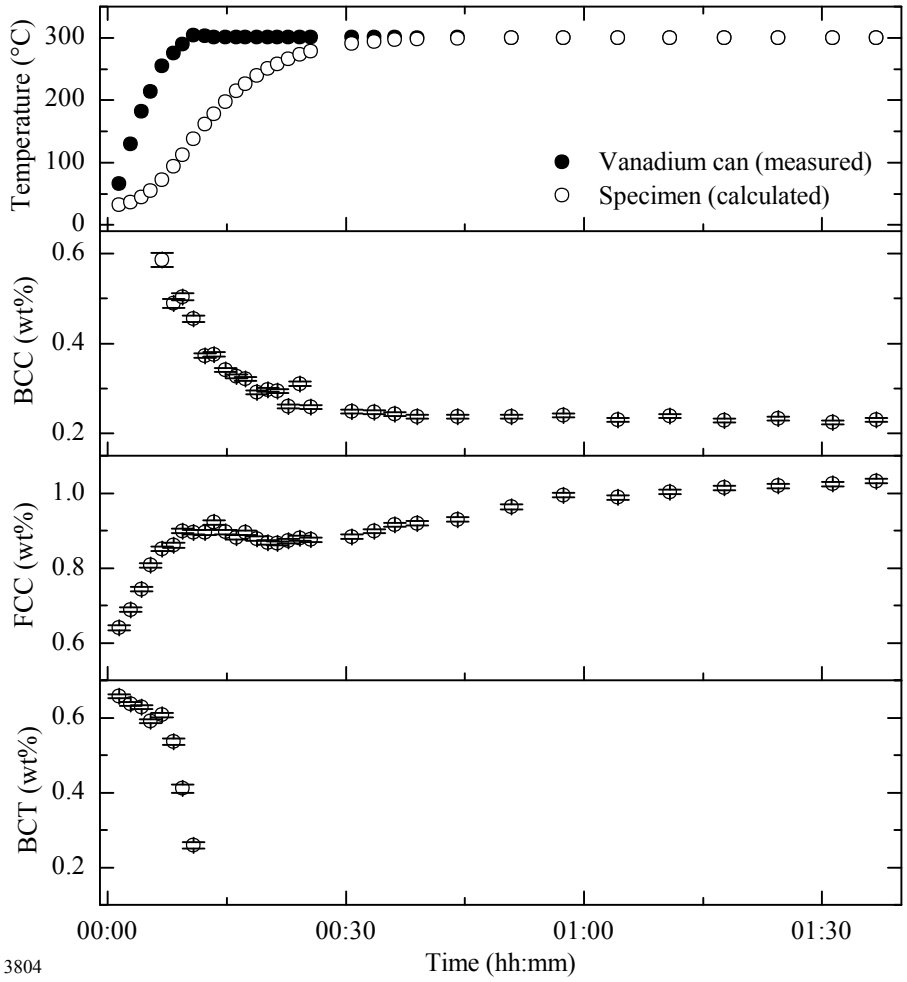

Figure 9.14 – Carbon concentrations for a Si-alloyed specimen quenched to 10°C and partitioned at 300°C (specimen 3804)

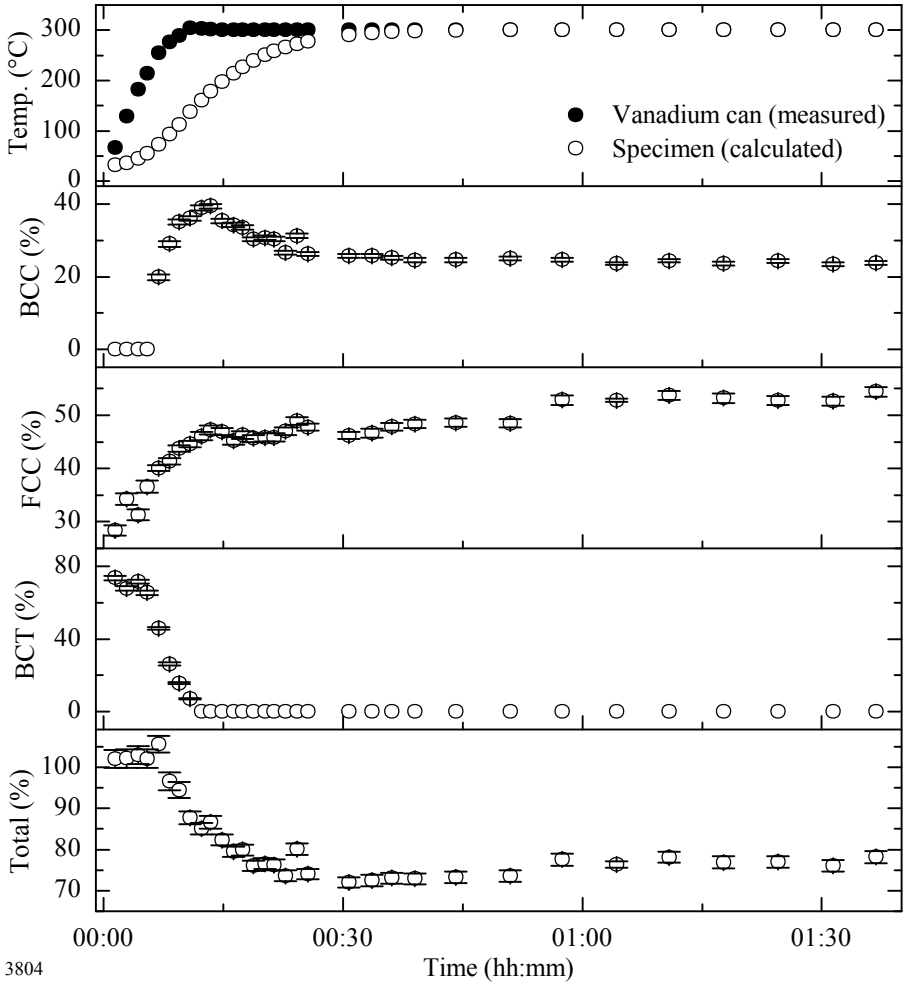

Figure 9.15 – Carbon distribution for a Si-alloyed specimen quenched to 10°C and partitioned at 300°C (specimen 3804)

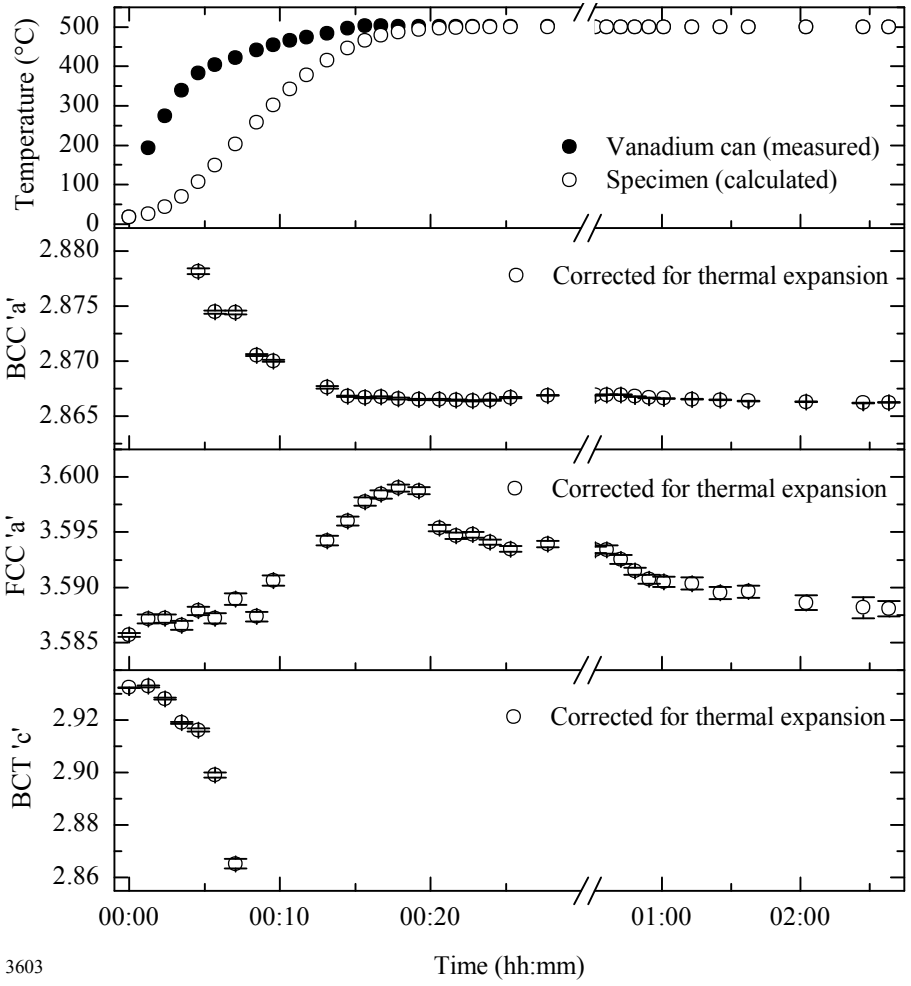

Figure 9.16 – Lattice parameters for a Si-alloyed specimen quenched to -61°C and partitioned at 500°C (specimen 3603)

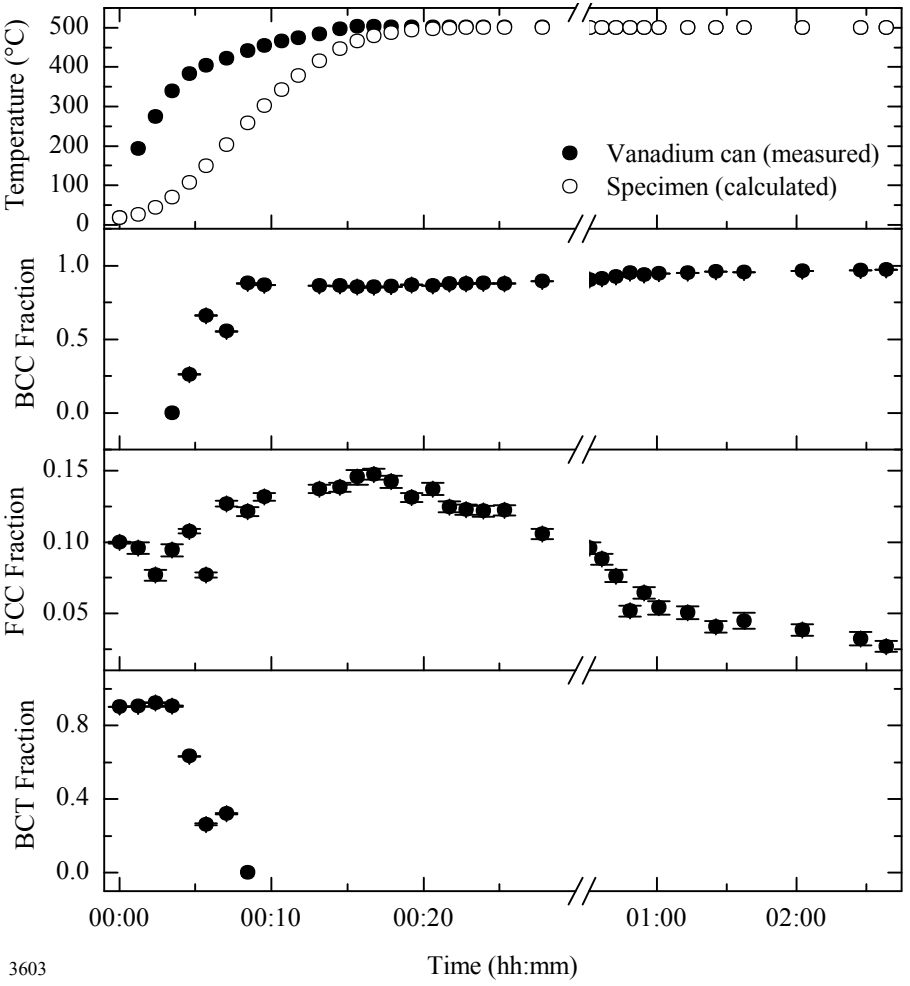

Figure 9.17 - Phase fractions for a Si-alloyed specimen quenched to -61°C and partitioned at 500°C (specimen 3603)

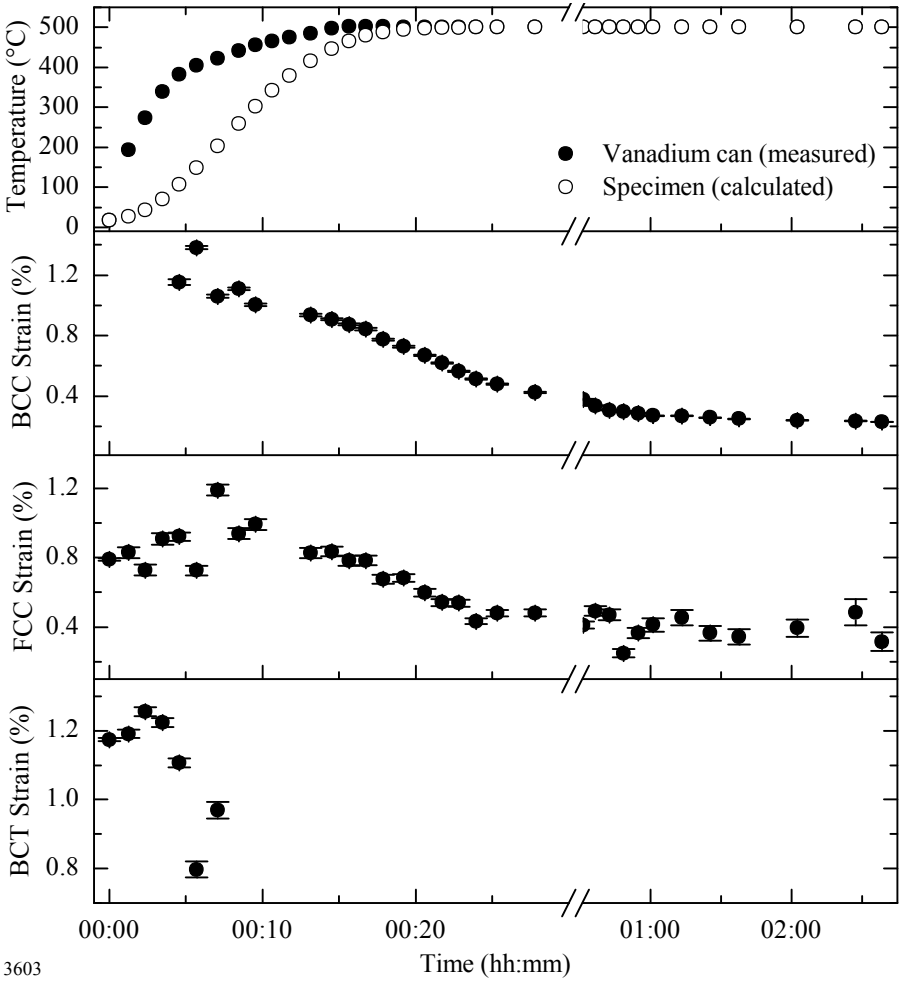

Figure 9.18 – Lattice strains for a Si-alloyed specimen quenched to -61°C and partitioned at 500°C (specimen 3603)

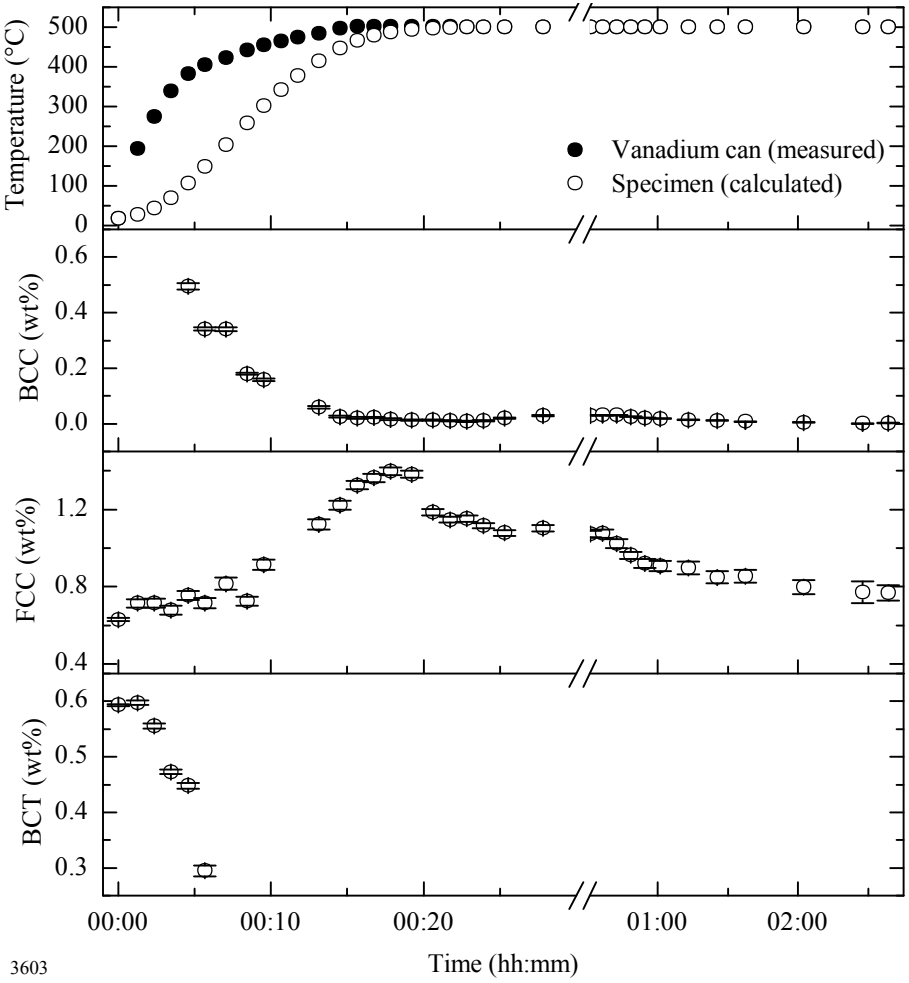

Figure 9.19 – Carbon concentrations for a Si-alloyed specimen quenched to -61°C and partitioned at 500°C (specimen 3603)

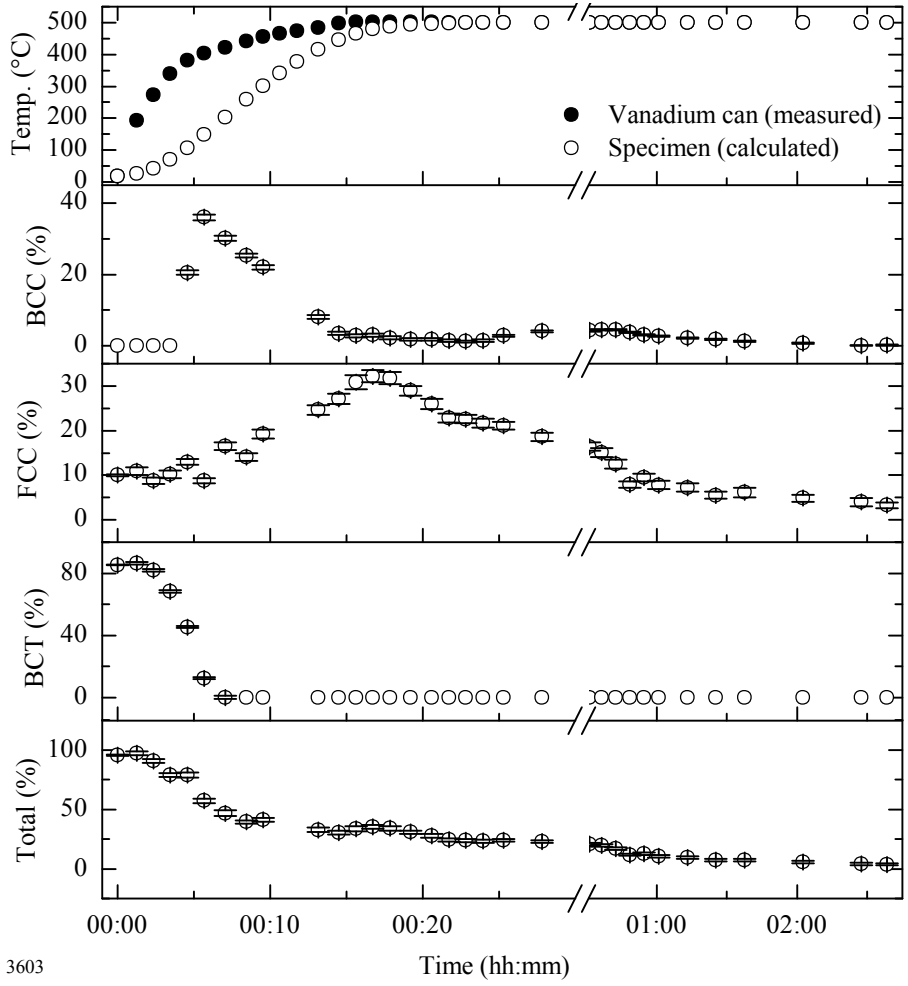

Figure 9.20 – Carbon distribution for a Si-alloyed specimen quenched to -61°C and partitioned at 500°C (specimen 3603)

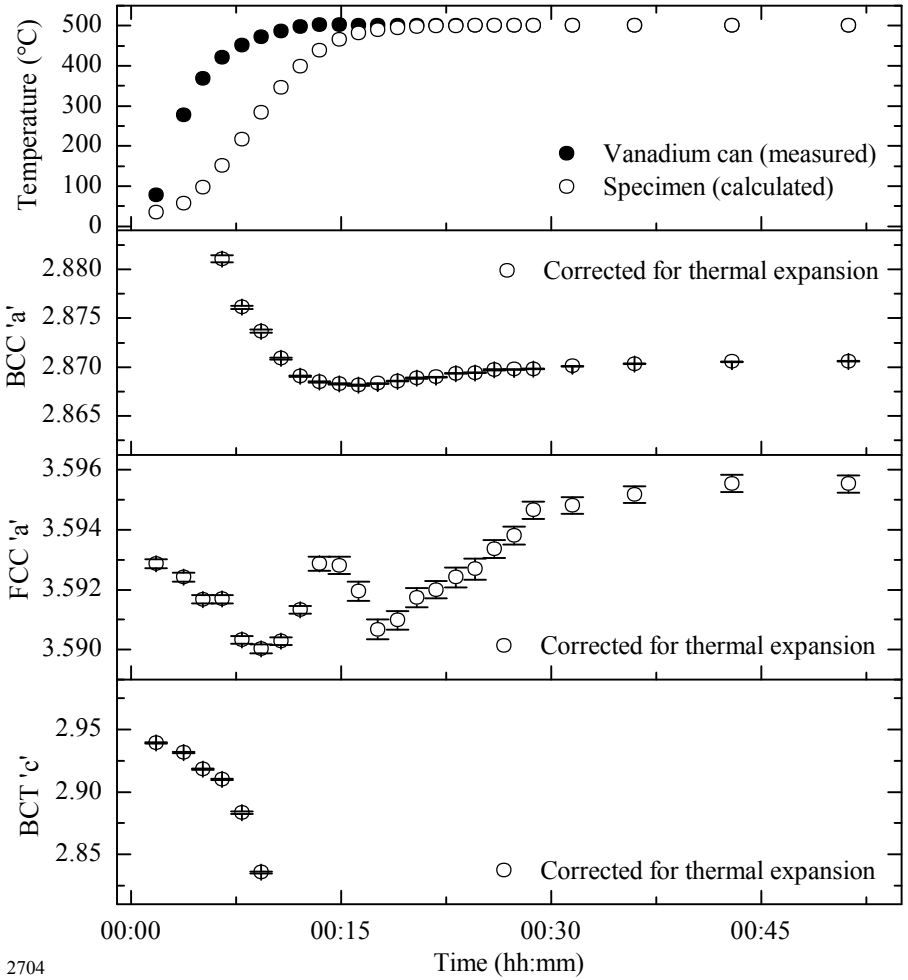

Figure 9.21 – Lattice parameters for a Si-free specimen quenched to 10°C and partitioned at 500°C (specimen 2704)

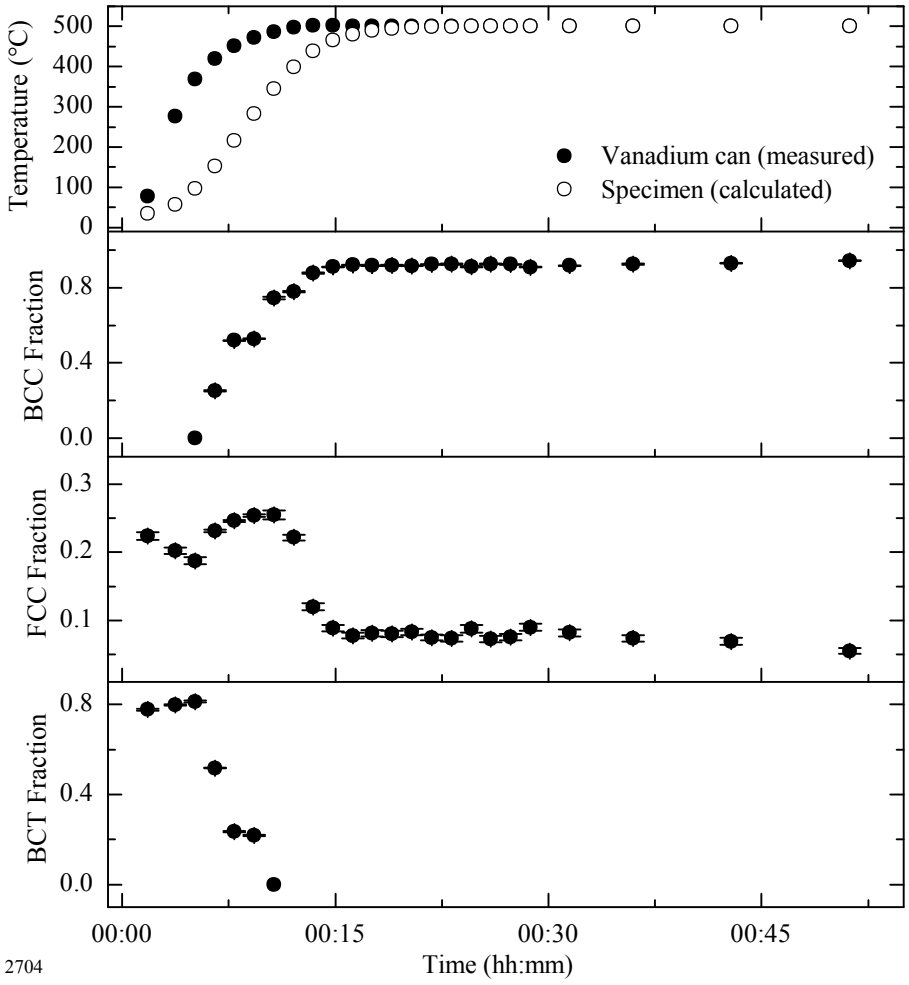

Figure 9.22 - Phase fractions for a Si-free specimen quenched to 10°C and partitioned at 500°C (specimen 2704)

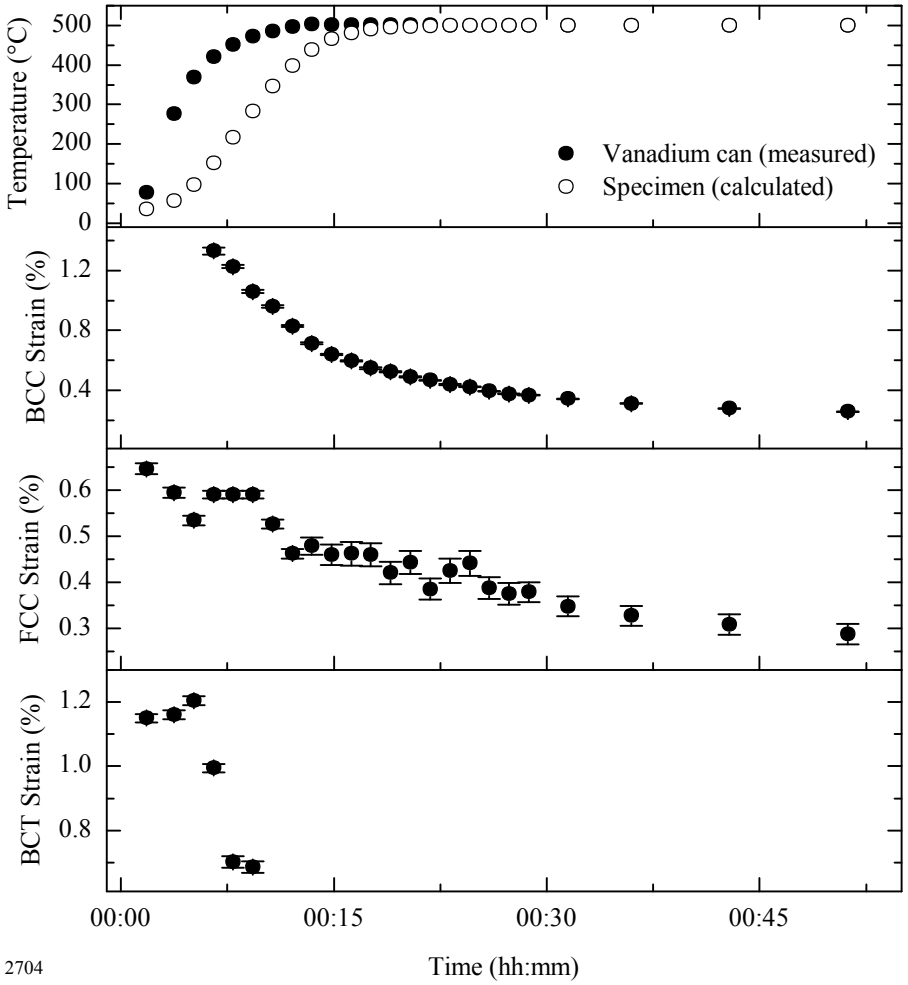

Figure 9.23 – Lattice strains for a Si-free specimen quenched to 10°C and partitioned at 500°C (specimen 2704)

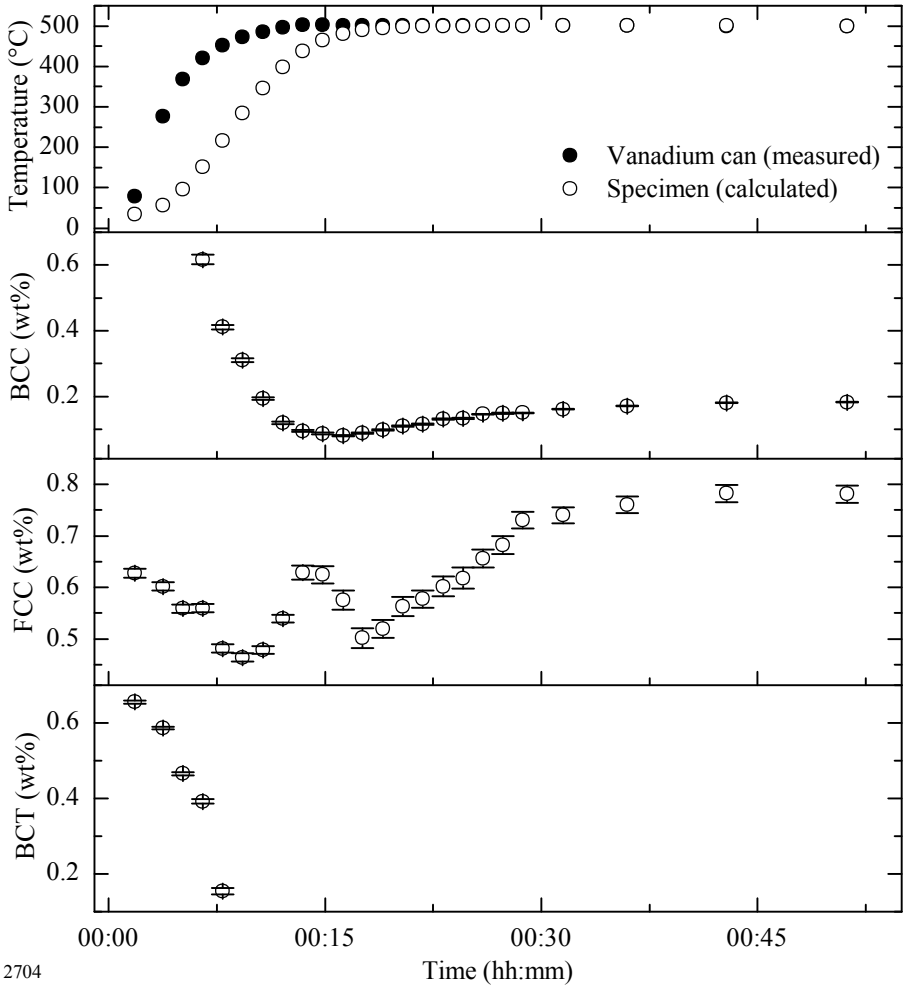

Figure 9.24 – Carbon concentrations for a Si-free specimen quenched to 10°C and partitioned at 500°C (specimen 2704)

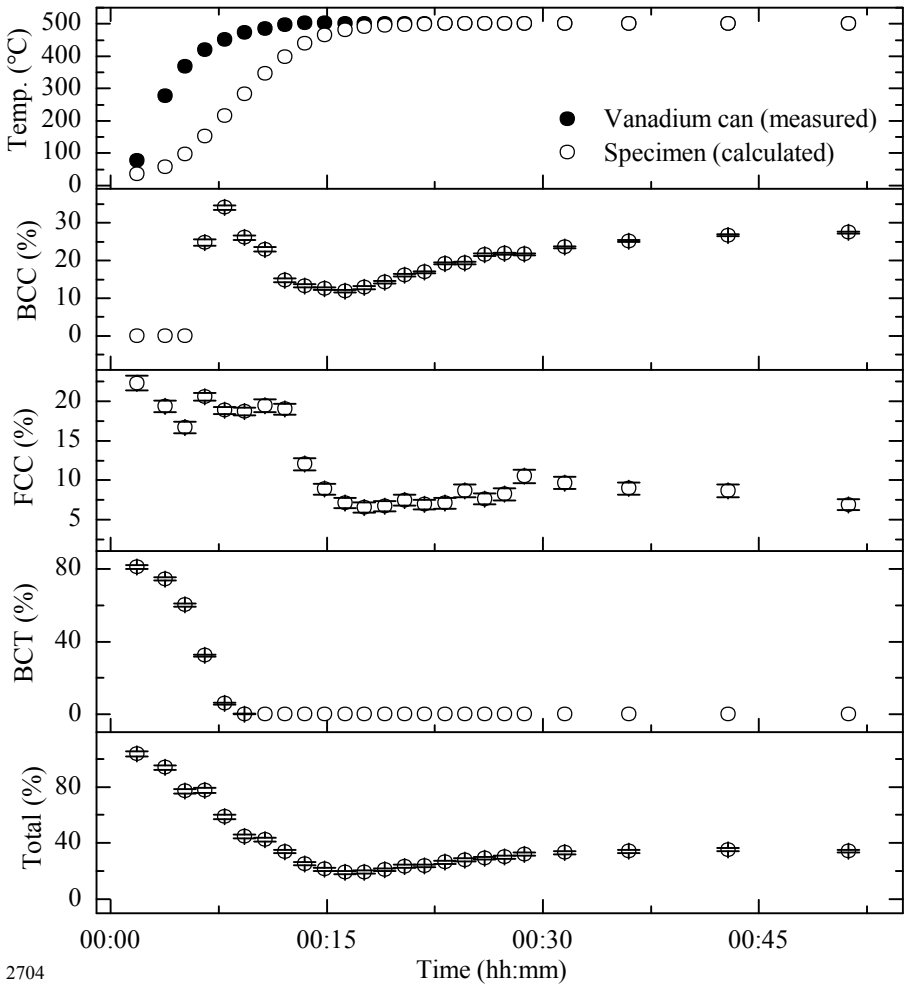

Figure 9.25 – Carbon distribution for a Si-free specimen quenched to 10°C and partitioned at 500°C (specimen 2704)

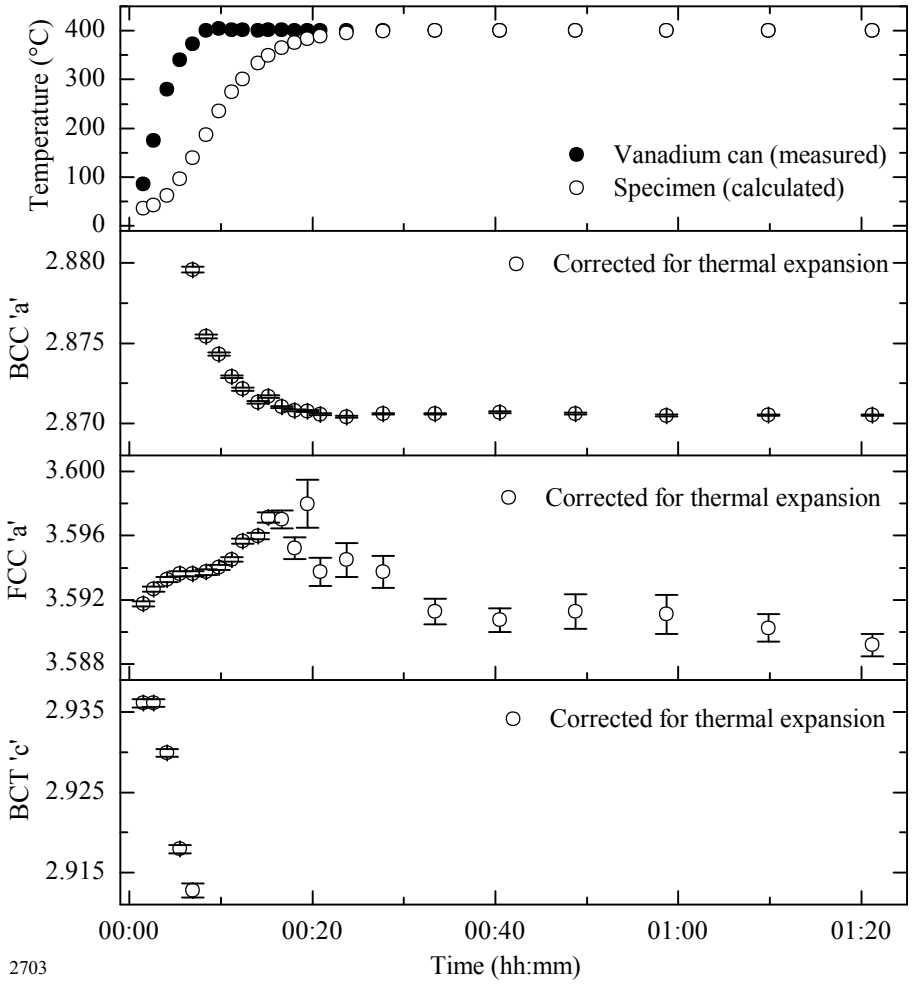

Figure 9.26 – Lattice parameters for a Si-free specimen quenched to 10°C and partitioned at 400°C (specimen 2703)

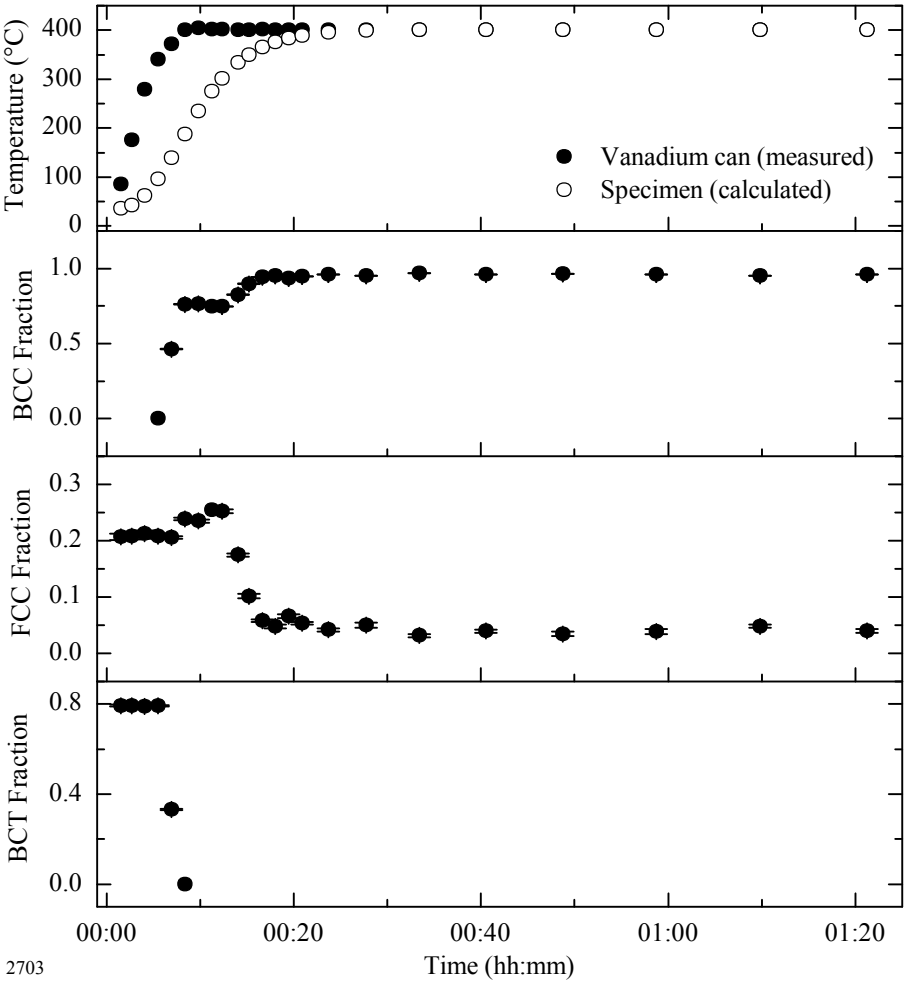

Figure 9.27 - Phase fractions for a Si-free specimen quenched to 10°C and partitioned at 400°C (specimen 2703)

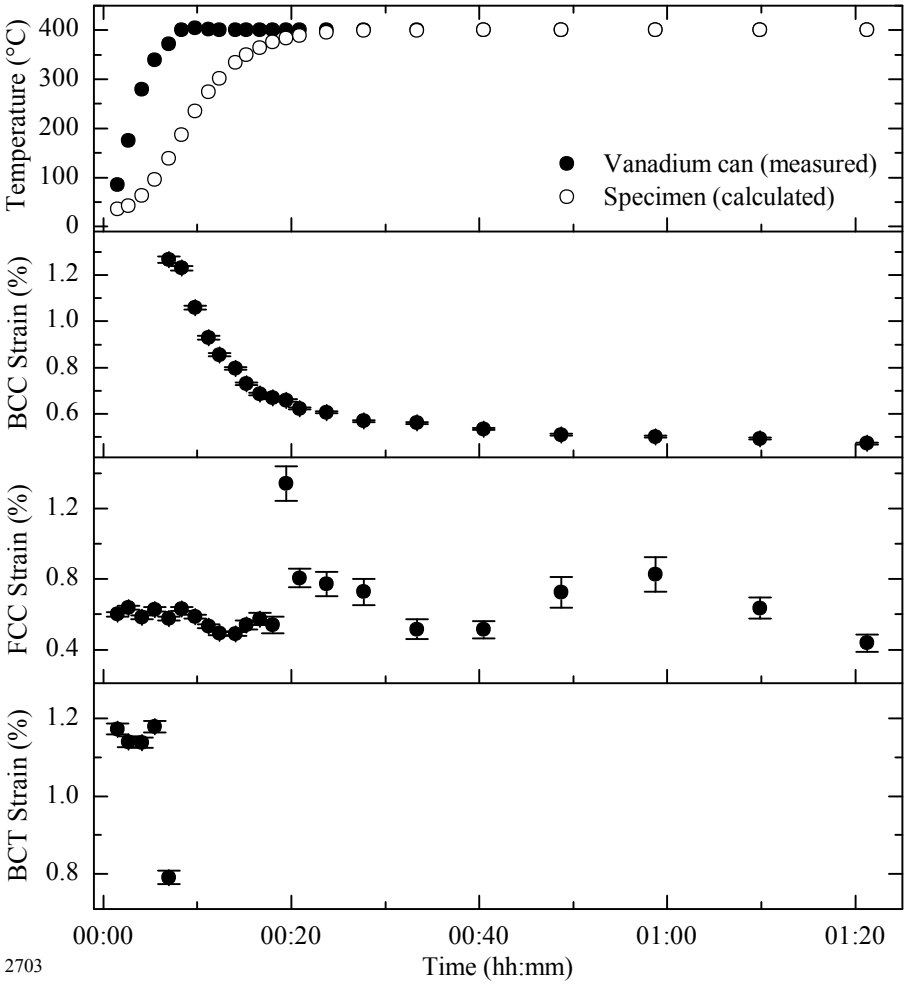

Figure 9.28 – Lattice strains for a Si-free specimen quenched to 10°C and partitioned at 400°C (specimen 2703)

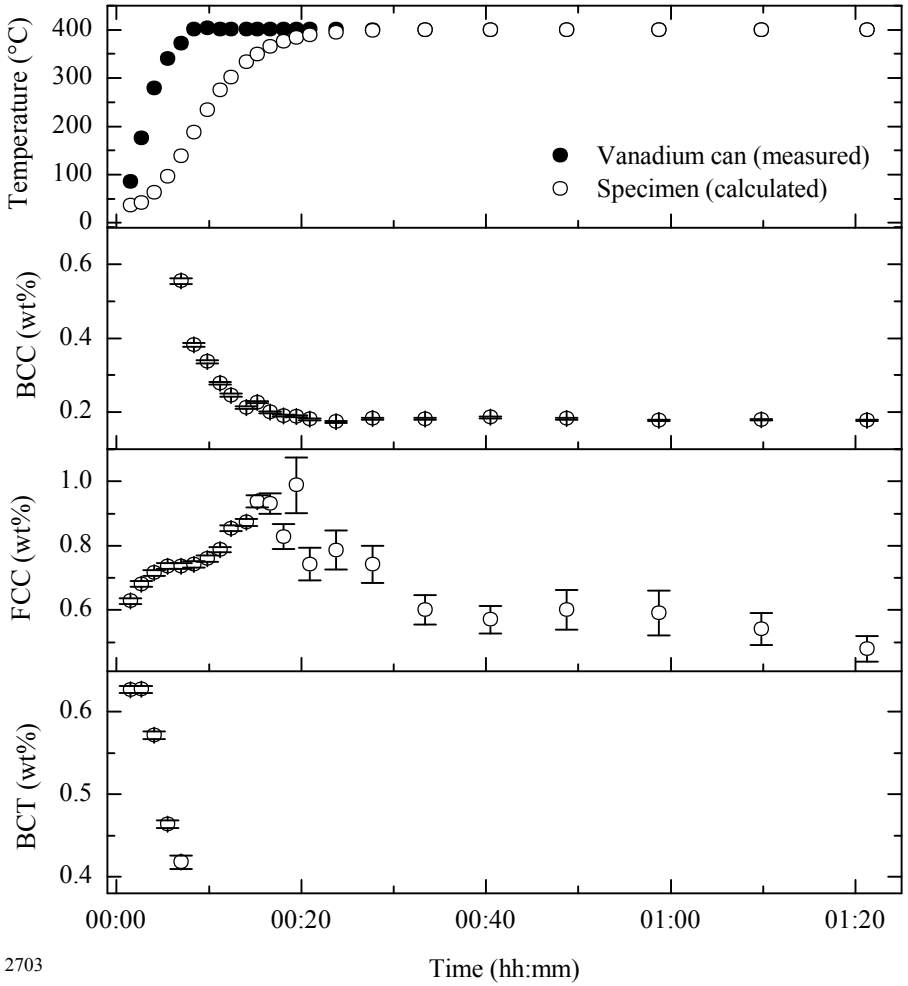

Figure 9.29 – Carbon concentrations for a Si-free specimen quenched to 10°C and partitioned at 400°C (specimen 2703)

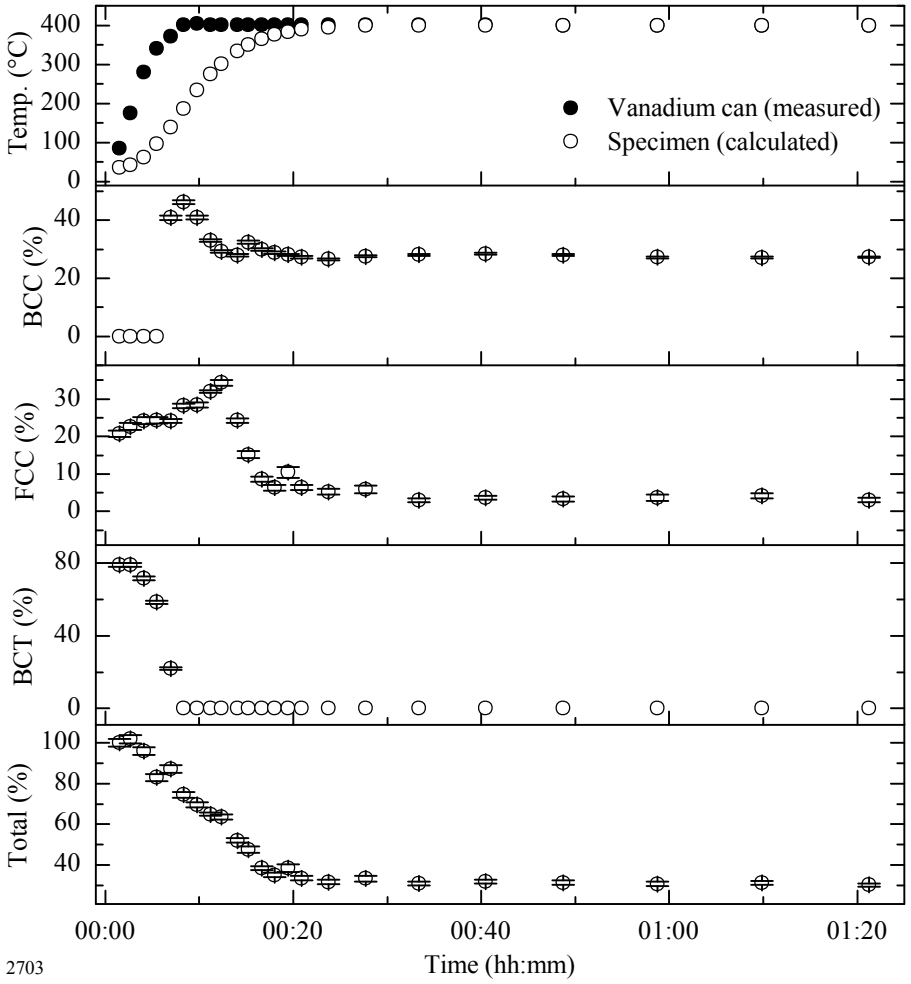

Figure 9.30 – Carbon distribution for a Si-free specimen quenched to 10°C and partitioned at 400°C (specimen 2703)

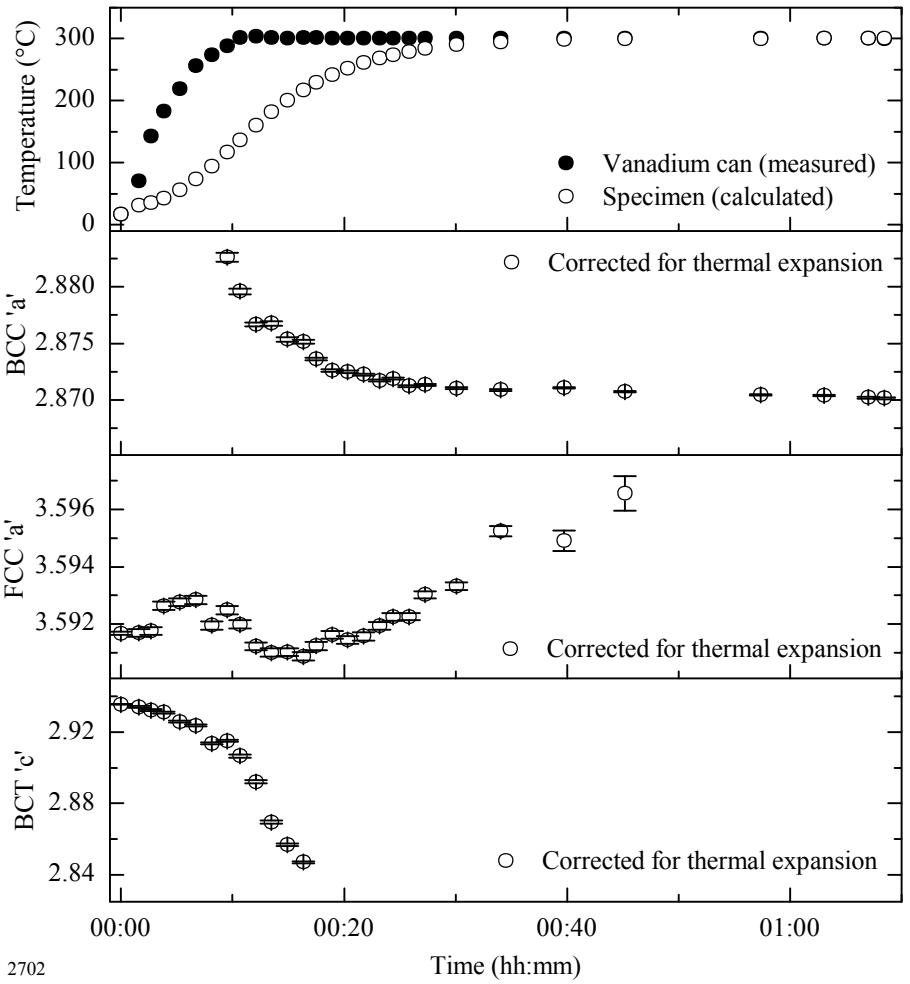

Figure 9.31 – Lattice parameters for a Si-free specimen quenched to 10°C and partitioned at 300°C (specimen 2702)

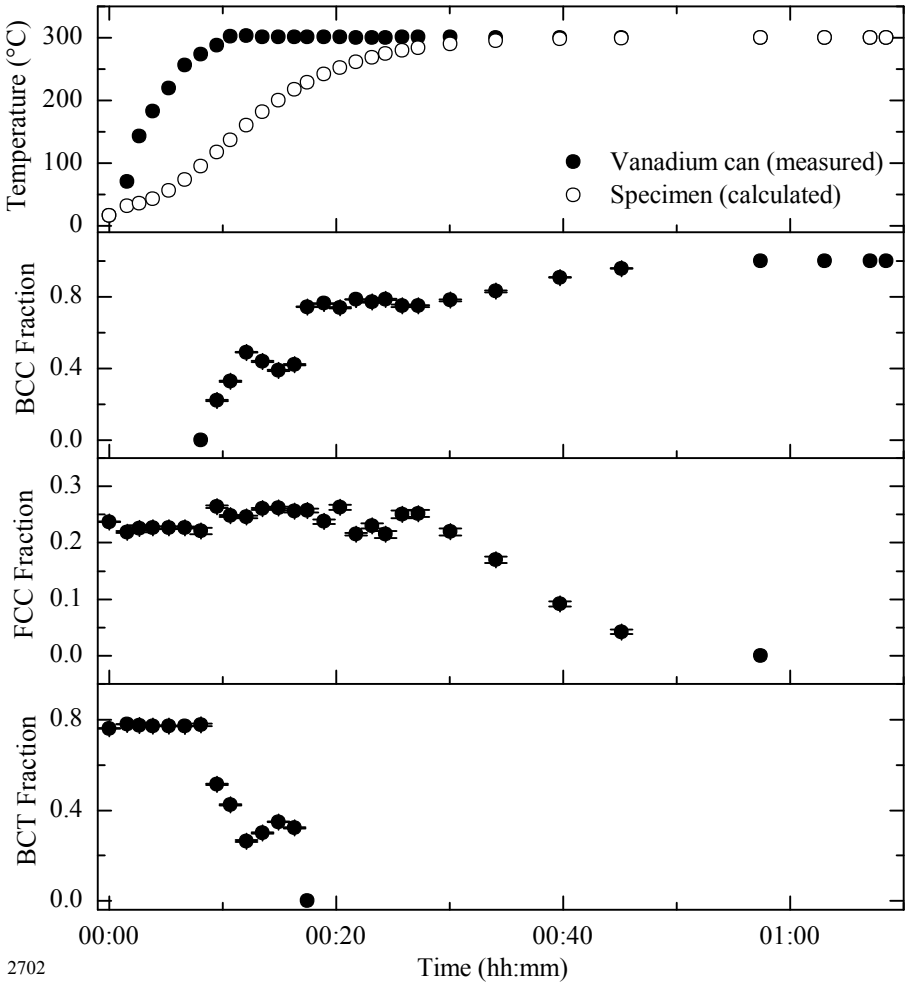

Figure 9.32 - Phase fractions for a Si-free specimen quenched to 10°C and partitioned at 300°C (specimen 2702)

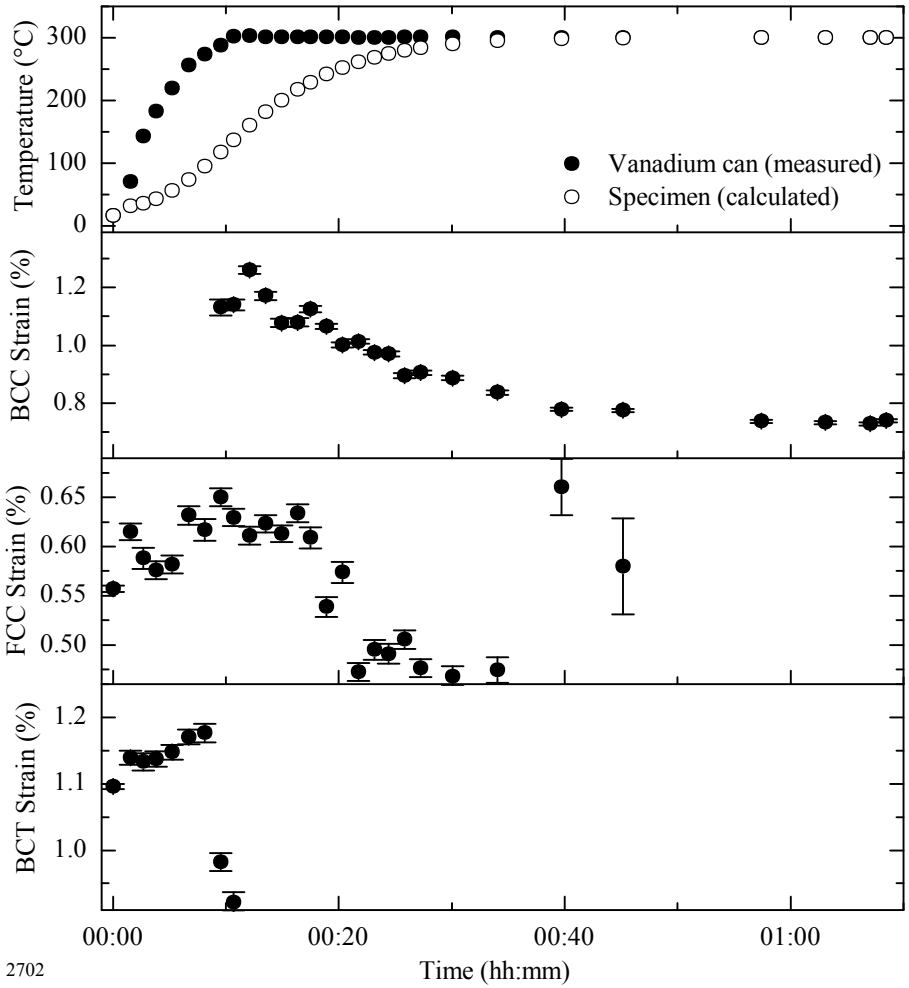

Figure 9.33 – Lattice strains for a Si-free specimen quenched to 10°C and partitioned at 300°C (specimen 2702)

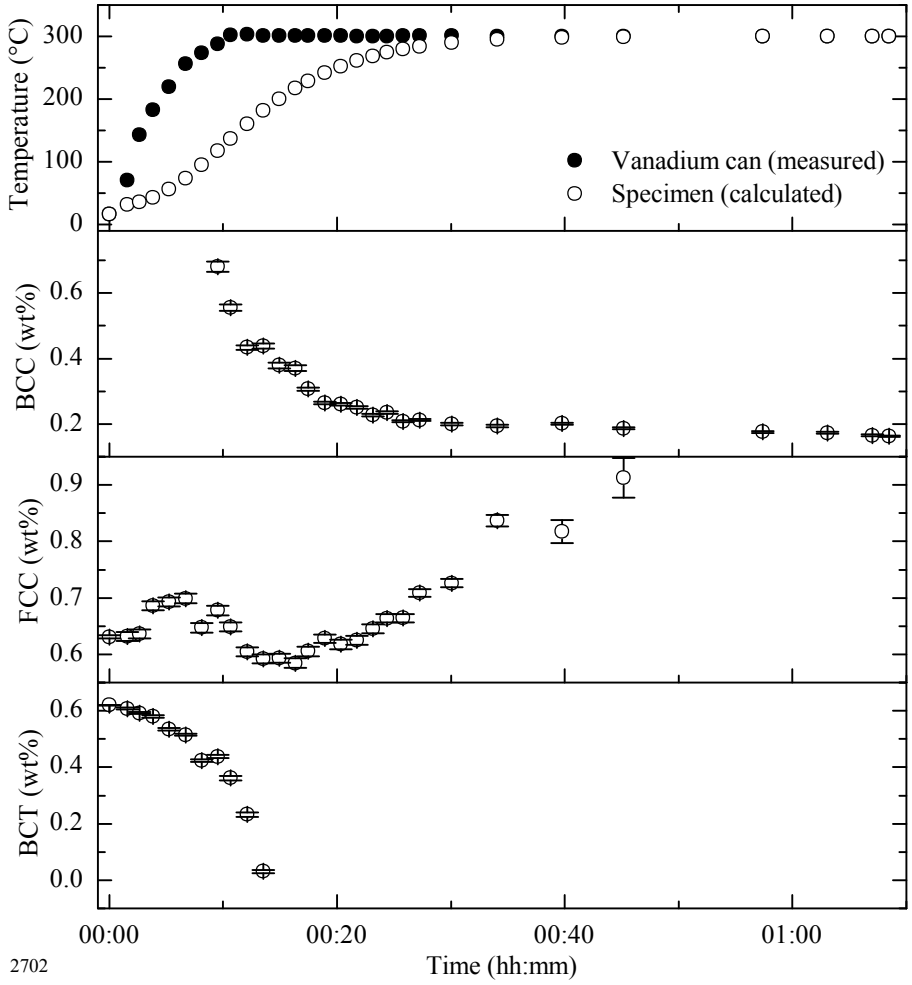

Figure 9.34 – Carbon concentrations for a Si-free specimen quenched to 10°C and partitioned at 300°C (specimen 2702)

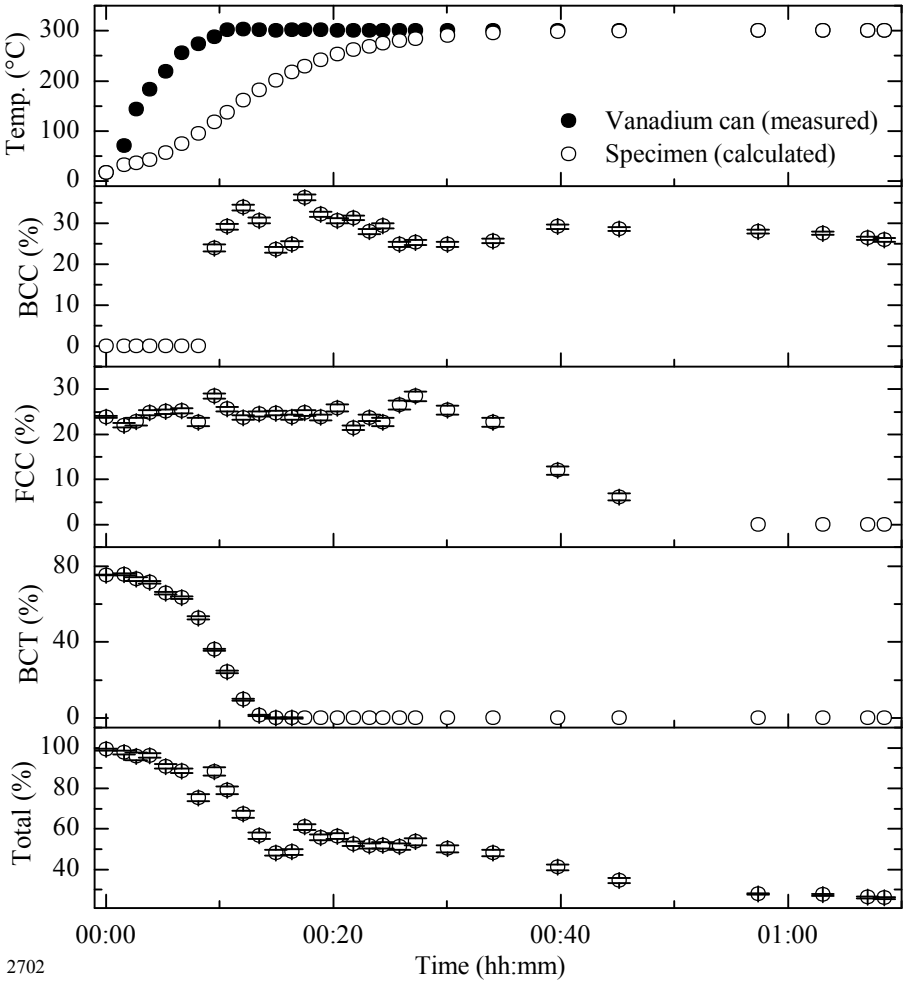

Figure 9.35 – Carbon distribution for a Si-free specimen quenched to 10°C and partitioned at 300°C (specimen 2702)

9.1 Discussion of in-situ partitioning results

9.1.1 Silicon alloyed specimen partitioned at 500°C (specimen 3802)

Tempering of the martensitic phase via decomposition of the BCT structure to a BCC structure, and subsequent reduction in lattice parameter of the BCC phase is observed to take place relatively early on during partitioning. However, observations of the austenite lattice parameter suggest that partitioning of carbon into austenite does not become kinetically significant until the specimen has reached higher temperatures. This is logical, as it is thought that for a given temperature, carbon is much more mobile in the body-centred lattices than in the face-centred lattice (as illustrated in Figure 1.11). Therefore, it is hypothesised that there exists an interim period, during which carbon is relatively mobile within body-centred phases, but insufficiently mobile within austenite to enable significant inter-phase partitioning of carbon to take place. During this interim period, it is postulated that the measurements which are indicative of martensite tempering can be explained by 'internal' partitioning of carbon to lattice defects within the martensite phase. The lattice strain measurements, and the width of diffraction peaks (compared to the silicon standard) suggest that there is no shortage of sites available for this to occur. This explanation fits well with previously published work which proposes that, dependant on alloy carbon concentration, a high proportion of the carbon present in martensite can be accommodated by the establishment of an equilibrium distribution of carbon between lattice defects and meta-stable (epsilon) carbides (see Section 1.10.5). Unfortunately, from the diffraction patterns obtained, it has not been possible to verify the presence or absence of epsilon carbides during partitioning, as the signal to noise ratio in the diffraction patterns obtained during in-situ measurements is too poor. However, previously published work (Edmonds, He et al. 2006) (Li, Lu et al. 2010b) indicates that epsilon carbides have been found in Quenched and Partitioned specimens (although in steel of a different chemical composition to the specimens reported on herein).

During the early stages of partitioning, the measurements indicate an increase in austenite phase fraction. More than one possible explanation exists for this observation; it could be interpreted as evidence of austenite-martensite interface migration, as has been postulated to occur (see Section 1.11.5), alternatively, it may be explainable by improvement or worsening of the Rietveld fit with respect to any of the phases present. Evidence of interface migration has previously been reported

in the context of the Q&P process (Zhong, Wang et al. 2006). Following the work of Zhong, Wang et al, a description of a thermodynamic route by which such a transformation could occur within the Q&P process has also been set out (Speer, Hackenberg et al. 2007). The validity of this observation as a genuine change in austenite phase fraction is discussed further in Section 9.1.8.

As the partitioning temperature continues to rise, evidence is present of inter-phase partitioning of carbon from martensite to austenite in the form of an increase in austenite lattice parameter. However, this increase is relatively short-lived; as the specimen temperature approaches 500°C a reduction in austenite lattice parameter is observed to occur, signalling a drop in austenite carbon concentration. The reduction in austenite carbon concentration is followed by a decrease in austenite phase fraction. Strain measurements in all phases are observed to decrease with partitioning time, hence it is considered that defects are being annealed from the structure, thereby reducing the concentration of energetically favourable locations where carbon may reside. Therefore, the combination of reduced austenite carbon concentration, lowered austenite phase fraction, and decreasing defect density is thought to mark the onset of another reaction which consumes carbon, namely, formation of equilibrium carbides.

Plotting carbon concentration in each phase with respect to partitioning time reveals some interesting and previously unseen characteristics of the Quenching and Partitioning process; likewise, the plotting of the distribution of carbon between the phases with respect to partitioning time. Compared to previously published partitioning simulations, decarburisation of martensite appears to occur relatively slowly (although unfortunately, direct comparisons are complicated due to the low heating rate of the experimental technique used). It is possible that the lower than expected rate at which carbon is rejected from martensite is a direct consequence of lattice defects competing with partitioning as a means of reducing the chemical potential of carbon in iron. Based on lattice parameter measurements, the partitioning process is able to increase austenite carbon concentration from 0.64wt% to almost 1.2wt%, this represents approximately 60% of the total available alloy carbon content. However, the 60% figure estimated from lattice parameter and phase fraction data falls well short of the 100% proposed in the ‘ideal’ Q&P theoretical model originally put forward (Speer, Streicher et al. 2003). The remaining 40% of the alloy carbon content is thought to remain trapped within lattice defects, and probably also as meta-stable carbides until slightly later, when the higher temperatures favour the formation of equilibrium carbides of an Fe_3C type structure.

Once formation of equilibrium carbides becomes kinetically siginificant, the percentage of the alloy carbon content which can be accounted for via lattice parameter measurements (plotted as 'Total Carbon' in Figure 9.5) enters a terminal decline. Further measurements after cooling to room temperature using much longer counting times demonstrated that carbide peaks commensurate with an Fe_3C type structure were present. Therefore, it may be concluded that silicon alloying additions are ineffective in preventing equilibrium carbide formation at 500°C, this is in agreement with the X-ray diffraction results presented in Chapter 7. As for the X-ray diffraction results, the decline in austenite carbon concentration signifies that a carbide-free-bainite reaction, which is often observed to occur in silicon alloyed steels, does not apply in this alloy at an isothermal hold of 500°C.

9.1.2 Silicon alloyed specimen partitioned at 400°C (specimen 3803)

This experiment suffered from an unexpected outage of the neutron spallation source, consequently some data was lost. However, some useful observations and conclusions can still be made. The partitioning response appears to proceed with similarity to that at 500°C (specimen 3802). At a time of approximately 18 minutes, the BCC martensite phase is observed to be significantly decarburised, while the austenite measurements indicate only the commencement of an increase in austenite carbon concentration. Hence, it is apparent that martensite decarburisation and austenite enrichment do not occur concurrently (i.e. the same as observed in specimen 3802). Therefore, it is hypothesised that the same concept of 'internal' partitioning of carbon to defects in the martensite lattice as described for specimen 3802 also applies here. The increase in austenite carbon concentration appears to be slower than for partitioning at 500°C, as would be expected when a diffusional process takes place at a lower temperature.

Unfortunately, at the time of making the measurements, the magnitude of the lag between vanadium can temperature and specimen temperature was not fully appreciated, hence, the experiment was ended prematurely. The peak austenite carbon content was ~1.19wt%, this is similar to that for specimen 3802. However, further increases were recorded during specimen cooling up to 1.23wt% (not plotted), therefore the figure of ~1.19wt% should not be considered the maximum possible austenite carbon concentration that is achievable. No evidence of austenite decomposition was observed during the latter stages of partitioning, although it is possible that the experiment was not continued long enough for this to occur. As for specimen 3802, there were some indications that austenite phase fraction increased during the early stages of partitioning. Lattice strain reductions take place, but are

retarded compared to partitioning at 500°C; the lower rate at which strain reductions occur is attributable to the diffusional mechanism by which annealing of the microstructure takes place. During partitioning, the total carbon 'accounted for' falls from almost 100% to a low of 54%, although as some data is missing the true minimum could be lower. Subsequently, austenite lattice parameter measurements indicate the occurrence of partitioning, and the carbon 'accounted for' increases to 72%. The distribution of carbon at the end point of the experiment was calculated to be: austenite 57%, and BCC martensite 15%, hence, approximately 28% of the total alloy carbon content is thought to be 'unaccounted for'. The location of this 'unaccounted for' carbon is considered to most likely be a combination of epsilon carbides and any other sites where the presence of carbon does not affect lattice parameter measurements. Re-measurement of this specimen at a much longer counting time after cooling to room temperature did not reveal any additional carbide peaks. However, X-ray diffraction work (see Section 7.5) suggests that detection and identification of carbide phases produced during partitioning at 400°C is difficult due to the diffuseness and low intensity of the additional peaks, hence, the apparent absence of evidence for meta-stable carbides is not surprising.

9.1.3 Silicon alloyed specimen partitioned at 300°C (specimen 3804)

The initial tempering of BCT and BCC martensite phases proceeds much the same as already observed and described for specimen 3802. However, the austenite lattice parameter undergoes an immediate and significant increase, which contrasts with those specimens previously discussed (3802 and 3803) in which carbon diffusion in austenite only becomes kinetically significant at ~300°C. Looking at data from all of the specimens together, in several cases the austenite lattice parameter is observed to initially undergo a slight ripple before a genuine lattice parameter increase occurs (as a result of carbon partitioning). The behaviour observed in Figure 9.11 is believed to be a similar but more pronounced effect, whereby the initial upswing of the ripple is much larger than the subsequent downswing. In all specimens, the ripple is thought to originate from inaccuracies in the calculation of specimen temperature. Naturally, small differences existed in the heat transfer rate for the different specimens, depending on such variables as specimen mass, partitioning temperature, and starting conditions (some specimens were heated from room temperature, while others were inserted into the furnace when it was still warm from the previous experiment). Furthermore, specimen 3804 did not totally conform to the schematic illustrated in Figure 2.39, as it was cut from one end of the sample and so was slightly rounded at one end (e.g. see Figure 2.2 which illustrates a sample before sectioning). However, for consistency, the same

heat transfer coefficient was used for all specimens. By slighty increasing the heat transfer coefficient (from 3E-07 to 5E-07), the response is modified to that shown in Figure 9.36, this modification is believed to be a closer approximation of the specimen response to partitioning than Figure 9.11.

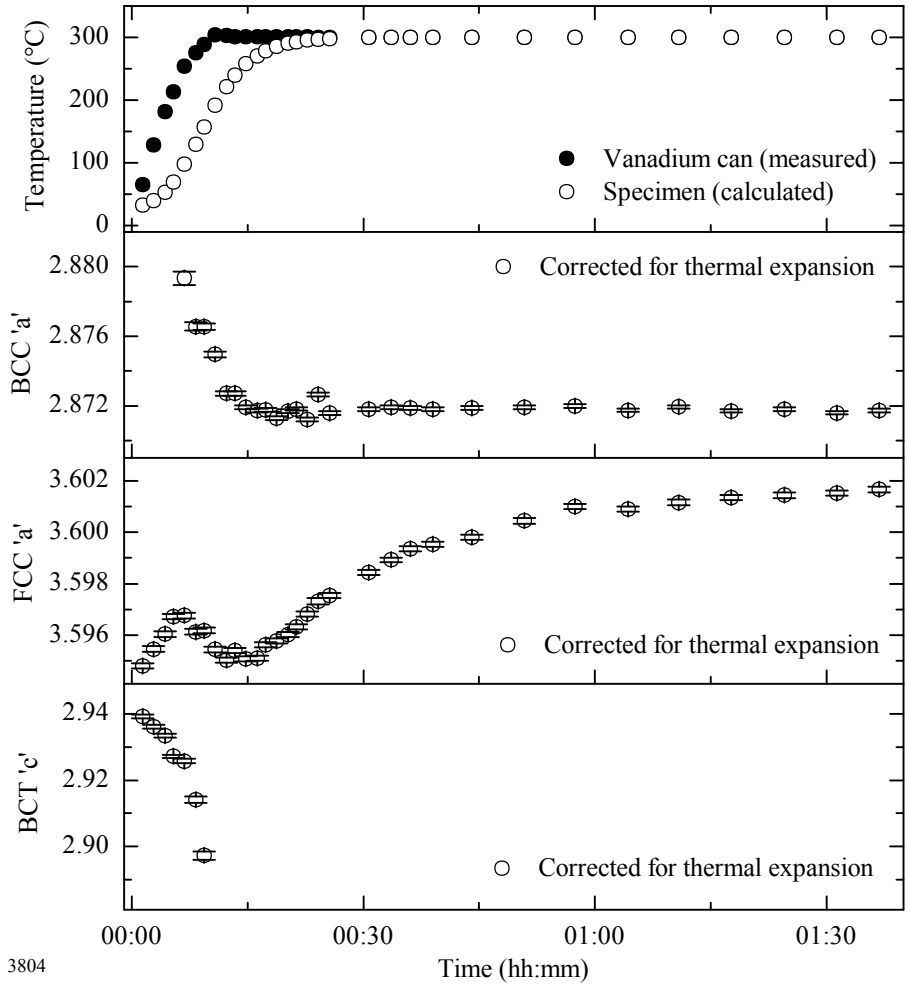

Figure 9.36 – Lattice parameters for specimen 3804 (recalculated with an adjustment to the heat transfer coefficient)

In common with the two specimens already discussed, the early stages of partitioning display evidence of an increase in austenite phase fraction. In Figure 9.36, at temperatures approaching 300°C, the austenite lattice parameter commences a gradual increase. As for previously discussed specimens, this increase is considered to be caused by carbon partitioning into the austenite phase, although the rate is observed to be much lower than that seen in specimens 3802 and 3803 due to the lower temperature. Austenite carbon concentration appeared to still be rising after 1.5 hours when the experiment was ended; maximum austenite carbon concentration recorded was approximately 1wt%, somewhat lower than the 1.2wt%

for specimens 3802 and 3803. Unfortunately, as the experiment was terminated, it is not known if further increases above 1wt% were possible at longer partitioning times. Similarly to specimen 3803, at the time of experiment termination, approximately 30% of the alloy carbon content remained 'unaccounted for'. The remaining carbon is assumed to be located in sites that did not form part of the measurements made (e.g. metastable carbides and crystallographic features). As for specimen 3803, although metastable carbides were considered likely to be present, re-measurement at room temperature for a longer counting time did not produce further insight in this area.

9.1.4 Silicon alloyed specimen partitioned at 500°C (specimen 3603)

This experiment was similar to that described in Section 9.1.1, but with a reduction in the initial quench temperature to cause a higher ratio between body-centred and face-centred phase fractions. The experiment was conducted specifically to investigate the effect of as-quenched austenite phase fraction on the level of austenite carbon enrichment. The initial stages of this experiment proceed almost identically to those of specimen 3802 and so it is considered superfluous to describe or discuss them here. The main subject of interest concerns the evolution of the austenite lattice parameter and associated calculations of carbon concentration. In this respect, the data suggests that as-quenched austenite phase fraction has some effect on maximum austenite carbon enrichment. Maximum austenite carbon concentration was calculated at 1.4wt%, compared to a maximum of 1.18wt% calculated for specimen 3802. However, although this is a notable increase, a much larger difference might have been expected, given that specimen 3802 contained 29wt% austenite in the as-quenched state and specimen 3603 contained only 10wt% austenite. Austenite decarburisation occurs in both specimens at almost exactly the same partitioning time and temperature, thereby terminating the investigation into austenite carbon enrichment. Unfortunately a similar comparison was not carried out at a partitioning temperature of 400°C (at which the austenite carbon content and phase fraction has been found to be more stable). Consequently it is not known if further austenite enrichment above 1.4wt% is possible.

9.1.5 Silicon free specimen partitioned at 500°C (specimen 2704)

Similarly to specimen 3804, significant inaccuracies are believed to be present in the calculation of specimen temperature during the early stages of the experiment resulting in misleading lattice parameter measurements. Possible sources of inaccuracy in the calculations have already been described in Section 9.1.3 and so are not repeated here. However, it is appropriate to note that specimen 2704 was also

cut from the end of a sample, and so was slightly rounded at one end (i.e. the same as specimen 3804). Attempts at improving the results by adjusting the heat transfer coefficient (i.e. as described for specimen 3804 in Section 9.1.3) were unsuccessful. Therefore, it is considered that the model for calculating specimen temperature was deficient in some way for this particular specimen. One possible source of error was the thermocouple used to measure the temperature of the vanadium can. The tip of the thermocouple was somewhat loosely held in place against the top portion of the vanadium can by a small loop of wire attached midway between the vanadium can and the end of the sample holder (Figure 2.26). Consequently, it is thought that if the thermocouple was not in good contact with the vanadium can, or moved during the experiment then the temperature log could represent a log of thermocouple temperature rather than vanadium can temperature.

Although the initial lattice parameter measurements are questionable, later measurements are unaffected as the temperatures of the thermocouple, vanadium can and specimen become equilibrated at the furnace setpoint. Measurements of phase fraction and lattice strain required no temperature correction and so are considered to be reliable records of the response to heat treatment for the entire duration of the experiment. Upon comparing to the results for specimen 3802 (silicon alloy partitioned at 500°C) it is apparent that the absence of silicon hastens the decomposition of austenite, this is expected as the barrier to Fe_3C formation is reduced (thereby enabling consumption of carbon by equilibrium carbides). Tempering of BCT martensite to a BCC structure and the hypothesised formation of meta-stable carbides proceeds in much the same way as observed for specimen 3802. Silicon is not noted for suppression of epsilon carbide and so no change is expected here. At the end point of the experiment, over half of the total alloy carbon content is ‘unaccounted for’. Upon cooling to room temperature and remeasuring at a longer counting time, it is evident that carbides fitting an Fe_3C type crystal structure are present. However, quantification of carbide phase fraction was not carried out for two reasons. Firstly, it has already been confirmed in Section 7.5 that carbide formation can account for the ‘missing’ carbon. Secondly, variations in the background count makes quantification of low phase fractions problematical, as illustrated in Figure 9.37.

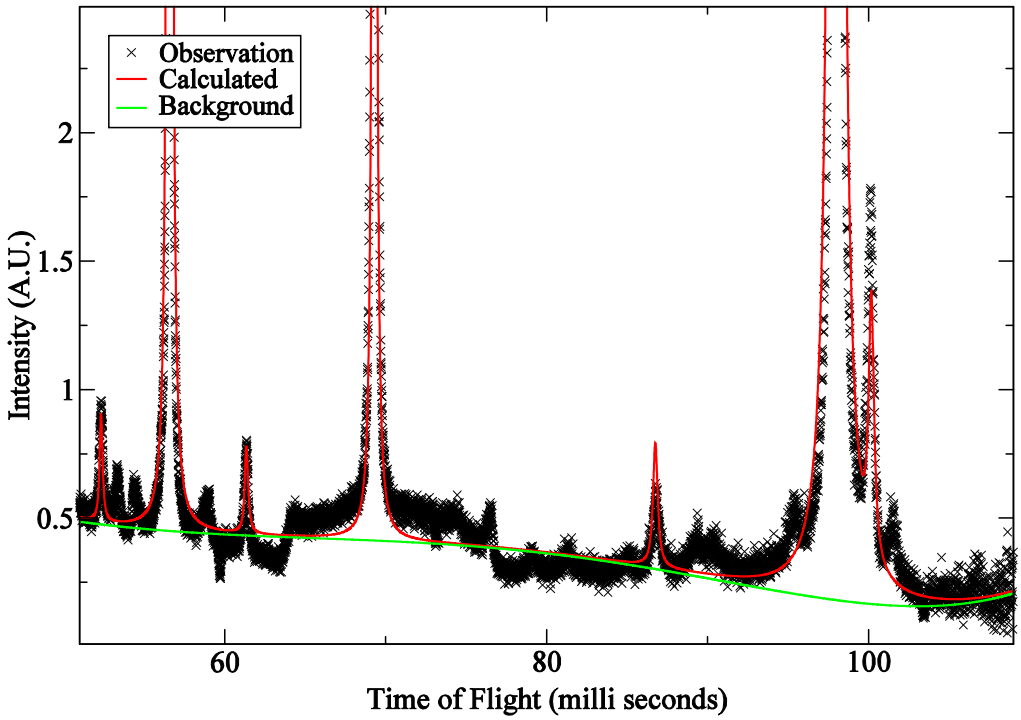

Figure 9.37 – Post-partitioning Rietveld fit for specimen 2704, using a structural model consisting of BCC martensite and FCC austenite, the unfitted low-intensity peaks correspond to an Fe_3C type carbide structure

9.1.6 Silicon free specimen partitioned at 400°C (specimen 2703)

The heat treatment is observed to proceed very similarly to that already described for specimen 2704. A small amount of 'premature' dilatation is observed in the austenite lattice parameter, however, as for specimen 3804 it was possible to remove this by increasing the heat transfer coefficient. Figure 9.38 shows the modified response obtained by increasing the heat transfer coefficient from 3.0E-07 to 3.8E-07. At the end of the partitioning experiment a similar amount of carbon was 'unaccounted for' as observed for specimen 2704. Examination of the post-partitioning diffraction pattern indicated additional peaks corresponding to the presence of carbides with an Fe_3C type structure, thereby revealing the ultimate destination of carbon rejected from BCC martensite and decomposing austenite. This behaviour differs markedly from that of specimen 3803 (silicon alloy partitioned at 400°C) where the austenite phase fraction and carbon concentration are observed to be relatively stable. Therefore, the logical conclusion is that silicon is an essential alloying addition when a Q&P heat treatment is carried out under the conditions pertaining to these experiments. However, as the heating rates here were relatively slow, and the partitioning times long, it would seem worthwhile to repeat some of the experiments reported in Section 7, to determine whether silicon is equally important at much shorter partitioning times. Following austenite

decomposition, austenite lattice strain measurements become erratic. This is believed to be a consequence of the low austenite phase fraction in combination with small variations in the background count.

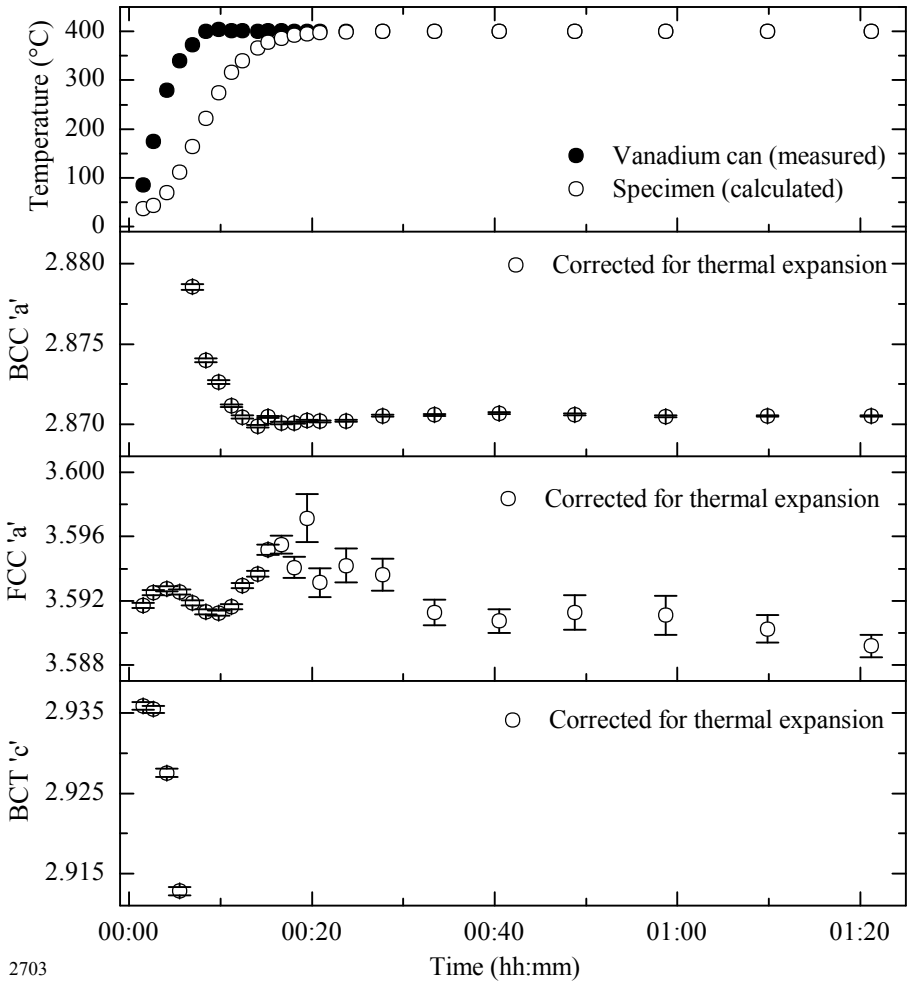

Figure 9.38 – Lattice parameters for specimen 2703 (recalculated with an increased heat transfer coefficient)

9.1.7 Silicon free specimen partitioned at 300°C (specimen 2702)

The partitioning process progresses similarly to that described for specimens 2704 and 2703, but at a slightly slower rate, as is expected at lower temperatures. Decomposition of austenite is delayed to slightly longer times, but when it does occur an interesting difference is apparent between this experiment and the previous two experiments reported. The austenite lattice parameter continues to increase during austenite decomposition, suggesting that carbon is being rejected into the remaining austenite. This is an unexpected observation as austenite carbon enrichment during austenite decomposition is usually associated with steels containing silicon alloying additions (e.g. as in the formation of carbide-free-

bainite). However, in this experiment no silicon alloying was present and so it might reasonably be concluded that even in the absence of a carbide suppressant, carbide formation did not consume all of the carbon rejected from austenite during the austenite-to-ferrite transformation. The exact mechanism of transformation is not known, however, assuming that the austenite is consumed by a Bainite reaction, the unimpeded decomposition of austenite signifies that the carbon concentration of untransformed austenite never reaches the concentration T'_0 (see Figure 1.12), at which the reaction is unable to continue.

As for specimens 2704 and 2703, re-measurement at room temperature for longer counting times produced evidence of carbides possessing an Fe_3C type structure. It is also notable that BCC martensite lattice strain did not diminish to the same extent as for specimens partitioned at 400 and 500°C, thereby hypothetically maintaining a greater concentration of lattice defects able to trap carbon. At the lowest austenite phase fractions, austenite lattice strain measurements become erratic for the same reasons as described for specimen 2703.

9.1.8 Consideration of all results

The extent of thermal lag between recorded (vanadium can) temperature and specimen temperature had not been envisaged at the planning stage. Nevertheless, estimation of specimen temperature for subtraction of thermal expansion effects worked well for all three specimens heated from room temperature (3802, 3803, and 3603). Of those samples inserted while the furnace was ‘hot’ the results were mixed. Specimen 2702 gave good results using the same heat transfer coefficient as for the three specimens heated from room temperature, a further two specimens (3804 and 2703) gave slightly poorer results, although improvement was possible by adjusting the heat transfer coefficient. Specimen 3804 required a larger adjustment of heat transfer coefficient than specimen 2703; this could be due to the slight difference in specimen format (3804 had one rounded end). One specimen (2704), for reasons unknown, exhibited behaviour which could not be improved by adjustment of the heat transfer coefficient. A possible explanation for specimen 2704 could be that the thermocouple was not in good contact with the vanadium can during all or part of the experiment.

Use of the HRPD instrument to enable real time measurement of partitioning response has added to the knowledge already accrued from static measurements using X-ray diffraction techniques. In particular, it is evident that when an as-

quenched specimen is heated relatively slowly, the initial stages of martensite tempering and austenite enrichment do not occur concurrently. Rather, carbon is thought to form an equilibrium distribution between strained interstitial sites and epsilon carbide prior to partitioning to austenite. Evidence of austenite carbon enrichment (partitioning) is present in all of the specimens. In those specimens where austenite decomposition is observed, austenite carbon enrichment takes place prior to austenite decomposition. Hence, the partitioning process is considered to be evidence of carbon partitioning from martensite to austenite, rather than austenite carbon enrichment due to the formation of carbide-free-bainite (as occurs in TRIP steels). Evidence of austenite carbon enrichment during austenite decomposition was only observed in one experiment, at 300°C in a silicon free alloy (specimen 2702). Therefore, it appears that carbide formation is unable to keep pace with austenite decomposition at the lowest partitioning temperature studied. Increasing the proportion of carbon available for partitioning (by lowering the temperature of the initial quench as per specimen 3603) appeared to have only a minimal effect on the maximum austenite carbon enrichment achieved. However, as this observation was followed by austenite decomposition and decarburisation it is not known if greater carbon enrichment could have been achieved at a lower partitioning temperature, such that austenite is more stable. Hence, further experiments at a lower temperature (e.g. 400°C) are required.

All of the specimens exhibited evidence of an increase in austenite phase fraction during the early stages of partitioning. These changes were observed to take place at temperatures somewhat below those at which diffusion of lattice atoms is expected to be significant, hence it is prudent to consider alternative causes. One possible explanation is that the observed changes in austenite phase fraction could have been caused by improvement or worsening of the Rietveld fit during tempering of BCT martensite to BCC martensite. A way to test this hypothesis is by looking for the presence or absence of a correlation between austenite phase fraction and the quality of the Rietveld fit. Within GSAS, several measures of quality of fit are calculated, the most logical measure to use for this exercise is the Bragg factor (R_B), as this is calculated based on integrated intensities, i.e. the same measure as is used to determine phase fractions. However, it must be cautioned that the Bragg factor is based on integrated intensities that have been apportioned by the structural model, therefore, R_B is biased in favour of the model that has been created. Another popular measure of fit is R_p (Pattern Residual), R_p has been regarded as the most meaningful measure from a mathematical point of view (Young 1993). For both R_B and R_p a ‘w’ prefix may be used to denote that a weighted residual has been calculated (e.g. wR_p

and wR_B). Weighted residuals are often preferred as they avoid the situation whereby observations that have a greater number of counts disproportionately influence the calculation. In Figure 9.39, austenite phase fraction and the residual measurements described above are plotted for specimen 3802 during the time period when evidence of an austenite-martensite interface migration is observed.

The residuals wR_p, R_p and wR_B remain relatively constant over the period of interest, therefore, it appears that there is little or no evidence of a correlation between austenite phase fraction and these measures of quality of fit. However, for the measure R_B, a slight change is observed around the same time that the austenite phase fraction is seen to increase (i.e. at approximately 7 minutes). This suggests that quality of fit could be influencing austenite phase fraction measurements. Since the correlation is present for R_B but not for wR_B, it seems likely that if quality of fit is influencing phase fraction measurements, it is the most intense 'reflections' which are implicated. However, as austenite-martensite interface migration has previously been reported, in terms of practical experimentation and a description of the theoretical mechanism by which it could occur, this area warrants further study.

For the alloy compositions studied, silicon is clearly an essential component under the partitioning conditions employed (i.e. relatively slow heating rate). However, it would be useful to determine if silicon is required when much more rapid partitioning is employed (e.g. the use of salt baths as described in Section 2.3.2). For the silicon alloy studied, the most effective partitioning temperature is considered to be 400°C, as this allows rapid diffusion of carbon without compromising the effectiveness of the silicon alloying addition in suppressing the formation of equilibrium carbides. The mechanism by which austenite decomposes to ferrite has not been determined, however, at the lowest temperatures studied (i.e. 300 and 400°C) it is considered likely that a bainitic reaction is occurring, at the highest partitioning temperature (500°C), it seems possible that a sluggish transformation to pearlite could occur.

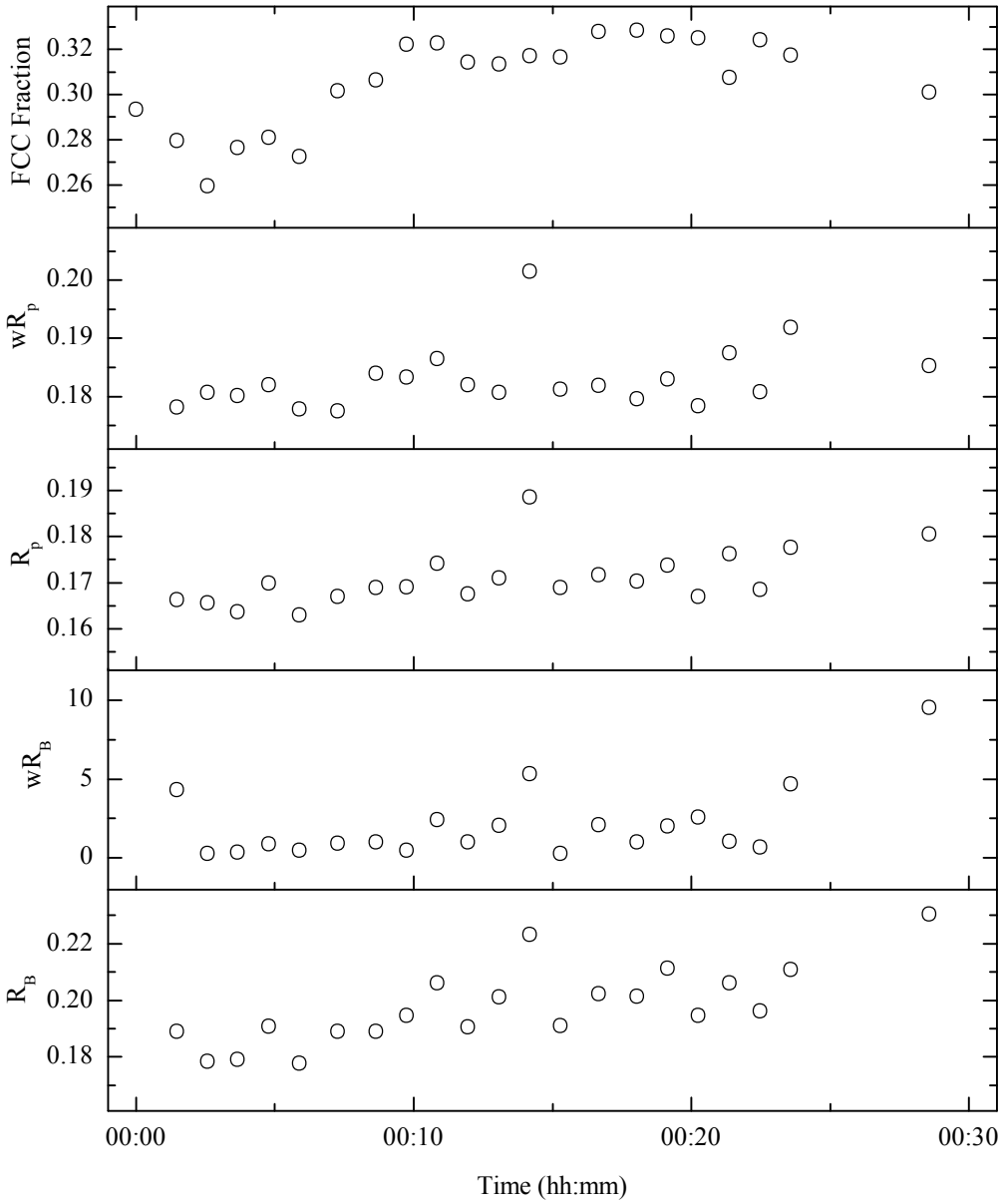

Figure 9.39 – Comparison of austenite phase fraction evolution with Rietveld fit residuals wR_p, R_p, wR_B and R_B for specimen 3802

Chapter 10
Refining for the presence of carbon in austenite interstitial positions

This chapter describes the use of neutron diffraction data to estimate carbon concentration in the austenite phase fraction.

10.1 Theory and approach

One of the advantages of utilising neutrons is that the diffracted intensities are less strongly affected by atomic mass (Figure 7.18 and Figure 10.1). Consequently, it is possible to add carbon atoms to the structural model and refine for interstitial site occupancy to determine the concentration of carbon 'dissolved' in the iron lattice (Choi, Sharpe et al. 1996). To carry out this analysis, the basic assumption was made that carbon resides in the octahedral interstices of the austenite and martensite lattices for as-quenched specimens, and in the octahedral interstices of the austenite lattice for partitioned specimens (for post-partitioning measurements the carbon concentration in the body-centred-cubic martensite lattice was considered to be too low to significantly contribute to the diffracted intensities).

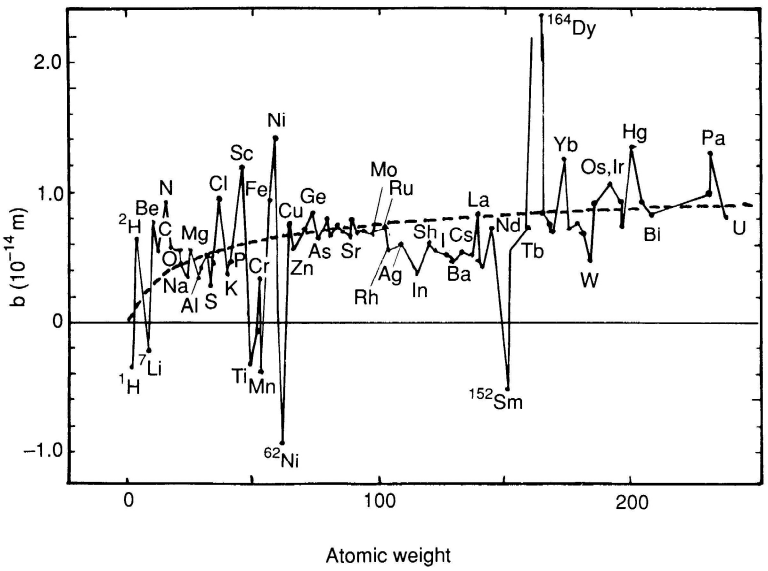

Figure 10.1 – Nuclear scattering lengths for thermal neutrons shown as a function of atomic weight (Young 1993)

The presence of interstitial carbon atoms modifies the structure factor of the austenite and martensite unit cells compared to the situation where interstitial sites are unoccupied. Therefore, if interstitial atoms are present in the specimen, but

absent from the structural model, discrepancies between the observed and calculated intensities can be expected. However, as there are many more interstitial sites available than there are carbon atoms to fill them, the intensity difference is relatively small. Consequently, diffraction data with a high signal-to-noise ratio is required to carry out this type of analysis, hence, only data from 'static' measurements was used. As the magnitude of the diffracted intensities is influenced by the placement of the background count, it was considered necessary to truncate the data to exclude the disturbance in the background count which occurs either side of the body-centred 200 peak (e.g. as seen in Figure 9.37 from 63.5-77ms). To further improve the Rietveld fit to the diffraction data, an extra term was refined within the profile parameters. Due to the negative scattering factor of manganese (Figure 10.1) it was necessary to include all substitutional alloying elements in the structural model, using atomic fractions derived from the data in Table 4.1.

10.2 Results of refining for carbon in austenite interstices

10.2.1 As-quenched specimens

Specimen	Measured alloy carbon concentration (wt%)	Occupancy (Fraction of octahedral sites occupied)		Carbon concentration based on occupancy (wt%)	
		Measurement	1σ	Measurement	1σ
0914	0.54	0.0389	0.0050	0.8298	0.1056
2211	0.53	0.0142	0.0040	0.3041	0.0854
2702	0.628	0.0240	0.0010	0.5140	0.0213
2803	0.610	0.0665	0.0060	1.4092	0.1253
3603	0.626	0.0328	0.0030	0.6997	0.0636
3802	0.640	0.0311	0.0010	0.6643	0.0212
3803	0.640	0.0290	0.0020	0.6203	0.0425

Table 10.1 – Comparison of austenite carbon concentration in as-quenched specimens, as measured for whole samples (i.e. as per Table 4.1), and as determined by refining for interstitial occupancy

The results for interstitial occupancy refinements on as-quenched specimens are presented in Table 10.1, for ease of comparison, the measured carbon concentration is included for the sample from which each specimen was cut (i.e. as per Table 4.1).

10.2.2 Partitioned specimens

As the retained austenite fraction was very low in most of the specimens which had been partitioned, only two specimens were suitable for assessment, specimens 3803 and 3804, partitioned at 400 and 300°C respectively. Specimen 3804 was measured twice as it was thought that the first measurement had been affected by a neutron spallation source outage. However, both datasets were later found to contain good quality data and so were refined simultaneously in one structural model.

Comparisons of the austenite carbon concentration as evaluated by the two different methods of lattice parameter measurements and interstitial occupancy measurements are given in Table 10.2 and Table 10.3 for specimens 3803 and 3804 respectively. For each specimen, the measurements are presented in the first row of the table while the standard deviations (expressed as 1σ) are given in the second row. The estimations based on lattice parameter were computed using the same method as that described in Section 2.9.9. It is notable that specimen 3804 (for which two datasets were refined) gave slightly lower standard deviations than specimen 3803, thus indicating the effect of counting time on the quality of the measurements obtained.

	Austenite 'a' lattice parameter (Å)	Carbon concentration based on austenite 'a' (wt%)	Occupancy (Fraction of octahedral sites occupied)	Carbon concentration based on occupancy (wt%)
Measurement	3.603030	1.2550	0.0602	1.2780
1σ	0.000023	0.0013	0.003	0.0628

Table 10.2 – Comparison of austenite carbon concentration in specimen 3803, as estimated from lattice parameter measurement, and as determined by refining for interstitial occupancy

	Austenite 'a' lattice parameter (Å)	Carbon concentration based on austenite 'a' (wt%)	Occupancy (Fraction of octahedral sites occupied)	Carbon concentration based on occupancy (wt%)
Measurement	3.600563	0.9683	0.0521	1.1073
1σ	0.000016	0.0009	0.001	0.0210

Table 10.3 – Comparison of austenite carbon concentration in specimen 3804, as estimated from lattice parameter measurement, and as determined by refining for interstitial occupancy

In recognition that the two measurement methods (i.e refining for occupancy and estimation from lattice parameter) do not produce identical values for carbon concentration, further calculations were undertaken utilising some of the other published relationships for lattice parameter versus carbon concentration. In Table 10.4 and Table 10.5, the results of these additional calculations are given for specimen 3803 and 3804 respectively.

Calculated carbon concentration (wt%)	Standard deviation (expressed as 1σ)	Method by which the relationship was derived	Source of relationship
1.5456	0.0013	Extrapolation	(Seki and Nagata 2005)
1.0916	0.0005	Retained	(Roberts 1953)
0.9100	0.0007	Extrapolation	(Ridley, Stuart et al. 1969)
1.2135	0.0005	Retained	Best fit to data in Figure 2.19
0.9018	0.0006	Extrapolation	(Scott and Drillet 2007) after (Onink, Brakman et al. 1993)
0.8891	0.0006	Alloying and Extrapolation	(Cheng, Bottger et al. 1990) (unstrained relationship)

Table 10.4 – Austenite carbon concentration for specimen 3803 calculated from the lattice parameter measurement using a variety of published relationships

Calculated carbon concentration (wt%)	Standard deviation (expressed as 1σ)	Method by which the relationship was derived	Source of relationship
1.4034	0.0009	Extrapolation	(Seki and Nagata 2005)
1.0355	0.0004	Retained	(Roberts 1953)
0.8352	0.0005	Extrapolation	(Ridley, Stuart et al. 1969)
1.1606	0.0003	Retained	Best fit to data in Figure 2.19
0.8386	0.0004	Extrapolation	(Scott and Drillet 2007) after (Onink, Brakman et al. 1993)
0.8139	0.0004	Alloying and Extrapolation	(Cheng, Bottger et al. 1990) (unstrained relationship)

Table 10.5 – Austenite carbon concentration for specimen 3804 calculated from the lattice parameter measurement using a variety of published relationships

Of the relationships used, the first five were derived via extrapolation (i.e. measurements at high temperature) or retained austenite measurements (i.e. from quenched steel). The sixth relationship (Cheng, Bottger et al. 1990) was determined by extrapolation of data from samples alloyed with manganese to derive the constant (i.e. the intersect), combined with extrapolation of high temperature data to determine the variation due to carbon concentration (i.e. the gradient).

10.3 Discussion of refining for carbon in austenite interstices

Five separate factors are considered to affect the reliability of the carbon concentration values obtained from occupancy refinements. The first three factors are expected to more strongly affect measurements on as-quenched specimens, while the last two apply equally to measurements on as-quenched, and partitioned specimens. Firstly, high lattice strains have the effect of reducing the signal to noise ratio, hence, measurements on as-quenched specimens might be expected to be less accurate than those on partitioned specimens. Secondly, the combination of the tetragonal structure of the BCT martensite phase and high lattice strains causes increased overlap of diffraction peaks, this is critical as the Rietveld software apportions intensities where overlaps occur, the apportionment being subject to error where room temperature tempering of martensite has occurred. Thirdly, the fraction of interstitial sites occupied by carbon is relatively small, consequently, the effect on

the structure factor is relatively low, particularly for as-quenched specimens. Fourthly, some specimens were presented for measurement in a disc format rather than a cylinder format (Table 10.6 and Table 10.7), thereby reducing the quantity of material available to diffract the neutron beam. Lastly, the amount of beamtime used to measure each specimen (the integrated neutron flux) was not equal for every measurement (Table 10.6 and Table 10.7).

Specimen	Integrated neutron flux (μA.Hours)	Specimen format
0914	57.6	Disc
2211	21.6	Disc
2702	41.2	Cylinder
2803	25.1	Cylinder
3603	28.7	Cylinder
3802	41.4	Cylinder
3803	15.6	Cylinder

Table 10.6 – Integrated neutron flux and specimen format of as-quenched specimens evaluated for carbon interstitial occupany

Specimen	Integrated neutron flux (μA.Hours)	Specimen format
3803	19.0	Cylinder
3804	37.8	Cylinder

Table 10.7 – Integrated neutron flux and specimen format of partitioned specimens evaluated for carbon interstitial occupany

10.3.1 As-quenched specimens

In the as-quenched condition, the carbon concentration of retained austenite should logically be the same as the overall alloy carbon concentration. However, in some cases significant differences are observed between the carbon concentration determined by the external analysis laboratory and the concentrations derived from refining for interstitial occupancy. Hence, some explanation is required to account for the disparities. The previous paragraph describes five different factors which are

considered to influence the accuracy of the occupancy measurements reported in Table 10.1. When the results in Table 10.1 are compared with the factors previously described, and with the data in Table 10.6, it is clear that the difference in carbon concentration for specimens 0914 and 2211 can reasonably be explained, whereas that for specimen 2803 cannot. One possible explanation is that specimen 2803 was not correctly positioned in the diffractometer for exposure to the full cross section of neutron radiation.

10.3.2 Partitioned specimens

The data presented in Table 10.4 and Table 10.5 illustrates the problems associated with attempting to estimate carbon concentration from lattice parameter measurements (as previously described in Section 2.9.9). There is no correlation between the method by which the relationship was determined (e.g. extrapolation, retained, alloying) and the estimated carbon concentration. However, Table 10.2 and Table 10.3 indicate that the two measurement methods place the specimens in the same high-low position (i.e. specimen 3803 has the highest carbon concentration for both measurement techniques). This gives some confidence in the reliability of the results. The carbon concentration measurements derived by refining for interstitial occupancy suggest that the relationship chosen for evaluating carbon concentration described in Section 2.9.9, and subsequently used in Chapter 7, Chapter 9, Table 10.2, and Table 10.3 was preferable to some of the other relationships illustrated in Table 10.4 and Table 10.5.

Previously published work (Choi, Sharpe et al. 1996) has indicated that neutron diffraction is able to detect carbon at concentrations of around 8 atomic percent (~1.69wt%) in Austempered Ductile Iron after aus-tempering for 2 hours at 350°C. The results presented and discussed herein suggest that detection of carbon is possible at lower concentrations, after tempering (partitioning) at similar temperatures, but for shorter times.

Chapter 11
Simulation of carbon partitioning from supersaturated martensite to austenite

This chapter contains results from computer simulations of partitioning carried out using the fortran program MAP_STEEL_PARTITION available from the Materials Algorithms Project website (MAP website) hosted by the materials department at the University of Cambridge.

11.1 Simulation Results

Prior to simulating the partitioning behaviour of the alloy reported on herein, it was considered worthwhile to attempt replication of a partitioning simulation previously published in the literature (as reproduced in Figure 1.9 and Figure 1.10). To do this, the values for EQFER, EQAUS, TAUS and TFER were scaled from Figure 1.9 and Figure 1.10, EBAR, the carbon concentration of the alloy was 0.19wt%. The attempted replication is shown in Figure 11.1, the simulation was terminated at 3.7 seconds as this was the point at which austenite equilibration was determined to have reached 99.5% (i.e. carbon concentration at the furthest point from the interface was 99.5% of the concentration at the interface).

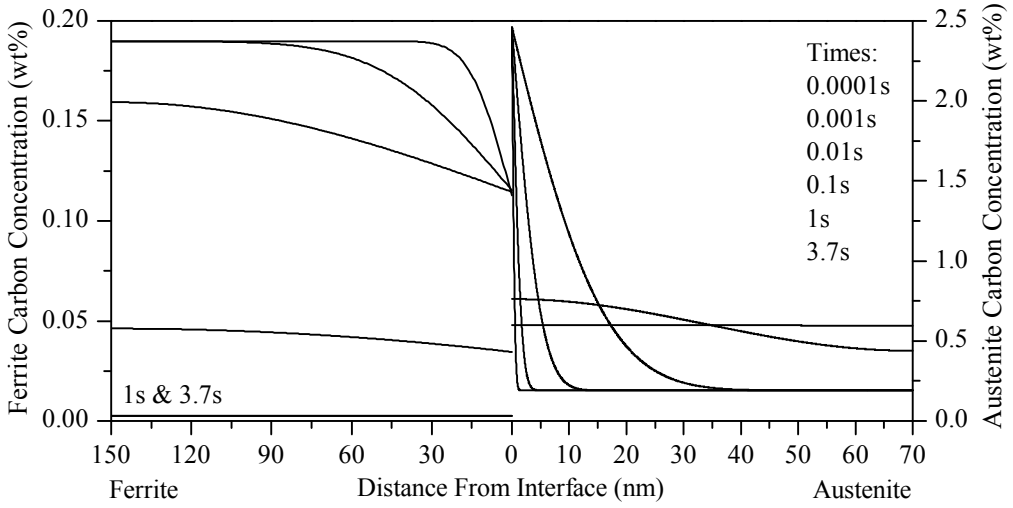

Figure 11.1 – Attempted replication of Figure 1.9 and Figure 1.10 using MAP_STEEL_PARTITION

A simulation for the alloy studied herein during partitioning at 400°C is shown in Figure 11.2. A full description of the way in which the model was constructed and justifications for the input values used can be found in Section 2.11.

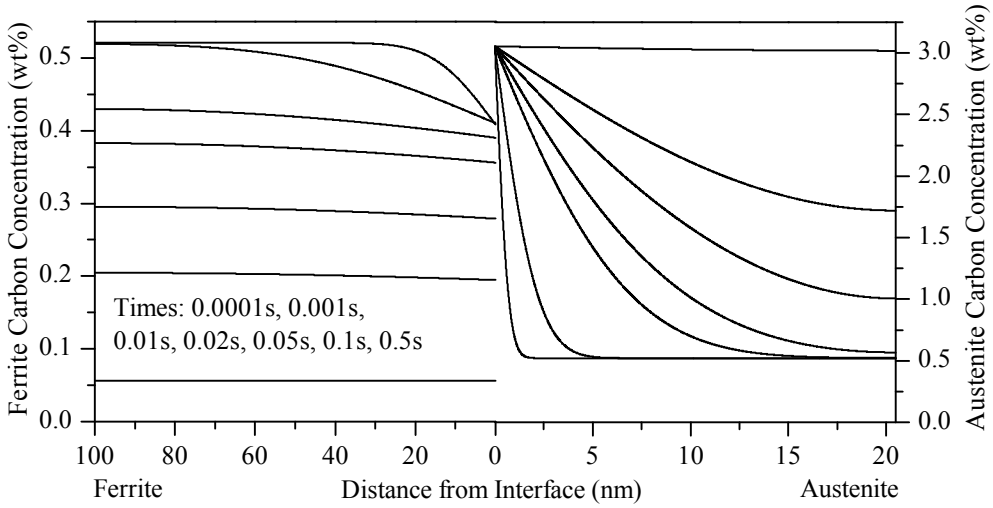

Figure 11.2 – Simulation of the model alloy at 400°C showing evolution of carbon concentration in the diffusion couple

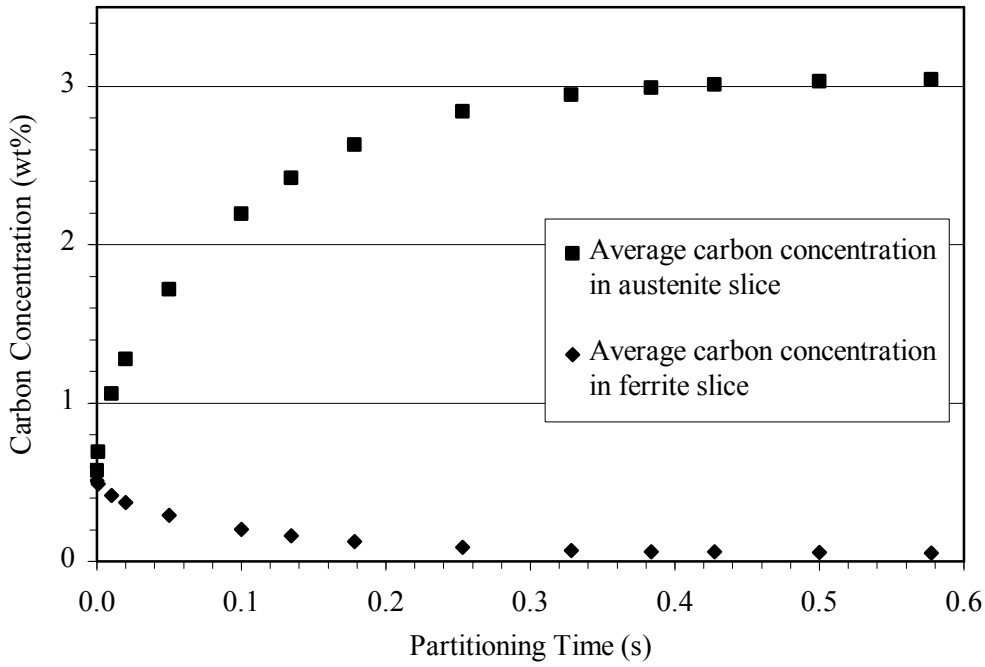

Figure 11.3 – Simulation of the model alloy at 400°C showing evolution of average carbon concentration in the austenite and ferrite slice with respect to partitioning time

Each datapoint presented in Chapter 7 represents an average of the entire range of lattice parameters and carbon concentrations present in the specimen measured. Hence, to enable a more direct comparison with experimental results, it is appropriate to integrate the data shown in Figure 11.2 to obtain the average carbon concentration within the austenite and ferrite slices of the diffusion-couple. In Figure 11.3 the average carbon concentration in each side of the diffusion couple is plotted with respect to partitioning time.

11.2 Discussion of simulation results

Comparing Figure 1.9 and Figure 1.10 to Figure 11.1, it is apparent that there are some differences between the two simulations. The MAP_STEEL_PARTITION simulation predicts somewhat slower decarburisation of the ferrite (martensite) slice, however, this does not affect austenite carbon enrichment, which is predicted to reach equilibration more quickly than is indicated in Figure 1.10. This creates a distinction between the two simulations; in MAP_STEEL_PARTITION, complete decarburisation of the ferrite slice occurs over a similar timescale to austenite enrichment, whereas in Figure 1.10 ferrite decarburisation is complete within 1% of the total time required for austenite equilibration. This dissimilarity may arise from differences in the diffusion coefficients used by the two separate simulations. Upon comparing Figure 11.2 to the results presented in Chapter 7 (e.g. Figure 7.2 and Figure 7.4) it is apparent that in practical experiments partitioning occurs significantly slower than is simulated. This variation is thought to be due to competing effects such as carbon trapping and formation of meta-stable carbides.

Although the simulation predicts the partitioning process to occur over a shorter time frame than that observed experimentally, it is nevertheless interesting to compare Figure 11.3 with Figure 7.4. The carbon concentration versus partitioning time profile presented in Figure 11.3 suggests that the experimental observations in Figure 7.4 could at least partly be due to the response of the diffusional couple during the process of reaching equilibrium (i.e. an initial rapid rise in austenite carbon concentration followed by a slower increase, as previously discussed in the second paragraph of Section 7.6.4).

Chapter 12
Conclusions and suggestions for future work

12.1 Summary

The main objective of this research project was to improve understanding of the novel heat treatment process for steel, Quenching and Partitioning. At the time of commencing this project, although some research had already been published concerning the Q&P concept, study of the partitioning stage of the heat treatment had proved somewhat elusive due to the high temperatures involved. In this project a model alloy with a significantly depressed martensite start temperature has been successfully employed to separate the heat treatment into discrete stages, thereby enabling measurement of previously unobserved characteristics of the Q&P heat treatment process.

Research commenced with basic metallographic studies of as-quenched and Q&P microstructures, followed by X-ray diffraction measurements to evaluate microstructural changes occurring during the Q&P process. As the project advanced, the X-ray diffraction measurements were built on by a beamtime allocation for the High Resolution Powder Diffractometer (HRPD) at ISIS, Rutherford Appleton Laboratory. The use of HRPD enabled real time measurements of the partitioning process as occurs in an as-quenched specimen (albeit at a rather low heating rate). The capability of neutron diffraction to detect 'light' elements was exploited to generate secondary measurements relating to the partitioning process. Finally, an open-source simulation was modified, compiled and run to provide a mathematical model of the martensite-austenite diffusional couple for comparison with previously published work and the experimental data presented herein.

12.2 Conclusions

1. Metallographic examination and X-ray measurement of as-quenched and Q&P specimens shows a duplex microstructure of martensite and retained austenite, as has previously been assumed to exist in conventional alloys subjected to Q&P heat treatment. This creates a clear distinction between the Q&P concept and heat treatments based on a bainite reaction (e.g. those for producing TRIP steel).

2. As-quenched specimens display strong relationships between retained austenite fraction, austenite lattice parameter and lattice strain. These correlations are considered logically to result from the expansive nature of the austenite to martensite transformation.

3. X-ray diffraction measurements exhibit evidence of carbon partitioning from supersaturated martensite to retained austenite, however, the estimated carbon concentration in the enriched austenite phase falls short of the theoretical maximum based on 100% of the alloy carbon content partitioning to the austenite phase.

4. The process of carbon migration from supersaturated martensite to austenite is experimentally observed to take place at a lower rate than has been predicted via mathematical models of the diffusional couple. This disparity is thought to be due to competing mechanisms, for example, formation of meta-stable epsilon carbides and trapping of carbon in energetically favourable locations such as interstitial sites around lattice defects and lath boundaries. These competing mechanisms are also postulated to account for the shortfall in carbon identified by the estimations of carbon distribution amongst the different phases.

5. During partitioning, lattice strains are observed to decrease, as would be expected during a low temperature annealing operation. The high, as-quenched lattice strains, followed by a reduction in lattice strain during partitioning are thought to influence the rate at which partitioning occurs. This is hypothesised to occur by the formation of an equilibrium distribution of carbon between strained interstitial sites and epsilon carbides, thereby controlling the release of carbon from supersaturated martensite into neighbouring austenite.

6. A combination of different measurement techniques and two different surface preparation methods has shown that austenite in partitioned specimens exhibits enhanced stability against stress or strain induced transformation to martensite compared to un-partitioned specimens. This observation supports the Q&P concept of austenite stabilisation via partitioning of carbon from supersaturated martensite to austenite.

7. At the lowest partitioning temperatures studied (300 and 400°C) the silicon alloying addition is highly effective in retarding the formation of equilibrium

carbides, while at the highest partitioning temperature studied (500°C) diffraction patterns matching those for a cementite type structure were observed. In silicon-free specimens diffraction patterns characteristic of cementite type structures were observed to be present at all partitioning temperatures studied (300, 400 and 500°C).

8. Neutron diffraction measurements have enabled refining for carbon in austenite interstitial positions thereby providing a third method of evaluating austenite carbon enrichment in addition to lattice parameter and atom probe measurements (atom probe reported by other researchers). In common with the other two techniques, refining for interstitial occupancy also supports the basic Q&P concept of austenite carbon enrichment by partitioning of carbon from supersaturated martensite.

9. Simulation of the partitioning process using MAP_STEEL_PARTITION suggests that in real-life, the partitioning process is significantly retarded by one or more complications that are not present in the mathematical model. It is hypothesised that one such contributor could be the trapping of carbon at low-energy sites around lattice defects and lath boundaries.

12.3 Suggestions for future work

1. Characterise the structures present in silicon-alloyed specimens partitioned at 500°C to determine the mechanism by which retained austenite decomposes.

2. Perform further experiments to clarify the extent to which the as-quenched retained austenite fraction is able to influence maximum austenite carbon enrichment.

3. Carry out in-situ straining measurements to investigate the TRIP behaviour of Q&P steel.

4. Investigate the feasibility of commercialising the alloy studied in this project (e.g. carry out appropriate mechanical tests).

References

Allen, N. P. (1961). Effects of solute elements on the mechanical properties of iron. Iron and its dilute solid solutions, Detroit, Michigan, USA, 23 October 1961. Interscience Publishers. p271-308.

Andrews, K. W. (1956). The calculation of transformation temperatures and austenite-ferrite equilibria in steels. Journal of the Iron and Steel Institute, Vol. 184(December), p414-427.

Andrews, K. W. (1965). Empirical formulae for the calculation of some transformation temperatures. Journal of the Iron and Steel Institute, Vol. 203(July), p721-727.

Angel, T. (1954). Formation of martensite in austenitic stainless steels. Effects of deformation, temperature, and composition. Journal of the Iron and Steel Institute, Vol. 177(May), p165-174.

Apayev, B. A., B. M. Yakovlev, et al. (1961). Influence of silicon on the processes of carbide formation and graphitization when quenched steel is tempered. The physics of metals and metallography (Translation of Fizika metallov i metallovedenie), Vol. 12(2), p208-216.

Apple, C. A., R. N. Caron, et al. (1974). Packet microstructure in Fe-0.2 pct C martensite. Metallurgical Transactions, Vol. 5(3), p593-599.

Arndt, R. A. and A. C. Damask (1964). Kinetics of carbon precipitation in irradiated iron. III. Calorimetry. Acta Metallurgica, Vol. 12(4), p341-345.

Arnell, R. D. (1968). Determination of retained austenite in steel by x-ray diffraction. Journal of the Iron and Steel Institute, Vol. 206(10), p1035-1036.

ASTM (2008). Standard practice for X-ray determination of retained austenite in steel with near random crystallographic orientation. ASTM International. Designation: E975-03.

Atkins, M. (Year of publication not known). Atlas of continuous cooling transformation diagrams for engineering steels. British Steel Corporation.

Avrami, M. (1939). Kinetics of phase change. I. General theory. Journal of Chemical Physics, Vol. 7, p1103-1112.

Avrami, M. (1940). Kinetics of phase change. II. Transformation-time relations for random distribution of nuclei. Journal of Chemical Physics, Vol. 8, p212-224.

Avrami, M. (1941). Granulation, phase change and microstructure. Kinetics of phase change. III. Journal of Chemical Physics, Vol. 9, p177-184.

Bain, E. C. (1924). The nature of martensite. Transactions of the American Institute of Mining Engineers, Vol. 70, p25-46.

Bain, E. C., E. S. Davenport, et al. (1932). The equilibrium diagram of iron-manganese-carbon alloys of commercial purity. Transactions of the American Institute of Mining and Metallurgical Engineers, Vol. 100(467), p228-249.

Baker, L. J., S. R. Daniel, et al. (2002). Metallurgy and processing of ultralow carbon bake hardening steels. Materials Science and Technology, Vol. 18(4), p355-368.

Banerjee, R. L. (1984). Effect of room temperature aging on low temperature transformation of retained austenite. Journal of Heat Treating, Vol. 3(4), p353-355.

Barber, S. J. (1963). Salt bath chemistry and control. Metals Engineering Quarterly, Vol. 3(4), p1-4.

Barnard, S. J., G. D. W. Smith, et al. (1981). Carbon atom distribution in a dual phase steel: an atom probe study. Scripta Metallurgica, Vol. 15(4), p387-392.

Becherer, B. A. (1991). Processes and furnace equipment for heat treating of tool steels. Volume 4 - Heat Treating, ASM Handbook. ASM International.

Bendicks, C. (1905). The nature of troostite. Journal of the Iron and Steel Institute, Vol. 68, p352-363.

Benz, R., J. F. Elliott, et al. (1973a). Solid phases of the manganese-carbon system. Metallurgical Transactions, Vol. 4(6), p1449-1452.

Benz, R., J. F. Elliott, et al. (1973b). Thermodynamics of the solid phases in the system iron-manganese-carbon. Metallurgical Transactions, Vol. 4(8), p1975-1986.

Bhadeshia, H. K. D. H. (1979). The theory and significance of retained austenite in steels. Department of Metallurgy and Materials Science, Darwin College, Cambridge. PhD Thesis.

Bhadeshia, H. K. D. H. (1981a). Thermodynamic extrapolation and martensite-start temperature of substitutionally alloyed steels. Metal Science, Vol. 15(4), p178-180.

Bhadeshia, H. K. D. H. (1981b). Driving force for martensitic transformation in steels. Metal Science, Vol. 15(4), p175-177.

Bhadeshia, H. K. D. H. (1985). Diffusional formation of ferrite in iron and its alloys. Progress in Materials Science, Vol. 29(4), p321-386.

Bhadeshia, H. K. D. H. (2001). Bainite in steels. Second Edition, IOM Communications Ltd.

Bhadeshia, H. K. D. H. (2002). TRIP-assisted steels? Iron and Steel Institute of Japan International, Vol. 42(9), p1059-1060.

Bhadeshia, H. K. D. H. (2004). Developments in martensitic and bainitic steels: role of the shape deformation. Materials Science & Engineering, Vol. A378(1-2), p34-39.

Bhadeshia, H. K. D. H. and D. V. Edmonds (1979). The bainite transformation in a silicon steel. Metallurgical Transactions, Vol. 10A(7), p895-907.

Bhadeshia, H. K. D. H. and A. R. Waugh (1982). Bainite: an atom-probe study of the incomplete reaction phenomenon. Acta Metallurgica, Vol. 30(4), p775-784.

Bhattacharyya, S. (1966). A friction and wear study of Hadfield manganese steel. Wear, Vol. 9(6), p451-461.

Bleck, W. (1996). Cold-rolled, high strength sheet steels for auto applications. Journal of Metals, Vol. 48(7), p26-30.

Borgenstam, A., A. Engstrom, et al. (2000). DICTRA, a tool for simulation of diffusional transformations in alloys. Journal of Phase Equilibria, Vol. 21(3), p269-280.

Bouchaud, J. P. (1967). Structure of manganese carbides. Annales de Chimie, Vol. 2(6), p353-366.

Bowles, J. S. (1951). Crystallographic mechanism of the martensite reaction in iron-carbon alloys. Acta Crystallographica, Vol. 4, p162-171.

Bragg, W. L. (1912). The diffraction of short electromagnetic waves by a crystal. Proceedings of the Cambridge Philosophical Society, Vol. 17, p43-57.

Burke, J. and W. S. Owen (1954). Kinetics of first-stage graphitization in iron-carbon-silicon alloys. Journal of the Iron and Steel Institute, Vol. 176(February), p147-155.

Butler, B. D. and J. B. Cohen (1992). The location of interstitial carbon in austenite. Journal de Physique I, Vol. 2(6), p1059-1065.

Caglioti, G., A. Paoletti, et al. (1958). Choice of collimators for a crystal spectrometer for neutron diffraction. Nuclear Instruments, Vol. 3, p223-228.

Cahn, R. W., P. Haasen, et al., Editors. (1992). Constitution and properties of steels, Materials science and technology. VCH.

Caul, M. and V. Randle (1997). Microtexture analysis of interstitial-free steel. Materials Characterization, Vol. 38(3), p155-163.

Chang, P. and A. G. Preban (1985). The effect of ferrite grain size and martensite volume fraction on the tensile properties of dual-phase steel. Acta Metallurgica, Vol. 33(5), p897-903.

Chen, P. C., B. O. Hall, et al. (1980). Atomic displacements due to C in Fe Ni C martensite. Metallurgical Transactions, Vol. 11A(8), p1323-1331.

Chen, P. C. and P. G. Winchell (1980). Martensite lattice changes during tempering. Metallurgical Transactions, Vol. 11A(8), p1333-1339.

Cheng, L., A. Bottger, et al. (1990). Lattice parameters of iron-carbon and iron-nitrogen martensites and austenites. Scripta Metallurgica et Materialia, Vol. 24(3), p509-514.

Choi, C. S., S. Sharpe, et al. (1996). Neutron diffraction study of austempered ductile iron. Metallurgical and Materials Transactions, Vol. 27A(4), p923-928.

Choi, S. D., H. S. Kim, et al. (2002). Annealing behaviour of retained austenite in low carbon steel: Real time synchrotron X-ray scattering study. Journal of Materials Science Letters, Vol. 21(5), p353-355.

Christian, J. W. (1965). Military transformations: an introductory survey. Physical properties of martensite and bainite, Scarborough, UK, 10-12 May 1965. Iron and Steel Institute. p1-19.

Christian, J. W. and D. V. Edmonds (1983). The bainite transformation. Phase Transformations in Ferrous Alloys, Philadelphia, Pennsylvania, USA. Metallurgical Society of AIME. p293-325.

Clarke, A. (2006). Carbon partitioning into austenite from martensite in a silicon-containing high strength sheet steel - T6142. Advanced Steel Processing and Products Research Center, Colorado School of Mines. PhD Thesis.

Clarke, A. J., J. G. Speer, et al. (2009). Influence of carbon partitioning kinetics on final austenite fraction during quenching and partitioning. Scripta Materialia, Vol. 61(2), p149-152.

Clarke, A. J., J. G. Speer, et al. (2008). Carbon partitioning to austenite from martensite or bainite during the quench and partition (Q&P) process: A critical assessment. Acta Materialia, Vol. 56(1), p16-22.

Cochardt, A. W., G. Schoek, et al. (1955). Interaction between dislocations and interstitial atoms in body-centered cubic metals. Acta Metallurgica, Vol. 3(Nov), p533-537.

Cottrell, A. H. and B. A. Bilby (1949). Dislocation theory of yielding and strain aging of iron. Proceedings of the Physical Society, Vol. 62A, p49-62.

Cullity, B. D. (1956). Elements of X-Ray Diffraction. Addison-Wesley Publishing Company Inc.

Dasarathy, C. (1959). Austenite formation in the hypo- and hypereutectoid and eutectoid plain carbon steels. Transactions of the Indian Institute of Metals, Vol. 12, p135-153.

Davies, R. G. (1977). On the ductility of dual phase steels. Formable HSLA and dual-phase steels, Chicago, Illinois, USA, 26 October 1977. The metallurgical society of AIME. p25-39.

Davies, R. G. (1978a). The deformation behavior of a vanadium-strengthened dual phase steel. Metallurgical Transactions, Vol. 9A(1), p41-52.

Davies, R. G. (1978b). The mechanical properties of zero-carbon ferrite-plus-martensite structures. Metallurgical Transactions, Vol. 9A(3), p451-455.

Davies, R. G. and C. L. Magee (1979). Physical metallurgy of automotive high-strength steels. Journal of Metals, Vol. 31(11), p17-23.

Davies, R. H., A. T. Dinsdale, et al. (2002). MTDATA - thermodynamic and phase equilibrium software from the national physical laboratory. CALPHAD: Computer Coupling of Phase Diagrams and Thermochemistry, Vol. 26(2), p229-271.

De, A. K., S. Vandeputte, et al. (1999). Static strain aging behavior of ultra low carbon bake hardening steel. Scripta Materialia, Vol. 41(8), p831-837.

De Cristofaro, N. and R. Kaplow (1977). Interstitial atom configurations in stable and metastable Fe-N and Fe-C solid solutions. Metallurgical Transactions, Vol. 8A(1), p35-44.

De Meyer, M., D. Vanderschueren, et al. (1999). The influence of the substitution of Si by Al on the properties of cold rolled C-Mn-Si TRIP steels. Iron and Steel Institute of Japan International, Vol. 39(8), p813-822.

De Moor, E. (2009). Assessment of quenching and partitioning as a fundamentally new way of producing advanced high strength martensitic steel grades with improved ductility. Faculty of Engineering, University of Gent. PhD Thesis.

De Moor, E., S. Lacroix, et al. (2006). Dilatometric study of the Quench and Partitioning process. The 3rd International Conference on Advanced Structural Steels, Gyeongju, Korea, 22-24 August 2006.

Dickson, M. J. (1969). Significance of texture parameters in phase analysis by x-ray diffraction. Journal of Applied Crystallography, Vol. 2(4), p176-180.

Dieter, G. E. (1988). Mechanical metallurgy. SI Metric Edition, Mc Graw Hill.

Dijk, N. H. v., A. M. Butt, et al. (2005). Thermal stability of retained austenite in TRIP steels studied by synchrotron X-ray diffraction during cooling. Acta Materialia, Vol. 53(20), p5439-5447.

Duggin, M. J., D. Cox, et al. (1966). Structural studies of the carbides (Fe,Mn)3C and (Fe,Mn)5C2. Transactions of the Metallurgical Society of AIME, Vol. 236(9), p1342-1346.

Duggin, M. J. and L. J. E. Hofer (1966). Nature of X-iron carbide. Nature, Vol. 212(5059), p248-250.

Dyson, D. J. and B. Holmes (1970). Effect of alloying additions on the lattice parameter of austenite. Journal of the Iron and Steel Institute, Vol. 208(5), p469-474.

Easterling, K. E. and P. R. Swann (1971). Nucleation of martensite in small particles. Acta Metallurgica, Vol. 19(2), p117-121.

Edmonds, D. V., K. He, et al. (2007). Microstructural features of 'quenching and partitioning': a new martensitic steel heat treatment. Materials Science Forum, Vol. 539-543 (Pt. 5, THERMEC 2006), p4819-4825.

Edmonds, D. V., K. He, et al. (2006). Quenching and partitioning martensite - A novel steel heat treatment. Materials Science and Engineering, Vol. A438-A440, p25-34.

Efron, L. I. (2004). Recent advances in metallurgy and the technology used to make steels for the automobile industry. Metallurgist, Vol. 48(3-4), p169-173.

Ellingham, H. J. T. (1944). Reducibility of oxides and sulphides in metallurgical processes. Journal of the Society of Chemical Industry, Vol. 63(May), p125-133.

Elsen, P. and H. P. Hougardy (1993). On the mechanism of bake-hardening. Steel Research, Vol. 64(8-9), p431-436.

Fasiska, E. J. and G. A. Jeffrey (1965). On the cementite structure. Acta Crystallographica, Vol. 19(3), p463-471.

Fletcher, D. A., R. F. McMeeking, et al. (1996). The United Kingdom Chemical Database Service. Journal of Chemical Information and Computer Sciences, Vol. 36(4), p746-749.

Fujine, M., S. Hayashi, et al. (2004). Vehicle mass reduction based on material technologies. Toyota technical review, Vol. 53(November), p39-47.

Fujita, F. E. and A. C. Damask (1964). Kinetics of carbon precipitation in irradiated iron. II. Electrical resistivity measurements. Acta Metallurgica, Vol. 12(4), p331-339.

Fujita, F. E., T. Moriya, et al. (1970). Low temperature phase and tetrahedral site of carbon in iron-carbon martensite. International Conference on Science and Technology of Iron and Steel, Tokyo, Japan. Iron and Steel Institute Japan. Vol. 11, Part 2, Section 6, p1273-1279.

Garmong, G. and R. B. Thompson (1973). Theory for the mechanical properties of metal-matrix composites at ultimate loading. Metallurgical Transactions, Vol. 4(3), p863-873.

Gavrilyuk, V. G., V. A. Duz, et al. (1987). Interaction of carbon and nitrogen atoms with dislocations in austenite. The physics of metals and metallography (Translation of Fizika metallov i metallovedenie), Vol. 64(6), p1132-1135.

Gavrilyuk, V. G. and Y. N. Yagodzinskiy (1986). Determination of the binding energy of interstitial impurities with dislocations from Snoek-Koester relaxation data. The physics of metals and metallography (Translation of Fizika metallov i metallovedenie), Vol. 62(6), p1229-1231.

Gerberich, W. W., C. F. Martin, et al. (1965). Serrated stress-strain curves of metastable austenite in alloy steels. Transactions of the American Society for Metals, Vol. 58(1), p85-94.

Gerdemann, F. L. H. (2004). Microstructure and Hardness of 9260 Steel Heat-Treated by the Quenching and Partitioning Process. Department of Materials Science and Testing, Aachen University of Technology (RWTH). Diploma Thesis.

Gerdemann, F. L. H., J. G. Speer, et al. (2004). Microstructure and hardness of steel grade 9260 heat-treated by the quenching and partitioning (Q&P) process. Material Science and Technology 2004, New Orleans, Louisiana, USA, 26-29 September 2004. Association for Iron & Steel Technology. Vol. 1, p439-449.

Giamei, A. F. and E. J. Freise (1967). Optimization of x-ray diffraction quantitative analysis. Transactions of the Metallurgical Society of AIME, Vol. 239(11), p1676-1685.

Gladman, T. (1997). The physical metallurgy of microalloyed steels. First Edition, The Institute of Materials.

Gordine, J. and I. Codd (1969). The influence of silicon up to 1.5 wt-%on the tempering characteristics of a spring steel. Journal of the iron and steel institute, Vol. 207(April), p461-467.

Gorton, A. T., G. Bitsianes, et al. (1965). Thermal expansion coefficients for iron and its oxides from x-ray diffraction measurements at elevated temperatures. Transactions of the Metallurgical Society of AIME, Vol. 233(8), p1519-1525.

Grobner, P. (1954). Diagram of free energy of carbides versus temperature. Hutnicke Listy, Vol. 9, p272-274.

Grossmann, M. A. and R. L. Stephenson (1941). The effect of grain size on hardenability. Transactions of the American Society for Metals, Vol. 29(3), p1-13.

Gullberg, R. and R. Lagneborg (1966). X-ray determination of the volume fraction of phases in textured materials. Transactions of the Metallurgical Society of AIME, Vol. 236(10), p1482-1485.

Hadfield, R., S. R. Williams, et al. (1921). Magnetic mechanical analysis of manganese steel. Proceedings of the Royal Society of London, Vol. 98A, p297-302.

Hall, E. O. (1951a). The deformation and ageing of mild steel: II Characteristics of the Luders deformation. Proceedings of the Physical Society, Vol. B64(9), p742-747.

Hall, E. O. (1951b). The deformation and ageing of mild steel: III Discussion of results. Proceedings of the Physical Society, Vol. B64(9), p747-753.

Hanzaki, A. Z., P. D. Hodgson, et al. (1995a). The influence of bainite on retained austenite characteristics in Si-Mn TRIP steels. Iron and Steel Institute of Japan International, Vol. 35(1), p79-85.

Hanzaki, A. Z., P. D. Hodgson, et al. (1995b). Hot deformation characteristics of Si-Mn TRIP steels with and without Nb microalloy additions. Iron and Steel Institute of Japan International, Vol. 35(3), p324-331.

Hehemann, R. F. (1968). The bainite transformation. American Society for Metals Seminar on Phase Transformations, Detroit, Michigan, USA, 12-13 October 1968. American Society for Metals, Metals Park, Ohio, USA.

Hehemann, R. F., K. R. Kinsman, et al. (1972). A debate on the bainite reaction. Metallurgical Transactions, Vol. 3(5), p1077-1094.

Herbstein, F. H. and J. Smuts (1964). Comparison of x-ray and neutron diffraction refinements of the structure of cementite Fe3C. Acta Crystallographica, Vol. 17(10), p1331-1332.

Hillert, M. and J. Agren (2004a). On the definitions of paraequilibrium and orthoequilibrium. Scripta Materialia, Vol. 50(5), p697-699.

Hillert, M. and J. Agren (2004b). Reply to comments on "On the definition of paraequilibrium and orthoequilibrium". Scripta Materialia, Vol. 52(1), p87-88.

Hirotsu, Y. and S. Nagakura (1972). Crystal structure and morphology of the carbide precipitated from martensitic high-carbon steel during the first stage of tempering. Acta Metallurgica, Vol. 20(4), p645-655.

Hobbs, R. M., G. W. Lorimer, et al. (1972). Effect of silicon on the microstructure of quenched and tempered medium-carbon steels. Journal of the Iron and Steel Institute, Vol. 210(10), p757-764.

Holman, J. P. (2010). Heat transfer. Tenth Edition, Mc Graw Hill.

Honda, K. (1926). Is the direct change from austenite to troostite theoretically possible. Journal of the Iron and Steel Institute, Vol. 114, p417-420.

Honda, K. and K. Iwase (1927). On the transformation of retained austenite into martensite by stress. Science Reports of Tohoku Imperial University, Vol. 16, p1-8.

Honeycombe, R. W. K. and H. K. D. H. Bhadeshia (1995). Steels - Microstructure and properties. Second Edition, Edward Arnold.

Hong, S. C., J. C. Ahn, et al. (2007). Mechanical properties of high-si plate steel produced by the quenching and partitioning process. Metals and Materials International, Vol. 13(6), p439-445.

Hongyan, L. I. and J. Xuejun (2009). Microstructure and mechanical properties of 50SiMnNiNb steel by a novel quenching-partitioning-austempering heat treatment. Chinese journal of mechanical engineering, Vol. 22(5), p645-650.

Hossein-Nedjad, S. and M. R. Movaghar-Gharabagh (2008). Dislocation structure and crystallite size distribution in lath martensite determined by X-ray diffraction peak profile analysis. International Journal of Materials Research, Vol. 99(11), p1248-1255.

Howard, C. J. (1982). The approximation of asymmetric neutron powder diffraction peaks by sums of gaussians. Journal of Applied Crystallography, Vol. 15(6), p615-620.

Hsu, T. Y. and Z. Xu (2007). Design of structure, composition and heat treatment process for high strength steel. Materials Science Forum, Vol. 561-565(Part 3, PRICM6), p2283-2286.

Hu, H. (1976). Effects of phosphorus on the annealing texture, plastic anisotropy, and mechanical properties of low-carbon steels. Texture of Crystalline Solids, Vol. 2(2), p113-141.

Huizing, R. and J. A. Klostermann (1966). Martensite transformation in small (0.1-0.3 mm.)iron-nickel single crystals. Acta Metallurgica, Vol. 14(12), p1693-1702.

Hultgren, A. (1947). Isothermal transformation of austenite. Transactions of the American Society for Metals, Vol. 39, p915-989.

Hume-Rothery, W. and J. W. Christian (1946). The equilibrium diagrams of certain alloys of iron. Philosophical Magazine, Vol. 36, p835-842.

Hume-Rothery, W., G. V. Raynor, et al. (1942). The lattice spacings and crystal structure of cementite. Journal of the Iron and Steel Institute, Vol. Advance copy, p143-149.

Ikeda, S. and J. M. Carpenter (1985). Wide-energy-range, high-resolution measurements of neutron pulse shapes of polyethylene moderators. Nuclear Instruments and Methods in Physics Research, Vol. A239(3), p536-544.

ISIS website. ISIS Homepage. from http://www.isis.rl.ac.uk/

Jaffe, L. D. and J. H. Hollomon (1946). Hardenability and quench cracking. American Institute of Mining and Metallurgical Engineers, Vol. 13(1), pTechnical Publication No. 1927 (8 pages).

Jatczak, C. F. (1980). Retained austenite and its measurement by X-Ray diffraction. Society of Automotive Engineers. Report: 800426.

Jatczak, C. F., J. A. Larson, et al. (1980). Retained austenite and its measurements by X-Ray diffraction - An information manual. Society of Automotive Engineers. Report: SP453.

Jencus, P., P. Lukas, et al. (2004). Neutron diffraction studies of Si-Mn TRIP steel in situ upon thermomechanical processing. Journal of Neutron Research, Vol. 12(1-3), p243-248.

Jette, E. R. and E. S. Greiner (1933). X-ray study of iron-silicon alloys containing 0-15 percent silicon. American Institute of Mining and Metallurgical Engineers, Vol. 8, p259-275.

Jimenez-Melero, E., N. H. van Dijk, et al. (2007). Characterization of individual retained austenite grains and their stability in low-alloyed TRIP steels. Acta Materialia, Vol. 55(20), p6713-6723.

John, V. and C. Challinor (1997). Precoated strip combats corrosion. Materials World, Vol. 5(3), p136-137.

Johnson, W. A. and R. F. Mehl (1939). Reaction kinetics in processes of nucleation and growth. Transactions of the American Institute of Mining and Metallurgical Engineers, Vol. 1089, p416-442.

Judd, R. R. and H. W. Paxton (1968). Kinetics of austenite formation from a spheroidized ferrite carbide aggregate. Transactions of the Metallurgical Society of AIME, Vol. 242(2), p206-215.

Jun, H. J., S. H. Park, et al. (2004). Decomposition of retained austenite during coiling process of hot rolled TRIP-aided steels. Materials Science and Engineering A, Vol. 379(1-2), p204-209.

Kalish, D. and M. Cohen (1970). Structural changes and strengthening in the strain tempering of martensite. Materials Science and Engineering, Vol. 6(3), p156-166.

Kalish, D. and E. M. Roberts (1971). On the distribution of carbon in martensite. Metallurgical Transactions, Vol. 2(10), p2783-2790.

Karen, P., H. Fjellvag, et al. (1991). On the phase relations and structural and magnetic properties of the stable manganese carbides Mn23C6, Mn5C2, and Mn7C3. Acta Chemica Scandinavica, Vol. 45(6), p549-557.

Kaufman, L. and M. Cohen (1958). Thermodynamics and kinetics of martenitic transformations. Progress in Metal Physics, Vol. 7, p165-246.

Kenneford, A. S. and T. Williams (1957). Effect of some common alloying elements on the breakdown of martensite in a water-quenched 0.35% carbon steel. Journal of the Iron and Steel Institute, Vol. 185(April), p467-474.

Kim, A. M. (1968). History of the development of iron-carbon diagram. Metallovedenie i Termicheskaya Obrabotka Metallov (translated from), Vol. 1968(5), p11-19.

Kim, S. J., H. S. Kim, et al. (2007). Dilatometric study of the quench and partitioning (Q&P) process. Materials Science and Technology, Detroit, Michigan, USA, 16-20 September 2007. Greyden Press.

King, H. W. and S. G. Glover (1959). A resistometric study of the first stage of tempering in plain carbon steels. Journal of the Iron and Steel Institute, Vol. 193(October), p123-132.

Kinsman, K. R. and H. I. Aaronson (1967). Structure and growth of widmanstatten ferrite and bainite - written discussion. Transformation and Hardenability in Steels Symposium, February 27-28, 1967. p33-38.

Kisi, E. H. and C. J. Howard (2008). Applications of neutron powder diffraction. First Edition, Oxford University Press.

Koistinen, D. P. and R. E. Marburger (1959). A general equation prescribing the extent of the austenite-martensite transformation in pure iron-carbon alloys and plain carbon steels. Acta Metallurgica, Vol. 7(1), p59-60.

Koiwa, M. (2004). A note on Dr. J.L. Snoek. Materials Science & Engineering, Vol. A370(1-2), p9-11.

Kuo, K. and L. E. Persson (1954). A contribution to the constitution of the ternary system Fe-Mn-C. Journal of the Iron and Steel Institute, Vol. 178(September), p39-44.

Kurdjumov, G. and L. Lyssak (1947). The application of single crystals to the study of tempered martensite. Journal of the Iron and Steel Institute, Vol. 156(May), p29-36.

Kurdjumov, G. V. (1960). Phenomena occurring in the quenching and tempering of steels. Journal of the Iron and Steel Institute, Vol. 195(May), p26-48.

Larson, A. C. and R. B. Von Dreele (2004). General Structure Analysis System (GSAS). Los Alamos National Laboratory. Report: LAUR 86-748.

Law, N. C. and D. V. Edmonds (1980). The formation of austenite in a low-alloy steel. Metallurgical Transactions, Vol. 11A(1), p33-46.

Leslie, W. C. (1972). Iron and its dilute substitutional solid solutions. Metallurgical Transactions, Vol. 3(1), p5-26.

Li, H. Y., X. W. Lu, et al. (2010a). Microstructure and mechanical properties of an ultrahigh-strength 40SiMnNiCr steel during the one-step quenching and partitioning process. Metallurgical and Materials Transactions, Vol. 41A(5), p1284-1300.

Li, H. Y., X. W. Lu, et al. (2010b). Bainitic transformation during the two-step quenching and partitioning process in a medium carbon steel containing silicon. Materials Science & Engineering, Vol. A527(23), p6255-6259.

Lihl, F. and H. Mayer (1960). The penetration depth of the deformation during the preparation of metallographic samples. Zeitschrift fur Metallkunde, Vol. 51(186-190).

Lipson, H. and N. J. Petch (1940). The crystal structure of cementite, Fe3C. Journal of the Iron and Steel Institute, Vol. Advance copy, p95-103.

Listhuber, F. E. (1970). High strength micro-alloyed steels. Symposium Low Alloy High Strength Steels, Nuremburg, Germany, 21-23 May 1970. The Metallurg Companies. p29-34.

Liu, X., F. Zhong, et al. (1995). Lattice-parameter variation with carbon content of martensite. I. X-ray-diffraction experimental study. Physical Review B, Vol. 52(14), p9970-9978.

Llewellyn, D. T. (1992). Steels - Metallurgy and applications. First Edition, Butterworth Heinemann.

Llewellyn, D. T. and R. C. Hudd (1998). Steels - Metallurgy and applications. Third Edition, Butterworth Heinemann.

Lobo, J. A. and G. H. Geiger (1976a). Thermodynamics and solubility of carbon in ferrite and ferritic iron-molybdenum alloys. Metallurgical Transactions, Vol. 7A(9), p1347-1357.

Lobo, J. A. and G. H. Geiger (1976b). Thermodynamics of carbon in austenite and iron-molybdenum austenite. Metallurgical Transactions, Vol. 7A(9), p1359-1364.

Lottermoser, W., K. Steiner, et al. (2002). The electric field gradient in synthetic fayalite alpha-Fe_2SiO_4 at moderate temperatures. Physics and Chemistry of Minerals, Vol. 29(2), p112-121.

Lutts, A. and P. Gielen (1971). The precise determination of the lattice parameter of alpha-iron and some of its alloys. Journal of Applied Crystallography, Vol. 4(Part 3), p242-250.

Luzginova, N., L. Zhao, et al. (2007). Evolution and thermal stability of retained austenite in SAE 52100 bainitic steel. Materials Science and Engineering A, Vol. 448(1-2), p104-110.

Ma, C. B., T. Ando, et al. (1983). Chi-carbide in tempered high carbon martensite. Metallurgical Transactions, Vol. 14A(6), p1033-1045.

Maalekian, M. and E. Kozeschnik (2008). A thermodynamic model for carbon trapping in lattice defects. Computer Coupling of Phase Diagrams and Thermochemistry, Vol. 32(4), p650-654.

Magee, C. L. (1970). The nucleation of martensite. American Society for Metals Seminar on Phase Transformations, Detroit, Michigan, USA, 12-13 October 1968. American Society for Metals, Metals Park, Ohio, USA.

Magee, C. L. (1982). The role of weight reducing materials in automotive fuel savings. Society of Automotive Engineers. Report: 820147.

Mahieu, J., S. Claessens, et al. (2001). Galvanizability of high-strength steels for automotive applications. Metallurgical and Materials Transactions, Vol. 32A(11), p2905-2908.

Mahieu, J., J. Maki, et al. (2002). Phase transformation and mechanical properties of Si-free CMnAl transformation-induced plasticity-aided steel. Metallurgical and Materials Transactions, Vol. 33A(8), p2573-2580.

Maki, J., J. Mahieu, et al. (2003). Galvanisability of silicon free CMnAl TRIP steels. Materials Science and Technology, Vol. 19(1), p125-131.

MAP website. Materials Algorithms Project Homepage. from http://www.msm.cam.ac.uk/map/mapmain.html

Marder, A. R. and G. Krauss (1971). The morphology of martensite in iron alloys. Metallurgical Transactions, Vol. 2(9), p2343-2357.

Marketz, F. and F. D. Fischer (1995). A mesoscale study on the thermodynamic effect of stress on martensitic transformation. Metallurgical and Materials Transactions, Vol. 26A(2), p267-278.

Massalski, T. B. (1968). Massive transformations. American Society for Metals Seminar on Phase Transformations, Detroit, Michigan, USA, 12-13 October 1968. American Society for Metals, Metals Park, Ohio, USA.

Matas, S. and R. F. Hehemann (1960). Retained austenite and the tempering of martensite. Nature, Vol. 187(4738), p685-686.

Matlock, D. K., V. E. Brautigam, et al. (2003). Application of the Quenching and Partitioning (Q&P) process to a medium-carbon, high-Si microalloyed bar steel. Materials Science Forum, Vol. 426-432(Pt. 2, THERMEC'2003), p1089-1094.

Matlock, D. K. and J. G. Speer (2006). Microstructural aspects of advanced high strength sheet steels. International conference on advanced structural steels, Arlington, Virginia, USA.

Matlock, D. K. and J. G. Speer (2010). Processing opportunities for new advanced high-strength sheet steels. Materials and Manufacturing Processes, Vol. 25(1-3), p7-13.

Mazur, J. (1950). Lattice parameters of martensite and austenite. Nature, Vol. 166(4228), p828-828.

Mazzone, G. (1987). The distribution of carbon among interstitial sites of the FCC iron-alloy lattice. Journal of Applied Crystallography, Vol. 20(3), p187-190.

McClune, W. F., T. M. Maguire, et al., Editors. (1982). Powder Diffraction File - Inorganic Phases. JCPDS - International Centre for Diffraction Data.

McLellan, R. B. and C. Ko (1987). The carbon-carbon interaction energy in iron-carbon solid solutions. Acta Metallurgica, Vol. 35(8), p2151-2156.

Mikus, E. B., T. J. Hughel, et al. (1960). The dimensional stability of a precision ball-bearing material. Transactions of the American Society for Metals, Vol. 52, p307-315.

Mileiko, S. T. (1969). Tensile strength and ductility of continuous fibre composites. Journal of Materials Science, Vol. 4(11), p974-977.

Miller, M. K., P. A. Beaven, et al. (1981). A study of the early stages of tempering of iron-carbon martensites by atom probe field ion microscopy. Metallurgical Transactions, Vol. 12A(7), p1197-1204.

Miller, R. L. (1964). A rapid x-ray method for the determination of retained austenite. Transactions of the American Society for Metals, Vol. 57(4), p892-899.

Molinder, G. (1956). A quantitative study of the formation of austenite and the solution of cementite at different austenitizing temperatures for a 1.27% C steel. Acta Metallurgica, Vol. 4(November), p565-571.

Mujahid, S. A. and H. K. D. H. Bhadeshia (1992). Partitioning of carbon from supersaturated ferrite plates. Acta Mettallurgica et Materialia, Vol. 40(2), p389-396.

Nagakura, S. and M. Toyoshima (1979). Crystal structure and morphology of the ordered phase in iron-carbon martensite. Transactions of the Japan Institute of Metals, Vol. 20(3), p100-110.

National Physical Laboratory (2006). MTDATA. Version 4.80. National Physical Laboratory

Navara, E., B. Bengtsson, et al. (1986). Austenite formation in manganese-partitioning dual-phase steel. Materials Science and Technology, Vol. 2(12), p1196-1201.

Navara, E. and R. Harrysson (1984). On the mechanism of austenite formation during inter- and subcritical annealing of a carbon-manganese steel. Scripta Metallurgica, Vol. 18(6), p605-610.

Naylor, J. P. (1979). The influence of the lath morphology on the yield stress and transition temperature of martensitic-bainitic steels. Metallurgical Transactions, Vol. 10A(7), p861-873.

Naylor, J. P. and R. Blondeau (1976). The respective roles of the packet size and the lath width on toughness. Metallurgical Transactions, Vol. 7A(6), p891-894.

Nelson, W. (1940). The use of salt baths. Metallurgia, Vol. 22(June), p55-57.

Ohman, E. (1931). X-ray investigations on the crystal structure of hardened steel. Journal of the Iron and Steel Institute, Vol. 123, p445-463.

Okudera, H. and H. Toyara (1998). Crystal structure refinements of InxFe3-xO4 spinels by the rietveld method. Zeitschrift fuer Kristallographie, Vol. 213(9), p461-465.

Oliveira, F. L. G., M. S. Andrade, et al. (2007). Kinetics of austenite formation during continuous heating in a low carbon steel. Materials Characterization, Vol. 58(3), p256-261.

Onink, M., C. M. Brakman, et al. (1993). The lattice parameters of austenite and ferrite in Fe-C alloys as functions of carbon concentration and temperature. Scripta Metallurgica et Materialia, Vol. 29(8), p1011-1016.

Park, K. K., S. T. Oh, et al. (2002). In situ deformation behavior of retained austenite in TRIP steel. Materials Science Forum, Vol. 408-412 (Pt. 1), p571-576.

Parr, J. G. (1952). X-ray investigation of the epsilon phase in an iron-manganese alloy. Journal of the Iron and Steel Institute, Vol. 171(6), p137-141.

Pati, S. R. and M. Cohen (1971). Kinetics of isothermal martensitic transformations in an iron-nickel-manganese alloy. Acta Metallurgica, Vol. 19(12), p1327-1332.

Perlade, A., O. Bouaziz, et al. (2003). A physically based model for TRIP-aided carbon steels behaviour. Materials Science & Engineering, Vol. A356(1-2), p145-152.

Petch, N. J. (1942). The positions of the carbon atoms in austenite. Journal of the Iron and Steel Institute, Vol. 145(1), p111-128.

Petch, N. J. (1953). The cleavage strength of polycrystals. Journal of the Iron and Steel Institute, Vol. 174(May), p25-28.

Porter, D. and K. Easterling (1992). Phase transformations in metals and alloys. Second Edition, Chapman and Hall.

Qiu, D. and W.-Z. Zhang (2003). A systematic study of irrational precipitation crystallography in fcc-bcc systems with an analytical O-line method. Philosophical Magazine, Vol. 83(27), p3093-3116.

Rashid, M. S. (1977). Relationship between steel microstructure and formability. Formable HSLA and dual-phase steels, Chicago, Illinois, USA, 26 October 1977. The metallurgical society of AIME. p1-24.

Ray, R. K., J. J. Jonas, et al. (1994). Transformation textures in steels. Iron and Steel Institute of Japan International, Vol. 34(12), p927-942.

Reynolds, J. E. and M. B. Bever (1952). On the reversal of the strain induced martensitic transformation in the copper-zinc system. Journal of Metals (Transactions), Vol. 4, p1065-1066.

Ridley, N., H. Stuart, et al. (1969). Lattice parameters of iron-carbon austenites at room temperature. Transactions of the American Institute of Mining and Metallurgical Engineers, Vol. 245(8), p1834-1836.

Rietveld, H. M. (1969). A profile refinement method for nuclear and magnetic structures. Journal of Applied Crystallography, Vol. 2(Part 2), p65-71.

Rizzo, F., A. R. Martins, et al. (2007). Quenching and partitioning of Ni-added high strength steels. Materials Science Forum, Vol. 539-543 (Pt. 5, THERMEC 2006), p4476-4481.

Rizzo, F. C., D. V. Edmonds, et al. (2005). Carbon enrichment of austenite and carbide precipitation during the quenching and partitioning (Q&P) process. Solid-Solid Phase Transformations in Inorganic Materials, Phoenix, Arizona, USA, 29 May - 3 June 2005. Metals & Materials Society. Vol. 1, p535-544.

Roberts, C. S. (1953). Effect of carbon on the volume fractions and lattice parameters of retained austenite and martensite. Journal of Metals, Vol. 5(February), p203-204.

Roberts, C. S., B. L. Averbach, et al. (1953). The mechanism and kinetics of the first stage of tempering. Transactions of the American Society for Metals, Vol. 45, p576-604.

Robertson, J. M. (1929). The microstructure of rapidly cooled steel. Journal of the Iron and Steel Institute, Vol. 119, p391-419.

Rollason, E. C. (1968). Metallurgy for engineers. Third Edition, Edward Arnold.

Roosz, A., Z. Gacsi, et al. (1983). Isothermal formation of austenite in eutectoid plain carbon steel. Acta Metallurgica, Vol. 31(4), p509-517.

Ruhl, R. C. and M. Cohen (1969). Splat quenching of iron-carbon alloys. Transactions of the Metallurgical Society of AIME, Vol. 245(2), p241-251.

Sadykov, V. A., L. A. Isupova, et al. (1996). Effect of mechanical activation on the real structure and reactivity of iron (III) oxide with corundum-type structure. Journal of Solid State Chemistry, Vol. 123(2), p191-202.

Saito, N., K. Abiko, et al. (1993). Effect of silicon on the kinetics of e-carbide precipitation in high purity iron-carbon alloys. Materials Transactions, Japanese Institute of Metals, Vol. 34(3), p202-209.

Saleh, M. H. and R. Priestner (2001). Retained austenite in dual-phase silicon steels and its effect on mechanical properties. Journal of Materials Processing Technology, Vol. 113(1-3), p587-593.

Samek, L., E. De Moor, et al. (2006). Influence of alloying elements on the kinetics of strain-induced martensitic nucleation in low-alloy, multiphase high-strength steels. Metallurgical and Materials Transactions, Vol. 37A(1), p109-124.

Samsonov, G. V. and L. A. Gaevskaya (1976). Study of the depth of the disturbed layer in refractory metals after abrasive finishing with micropowders of titanium, niobium, or tungsten carbides. Translated from Poroshkovaya Metallurgiya, Vol. 5(161), p24-27.

Samuels, L. E. (1957). The nature of mechanically polished metal surfaces: The surface deformation produced during the abrasion and polishing of zinc. Journal of the Institute of Metals, Vol. 86(Part 1), p43-48.

Samuels, L. E. (1985). Abrasives - Their use in the machining of metals. Physics in Technology, Vol. 16(5), p214-220.

Sandvik, B. P. J. and C. M. Wayman (1983). Some crystallographic characteristics of the (252)f martensite transformation in iron-alloys. Metallurgical Transactions, Vol. 14A(12), p2469-2477.

Santofimia, M. J., J. G. Speer, et al. (2009). Influence of interface mobility on the evolution of austenite-martensite grain assemblies during annealing. Acta Materialia, Vol. 57(15), p4548-4557.

Santofimia, M. J., L. Zhao, et al. (2008). Model for the interaction between interface migration and carbon diffusion during annealing of martensite-austenite microstructures in steels. Scripta Materialia, Vol. 59(2), p159-162.

Sarikaya, M., G. Thomas, et al. (1981). Solute element partitioning and austenite stabilization in steels. International Conference on Solid-Solid Phase Transformations, Carnegie Mellon University, Pittsburgh, Pennsylvania, USA. Metallurgical Society of AIME.

Sarrak, V. I. and S. O. Suvorova (1969). Energy of elastic interaction between dislocations and interstitial atoms in alpha iron. The physics of metals and metallography (Translation of Fizika metallov i metallovedenie), Vol. 28(5), p941-943.

Schmatz, D. J. and V. F. Zackay (1959). Mechanical properties of deformed metastable austenitic ultra high strength steel. Transactions of the American Society for Metals, Vol. 51, p476-494.

Scott, C. P. and J. Drillet (2007). A study of the carbon distribution in retained austenite. Scripta Materialia, Vol. 56(6), p489-492.

Seki, I. and K. Nagata (2005). Lattice constant of iron and austenite including its supersaturation phase of carbon. Iron and Steel Institute of Japan International, Vol. 45(12), p1789-1794.

Sherif, M. Y., C. GarciaMateo, et al. (2004). Stability of retained austenite in TRIP-assisted steels. Materials Science and Technology, Vol. 20(3), p319-322.

Shiflet, G. J., J. R. Bradley, et al. (1978). A re-examination of the thermodynamics of the proeutectoid ferrite transformation in Fe-C alloys. Metallurgical Transactions, Vol. 9A(7), p999-1008.

Sinha, A. K. (1989). Ferrous physical metallurgy. First Edition, Butterworths.

Smith, R. P. (1953). Diffusivity of carbon in iron by the steady-state method. Acta Metallurgica, Vol. 1(September), p578-587.

Snoek, J. L. (1941). Effect of small quantities of carbon and nitrogen on the elastic and plastic properties of iron. Physica, Vol. 8(7), p711-733.

Snoek, J. L. (1942). Tetragonal martensite and elastic after effect in iron. Physica, Vol. 9(8), p862-864.

Speer, J. G., D. V. Edmonds, et al. (2004). Partitioning of carbon from supersaturated plates of ferrite, with application to steel processing and fundamentals of the bainite transformation. Current Opinion in Solid State and Materials Science, Vol. 8(3-4), p219-237.

Speer, J. G., R. E. Hackenberg, et al. (2007). Influence of interface migration during annealing of martensite/austenite mixtures. Philosophical Magazine Letters, Vol. 87(6), p379-382.

Speer, J. G., D. K. Matlock, et al. (2003). Carbon partitioning into austenite after martensite transformation. Acta Materialia, Vol. 51(9), p2611-2622.

Speer, J. G., D. K. Matlock, et al. (2004). Comments on "On the definitions of paraequilibrium and orthoequilibrium" by M. Hillert and J. Agren, Scripta Materialia, 50, 697–9 (2004). Scripta Materialia, Vol. 52(1), p83-85.

Speer, J. G., F. C. Rizzo, et al. (2005). The "Quenching and Partitioning" process: background and recent progress. Materials Research, Vol. 8(4), p417-423.

Speer, J. G., A. M. Streicher, et al. (2003). Quenching and partitioning: a fundamentally new process to create high strength trip sheet microstructures. Austenite Formation and Decomposition, Proceedings of a Symposium held at the Materials Science & Technology Meeting, Chicago, Illinois, USA, 9-12 November 2003. Minerals, Metals & Materials Society.

Speich, G. R. (1969). Tempering of low-carbon martensite. Transactions of the Metallurgical Society of AIME, Vol. 245(12), p2553-2564.

Speich, G. R., V. A. Demarest, et al. (1981). Formation of austenite during intercritical annealing of dual-phase steels. Metallurgical Transactions, Vol. 12A(8), p1419-1428.

Speich, G. R. and W. C. Leslie (1972). Tempering of steel. Metallurgical Transactions, Vol. 3(5), p1043-1054.

Speich, G. R., A. Szirmae, et al. (1969). Formation of austenite from ferrite and ferrite-carbide aggregates, with appendix [on diffusion equations for pearlite dissolution]. Transactions of the Metallurgical Society of AIME, Vol. 245(5), p1063-1074.

Speich, G. R. and H. Warlimont (1968). Yield strength and transformation substructure of low-carbon martensite. Journal of the Iron and Steel Institute, Vol. 206(4), p385-392.

Steven, W. and A. G. Haynes (1956). The temperature of formation of martensite and bainite in low-alloy steels. Some effects of chemical composition. Journal of the Iron and Steel Institute, Vol. 183(August), p349-359.

Streicher, A. M., J. G. Speer, et al. (2004). Quenching and partitioning response of a Si-added TRIP sheet steel. International Conference on Advanced High-Strength Sheet Steels for Automotive Applications, Winter Park, Colorado, USA, 6-9 June 2004. Association for Iron and Steel Technology. Vol. 2004, p51-62.

Suryanarayana, C. and M. G. Norton (1998). X-Ray diffraction - A practical approach. Plenum Press.

Sutton, A. L. and W. Hume-Rothery (1955). The lattice spacings of solid solutions of titanium, vanadium, chromium, manganese, cobalt, and nickel in alpha-iron. Philosophical Magazine, Vol. 46(December), p1295-1309.

Swarr, T. and G. Krauss (1976). The effect of structure on the deformation of as quenched and tempered martensite in an Fe-0.2Pct C alloy. Metallurgical Transactions, Vol. 7A(1), p41-48.

Sylwestrowicz, W. and E. O. Hall (1951). The deformation and ageing of mild steel. Proceedings of the Physical Society, Vol. B64(6), p495-502.

Takechi, H. (1987). Developments in high-strength hot and cold-rolled steels for automotive applications. Hot and cold-rolled sheet steels, Cincinnati, Ohio, USA, 12-13 October 1987. The metallurgical society of AIME. p117-138.

Takechi, H. (1994). Metallurgical aspects on interstitial free sheet steel from industrial viewpoints. Iron and Steel Institute of Japan International, Vol. 34(1), p1-8.

Tanaka, Y. and K. Shimizu (1981). Carbide formation upon tempering at low temperatures in iron-manganese-carbon alloys. Transactions of the Japan Institute of Metals, Vol. 22(11), p779-788.

Thomas, W. R. and G. M. Leak (1955). The binding energy of nitrogen in a dislocation. Proceedings of the Physical Society, London, Vol. 68B(12), p1001-1007.

Thompson, P., D. E. Cox, et al. (1987). Rietveld refinement of Debye-Scherrer synchrotron x-ray data from alumina. Journal of Applied Crystallography, Vol. 20(2), p79-83.

Toby, B. H. (2001). EXPGUI, a graphical user interface for GSAS. Journal of Applied Crystallography, Vol. 34(2), p210-213.

Totten, G. E., C. E. Bates, et al., Editors. (1993). Handbook of quenchants and quenching technology. ASM International.

Towers, T. A. and J. H. Woodhead (1994). The effects of small additions of titanium on the yielding characteristics of mild steel. Titanium technology in microalloyed steels, The University of Sheffield. The Institute of Materials. p1-9.

Traint, S., A. Pichler, et al. (2002). Influence of silicon, aluminium, phosphorous and copper on the phase transformations of low alloyed TRIP-steels. Steel Research, Vol. 73(6+7), p259-266.

Tsukatani, I., S. Hashimoto, et al. (1991). Effects of silicon and manganese addition on mechanical properties of high-strength hot-rolled sheet steel containing retained austenite. Iron and Steel Institute of Japan International, Vol. 31(9), p992-1000.

Tsunoyama, K. (1998). Metallurgy of ultra-low-C interstitial-free sheet steel for automobile applications. Physica Status Solidi A: Applied Research, Vol. 167(2), p427-433.

Turley, D. M. and L. E. Samuels (1985). The nature of mechanically polished surfaces of copper: Polishing with fine diamond abrasives. Metallography, Vol. 18(2), p149-160.

Uhrenius, B. (1973). Optimization of parameters describing the carbon-metal interaction in ternary austenite. Scandinavian Journal of Metallurgy, Vol. 2(4), p177-182.

USDOD (1977). Salts, Heat-treating (for metals). US Department of Defense. Designation: MIL-S-10699B.

VanderVoort, G. F., Editor. (2004). Metallography and microstructures, ASM handbook. ASM International.

Wagenblast, H. and A. C. Damask (1962). Kinetics of carbon precipitation in irradiated iron. Physics and Chemistry of Solids, Vol. 23, p221-227.

Wagenblast, H., F. E. Fujita, et al. (1964). Kinetics of carbon precipitation in irradiated iron. IV. Electron-microscope observations. Acta Metallurgica, Vol. 12(4), p347-353.

Wang, X. D., N. Zhong, et al. (2009). Novel ultrahigh-strength nanolath martensitic steel by quenching-partitioning-tempering process. Journal of Materials Research, Vol. 24(1), p260-267.

Wang, Y., S. Zhou, et al. (2010). Study of a novel ultra-high strength steel with adequate ductility and toughness by Quenching-Partitioning-Tempering process. Materials Science Forum, Vol. 654-656(Part 1, PRICM7), p37-40.

Waugh, A. R., S. Paetke, et al. (1981). A study of segregation to the dislocation substructure in patented steel wire using atom-probe techniques. Metallography, Vol. 14(3), p237-251.

White, C. H. and R. W. K. Honeycombe (1962). Structural changes during the deformation of high-purity iron-manganese-carbon alloys. Journal of the Iron and Steel Institute, Vol. 200(June), p457-466.

Whiteley, J. H. (1925). Observations on martensite and troostite. Journal of the Iron and Steel Institute, Vol. 111(1), p315-338.

Wilde, J., A. Cerezo, et al. (2000). Three-dimensional atomic-scale mapping of a Cottrell atmosphere around a dislocation in iron. Scripta Materialia, Vol. 43(1), p39-48.

Williamson, G. K. and R. E. Smallman (1953). X-ray evidence for the interstitial position of carbon in alpha-iron. Acta Crystallographica, Vol. 6, p361-362.

Willis, B. T. M. and H. P. Rooksby (1953). Change of structure of ferrous oxide at low temperature. Acta Crystallographica, Vol. 6, p827-831.

Wilson, D. V. (1957). Effects of plastic deformation on carbide precipitation in steel. Acta Metallurgica, Vol. 5(Jun), p293-302.

Wojdyr, M. (2007). Fityk - A curve fitting and data analysis program. Version 0.8.1.

Wojdyr, M. (2010). Fityk: a general-purpose peak fitting program. Journal of Applied Crystallography, Vol. 43(5-Part 1), p1126-1128.

Wuebbels, T., D. K. Matlock, et al. (2002). The effects of room temperature ageing on subsequent bake-hardening of automotive sheet steels. Society of Automotive Engineers. Report: 2002-01-0041.

Yang, D. Z., E. L. Brown, et al. (1985). The formation of austenite at low intercritical annealing temperatures in a normalized 0.08C-1.45Mn-0.21Si steel. Metallurgical Transactions, Vol. 16A(8), p1523-1526.

Yershov, V. M. and N. L. Oslon (1968). Change in the linear expansion coefficient of austenite on transformation to martensite. The physics of metals and metallography (Translation of Fizika metallov i metallovedenie), Vol. 25(5), p874-881.

Yi, J. J., K. J. Yu, et al. (1983). Role of retained austenite on the deformation of an iron-0.07 carbon-1.8 manganese-1.4 silicon dual-phase steel. Metallurgical Transactions, Vol. 14A(7), p1497-1504.

Young, R. A. (1993). The rietveld method. First Edition, Oxford University Press.

Zackay, V. F., E. R. Parker, et al. (1967). The enhancement of ductility in high-strength steels. Transactions of the American Society for Metals, Vol. 60(2), p252-259.

Zener, C. (1946). Kinetics of the decomposition of austenite. Metals Technology, Vol. 13(No. 1, Tech. Pub. No. 1925), p34.

Zener, C. (1948a). Theory of strain interaction of solute atoms. Physical Review, Vol. 74(6), p639-647.

Zener, C. (1948b). Elasticity and anelasticity of metals. First Edition, The University of Chicago Press.

Zhong, F., X. Liu, et al. (1995). Lattice-parameter variation with carbon content of martensite. II. Long-wavelength theory of the cubic-to-tetragonal transition. Physical Review B, Vol. 52(14), p9979-9987.

Zhong, N., X. Wang, et al. (2006). Interface migration between martensite and austenite during Quenching and Partitioning (Q&P) process. Journal of Materials Science Technology, Vol. 22(6), p751-754.

Zhong, N., X. D. Wang, et al. (2009). Enhancement of the mechanical properties of a Nb-microalloyed advanced high-strength steel treated by quenching-partitioning-tempering process. Materials Science & Engineering, Vol. A506(1-2), p111-116.

Zhou, S., Y. Wang, et al. (2010). Application of Quenching-Partitioning-Tempering process in hot rolled plate fabrication. Materials Science Forum, Vol. 654-656(Part 1, PRICM7), p82-85.

Zrnik, J., O. Muransky, et al. (2006). Retained austenite stability investigation in TRIP steel using neutron diffraction. Materials Science & Engineering, Vol. A437(1), p114-119.